

## ABSTRACT

AMIN, SAMIUL. Brownian Motion in Viscoelastic Media. (Under the direction of Dr. John van Zanten)

The motivation of this experimental research project is to gain a better understanding of the potential connection between the Brownian motion of a probe particle and the dynamic response of the suspending media. Specifically, the objective is to gain an understanding of the effects of longitudinal and transverse modes on the extracted viscoelastic parameters. This is achieved through tracer microrheology/mechanical rheometry study of three representative complex fluid systems. The chosen systems are, (1) aqueous poly ethylene oxide (PEO) solution, (2) cetyltrimethylammonium bromide/ sodium salicylate worm like micelle solutions and (3) a poly ethylene oxide-poly propylene oxide-polyethylene oxide (PEO-PPO-PEO) triblock copolymer, Pluronic™ F108 in an aqueous solution.

The PEO system exhibits a flat plateau followed by a diffusive escape at concentrations above 1wt% and exhibits increasing elasticity with increasing concentration. The PEO system tracer microrheology and mechanical rheometry measurements agree very well. A notable result for this system is that the longitudinal dynamical modes and structural features do not significantly affect the extracted viscoelastic data, as revealed through a sphere size sweep on the system.

The CTAB/NaSal system exhibits polyelectrolyte like behavior in that the static and dynamic properties in these solutions exhibit a complex dependence on ionization

and electrostatic screening effects. Tracer microrheology exhibits deviations from the mechanical rheometry measurements, as manifested through the creep compliance measurements. Sphere size sweeps and tracking of the deviation with the bulk longitudinal elastic modulus tends to indicate the possible role of the longitudinal dynamical modes on the extracted parameters.

Tracer microrheology measurements on the Pluronic<sup>TM</sup> F108 system exhibits widely varying behavior as the system passes from an isotropic micellar solution to an FCC soft crystal, illustrating the sensitivity of the tracer microrheology technique to changes in microstructure and dynamics. The tracer microrheology complex viscoelastic moduli  $G^*$  is seen to underestimate the mechanical rheometry  $G^*$  especially at high concentrations. Sphere size sweeps on the system indicates that the significance of the longitudinal dynamical modes in affecting the extracted viscoelastic properties is very sensitive to the intermicellar separation and probe size.

# BROWNIAN MOTION IN VISCOELASTIC MEDIA

By

SAMIUL AMIN

A thesis submitted to the Graduate Faculty of North  
Carolina State University in partial fulfillment of  
the requirements for the Degree of Doctor of  
Philosophy

**DEPARTMENT OF CHEMICAL ENGINEERING**

Raleigh  
2002

**APPROVED BY:**

---

Dr. Peter K. Kilpatrick

---

Dr. Jan Genzer

---

Dr. Christopher R. Daubert

---

Dr. John H. van Zanten  
Chairman of Advisory Committee

## **DEDICATION**

This work is dedicated to my parents, Hamida and Late Ruhul Quddus and my wife Sadaf for their never-ending support and encouragement in my educational endeavours and the pursuit of life.

## **BIOGRAPHY**

Samiul Amin was born in Dhaka, Bangladesh on March 4th 1971. He was the third child of his parents Ruhul and Hamida Quddus. After completing his high school education in the U.K and Bangladesh, he came to the United States in 1991 for the pursuit of higher education. He received a B.S. in Chemical Engineering from Rutgers University and an M.S. in Chemical Engineering from Johns Hopkins University under the direction of Dr. John van Zanten. After the completion of his M.S. degree he returned to Bangladesh for a period of three years at which time he met and married Sadaf Karim.

In 1999 Samiul decided to pursue a Phd under the direction of Dr. John van Zanten at NC State University. This led to his return to the United States in 1999 and the venture into the exciting world of Brownian motion in viscoelastic media. On a personal level, he and his wife were blessed with a daughter, Safiya Amin, in March 2001.

After completion of his degree Samiul will take up a position as a Project Analyst at IPA, a consulting firm for the chemical and process industries, based in Ashburn Virginia.

## **Acknowledgements**

First and foremost I am grateful to my advisor Dr. John van Zanten for his guidance support and encouragement during my pursuit of graduate studies both at NC State and at Johns Hopkins. Without his guidance and motivation it would never have been possible for me to consider pursuing a Phd. I am also grateful to the faculty and staff at the Chemical Engineering Department at NC State for their support, assistance and encouragement.

I must particularly thank Chris Kloxin, Jamie Arroway, Ke Wang, Shaun Tanner, Stephen Dees, and TJ Bell of the van Zanten group and Ahmed Abdala and Ahmed Eissa of Dr.Saad Khan;s group for their assistance support and encouragement.

## TABLE OF CONTENTS

	Page
List of Figures	ix
1. Introduction	1
1.1 Brownian Motion In Viscoelastic Media	1
1.2 Investigation of complex fluid dynamics through tracer particles: long time limit	1
1.3 Failure of Stoke Einstein Relationship: Long Time Limit	4
1.4 The Generalized Stokes-Einstein Relationship	6
1.5 Applicability of GSE to describe viscoelastic response of complex fluids	9
1.6 Diffusing Wave Spectroscopy: the passive tracer microrheology technique	12
1.7 Objectives of present study	15
References	17
2. Probe Brownian Motion in PEO Solutions	21
2.1 Abstract	21
2.2 Introduction	22
2.3 Materials and Methods	24
2.3.1 Diffusing Wave Spectroscopy	25
2.3.2 Mechanical Rheometry	27
2.4 Results and Discussion	27
2.4.1 Brownian Motion in Aqueous PEO Solutions	28
2.4.2 Comparison of Tracer Microrheology and Mechanical Rheometry	29
2.4.3 Sphere Size Sweep	31
2.4.4 Low Frequency or Long Time Behavior	32
2.4.5 High Frequency or Short Time Behavior	36
2.4.6 Creep Compliance Concentration Scaling	39
2.5 Conclusion	40
References	42
3. Concentration Fluctuations, Viscoelasticity and Brownian Motion in CTAB/NaSal Wormlike Micellar Solutions	44
3.1 Abstract	44
3.2 Introduction	47
3.3 Materials and Methods	50
3.3.1 Dynamic Light Scattering	51
3.3.2 Static Light Scattering	52

3.3.3 Tracer Microrheology	52
3.4 Results and Discussion	53
3.4.1 Phase Behavior	53
3.4.2 Dynamic Light Scattering	54
3.4.2.1 Evolution of the Electric Field Autocorrelation Function with CTAB Concentration	54
3.4.2.2 Effect of NaSal:CTAB Mole Ratio on the Hydrodynamic Correlation Length	56
3.4.2.3 Effect of CTAB Concentration on Hydrodynamic Correlation Length	58
3.4.2.4 Effect of NaSal:CTAB Mole Ratio on the Slow Mode Relaxation Time	61
3.4.2.5 Effect of CTAB Concentration on the Slow Mode Relaxation Time	64
3.4.2.6 Effect of NaSal:CTAB Mole Ratio on the Slow Mode Amplitude	67
3.4.2.7 Effect of CTAB Concentration on Slow Mode Amplitude	70
3.4.3 Static Light Scattering	72
3.4.3.1 The Rayleigh Ratio Behavior	72
3.4.3.2 Osmotic Compressibility dependence on CTAB and NaSal:CTAB molar ratio	78
3.4.3.3 Osmotic Pressure dependence on concentration...	80
3.4.3.4 Effect of NaSal:CTAB molar ratio and CTAB concentration on the static correlation length	82
3.4.4 Tracer Microrheology	86
3.4.4.1 Evolution of the Mean Squared Displacement	87
3.4.4.2 Evolution of the Time Dependent Diffusion Coefficient	88
3.4.4.3 Complex Viscoelastic Modulus Frequency Dependence	89
3.4.4.4 Maxwellian Fluid Analysis	90
3.4.4.5 Mechanical Rheometry Tracer Microrheology Comparison	95
3.5 Conclusions	103
References	107
4. Micellar Soft Crystal Rheology	110
4.1 Abstract	110
4.2 Introduction	111
4.3 Materials and Method	113
4.3.1 Determination of the linear viscoelastic regime	114
4.4 Results and Discussion	116
4.4.1 Frequency Dependence of $G'$ , $G''$	116

4.4.2 Behavior of the complex viscoelastic modulus, $G^*$	119
4.4.3 Behavior of the Creep Compliance, $J(t)$	121
4.4.4 Dynamic Viscosity Concentration Dependence	122
4.5 Conclusion	124
References	126
5. A Tracer microrheology study of a Triblock Copolymer in the Cubic Crystalline Phase	128
5.1 Abstract	128
5.2 Introduction	129
5.3 Materials and Methods	130
5.3.1 Diffusing Wave Spectroscopy	131
5.3.2 Mechanical Rheometry	133
5.4 Results and Discussion	133
5.4.1 Evolution of the Mean Squared Displacement	133
5.4.2 Zero shear viscosity concentration dependence	136
5.4.4 Complex viscoelastic modulus frequency dependence	141
5.4.5 Viscosity Frequency Dependence	143
5.4.6 Tracer microrheology and mechanical rheometry comparison	148
5.4.7 Sphere size sweep	150
5.5 Conclusions	155
References	157
6 High Frequency Elastic Modulus of Triblock Copolymer Soft Crystals	160
6.1 Abstract	160
6.2 Introduction	161
6.3 Materials and Methods	162
6.3.1 Diffusing Wave Spectroscopy	163
6.3.2 Mechanical Rheometry	165
6.4 Results and Discussion	166
6.4.1 Determination of High Frequency $G'$	166
6.4.2 High Frequency Elastic Modulus Behavior Modelling	168
6.4.3 High Frequency Elastic Modulus Frequency Dependence.	174
6.4.4 Concentration Dependence of High Frequency Modulus	176
6.5 Conclusions	177
References	179
7 Static Light Scattering Measurements Of Micellar Soft Crystals	181
7.1 Abstract	181
7.2 Introduction	182
7.3 Materials and Methods	184
7.4 Results and Discussion	184
7.4.1 Variation of the zero angle Rayleigh Ratio	184

7.4.2 Ornstein-Zernicke fit of data	189
7.4.3 Osmotic compressibility behavior	190
7.4.4 Osmotic Pressure Behavior	192
7.5 Conclusion	193
References	195
8. Conclusions and Recommendations for Future Work	197
8.1: Conclusions	197
8.1.1 Poly ethylene oxide (PEO) aqueous solution	197
8.1.2CTAB/NaSal Wormlike Micellar Solution	198
8.1.2.1Dynamic Light Scattering Measurements	199
8.1.2.2 Static Light Scattering Measurements	199
8.1.2.3Tracer Microrheology and Mechanical Rheometry	199
8.1.3 Pluronic <sup>TM</sup> F108 Triblock Copolymer	201
8.1.3.1 Mechanical Rheometry	201
8.1.3.2 Tracer Microrheology	202
8.1.3.3 Static Light Scattering	204
8.2 Recommendations for Future Work	205
9. Appendices	
9.1 FORTRAN program for computing mean squared displacement	208
9.2 MATLAB program for computing viscoelastic parameters from mean squared displacement.	212

## LIST OF FIGURES

	Page
<b>Chapter 2</b>	
2.1. Evolution of the mean squared displacement for PEO solutions	28
2.2. Comparison of the creep compliance obtained from mechanical rheometry and tracer microrheology	29
2.3. Frequency dependence of the complex viscoelastic moduli, $G^*$	30
2.4. Mean squared displacement for a 7% PEO solution having probe sizes	32
2.5. Creep Compliance for a 7% PEO solution having probe sizes 0.195	33
2.6. Terminal relaxation time PEO concentration dependence	34
2.7. Dependence of zero shear viscosity and diffusion coefficient	35
2.8. Evolution of the time dependent diffusion coefficient for PEO solutions	36
2.9. Evolution of $D(t)/D_L$ with time for four PEO solutions	38
2.10. Velocity autocorrelation function time dependency exponent variation	39
2.11. Creep compliance concentration scaling for 5 time decades	40
<b>Chapter 3</b>	
3.1. Viscoelastic behavior dependence on CTAB concentration and NaSal:CTAB molar ratio	54
3.2. The variation of the electric field autocorrelation function with CTAB	55
3.3. NaSal:CTAB mole ratio dependence of the hydrodynamic correlation length for five CTAB concentrations	56
3.4. CTAB concentration dependence of the hydrodynamic correlation length for three NaSal:CTAB mole ratios	59
3.5. NaSal:CTAB mole ratio dependence of the hydrodynamic correlation length	60

3.6.NaSal:CTAB mole ratio dependence of the slow or terminal relaxation time	61
3.7.CTAB concentration dependence of the slow or terminal relaxation time	65
3.8.CTAB concentration dependence of the slow or terminal relaxation time	66
3.9.NaSal:CTAB mole ratio dependence of the slow mode amplitude	68
3.10.A strong correlation is observed between the slow mode amplitude	69
3.11.CTAB concentration dependence of the slow mode amplitude	71
3.12.Variation of the Rayleigh Ratio with $q^2$	73
3.13.Variation of the Zero angle Rayleigh Ratio $R(0)$ with CTAB concentration	74
3.14.Variation of $R(0)$ with NaSal:CTAB molar ratios for CTAB concentrations	75
3.15.Variation of the $dn/dc$ with the NaSal:CTAB molar ratio	76
3.16.Variation of the osmotic compressibility with the NaSal:CTAB molar ratio	77
3.17.Osmotic compressibility variation with total concentration for solutions	78
3.18.Osmotic compressibility variation with CTAB concentration for solutions	79
3.19.Osmotic Pressure variation with CTAB concentration	81
3.20.Variation of static correlation length with NaSal:CTAB molar ratio	83
3.21.The static correlation concentration scaling exponent	85
3.22.Evolution of the mean square displacement time trace for a series of solutions	87
3.23.Evolution of the time trace of the time dependent diffusion coefficient for a series of solutions.	88
3.24.Frequency dependence of the complex viscoelastic moduli $G^*$ for a series of solutions	90
3.25.Probe diffusion rescaled with respect to the terminal relaxation time and plateau	91
3.26.Probe diffusion rescaled with respect to the plateau onset time predicted for a single relaxation time	92
3.27.Cole-Cole plot for three NaSal:CTAB molar ratios	93
3.28.Variation of the slow relaxation time with the NaSal:CTAB molar ratio	94
3.29.Comparison between viscoelastic parameters obtained from tracer microrheology and mechanical rheometry	96

3.30. Effect of multiplicative factor in $G^*$ agreement	98
3.31. Relaxation time variation with NaSal:CTAB molar ratio	99
3.32. Variation of zero shear viscosity with the NaSal:CTAB molar ratio	100
3.33. Variation of the deviation in the plateau modulus and the moduli Mg and K with the NaSal:CTAB molar ratio	101
3.34. Creep compliance for sphere sweep	102
 Chapter 4	
4.1. Stress dependence of the elastic modulus for a 24 wt % F108 sample	114
4.2. Creep compliance for a 24wt% F108 sample for five different stresses	115
4.3. Frequency dependence of the storage and loss moduli, $G'$ and $G''$	117
4.4. Frequency dependence of the complex viscoelastic modulus $G^*$	119
4.5. Concentration dependence of the plateau modulus	120
4.6. Creep compliance behavior for seven F108 concentrations	122
4.7. Frequency dependence of the viscosity for three F108 concentrations	123
4.8. Concentration dependence of the frequency scaling exponent of the viscosity	124
 Chapter 5	
5.1. Evolution of the $\langle \square r^2(t) \rangle$ time trace for a series of pluric concentrations	134
5.2. Variation of the rescaled $\langle \square r^2(t) \rangle$ with time. The $\langle \square r^2(t) \rangle$ was re-scaled with concentration	137
5.3. Variation of the zero shear viscosity with Pluronic F108 concentration	138
5.4. Evolution of $D(t)$ for Pluronic F108 samples	140
5.5. Variation of $D(t)$ with the probe displacement for pluronic concentrations	141
5.6. Frequency dependence of the $G^*$ for pluronic F108 samples	142
5.7. Frequency dependence of the viscosity for a series of Pluronic F108 samples	144
5.8. Frequency dependence of storage modulus $G'$ and loss modulus for three Pluronic F108 concentrations	146
5.9. Comparison between viscoelastic parameters extracted from tracer microrheology and mechanical rheometry	149
5.10. $\langle \square r^2(t) \rangle$ data for a sphere size sweep carried out on	

(a) 15% (b) 25% and (c) 35% Pluronic F108 solution	152
5.11. Creep compliance data for a sphere size sweep carried out on (a) 15% (b) 25% and (c) 35% Pluronic F108 solution	153
Chapter 6	
6.1. Frequency dependence of elastic modulus $G'$	167
6.2. High frequency tracer microrheology elastic modulus dependence on the relative compression	169
6.3. High frequency rheometry elastic modulus dependence on the relative compression	170
6.4. High frequency tracer microrheology elastic modulus dependence on the interparticle separation	173
6.5. High frequency elastic modulus frequency scaling factor dependence on the concentration	175
Chapter 7	
7.1. Variation of the Rayleigh Ratio with $q^2$	185
7.2. Variation of Zero Angle Rayleigh Ratio with Pluronic™ Concentration	187
7.3. Concentration dependence of the zero angle Rayleigh Ratio and the zero shear viscosity with Pluronic™ F108 concentration	188
7.4. An Ornstein-Zernicke fit of the angular dependence	189
7.5. Variation of the osmotic compressibility with concentration	191

# CHAPTER 1

## Introduction

---

### ***1.1. Brownian Motion In Viscoelastic Media***

The use of tracer microrheology as an experimental probe of soft material dynamics is gaining increasing interest (1-30). This is primarily due to the potential ability of microrheological techniques to probe the viscoelastic response of fluids through application of very small strains and over a much wider frequency range than accessible by conventional mechanical rheometry techniques. Passive tracer microrheological techniques monitor the Brownian fluctuations of micron size probe particles with the dynamical properties of the suspending matrix being inferred from the temporal evolution of the probe particles' mean squared displacement. The thermal or Brownian particle motion is typically measured with light scattering or optical microscopy techniques.

### ***1.2. Investigation of complex fluid dynamics through tracer particles: long time limit***

The use of tracer particles to probe the slow dynamics of complex viscoelastic media is however not a new concept(32-51). Over more than two decades, optical probe diffusion experiments have been carried out in order to gain a deeper insight into the slow dynamics of complex fluids. A large amount of this work has been carried out by Phillies et al(31-44) in which the dynamics of polymeric systems have been investigated through dynamic light scattering studies of complex fluid systems which have optical probe particles embedded in

them. These investigations have illustrated a wide spectrum of observed behavior, depending upon the complex fluid system and the size of the probe particles (31-44).

The concept of using probe particles to investigate the dynamic behavior of polymeric systems was pioneered by Turner and Hallett(45), in which they carried out quasi elastic laser light scattering (QELSS) on dextran solutions spanning in molecular weight from 20 to 2000 kDa and with spheres ranging from 47 to 123 nm. The measured diffusion coefficient was seen to obey the following relationship:

$$D_p = D_0 \exp(-\alpha c) \quad (1)$$

at each molecular weight.  $D_0$  is the probe diffusion coefficient in pure water and  $c$  is the polymer concentration. The  $\alpha$  parameter was seen to increase with polymer concentration. The value of  $D_p/D_0$  was however seen to be independent of probe radius. The relationship between the diffusion coefficient and the hydrodynamic radius of the diffusing probe particles were seen to follow the Stokes-Einstein relationship:

$$D = \frac{k_B T}{6\pi\eta R_h} \quad (2)$$

Here,  $K_b$  is Boltzmann's constant,  $T$  is the absolute temperature and  $R_h$  is the hydrodynamic radius of the diffusing particle. Dynamic Light Scattering experiments (31-48) carried out over a relatively wide range of polymer systems and sphere sizes have focused on the applicability of equations 1 and 2 to adequately describe the observed experimental behavior. The Stokes-Einstein relationship has been seen to hold for probe diffusion in small molecule low viscosity solvents but has been seen to fail drastically in more complex large molecule high viscosity systems.

It was stated earlier that the primary investigation tool that has been utilized to a large extent to study the dynamics of complex fluids through use of tracer particles, has been dynamic light scattering. Here it was observed that a single exponential decay was obtained for tracer particle studies of simple systems such as water and dextran(45). However, a more complex bimodal decay of the auto correlation function was observed for the more complicated hydroxypropylcellulose (HPC) system (31-34). The amplitude of the observed slow mode in these tracer dynamic light scattering studies was seen to be extremely sensitive to the polymeric system being investigated, the concentration of the polymer and the radius of the probe particles .

The physical basis for the evolution of a slow mode in tracer dynamic light scattering measurements in certain polymeric systems has been discussed quite extensively through a number of studies carried out by Philies et al on the hydroxypropylcellulose (HPC) system(31-34). Probe sizes in these studies were varied from 14nm to 455nm. All the spectra were seen to be highly bimodal. Based on the probe sizes the relaxation spectra was seen to consist of four relaxation modes which were divided into three physical regimes by Philies et al, namely: (1) a long time scale regime consisting of the large probe slow mode; (2) an intermediate time scale regime, consisting of the small probe slow mode and the large-probe fast mode ; and (3) a short time scale regime represented by the small-probe fast mode. As for the physical basis for these different time regimes, it was attributed to the dynamical processes that were being probed. The characteristic length scale in the system that separated the probe size behavior was the radius of gyration of the polymeric system being investigated. This was true for dilute polymer systems. For semi-dilute and concentrated polymer solutions there does not seem to be a conclusive agreement on whether the appropriate characteristic length scale is the radius of gyration of the polymer or the hydrodynamic correlation length. According to measurements by Philies et al the

crossover from small to large probe behavior involves probes of the same size, namely probes having diameters approximately equal to the radius of gyration. This indicates that the cross over is concentration independent. The difficulty in using the hydrodynamic correlation length as the cross over length scale is due to its strong concentration dependence.

The large-probe slow mode describes the motion of probes on a time scale so long that the system has relaxed completely and behaves as a viscous liquid. The large probe slow mode dynamics is seen to obey the Stokes-Einstein relationship. In the intermediate time scale regime, the large probes are fully coupled to the polymer solution motions at all but very long distances. This is due to the fact that at long distances probes have a chance to decouple from internal chain motions and experience the long wavelength shear viscosity. Small probes are small enough to the solution structure in order for them to sense the shear viscosity of the medium. The third regime corresponds to probing the extremely short time scale dynamics. At short distances and times chain interactions have not yet fully established themselves, therefore the probes will sample local chain relaxations. It is thus clearly evident that the bimodal decay spectra of tracer dynamic light scattering studies provides a deep insight into a host of dynamic behaviors taking place at different time scales. A notable result in these studies was inability of the Stokes-Einstein relationship to adequately describe the experimental data in the intermediate and short time scale regime.

### ***1.3 Failure of Stoke Einstein Relationship:Long Time Limit***

The failure of the Stokes-Einstein behavior as revealed in a number of tracer dynamic light scattering experiments has been described to a quite an extent by Won et al (48). The deviations from the Stokes-Einstein (SE) behavior has been described in terms of positive and negative deviations based upon the relative values of  $D_{\square}/D_0\square_0$ , Where  $D_0$  and  $\square_0$  correspond to

infinite dilution diffusivity and solvent viscosity respectively. A positive deviation,  $D_{\square}/D_0 > 1$ , corresponds to a diffusivity that decreases with increasing concentration less rapidly than the solution viscosity increases. Negative deviations from SE behavior have been attributed to chain adsorption and/or sphere aggregation. Positive deviations have been ascribed to the case of small sphere relative to the polymer correlation length. When  $R/\xi \ll 1$ , the spheres can move through the solution without waiting for the chains to relax their conformations, giving rise to positive deviations from SE behavior. The interesting fact is that deviations have also been observed for the case when,  $R/\xi > 1$ . Won et al (48) carried out tracer dynamic light scattering experiments on Poly(vinyl methyl ether) PVME using polystyrene spheres having a radii of 170 nm. The PVME concentration was varied in order to investigate the behavior in going from the unentangled to the entangled regime. The behavior that was observed was a deviation away from SE behavior with increasing PVME concentration but a return to SE behavior at high concentrations (beyond  $c^*$ ). One possible explanation of this return to SE behavior, as discussed by Won et al was that at these high concentrations, the matrix appears as a continuum to the spheres, i.e the motion of the spheres is now limited by the relaxation of the matrix entanglements. Near the cross-over concentration,  $c^*$ , the spatial inhomogeneity of the solution concentration is the greatest and the motion of the spheres is not completely coupled to the chain relaxation. Another interesting aspect discussed by Won et al was with regard to the PS spheres as true "probes" of the system dynamics. The structure and dynamics of the solution is perturbed over a significant distance away from the sphere. In the case of neutral surface-chain interactions, there is a depletion zone which extends a distance  $\approx R_g$  in the solution for a dilute solution and decreases with the correlation length  $\xi$  for a semi dilute

polymer solution. For the case of attractive surface-chain interactions there is a concentration enhancement within a layer of width  $\lambda$  adjacent to the sphere surface. In either case the properties of the fluid in the vicinity of the sphere surface will be markedly different from the bulk properties. This will cause the spheres to not necessarily "probe" the bulk properties. The existence of a depletion layer would also account for the enhanced short time diffusion and therefore the positive deviations away from the SE behavior. The effect of the depletion layer has also been discussed in the context of sedimentation velocities of colloidal particles(49-51). Deviations away from SE behavior and the ability of tracer particles to probe the bulk properties will be discussed further in the context of tracer microrheology studies.

#### ***1.4 The Generalized Stokes-Einstein Relationship***

The tracer dynamic light scattering studies discussed thus far have played a significant role in helping to gain a deeper insight into the dynamics of complex fluids. The dynamics that was investigated through this technique was however restricted primarily to the long time regime. Although the observation of 'fast' modes have been seen in some experimental investigations the technique did not provide a consistent method to probe the very short time dynamics. The dynamics of polymeric and other complex system shows a wide spectrum of behavior at different time scales and in order to gain a better understanding of the microstructure-property relationship, it is essential to extract the dynamic behavior over a much wider time scale than allowed by single scattering dynamic light scattering. Pioneering work done by Weitz and Pine (49) on the diffusing wave spectroscopy technique and by Mason and Weitz (1) on establishing the connection between the tracer particle motion and the viscoelastic response function has led to the development of the tracer microrheology technique which allows one to investigate the dynamic response function of a complex fluid over a wide time scale.

Diffusing Wave Spectroscopy (DWS), is a multiple light scattering technique which allows one to measure the time evolution of the mean squared displacement,  $\langle \Delta r^2(t) \rangle$ , of a probe scattering particle in a complex fluid. The mean squared displacement will directly reflect the viscoelastic response of the complex fluid being investigated under certain conditions. As is clearly evident in the case of a purely viscous fluid, the probe particle will diffuse and the  $\langle \Delta r^2(t) \rangle$  will increase linearly with time, while in a strongly elastic medium the probe particle will undergo thermally induced overdamped vibrations. The potential connection between the mean squared displacement and the response of a viscoelastic medium has been established by Mason and Weitz (1) through development of the Generalized Stokes-Einstein Relationship (GSER) and is outlined in the following paragraphs.

Spherical particles, when suspended in a simple viscous fluid, exhibit purely diffusive behavior. The dynamic behavior of the Brownian particles is typically described by a Langevin equation (53):

$$m \frac{d\bar{v}(t)}{dt} = -\zeta \bar{v}(t) + \bar{f}_R(t) \quad (3)$$

where  $m$  is the mass of the particle,  $\zeta$  is the friction factor,  $\bar{v}$  is the velocity of the particle and  $\bar{f}_R$  is a random Brownian or thermal force acting on the particle. The thermally driven motion of spherical particles is significantly different in viscoelastic media than in simple viscous fluids. Viscoelastic fluids have the ability to both store and dissipate energy. The ability of viscoelastic

fluids to store energy can be taken into account in the Langevin formalism through the use of a memory function (53),

$$m \frac{d\bar{v}(t)}{dt} = \int_0^t \Gamma(t-t') \bar{v}(t') dt' + \bar{f}_R(t) \quad (4)$$

Here  $\Gamma(t)$  is a time dependent memory function for an isotropic, incompressible viscoelastic fluid allowing for both energy loss and storage and is related to the instantaneous friction coefficient. For viscoelastic fluids, the correlations between the random forces acting on the particles exist over a much longer time then in the case of the simple viscous fluid and the fluctuation-dissipation relationship takes the following form:

$$\langle \mathbf{f}_R(0) \cdot \mathbf{f}_R(t) \rangle = k_B T \Gamma(t) \quad (5)$$

Using the equipartition of energy the Langevin equation can be solved to yield an expression for the velocity autocorrelation. In an isotropic medium, the one dimensional velocity autocorrelation function can be related to the  $\langle \square r^2(t) \rangle$  through:

$$\langle v(0)v(t) \rangle = \frac{1}{6} \frac{\partial^2 \langle \square r^2(t) \rangle}{\partial t^2} \quad (6)$$

The memory function can in turn be related to the velocity autocorrelation function and therefore to  $\langle \square r^2(t) \rangle$  through:

$$\tilde{\Gamma}(s) = \frac{6k_B T}{s^2 \langle \square r^2(s) \rangle} \quad (7)$$

The viscoelastic response of the fluid is completely described by the stress relaxation modulus,  $G_r(t)$ , which relates the macroscopic stress to the past strain rate. The macroscopic

linear viscoelastic moduli is obtained from the microscopic memory function by assuming that the bulk stress relaxations have the same spectrum as the local stress relaxations affecting the particle motions. The relationship that is used (due to the exceeding difficulty of a full treatment) is the relationship in the limiting case of a dilute suspension of spherical particles in a purely viscous solvent at zero frequency and generalizing this to all frequencies:

$$G_r(s) = \frac{\tilde{\lambda}(s)}{6\eta a} \quad (8)$$

This relationship is assumed to remain valid for a viscoelastic fluid. Utilizing the expression for the memory function, the Generalized Stokes-Einstein (GSE) is obtained:

$$\tilde{G}(s) \square \frac{k_B T}{6\eta a \langle \square r^2(s) \rangle} \quad (9)$$

### ***1.5 Applicability of GSE to describe viscoelastic response of complex fluids***

The applicability of the GSE to adequately describe the viscoelastic response of fluids in tracer microrheology experiments has been the subject of a number of theoretical developments, carried out by Levine and Lubensky(15-17). The theoretical developments carried out by Levine and Lubensky have focused on primarily addressing two fundamentally relevant questions for tracer microrheology experiments, namely, (1) Does the GSER provide the correct response function to an applied force in a homogeneous viscoelastic medium and (2) How are the unperturbed bulk rheological properties extracted in the event that the introduction of probe particles perturbs the local rheological properties. In order to address the first of these questions, a viscoelastic media is modeled as an elastic network that is viscously coupled to a fluid in which the network is embedded. The frequency dependent compliance relating bead displacement to an external force is calculated through solving the equations of motion for the elastic network and the fluid. Conditions under which the response function is equivalent to the GSER are then

determined in order to ascertain the conditions for the applicability of the GSER. There were three parameters of importance which emerged as controlling factors for conditions of applicability of GSE to be met. One of these is a characteristic frequency,  $\omega_B$ , below which the GSE equation would not hold. This characteristic frequency is given by(16):

$$\omega_B = \frac{(2\lambda + \mu)}{a^2 \zeta} \quad (10)$$

where,  $\lambda$  and  $\mu$  are the Lamé coefficients,  $a$  is the particle radius and  $\zeta$  is a friction factor. The

other condition is that two dimensionless parameters given by:  $\omega_F(\omega) = \frac{4\omega^2 \rho_f a^2}{G(\omega) \zeta^2}$  and

$\omega = \frac{\omega \zeta}{a}$  are both  $\ll 1$ . Here,  $\rho_f$  is the mass density of the fluid and  $\zeta$  is the network mesh size.

As will be discussed, besides having a mathematical basis for meeting the conditions under which the GSE will be applicable, these parameters also have a physical significance.

One of the fundamental issues that emerged from the theoretical development is the requirement of gaining a thorough understanding of the entire mode structure of the viscoelastic medium. For a simple viscous fluid, due to its incompressibility, the only relevant mode is the shear mode. This is also the case for a polymer or viscoelastic media consisting of a network and a solvent at frequencies above a characteristic frequency under which the network and incompressible solvent are strongly coupled. Below this characteristic frequency, modes other than the shear mode, especially the longitudinal compression mode will contribute significantly to the overall response function of the viscoelastic media. This characteristic cutoff frequency is the same cutoff frequency that was mathematically derived by Levine and Lubensky as one of the parameters which determines the applicability of the GSER equation. An order of magnitude estimate of this cutoff frequency has been developed by Gittes et al (12.13) and is

based on a balance between viscous and elastic forces. According to this development the viscous force of the solvent on the network can be estimated as  $\frac{\eta v}{\lambda}$  per volume, where,  $\lambda$  is the mesh size and  $v$  is the solvent velocity relative to the mesh. The local elastic force in the network can be estimated as  $G\lambda^2 u \sim \frac{Gu}{R^2}$  per volume, where,  $u$  is the network displacement field. Viscous coupling will be dominant and the network and solvent will move together above a frequency(12)

$$\omega \sim \frac{G\lambda^2}{\eta R^2} \quad (11)$$

Below this frequency the response function will include compressional modes which are not accounted for in the GSE equation and will therefore invalidate the use of the GSER for experiments carried out below this frequency. Estimates of this frequency based on the order of magnitude estimate (12,13) and based on the expression derived from the rigorous derivation (16) have both shown a value of 10Hz for the case of Actin filament solutions. Since this was at the lower limit of the instrumental resolution for tracer microrheology experiments, the GSER was valid for extracting the rheological response for the case of experiments carried out on Actin filaments. As stated previously the other two parameters derived by Levine and Lubensky(15-17) also have a physical significance. The  $\lambda_F$  parameter represents the ratio of of the sphere's radius to inertial decay length and  $\lambda$  represents the ratio of the network mesh size to the sphere radius. Estimations for actin filament solutions have shown that the  $\lambda_F$  remains small up to frequencies on the order of 100kHz and in typical tracer microrheology experiments, the probe sphere is chosen such that it is orders of magnitude larger then the mesh size. Another notable feature of the Levine development was the mathematical illustration that in the case where the probe particles perturb the media around them, the mutual fluctuations of two separated spheres

provides a more accurate determination of the complex shear modulus than do the fluctuations of a single sphere. This has led to further developments of experimental techniques which allow cross correlation of particle thermal fluctuations (14).

### ***1.6 Diffusing Wave Spectroscopy: the passive tracer microrheology technique***

The theoretical developments of Mason and Weitz (1) has laid the foundation for tracer microrheology experiments. The essential parameter that has to be determined experimentally is the mean squared displacement of the probe particles. There are mainly two classes of techniques which allow the experimental determination of  $\langle \Delta r^2(t) \rangle$ , these being (1) Active techniques and (2) Passive techniques. In the active technique probe particles are subjected to an external force and their displacements are measured with the aid of microscopes and imaging technology. In the passive technique, the thermally fluctuating positions of particles are measured via direct observation or via light scattering.

The technique that was utilized in this experimental study was a passive technique, which involved the determination of  $\langle \Delta r^2(t) \rangle$  through light scattering. Specifically the light scattering technique, known as diffusing wave spectroscopy (DWS), is essentially based on the principles of dynamic light scattering but approached from a strongly multiple scattering limit (49). Both DLS and DWS are very similar in that both entail the detection of a single speckle spot of scattered light and the measurement of its temporal fluctuations. In both cases the intensity fluctuations reflect the dynamics of the scattering medium. As was mentioned, DWS however approaches the problem of multiple light scattering from the limit of very high multiple scattering. In this limit the direction of light is totally randomized. The propagation of light and the effects of the dynamics of scatterers can then both be treated with statistical approximations.

In DWS, the fluctuation in the scattered intensity arises due to a change in phase of the light. This is brought about by the change in the total path length of the light through the sample by one wavelength. In order to determine this phase change, there are two fundamental approximations. The first is that due to high multiple scattering, the path followed by a photon can be described as a random walk. This allows the transport of photons through the sample to be approximated with a diffusion approximation. The second approximation is that the conservation of scattering momentum at every point along the full path length can be neglected, such that the individual scattering events are approximated by the contribution of an average scattering event. One notable point about DWS is its ability to measure angstrom scale particle motions. In the case of DWS the change in phase which causes the fluctuation in the intensity is brought about by the cumulative motion of a very large number of scatterers. As a result each scatterer needs to move only a small fraction of a wavelength. This allows the measurement of the motion of micron size particles on length scales as small as a few angstroms.

The use of the diffusion approximation to describe the photon transport in turn determines the types of samples that can be probed using DWS. Samples that scatter light strongly and have an opaque white or milky appearance are suitable. Also as light has to diffuse through the medium with very little absorption, the use of coloured samples is very limited. Another notable feature of the diffusion approximation is that the scattering wave vector, which relates the incident and detected light has little relevance to the resultant correlation function. As such, unlike DLS, the angle between the incident and detected light is not important in DWS. The exact experimental geometry is however essential as it determines the lengths of the paths that the photons follow. There are essentially two geometries that can be utilized to carry out DWS experiments, namely, (1) the transmission geometry and (2) the

backscattering geometry. In the transmission geometry, light is incident on one side of the sample and the scattered light transmitted through the sample is detected. In the backscattering geometry, the light is incident on one side of the sample and it is detected on the same side.

In the multiple light scattering limit there are essentially two length scales of interest which characterize the light scattering and transport. These are the mean free path,  $l$ , between scattering events and the transport free path  $l^*$ . The transport mean free path is the length scale over which the direction of light propagation is randomized. It is related to the mean free path through (52):

$$l^* = \frac{l}{\langle 1 - \cos \theta \rangle} \quad (12)$$

where,  $\theta$  is the scattering angle. In order for the diffusion approximation to be valid, the sample thickness,  $L$ , must be several times greater than  $l^*$ . In order that the internal reflections do not modify the boundary conditions, the most appropriate values of the relative ratio should be,  $L/l^* \geq 5$ .

The theoretical development of calculating the temporal autocorrelation function for DWS measurements has been detailed for both the transmission geometry and the backscattering geometry by Weitz and Pine (52). According to this development, the light propagation through the scattering medium is described as diffusive photon transport, which allows the determination of all different paths that a photon can take as it traverses the medium, as well as the probability that a photon will follow a given path. Each individual scattering event is then approximated by an average scattering event. Then the contribution of individual paths to the correlation functions is obtained by replacing the sum over individual scattering events by a sum over the same number of average scattering events. The total correlation function is obtained by summing the

contributions of the individual paths, weighed by the probability that a diffusing photon follows that path. Using this methodology to obtain an expression for the auto correlation function and solving the diffusion equation for light transport for the transmission geometry, the following expression is obtained for relating the electric field autocorrelation function to the mean square displacement through (52):

$$g_1(t) = \int_0^\infty P(s) \exp\left[-\frac{1}{3} k_0^2 \langle r^2(t) \rangle \frac{s}{l^*}\right] ds \quad (13)$$

where  $g_1(t)$  is the electric field autocorrelation function,  $P(s)$  is the path length distribution function,  $k_0$  is the wave vector,  $\langle r^2(t) \rangle$  is the particle mean squared displacement and  $l^*$  is the distance over which light becomes completely randomized.

### ***1.7.Objectives of Present Study and Systems Investigated***

It is clearly apparent from the above overview of the current state of tracer dynamic light scattering and tracer microrheology studies, that as a technique, the use of probe motion to investigate the dynamics of complex fluids is gaining increasing recognition. However what is also clearly apparent, is the lack of a true understanding of the connection between the Brownian motion of the probe particle and the viscoelastic response of the suspending media. This lack in understanding became more clear through the discussions on the deviations away from Stokes-Einstein behavior in the long time limit, as discussed by Won et al (48) as well as through the GSER applicability as discussed through the theoretical developments of Levine and Lubensky (15-17). In order to gain a deeper insight into the Brownian motion of probe particles in complex fluids, this experimental study undertook a comprehensive tracer microrheology/mechanical rheometry investigation of three complex fluid systems, (1) poly ethylene oxide (PEO), (2) poly ethylene oxide-poly propylene oxide-polyethylene oxide (PEO-

PPO-PEO) triblock copolymer and (3) cetyltrimethylammonium bromide/ sodium salicylate worm like micellar system. The objective was to study the viscoelastic response in these systems, as revealed through tracer probe motions and to try to gain an understanding of the effects of longitudinal and transverse modes on the extracted viscoelastic parameters. The PEO system was chosen as a representative flexible polymer, where the longitudinal modes should not play a significant role on the extracted parameters. The pluronic<sup>TM</sup> system was chosen as it was expected that tracer microrheology experiments should reveal interesting high frequency behavior and the system should not be challenging from a tracer microrheology experimental standpoint. The wormlike micellar system was chosen as it exhibited interesting dynamics and was expected to exhibit Maxwellian fluid behavior,

## ***References***

1. Mason, T. and Weitz, D.; *Phys. Rev. Lett.*, **1995**, *74*, 1250
2. van Zanten, J. and Rufener K.; *Phys. Rev. E*, **2000**, *62*, 5389
3. Mason, T., Ganesan, K., van Zanten, J., Wirtz, D. and Kuo, S.; *Phys. Rev. Lett.*, **1997**, *79*, 3282
4. Palmer, A., Xu, J. and Wirtz, D.; *Rheol. Acta*, **1998**, *37*, 97
5. Palmer, A., Mason, T., Xu, J., Kuo, S. and Wirtz, D.; *Biophysical Journal*, **1999**, *76*, 1063
6. Palmer, A., Cha, B. and Wirtz, D.; *J. Polym. Sci., Part B: Polym. Phys*, **1998**, *36(17)*, 3007.
7. Xu, J., Palmer, A. and Wirtz, D.; *Macromolecules*, **1998**, *31*, 6486.
8. Rufener, K., Palmer, A., Xu, J. and Wirtz, D.; *Journal of Non-Newtonian Fluid Mechanics* **1999**, *82*, 303
9. Mason, T., Gisler, T., Kroy, K., Frey, E. and Weitz, D.; *J of Rheol.*, **2000**, *44*, 917
10. Mason, T.; *Rheol. Acta*, **2000**, *39*, 371
11. Mason, T.G., Dhople, A. and Wirtz, D.; *Mater. Res. Soc. Symp. Proc.*, **1997**, *463*, 153
12. Gittes, F., Schnurr, B., Olmsted, P.D., MacKintosh, F.C. and Schmidt, C.F.; *Phys. Rev. Lett* **1997**, *79*, 3286
13. Schnurr, B., Gittes, F., MacKintosh, F.C. and Schmidt, F.C. *Macromolecules*, **1997**, *30*, 7781
14. Crocker, J., Valentine, M., Weeks, E., Gisler, T., Kaplan, P., Yodh, A. and Weitz, D.; *Phys. Rev. Lett.*, **2000**, *85*, 888
15. Levine, A. J. and Lubensky, T. C.; *Phys Rev E*, **2002**, *65*, 011501/1.
16. Levine, A.J. and Lubensky, T.C. ;*Phys. Rev. Lett.*, **2000**, *85*, 1774
17. Levine, A.J. and Lubensky, T.C.; *Phys Rev E*, **2001**, *63*, 1510
18. Gittes, F. and MacKintosh, F.C.; *Phys Rev E*, **1998**, *58*, R1241

19. MacKintosh, F. C. and Schmidt, C. F.; *Current Opinion in Colloid & Interface Science*, **1999**, *4*, 300.
20. Gisler, T. and Weitz, D. A.; *Phys. Rev. Lett*, **1999**, *82*, 1606.
21. Xu, J., Tseng, Y., Carriere, C. J., Wirtz, D.; *Biomacromolecules*, **2002**, *3*, 92.
22. Tseng, Y. and Wirtz, D.; *Biophys Journal*, **2001**, *81*, 1643
23. Yamada, S., Wirtz, D., Kuo, S. C.; *Biophys. J.*; **2000**, *78*, 1736
24. Harden, J. L. and Viasnoff, V.; *Current Opinion in Colloid & Interface Science*, **2001**, *6*, 438
25. Narita, T., Knaebel, A., Munch, J-P., Candau, S J.; *Macromolecules*, **2001**, *34*, 8224
26. Stradner, A., Romer, S., Urban, C., Schurtenberger, P.; *Progress in Colloid & Polymer Science*, **2001**, *118*, 136
27. Knaebel, A., Bellour, M., Munch, J.-P., Viasnoff, V., Lequeux, F., Harden, J. L.; *Europhys Letters*, **2000**, *52*, 73.
28. Urban, C., Romer, S., Scheffold, F., Schurtenberger, P.; *Progress in Colloid & Polymer Science*, **2000**, *115*, 270.
29. Nisato, G., Hebraud, P., Munch, J.-P., Candau, S. J.; *Physical Review E*, **2000**, *6*, 2879
30. Phillies, G.D.J., Streletzky, K. A.; *Recent Research Developments in Physical Chemistry*, **2001**, 5(Pt. 1), 269-285.
31. Streletzky, K. A and Phillies, G.D.J.; *J of Polm Sci- Part B Polym Phys*, **1998**, *36*, 3087
32. Streletzky, K. A and Phillies, G.D.J.; *J.Phys.Chem. B*, **1999**, *103*, 1811
33. Streletzky, K. A and Phillies, G.D.J; *Macromolecules*, **1999**, *32*, 145
34. Streletzky, K. A and Phillies, G.D.J; *J Chem Phys*, **1998**, *108*, 2975
35. Ngai, K.L. and Phillies, G.D.J; *J.Chem. Phys*, **1996**, *105*, 8385

36. Phillies, G.D.J., Gong, J., Li, L., Rau, A., Zhang, K., Yu, L., and Rollings, J., *J. Phys. Chem*, **1989**, 93, 6219.
37. Lin, T.-H. and Phillies, G.D.J.; *J. Phys. Chem*, **1982**, 86, 4073
38. Lin, T.-H. and Phillies, G.D.J.; *J. Colloid Interface Sci*, **1984**, 100, 82
39. Lin, T.-H. and Phillies, G.D.J.; *Macromolecules*, **1984**, 17, 1686
40. Ullmann, G.S. and Phillies, G.D.J.; *Macromolecules*, **1983**, 16, 1947
41. Phillies, G.D.J., Ullmann, G.S., Ullmann, K. and Lin, T.-H.; *J. Chem Phys*, **1985**, 82, 5242
42. Phillies, G.D.J., and Lacroix, M., *J. Phys. Chem B*, **1997**, 101, 39
43. Phillies, G.D.J.; *J. Chem. Phys.*, **1974**, 60, 983
44. Phillies, G.D.J.; *Biopolymers*, **1975**, 14, 499
45. Turner, D.N. and Hallett, F.R.; *Biochem. Biophys. A*, **1976**, 451, 305
46. Tokita, M., Miyoshi, T., Takegoshi, K. and Hikichi, K.; *Phys Rev E*, **1996**, 53, 1823
47. Reina, J.C., Bansil, R. and Konak, C.; *Polymer*, **1990**, 31, 1038
48. Won, J., Onyenemezu, C., Miller, W.G. and Lodge T.P.; *Macromolecules*, **1994**, 27, 7389
49. Tong, P., Ye, X., Ackerson, B.J. and Fetters, L.J.; *Phys Rev Lett*, **1997**, 79, 2363
50. Tong, P., Ye, X., Ackerson, B.J. and Fetters, L.J.; *Macromolecules*, 1998, 31, 5785
51. Tong, P., Ye, X., Ackerson, B.J. and Fetters, L.J.; *Macromolecules*, 1998, 31, 6534
52. Weitz, D. and Pine, D.; *Diffusing Wave Spectroscopy-in Dynamic Light Scattering-the method and some applications* (Clarendon Press 1993)

53. Chaikin, P. and Lubensky, T.; *Principles of Condensed Matter Physics*(Cambridge University Press)

## Chapter 2

### Probe Brownian Motion in PEO Solutions

---

#### *2.1 Abstract*

This chapter reports on a detailed tracer microrheology and mechanical rheometry study of aqueous solutions of the flexible polymer polyethylene oxide (PEO). The study is carried out on PEO solutions in which the concentration is varied from 0.2 to 15 wt%. This ensures the examination of the viscoelastic properties as the polymer solution progresses from the unentangled to the entangled regime. PEO solutions having concentrations greater than 1 wt% exhibit considerable elasticity, as manifested through development of a plateau in the evolution of the mean square displacement. The tracer microrheology measurements show excellent agreement with the mechanical rheometry measurements especially for the higher concentrations as manifested by the excellent agreement of the creep compliance measured from the two techniques. A sphere size sweep on a 7 wt% PEO solution exhibits that the creep compliance was independent of probe size. This is indicative that neither structural effects nor longitudinal dynamical modes are playing a role in affecting the extracted viscoelastic properties.

The terminal relaxation times and the zero shear viscosity extracted from the long time mean squared displacement behavior and from mechanical rheometry measurements exhibit deviations in quantitative agreement at low concentration, but excellent agreement at high concentrations. Power law fits of the zero shear viscosity and the terminal relaxation time concentration dependence exhibit stronger variations with concentration than expected for semi-dilute polymer solutions. The time-dependent diffusion coefficient exhibits the expected behavior of increasing time dependency and decreasing magnitude with increasing PEO

concentration. This is due to the particle diffusion becoming highly restricted by the increasingly entangled PEO network.

## ***2.2 Introduction***

The use of tracer microrheology as an experimental probe of soft material dynamics is gaining increasing interest (1-7). This is primarily due to the ability of microrheological techniques to probe the viscoelastic response of fluids through application of very small strains and over a much wider frequency range than allowed by conventional mechanical rheometry techniques. Passive tracer microrheological techniques monitor the Brownian fluctuations of micron size probe particles with the dynamical properties of the suspending matrix being inferred from the temporal evolution of the probe particles' mean squared displacement. The thermal or Brownian particle motion is typically measured with light scattering or optical microscopy techniques.

The ability of tracer microrheological techniques to extract the rheological parameters of complex fluids may however be limited due to (i) the presence of local heterogeneities in these complex systems, (ii) the possible perturbation of the local rheological properties brought about by the probe particles themselves and (iii) the influence of longitudinal dynamical modes. The influence of matrix heterogeneities can be investigated via optical microscopy-based single and multiple particle tracking methods whereby the motion of different particles will vary if heterogeneities are important. The influence of the particles on the matrix can be eliminated by cross correlating the motion of two particles thereby isolating the bulk dynamical properties from the local ones (7). Levine and Lubensky have discussed the effect of the longitudinal modes on Brownian motion in recent theoretical papers (8,9). These authors provide an estimate for the characteristic frequency below which the longitudinal modes may affect the extracted

viscoelastic modulus (transverse modes) of a solvent swollen network. This characteristic frequency,  $\omega_B$ , is basically an estimate of the frequency below which solvent and network motions are decoupled and is estimated as

$$\omega_B = \frac{2\lambda + \mu}{a^2 \zeta} \quad (1)$$

where  $\lambda$  and  $\mu$  are the Lamé coefficients,  $a$  is the radius of the particle and  $\zeta$  is the friction coefficient between the solvent and network. If the characteristic frequency is below the lowest frequency range probed in the diffusing wave spectroscopy technique, then the network and solvent will remain coupled for the entire frequency range that is probed and longitudinal modes should not significantly affect the observed Brownian motion. For the PEO solutions studied here this frequency was estimated to be  $0.1 \text{ s}^{-1}$ . Since this is the lowest frequency which is probed in this set of experiments, longitudinal modes should not play a significant role in the tracer microrheological studies presented here. However, an unresolved issue is whether the solvent quality itself influences network-solvent decoupling. For instance, one might expect that such decoupling might be enhanced in a theta condition polymer solution relative to a good one. Fortunately, the osmotic modulus of aqueous PEO solutions is quite large owing to good solvent quality thereby diminishing this effect if it is at all relevant.

Most tracer microrheology studies have utilized diffusing wave spectroscopy as a means for monitoring the average mean squared displacement of an ensemble of spherical probe particles (10). Especially notable among these investigations is systematic studies of actin filament solutions (11-14). Actin is an excellent semi-flexible polymer model owing to its relatively long persistence length. These previous tracer microrheological measurements have provided extensive insight into the short time dynamics of these solutions and indicate that recent

theoretical predictions for the high frequency scaling of the viscoelastic modulus are close to reality (15-17).

More recently microrheological techniques have been applied to worm-like micelle and associating polymer systems (18-21). During the course of these investigations it became apparent that a tracer microrheology study of simple flexible polymer solutions would provide an excellent means for interpreting Brownian motion in the more structurally complex systems. Although some flexible polymer solutions had been investigated in limited detail previously, these earlier studies had not considered a wide range of polymer concentrations and were essentially used to demonstrate the tracer microrheology approach in a one shot manner (1-7,22). In this study we carry out a detailed investigation of aqueous polyethylene oxide (PEO) solutions as a model flexible polymer system. Aqueous PEO solutions have been chosen primarily because it is very easy to disperse the required optical probes in these systems and that they behave as good solvent systems at room temperature. This indicates that the osmotic modulus for the system should be very high, thus diminishing the influence, if any, of concentration fluctuation induced longitudinal modes on the Brownian motion and any extracted dynamical moduli. Aqueous polyethylene oxide (PEO) solutions have been studied quite extensively (23-30). Most germane to the current investigation is the fact that mechanical rheometry measurements indicate that aqueous PEO solutions exhibit the concentration, molecular weight and temperature dependencies expected for polymer solutions under good solvent conditions (30, 31).

## ***2.3 Materials and Methods***

### ***Materials***

Polyethylene oxide (PEO,  $M_w = 333,000$  g/mol) was obtained from Polymer Source

(Montreal, Quebec, Canada). Dust free PEO aqueous solutions were prepared with deionized water that had been filtered through a 0.02  $\mu\text{m}$  filter (Whatman-Anotop 25). Polystyrene latex spheres ranging in size from 0.195 to 1.55  $\mu\text{m}$  in diameter were utilized as optical probes (Duke Scientific, Palo Alto, CA). The optical probes were typically dispersed in the PEO solutions at 1 vol%. All of the tracer microrheology samples were examined with optical microscopy to ensure that the optical probes were not aggregated prior to further measurements. The samples were maintained at 40°C for 3 days and then transferred to flat sided 2 mm and 10 mm thick spectrophotometric cells for diffusing wave spectroscopy measurements (Spectrocell, Oreland, Pa).

### ***2.3.1 Diffusing Wave Spectroscopy***

Transmission mode diffusing wave spectroscopy (DWS) was utilized to monitor the mean squared displacement of the optical probe particles (10). The beam from a diode pumped solid state (DPSS) Nd-YAG laser operating at a wavelength of 532 nm *in vacuo* was incident upon a flat scattering cell, containing the polymer solution and spherical optical probes. An ALV SI/SIPD photon detector (ALV GMBH Germany) collects the multiply scattered light via a single mode optical fiber. In order to ensure the point-point geometry, the single mode optical fiber is coupled to a gradient refractive index (GRIN) lens with a very narrow angle of acceptance (Wave Optics, CA). The output from the ALV SI/SIPD photon detector is fed to an ALV fast digital correlator (ALV GMBH Germany) operating in the cross correlation mode. The measured intensity auto correlation function was converted into the electric field autocorrelation function using the Siegert relationship.

The electric field autocorrelation function obtained from a DWS measurement can be related to the mean square displacement through (10)

$$g_1(t) = \int_0^L P(s) \exp\left[-\frac{1}{3} k_0^2 \langle r^2(t) \rangle \frac{s}{l^*}\right] ds \quad (2)$$

where  $g_1(t)$  is the electric field autocorrelation function,  $P(s)$  is the path length distribution function which is determined by the experimental geometry,  $k_0$  is the incident wavevector,  $\langle r^2(t) \rangle$  is the particle mean squared displacement and  $l^*$  is the distance over which light becomes completely randomized. The mean squared displacement of the probe spheres was extracted pointwise from the electric field autocorrelation function from equation (2) via a bisection root searching algorithm. For the case of standard dynamic light scattering (*i.e.* single photon scattering) the length scale over which particle motion is probed can be adjusted by varying the scattering angle, in DWS the length scale over which the motion is probed is adjusted by varying the cell thickness  $L$ . Most importantly, owing to multiple scattering nature of DWS the technique is capable of resolving *angstrom*-scale particle motions and thereby short time dynamics.

The comparison of viscoelastic properties obtained from tracer microrheology and mechanical rheometry is usually carried out in one of two ways: (1) through comparison of the complex viscoelastic modulus,  $G^*$  or (2) via direct comparison of the creep compliance measured by the two methods. The conversion of the measured mean squared displacement into the complex viscoelastic moduli involves a transformation of the data from the time domain to the frequency domain. A more direct method and one that has been shown to give better results is the use of the creep compliance. If one assumes that the generalized Stokes-Einstein relationship is obeyed it is readily shown that the time domain creep compliance,  $J(t)$ , is directly proportional to the mean squared displacement of a spherical probe of radius  $a$  (12,14,32)

$$J(t) = \frac{a^3}{k_B T} \langle r^2(t) \rangle \quad (3)$$

The creep compliance represents the ratio of the temporally evolving strain or displacement of the sphere in solution to an equilibrium Brownian stress. It is essentially equivalent to the frequency-domain representation of the modulus.

### ***2.3.2 Mechanical Rheometry***

Mechanical rheometry measurements were performed with a Rheometrics controlled stress rheometer (DSR,). A 40 mm cone and plate geometry was utilized for all the measurements reported. The PEO samples were placed on the plate and the cone lowered onto it. In order to eliminate edge effects the cone was first lowered to a position slightly larger than the final gap width and the sides were cleaned off. The cone was then brought down to its operating width. The temperature was kept fixed at 25°C throughout the measurements. In order to minimize evaporation effects, the cone and plate were enclosed in a custom made vapor trap. Both creep measurements and dynamic measurements were carried out on each PEO concentration. In order to determine the linear viscoelastic regime, a dynamic steady stress measurement was first carried out for each PEO concentration. Once the linear viscoelastic regime was determined all experiments were carried out using a stress for which the sample was within the linear viscoelastic regime.

## ***2.4 Results and Discussion***

The main objective of this experimental study was to investigate both the high and low frequency dynamic behavior of aqueous PEO solutions over a wide concentration range via ensemble tracer microrheology. Zero shear viscosity measurements indicate that for the 330k molar mass PEO investigated the crossover to the entangled regime occurs at 1.75 wt%. In order to study the behavior in a concentration range that ranges from the unentangled to the entangled

regimes eight PEO concentrations were prepared in which the concentration was varied from 0.2 to 15 wt%.

### 2.4.1 Brownian Motion in Aqueous PEO Solutions

The mean squared displacement of 0.966  $\mu\text{m}$  diameter polystyrene spheres in aqueous PEO solutions with concentrations ranging from 0.2 to 15 wt% is shown in Figure 2.1.

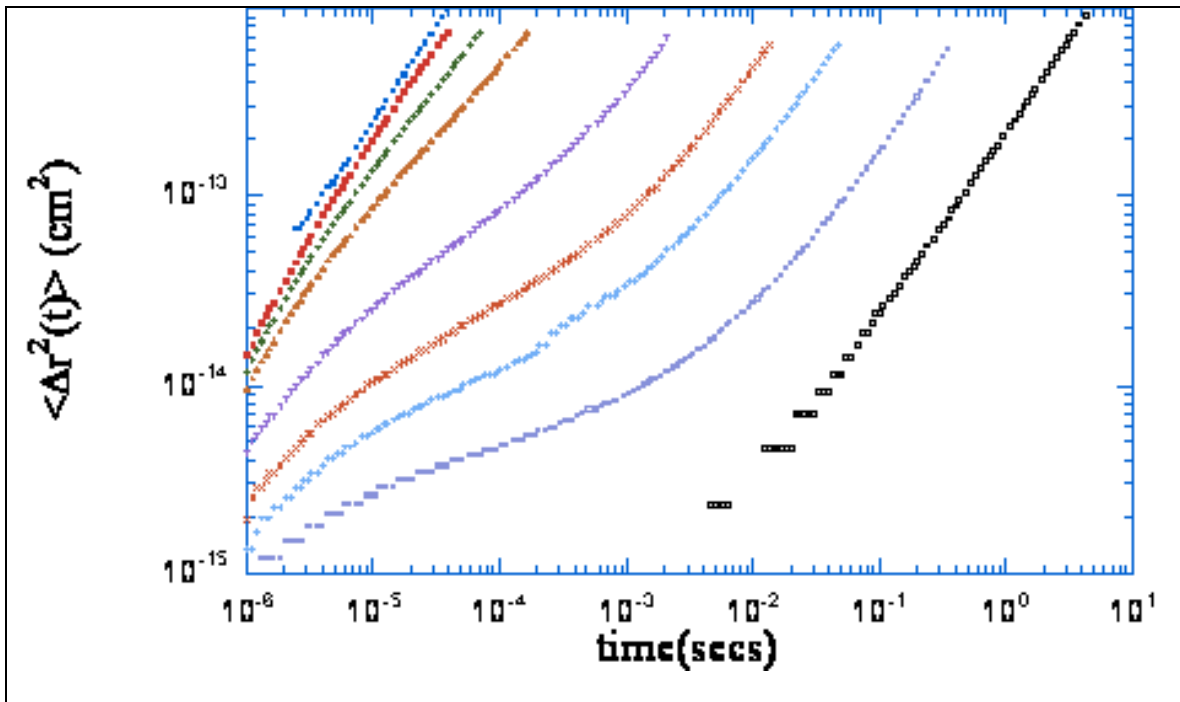


Figure 2.1: Evolution of the mean squared displacement for PEO solutions having concentrations: (■) 0.2% (◆) 0.5% (▲) 1.0% (▼) 3.0% (✖) 5.0% (+) 7.0% (○) 10.0% and (□) 15.0%. The (●) water MSD is shown as a basis for comparison.

The observed probe sphere Brownian motion is intimately connected to the dynamics of the suspending medium. An expected and readily observable feature is the shift of mean squared displacement time traces to longer times with increasing PEO concentrations. This is expected as the solution viscosity and elasticity increases with increasing PEO concentration. While the probe mean squared displacement in the three lowest PEO concentration solutions, 0.2, 0.5 and 1.0 wt%, are somewhat similar to that found for probe diffusion in water, they do exhibit a slight subdiffusive behavior that increases with increasing PEO concentration. Upon close

examination the probe mean squared displacement in the 1 wt% solution appears to exhibit a slight kink near  $10^{-4}$  seconds which may be an indication of the beginnings of an elastic plateau.

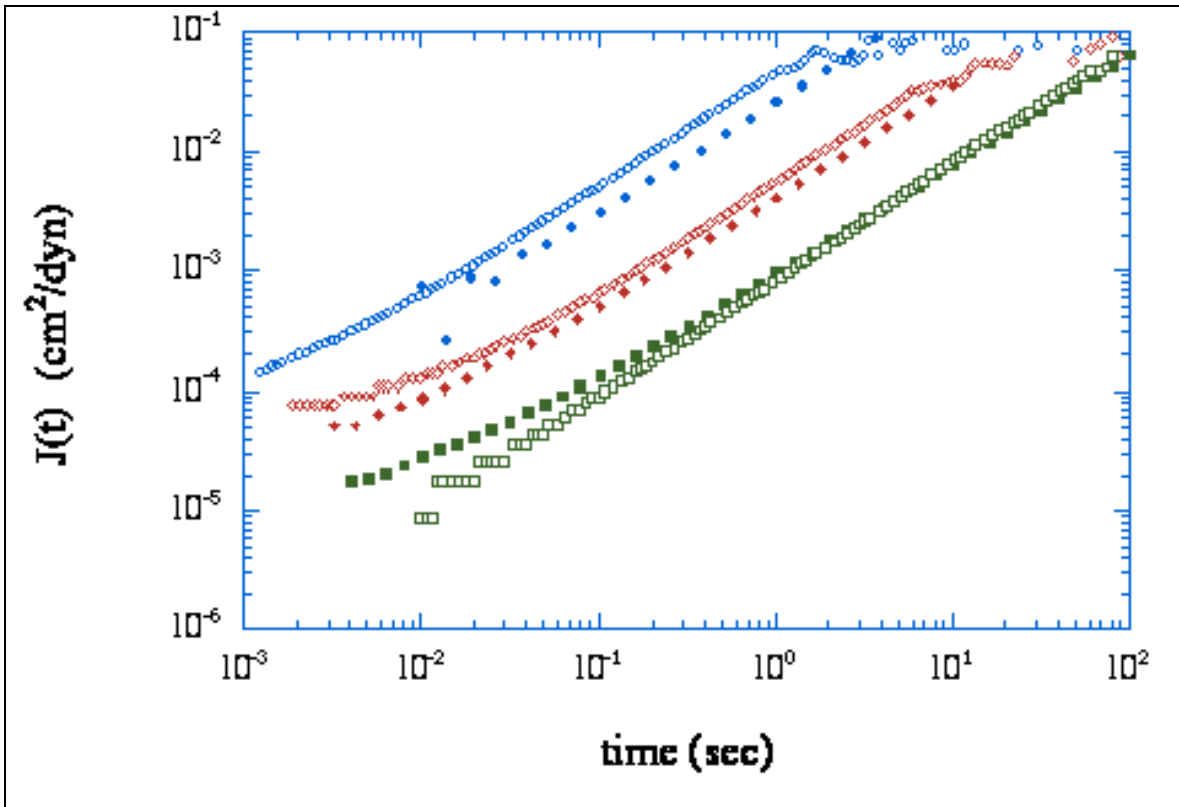


Figure 2.2: Comparison of the creep compliance obtained from mechanical rheometry and tracer microrheology for three PEO concentrations: (●)7.0%(◆) 10% and (■) 15%. Closed symbols refer to mechanical rheometry and open symbols to mechanical rheometry. Good agreement is seen especially for the 10 and 15% solutions.

A plateau in the mean squared displacement is apparent for PEO concentrations exceeding the measured entanglement concentration of 1.75 wt%. The plateau value mean squared displacement is inversely proportional to the plateau modulus and should decrease with increasing PEO concentration as observed here (1-3,18,31).

#### 2.4.2 Comparison of Tracer Microrheology and Mechanical Rheometry

In order to form a basis for comparison with the rheological parameters extracted from tracer microrheology measurements creep compliance measurements were conducted using mechanical rheometry. A direct comparison of the creep compliances obtained from mechanical rheometry

and tracer microrheology is illustrated in Figure 2.2 for three representative PEO concentrations. The agreement between the two techniques is exceptionally good at the frequencies probed. The agreement is better at longer times and at higher concentrations.

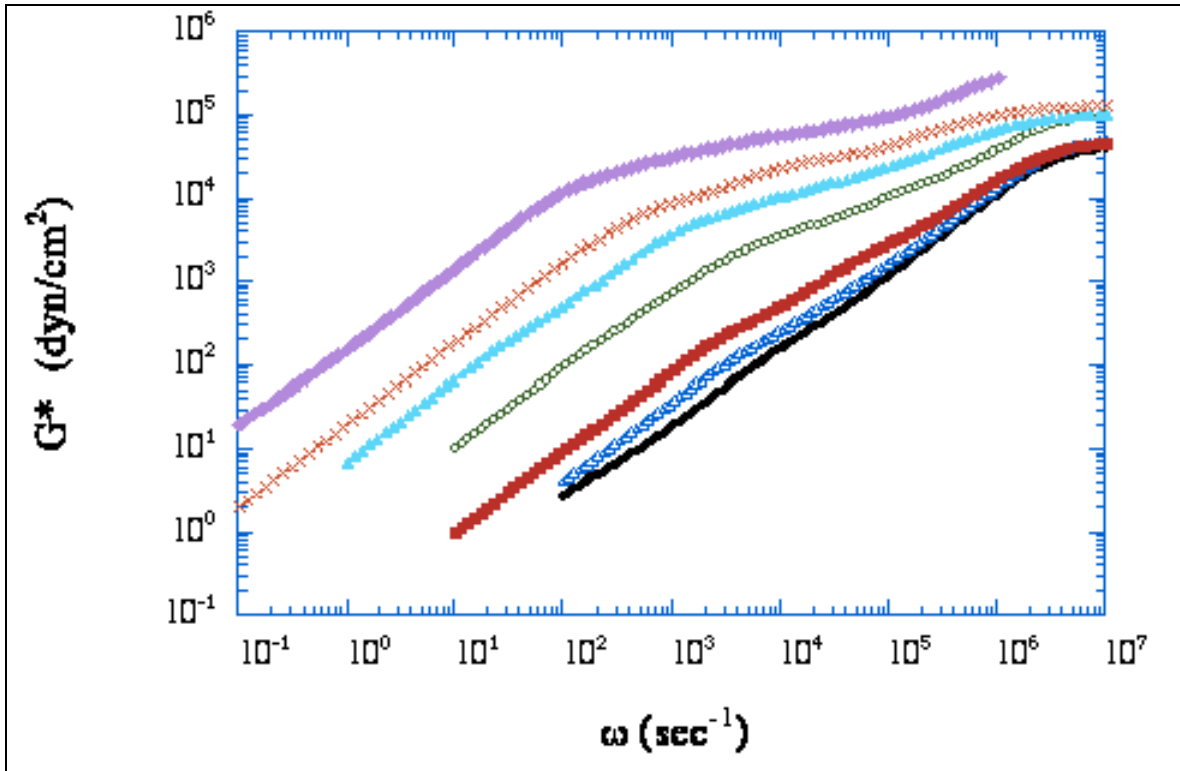


Figure 2.3: Frequency dependence of the complex viscoelastic moduli,  $G^*$  for PEO solutions having concentrations: (●) 0.2% (△) 0.5% (■) 1.0% (○) 3.0% (▲) 5.0% (×) 7.0% and (◆) 10%. The plateau moduli increases with increasing concentration, indicating the higher elasticity of the more concentrated solutions.

The discrepancies between tracer microrheology and mechanical rheometry is due to the unreliability of the high frequency mechanical measurements. It should be noted that reliable mechanical rheometry data were not obtained for PEO concentrations lower than 7 wt% with the data found for the 7 wt% solution being somewhat questionable as they were collected near the sensitivity limit of the rheometer utilized for this study.

The complex viscoelastic moduli was obtained from the creep compliance using a modification of the procedure introduced by Mason and coworkers in which the creep data was fitted to a Voigt model plus a linear region, and the retardation spectrum was obtained (14). The

complex viscoelastic moduli are extracted from the retardation spectrum (see Figure 2.3). The observed frequency dependence of the complex viscoelastic moduli is that which is expected for polymer solutions (31). The plateau moduli increase with increasing concentration, indicating the higher elasticity of the more concentrated solutions.

#### *2.4.3 Sphere Size Sweep*

The close agreement between the creep compliance extracted from both tracer microrheological and mechanical rheometry measurements indicates that the influence of longitudinal modes on Brownian motion in this system is minimal at most. This can be further demonstrated by examining the effect of optical probe size on the measured creep compliance. Such a sphere size sweep would change the characteristic longitudinal mode frequency (see equation (1)) below which longitudinal modes are predicted to affect the extracted rheological parameters. In the event that the longitudinal modes do not play a significant role, the recovered creep compliance should be independent of sphere size. A sphere size sweep was conducted on 7 wt % PEO solutions in which the sphere diameter was varied from 0.195 to 1.55  $\mu\text{m}$ . Figure 2.4 shows the temporal evolution of the probe mean squared displacement as a function of sphere size. The mean squared displacements are simply offset from one another in the vertical direction in direct proportion to the relative sphere size with smaller spheres moving more rapidly than larger ones. The measured creep compliance is shown to be independent of probe

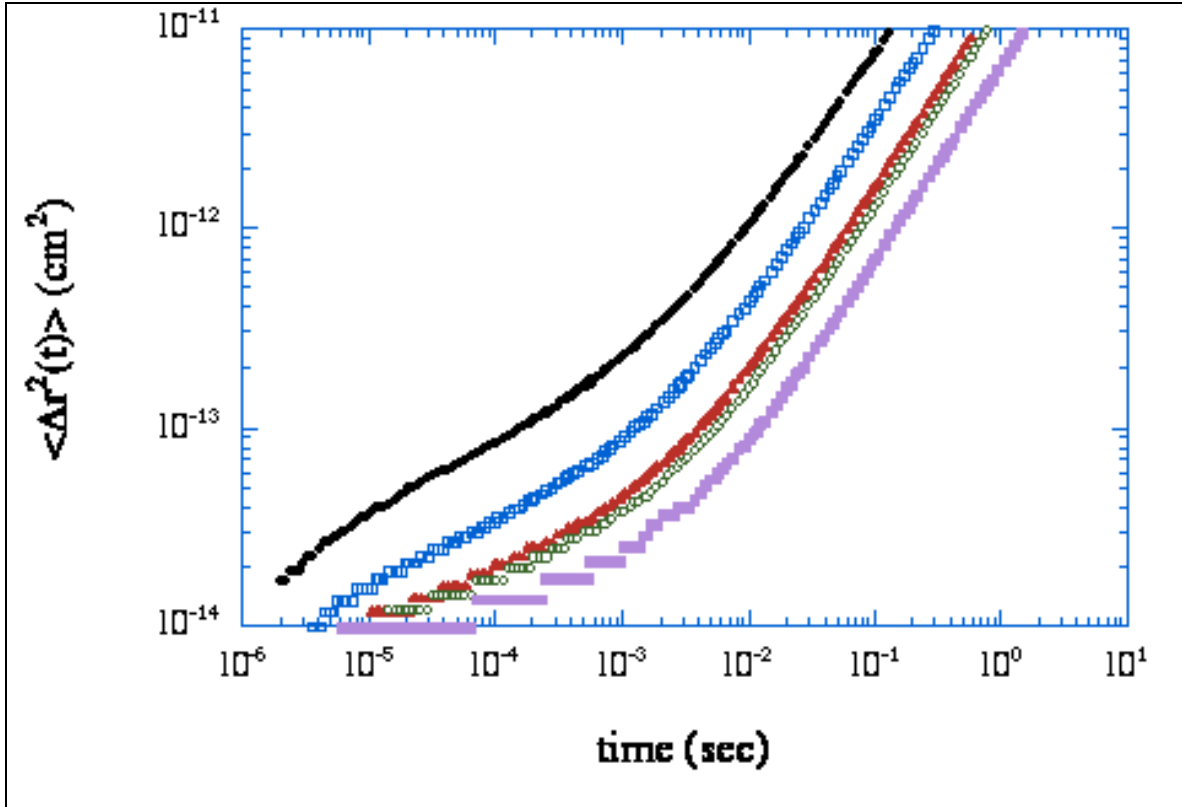


Figure 2.4: Mean squared displacement for a 7% PEO solution having probe sizes (●) 0.195 (□) 0.511 (▲) 0.739 (○) 0.966 and (■) 1.55 microns. The MSD's are vertically offset from another in direct proportion to the relative sphere size.

size in Figure 2.5. These observations illustrate three important facts: (1) that the Stokes-Einstein relationship is obeyed; (2) that the probe size range considered here is insensitive to the underlying microstructure of the PEO solutions under consideration; and (3) that longitudinal modes are not playing a significant role in these PEO solutions.

#### 2.4.4 Low Frequency or Long Time Behavior

##### *Longest Relaxation Times (escape times)*

In order to gain an insight into the longest relaxation times (escape times), the Maxwell model was fit to the long time behavior of the mean square displacement(18)

$$\langle \square r^2(t) \rangle = 6D(t + \square) \quad (4)$$

It was observed that the Maxwell model was a reasonable fit for the long time behavior of PEO at concentrations greater than 1%.

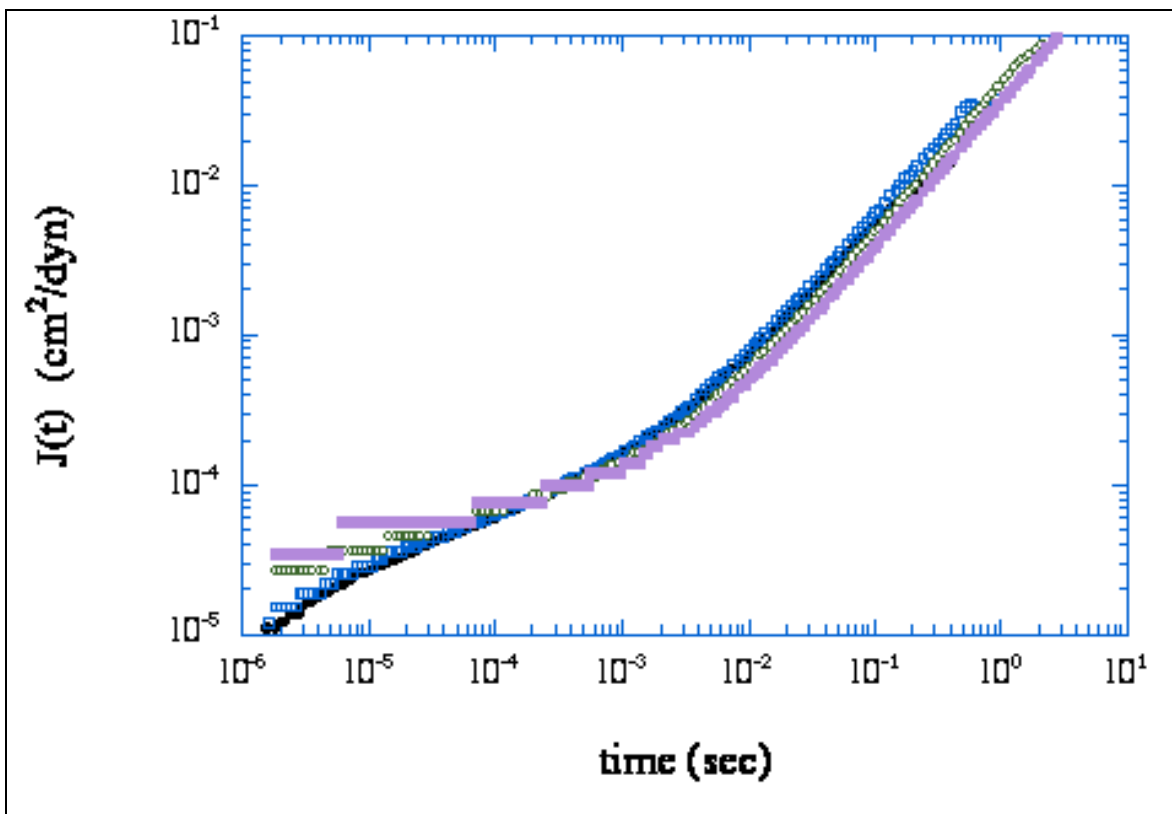


Figure 2 5: Creep Compliance for a 7% PEO solution having probe sizes (●) 0.195 (□) 0.511(▲) 0.739 (○) 0.966 and(■)1.55 microns. The Creep compliance is independent of probe size. This indicates that longitudinal modes are not playing a significant role in effecting the extracted viscoelastic properties in these systems.

The diffusion coefficients and the escape times were therefore extracted for these concentrations. The longest relaxation time was also extracted from the cross over of the elastic moduli  $G'$  and the viscous moduli  $G''$ . The variation of the longest relaxation time with the PEO concentration is illustrated in figure 2.6. It is observed that the relaxation time increases with increasing PEO concentration. This is expected since increasing elasticity associated with increasing PEO concentration will cause the probe particle to spend more time in the network before finally escaping. The agreement between the relaxation times from the  $G' G''$  cross over and from the fit of the long time mean square displacement deviates significantly, especially at the low PEO concentrations. It is observed that the agreement improves considerably with increasing PEO concentration and at 10% PEO concentration both methods of analysis yield the

same value for the relaxation time. The deviation at the low concentrations may be due to the two analysis methods measuring different relaxation phenomena especially at low PEO concentrations.

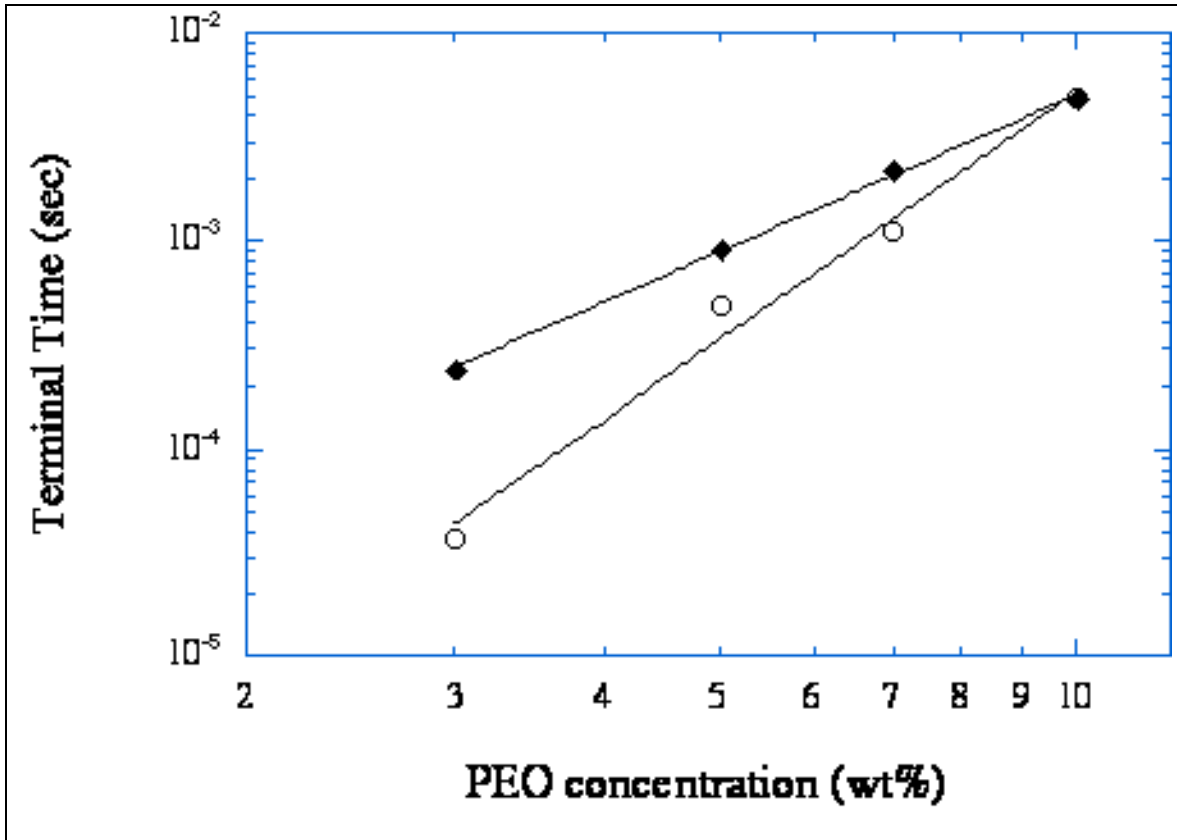
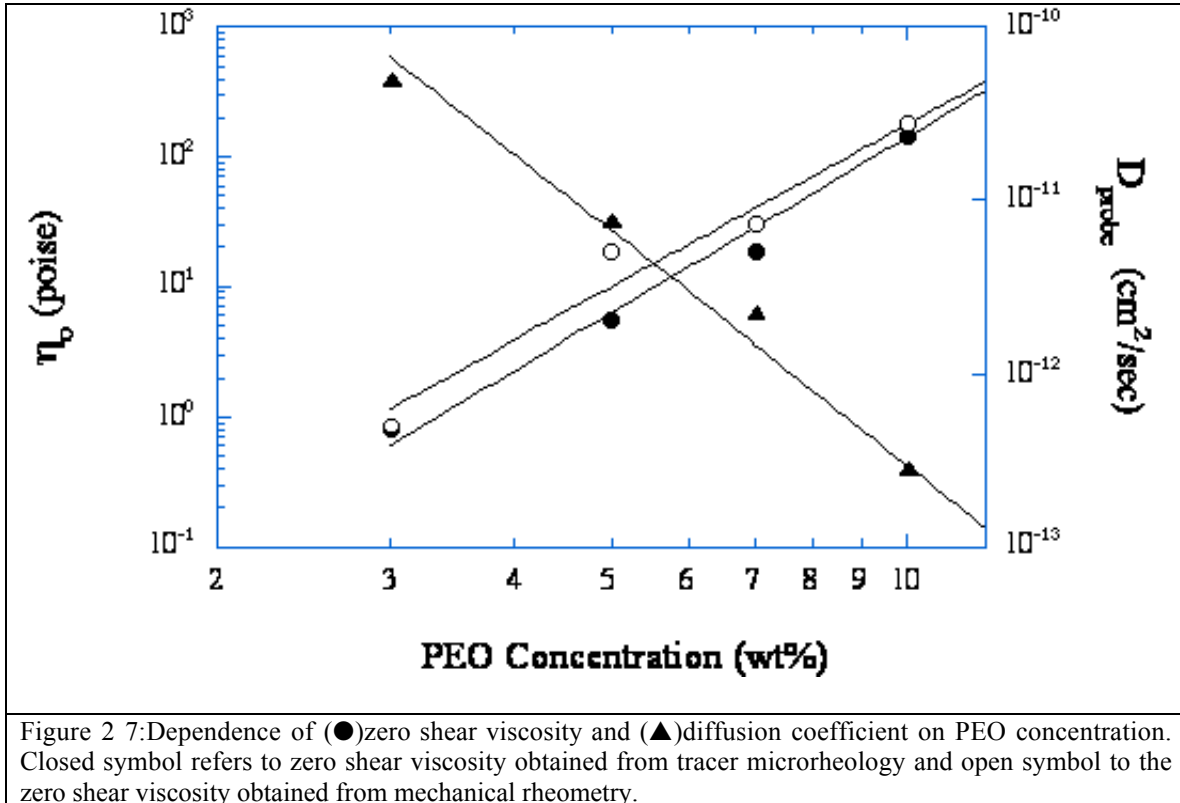


Figure 2 6: Terminal relaxation time PEO concentration dependence. Relaxation times obtained from (O) G'G'' cross over and (◆) maxwell fit of long time msd. The concentration dependence fit was well represented by a power law fit of the data. The power law exponent was stronger than that predicted for semi-dilute polymer solutions.

The relaxation time dependence on concentration was obtained through a power law fit of the data. It was observed that the power law dependence was significantly different for the two analysis methods. For the long time maxwell fit the scaling exponent was 3.971 while for the G'G'' cross over it was 2.5173. Both these dependencies on concentration are significantly stronger than the predicted 1.5 exponent for semi dilute polymer solutions(31).

### Zero Shear viscosities

The zero shear viscosity was obtained both from the long time fit of the mean square displacement data as well as from mechanical rheometry measurements. The zero shear viscosities obtained from these two different techniques is plotted together with the diffusion coefficient in figure 2.7.



The zero shear viscosities obtained from the two techniques agree reasonably well for 3, 7, 10 and 15% solutions. The largest deviation is for the 5% solution. The concentration dependencies of the zero shear viscosities were obtained through a power law fit of the data. It was observed that the power law exponents were not significantly different for the two techniques. For the tracer microrheology measurements the exponent was 4.52, while for the rheometry measurements it was 4.17. Both of these indicate a stronger concentration dependency than the 3.5 dependency predicted for polymers in semi-dilute solutions (31).

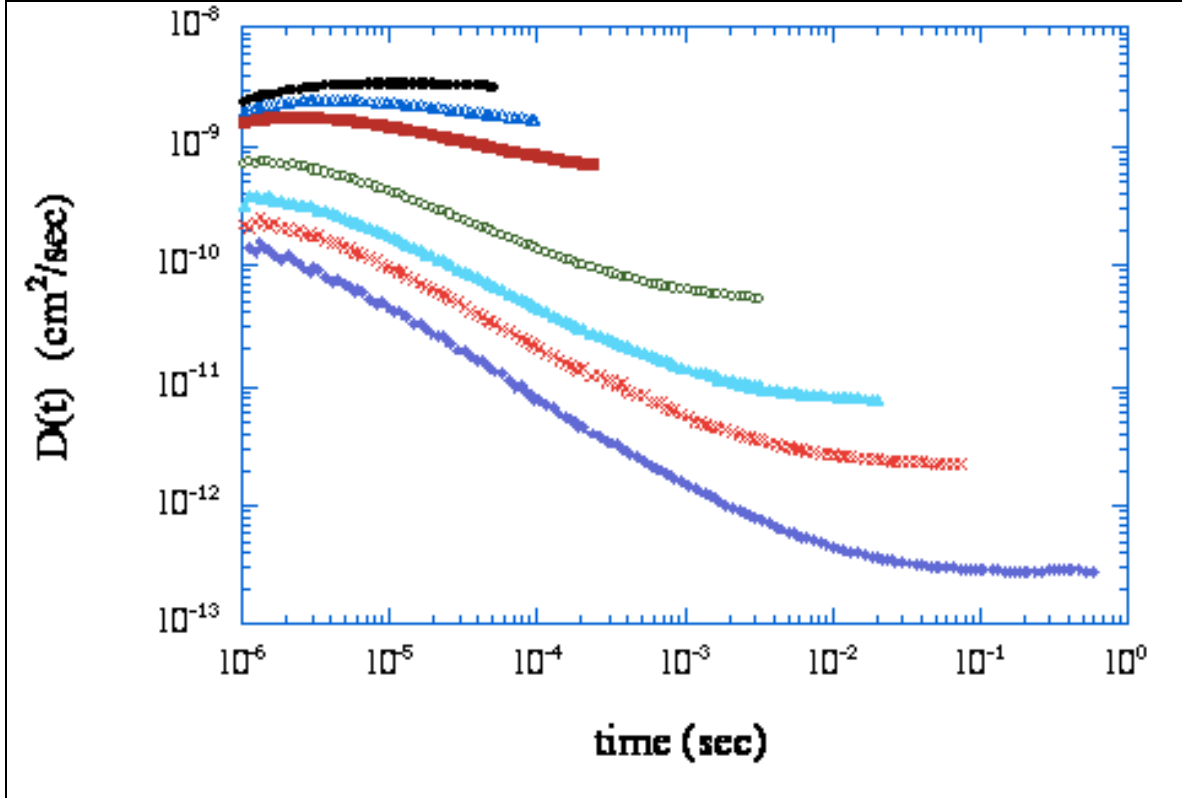


Figure 2 8: Evolution of the time dependent diffusion coefficient for PEO solutions having concentrations: (●) 0.2%(△)0.5%(■)1.0%(○) 3.0%(▲) 5.0%(×) 7.0% and (◆) 10%. The  $D(t)$  time dependency increases and its magnitude decreases with increasing PEO concentration due to hindered motion of the spheres. This is due to the increased elasticity associated with increased concentration.

#### 2.4.5 High Frequency or Short Time Behavior

In order to attain better resolution of short time behavior, diffusing wave spectroscopy measurements were carried out on PEO solutions placed in thicker cells (10mm pathlength). This was combined with the mean square displacement time trace obtained through use of 2mm path length cells in order to extract the viscoelastic behavior over a wide frequency range.

In order to gain a deeper insight into the state of the suspending media, the time dependent diffusion coefficient was extracted. The time dependent diffusion coefficient is defined as:

$$D(t) = \frac{\langle \Delta r^2(t) \rangle}{6t} \quad (5)$$

The variation of the time dependent diffusion coefficient with increasing PEO concentration is plotted in figure 2.8. It is seen that  $D(t)$  becomes more time dependent with increasing PEO concentrations indicating more deviation away from a purely diffusive behavior. The diffusion coefficients even in the lowest PEO concentrations of 0.2 and 0.5% show a slight time dependency and have values which are close to but smaller than the diffusion coefficient value for 0.966 micron spheres in water of  $4.5 \times 10^{-9} \text{ cm}^2/\text{sec}$ . With increasing PEO concentrations the time dependency increases and the diffusion coefficient becomes increasingly smaller. This is due to the enhanced hindered motion of the spheres due to the increased elasticity associated with higher PEO concentrations. At long time scales, the particle diffusion becomes highly restricted by the PEO entanglements and  $D(t)$  becomes several orders of magnitude smaller than the value in water.

The deviation away from purely diffusive behavior is more clearly evident on plotting  $D(t)$  vs time (figure 2.9). The diffusion coefficient used in this expression was the long time diffusion coefficient extracted from a Maxwell fluid model fit of the long time behavior of the mean square displacement. At short times the deviation away from pure diffusive behavior is higher for higher PEO concentrations. Also, the final attainment of the long time diffusive behavior takes longer for higher PEO concentrations, illustrating once again that with increased elasticity the spheres spend more time in the elastic network before finally escaping.

A more detailed understanding of probe motion in an entangled polymer solution can be obtained through extraction of the probe velocity auto correlation function,  $\langle v(t)v(0) \rangle$ . The velocity auto correlation function can be obtained from the time dependent diffusion coefficient via:

$$\langle v(t)v(0) \rangle = \square \frac{dD(t)}{dt} \quad (6)$$

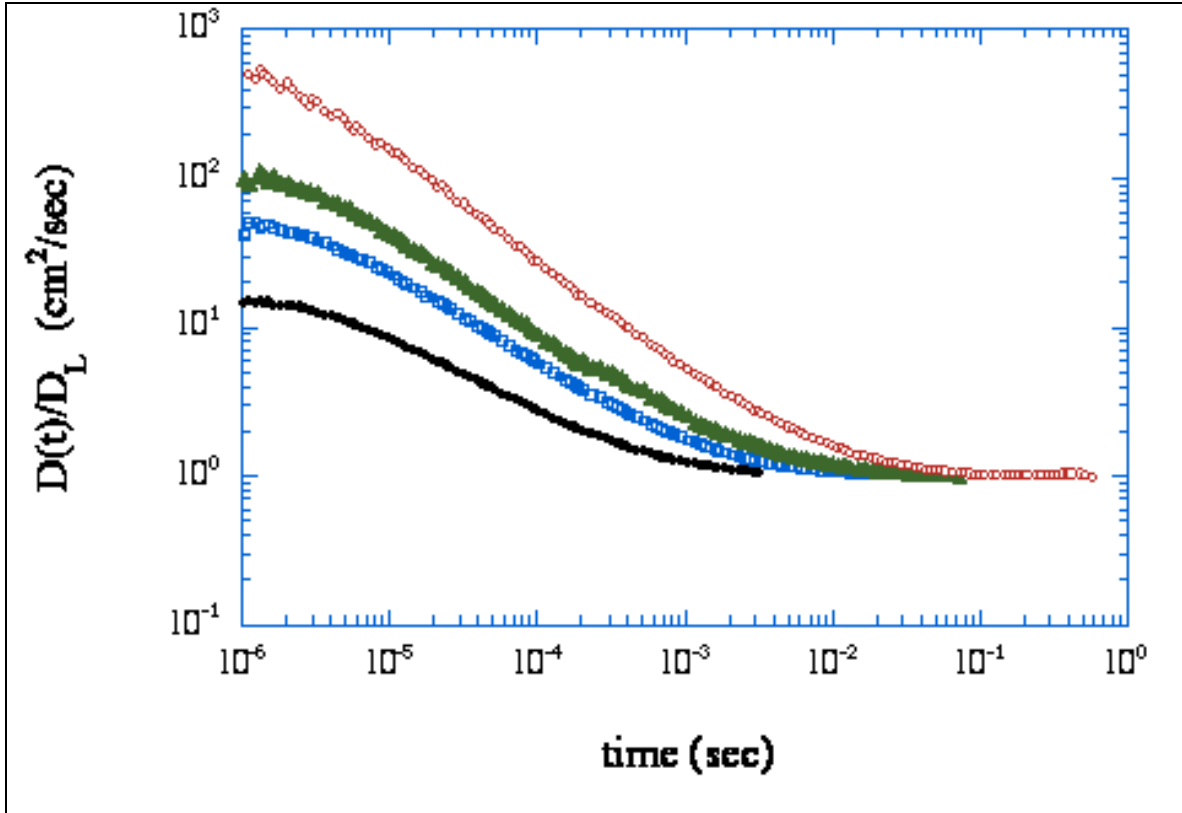


Figure 2 9: Evolution of  $D(t)/D_L$  with time for four PEO solutions: (●) 3.0%(□)5.0% and (▲) 7.0% and (○) 10.0%. It is observed that at short times the deviation away from pure diffusive behavior takes longer for higher PEO concentrations.

Qualitatively the velocity auto correlation function can be associated with the dissipation of the microsphere due to interaction with the mesh. Dissipation is proportional to  $v^2$  which scales as  $t^{0.75}$ . The velocity auto correlation function time trace for the PEO concentrations investigated was fit with a power law in order to extract the time dependency. It was observed that the exponent became increasingly more negative with increasing PEO concentrations (figure 2.10). The higher PEO concentrations(3% onwards) had a scaling exponent very close to -1.75.

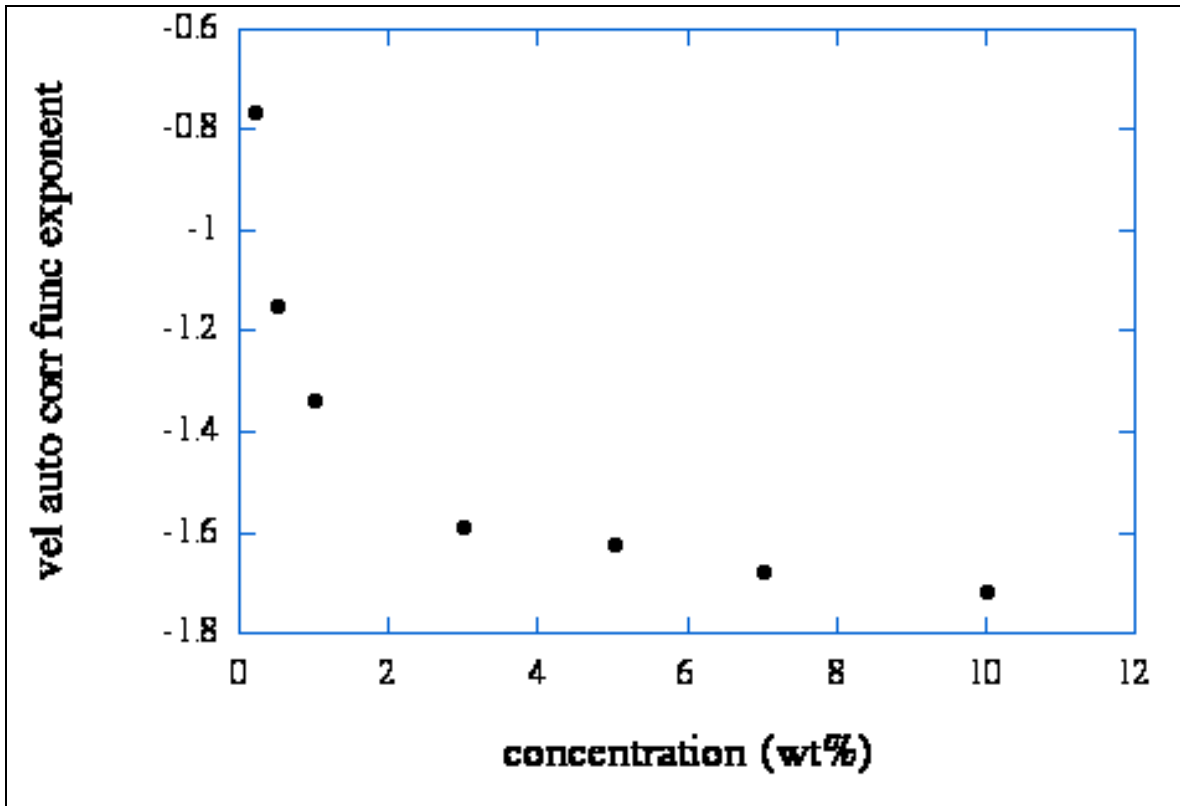


Figure 2.10: Velocity autocorrelation function time dependency exponent variation with concentration. The exponent was seen to become increasingly more negative with increasing PEO concentration.

#### 2.4.6 Creep Compliance Concentration Scaling

The concentration scaling of the creep compliance over several time decades is shown in figure 2.11. With increasing time the concentration dependence of the creep compliance became increasingly more steeper. The scaling exponent varies from -1.08 for  $t=1e-6$  seconds to -2.89 for  $t=1e-2$  seconds. For flexible polymer the plateau modulus scales as  $G_0 \sim c^{2.25}$  for semi dilute solutions(31). It is observed that the creep compliance does go through this dependency at times intermediate between  $t=1e-4$  and  $t=1e-3$ .

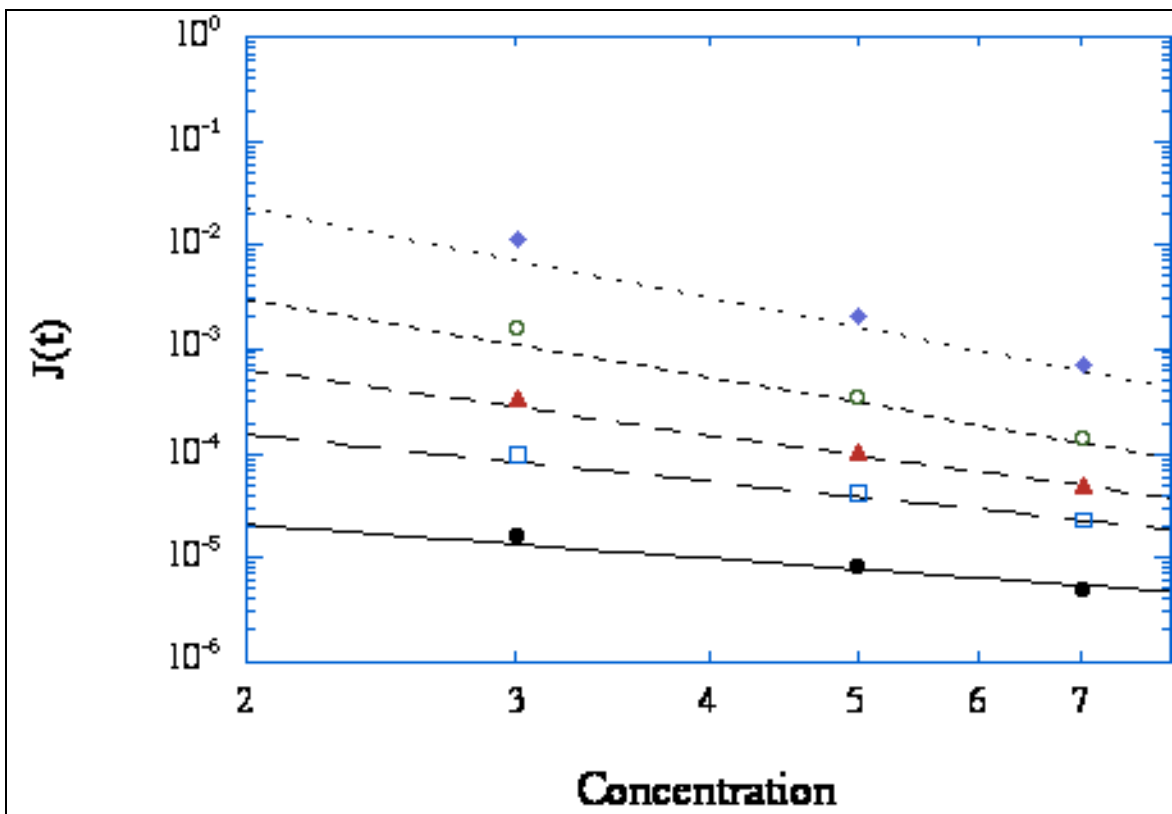


Figure 11: Creep compliance concentration scaling for 5 time decades: (●) 1E-6 (□) 1E-5 (▲) 1E-4 (○) 1E-3 and (◆) 1E-2.

## 2.5 Conclusion

This work was a detailed tracer microrheology and mechanical rheometry study of aqueous solutions of the flexible polymer polyethylene oxide (PEO). The study was carried out on PEO solutions in which the concentration was varied from 0.2 to 15 wt%. This ensured the examination of the viscoelastic properties as the polymer solution progressed from the unentangled to the entangled regime. PEO solutions having concentrations greater than 1 wt% exhibited considerable elasticity, as manifested through development of a plateau in the evolution of the mean square displacement. The tracer microrheology measurements showed excellent agreement with the mechanical rheometry measurements especially for the higher concentrations as manifested by the excellent agreement of the creep compliance measured from

the two techniques. A sphere size sweep on a 7 wt% PEO solution exhibited that the creep compliance was independent of probe size. This was indicative that neither structural effects nor longitudinal dynamical modes are playing a role in affecting the extracted viscoelastic properties.

The terminal relaxation times and the zero shear viscosity extracted from the long time mean squared displacement behavior and from mechanical rheometry measurements exhibited deviations in quantitative agreement at low concentration, but excellent agreement at high concentrations. Power law fits of the zero shear viscosity and the terminal relaxation time concentration dependence exhibited stronger variations with concentration than expected for semi dilute polymer solutions. The time dependent diffusion coefficient exhibited the expected behavior of increasing time dependency and decreasing magnitude with increasing PEO concentration. This is due to the particle diffusion becoming highly restricted by the increasingly entangled PEO network.

## **References**

1. Mason, T.G. and Weitz, D.A.; *Phys. Rev. Lett.*, **1995**, 74, 1250
2. Mason, T.G., Gang, H. and Weitz, D.A.; *J. Mol. Struct.*, **1996**, 383, 81
3. Mason, T.G., Gang, H. and Weitz, D.A.; *J. Opt. Soc. Am. A*, **1997**, 14, 139
4. Mason, T.G., Ganesan, K., van Zanten, J.H., Wirtz, D. and Kuo, S.C.; *Phys. Rev. Lett.*, **1997**, 79, 3282
5. Gittes, F., Schnurr, B., Olmsted, P.D., MacKintosh, F.C. and Schmidt, C.F.; *Phys. Rev. Lett.*, **1997**, 79, 3286
6. Schnurr, B., Gittes, F., MacKintosh, F.C. and Schmidt, F.C.; *Macromolecules*, **1997**, 30, 7781
7. Crocker, J., Valentine, M., Weeks, E., Gisler, T., Kaplan, P., Yodh, A. and Weitz, D.; *Phys. Rev. Lett.*, **2000**, 85, 888
8. Levine, A.J. and Lubensky, T.C.; *Phys. Rev. Lett.*, **2000**, 85, 1774
9. Levine, A.J. and Lubensky, T.C.; *Phys Rev E*, **2001**, 63, 1510
10. Weitz, D.A. and Pine, D.J.; *Diffusing Wave Spectroscopy in Dynamic Light Scattering- the method and some applications* (Clarendon Press 1993)
11. Palmer, A., Xu, J. and Wirtz, D.; *Rheol. Acta*, **1998**, 37, 97
12. Xu, J., Viasnoff, V. and Wirtz, D.; *Rheol. Acta*, **1998**, 37, 387
13. Palmer, A., Mason, T., Xu, J., Kuo, S. and Wirtz, D.; *Biophys. J.*, **1999**, 76, 1063
14. Mason, T., Gisler, T., Kroy, K., Frey, E. and Weitz, D.; *J. Rheol.*, **2000**, 44, 917
15. Morse, D.C.; *Macromolecules*, **1998**, 31, 7044
16. Morse, D.C. ; *Phys Rev E*, **1998**, 58, R1237
17. Gittes, F. and MacKintosh, F.C.; *Phys Rev E*, **1998**, 58, R1241

18. van Zanten, J.H. and Rufener, K.P.; *Phys. Rev. E*, **2000**, *62*, 5389
19. Amin, S, van Zanten, R.M, Rufener, K.P., Wirtz, D. and van Zanten, J.H.; in preparation
20. Abdala, A., Amin, S., Khan, S.A. and van Zanten, J.H.; in preparation
21. Solomon, M.J.; personal communication.
22. Gisler, T. and Weitz, D.A.; *Curr. Op. Coll. Interface. Sci.*, **1998**, *3*, 586
23. Polik, W. F. and Burchard, W.; *Macromolecules*, **1983**, *16*, 978
24. Brown, W.; *Macromolecules*, 1984, *17*, 66
25. Brown, W. and Stilbs, P.; *Polymer*, **1982**, *23*, 1780
26. Brown, W.; *Polymer*, **1985**, *26*, 1647
27. Zhou, P. and Brown, W.; *Macromolecules*, **1990**, *23*, 1131
28. Depner, M., Schurmann, B.L. and Auriemma, F.; *Molecular Phys*, **1991**, *74*, 715
29. Venhor, H., Fraaije, V., Strunk, H. and Burchard, W.; *Eur. Polym. J*, **1998**, *34*, 723
30. Plazek, D. J. and Frund, Z. N.; *Journal of Rheology*, **2000**, *44*, 929
31. Doi, M. and Edwards, S.F.; *The Theory of Polymer Dynamics*, **1986**, Oxford University Press: Oxford
32. Viasnoff, V.; personal communication.
33. Dimitrakopoulus, P., Brady, J.F. and Wang, Z.-G.; submitted to *Phys Rev Lett*

## Chapter 3

### Concentration Fluctuations, Viscoelasticity and Brownian Motion in CTAB/NaSal Wormlike Micellar Solutions

---

#### 3.1 Abstract:

This chapter details a tracer microrheology/mechanical rheometry, dynamic light scattering and static light scattering investigation of CTAB/NaSal solutions over a wide range of CTAB concentration and NaSal:CTAB mole ratio. The main experimental findings :

9) *Dynamic Light Scattering Measurements*: From the DLS measurements two distinct relaxation times are observed for CTAB concentration  $\geq 0.02$  M. The hydrodynamic correlation length,  $\zeta_H$ , associated with the fast relaxation mode is found to depend on both the CTAB concentration and NaSal:CTAB mole ratio. In particular, the CTAB concentration scaling of  $\zeta_H$  is seen to vary in a nonmonotonic manner with the NaSal:CTAB mole ratio. The scaling exponent is found to range from  $-0.25$  to  $-0.67$  where its minimum value is found for NaSal:CTAB mole ratios near 1.5-2.0. This is in strong support of the decreasing micellar ionization picture associated with increasing NaSal:CTAB molar ratio. The distinct minimum of the scaling exponent followed by a re-increase is indicative of micellar neutrality followed by a charge reversal at higher NaSal:CTAB molar ratios. The amplitude of the slow relaxation mode is observed to be strongly correlated with the hydrodynamic correlation length for NaSal:CTAB mole ratios less than or equal to 2 thereby strongly suggesting polymer/polyelectrolyte solution behavior at these conditions. The behavior of the hydrodynamic correlation length and slow mode amplitude are described quite well within a framework of micelle ionization and

electrostatic screening effects. The behavior of these parameters However, the NaSal:CTAB mole ratio and CTAB concentration dependence of the slow relaxation time can not be entirely explained within the context of electrostatic interactions. In order to account for the observed slow relaxation time behavior it is hypothesized that the micelle breaking time is influenced by bound salicylate ions whose degree of binding depends on both the NaSal:CTAB mole ratio and CTAB concentration.

*10) Static Light Scattering Measurements:* Most of the static parameters of interest corroborates the results of the dynamic light scattering measurements. The static correlation length showed a similar dependence on the NaSal:CTAB molar ratio as the hydrodynamic correlation length did, in that it increased to a maximum and then decreased to an almost constant value. The behavior however is limited to concentrations below 0.3M. The  $\chi$  parameter exhibits a similar monotonically decreasing behavior with the NaSal:CTAB molar ratio, supporting the decreasing micellar ionization picture associated with increasing NaSal:CTAB molar ratio. The distinct minimum followed by a re-increase to indicate neutrality and a charge reversal is however not observed in this case. One of the main results obtained from the static light scattering measurements is the extraction of the osmotic compressibility. The osmotic compressibility dependence on the NaSal:CTAB molar ratio exhibits a very interesting sharp transition at a particular NaSal:CTAB molar ratio after which the osmotic compressibility exhibited a much stronger dependence on the ratio. The ratio at which this sharp transition occurs is highly dependent on the CTAB concentration. This again supports the idea of charge reversal and its dependence on both the CTAB concentration and the NaSal:CTAB molar ratio. The osmotic pressure exhibited a power law dependence on the total concentration for each NaSal:CTAB ratio examined. The power law behavior was however divided into two

concentration regimes for each NaSal:CTAB molar ratio. The low concentration regime corresponded with viscous samples and at high ratios showed behavior similar to the theoretical behavior exhibited by equilibrium polymers. The high concentration regime corresponded with mostly gellike samples and exhibited a behavior similar to polyelectrolyte gels.

The overall picture that emerges from the static and dynamic light scattering measurements on CTAB/NaSal system is that of a system where the competition between micellar charge, electrostatic screening and micelle breaking controls the system dynamics.

**11) Tracer Microrheology and Mechanical Rheometry:** The tracer microrheology measurements on this system has revealed the viscoelastic response of the system over a wide frequency range, not accesible through mechanical rheometry. A series of solutions having a constant CTAB concentration [0.1M] and varying amounts of NaSal:CTAB molar ratio are observed to exhibit very similar viscoelasticity. The major difference showing up in the long time behavior after the system has relaxed. The plateau modulus exhibits a nonmonotonic dependence on the NaSal:CTAB molar ratio. The tracer microrheology and mechanical rheometry comparisions are also very interesting. The agreement between the two techniques is highly dependent on the frequency and the NaSal:CTAB molar ratio. The best agreement which is seen at lower frequencies or longer times is for the highest and lowest ratios examined. Sphere size sweeps also reveals that the creep compliance data cannot be collapsed onto a single master curve. This indicates that longitudinal dynamical modes or structural features may be affecting the extracted viscoelastic parameters. The deviations in the tracer microrheology and mechanical rheometry plateau moduli are also seen to track with the bulk longitudinal elastic modulus,  $M_G$ . However, the location of maximum deviation seems to occur at lower

NaSal:CTAB molar ratios then that of the longitudinal elastic modulus. Therefore it is difficult to make any definitive conclusions at this stage.

### ***3.2 Introduction:***

The utility of the tracer microrheology technique in gaining a deeper insight into the viscoelastic response of complex fluids has been discussed thus far in the context of the polyethylene oxide (PEO) system and will later be discussed in the context of the more complex FCC forming triblock copolymer Pluronic™ F108. For the simple flexible polymer, PEO, it was observed that the Generalized Stokes-Einstein Equation adequately described the tracer Brownian motion in this system, as evidenced through the good quantitative agreement between the viscoelastic properties extracted from tracer microrheology and those extracted from mechanical rheometry. The sphere size sweeps carried out on this system also exhibited a complete collapse of the data into a single master  $J(t)$  curve. This was indicative that longitudinal compression modes did not affect the extracted rheological parameters. In order to extend the understanding of probe motion in viscoelastic media further, a systematic tracer/mechanical rheometry investigation was extended to a worm like micellar system. The system that was chosen was the worm like micellar system-Cetyltrimethylammonium Bromide/ Sodium Salicylate. This system was chosen because wormlike micelles have striking similarities with polymeric systems, yet exhibits more interesting and complicated static and dynamic behavior(1-15).

Surfactant molecules are known to self assemble into a wide variety of microstructures when dispersed in aqueous solution. At very low surfactant concentrations spherical micelles may be formed or, if the hemispheres making up the micelle are of excessively high curvature energy owing to surfactant packing constraints and head group interactions, uniaxial growth will

occur leading to rod-like or long, worm-like micelles (1). When the length of these micelles becomes greater than their entanglement length, they become entangled and are known to exhibit properties similar to semi-dilute polymer solutions. These worm-like micelles are similar to polymers in that they are quite flexible (typical persistence lengths of  $\sim 20$  nm versus diameters of  $\sim 5$  nm) and they exhibit contour lengths on the order of microns (1). These so-called equilibrium polymers differ from classical polymers in that they are constantly breaking and recombining and, therefore, do not exhibit a quenched contour length (molecular weight) distribution.

The dynamics of several worm-like micelle systems have been investigated (1-13). These earlier studies primarily considered viscoelastic properties with a focus on distinguishing the differences and similarities between entangled worm-like micelle and polymer solutions. One distinct difference that was noted is the observation that worm-like micelle solutions exhibit a single relaxation time at low frequencies as opposed to polymer solutions where a spectrum of relaxation times is observed (1). The existence of a single relaxation time is directly due to the fact that worm-like micelles are equilibrium polymers capable of breaking and recombining with one another (14). In addition to the typical mechanical rheometry measurements, several investigators have carried out forced Rayleigh scattering (9) and dynamic light scattering studies of worm-like micelle systems (8,10,12,13). The previous investigators have observed a bimodal relaxation in the concentration fluctuation spectrum of worm-like micelles as measured by dynamic light scattering. Although similar bimodal relaxation spectra have been observed for semi-dilute polymer solutions under theta conditions, the so-called slow mode is absent under good solvent conditions (15).

Most investigators believe that the existence of two characteristic decay times is indicative of two dynamical regimes—a liquid regime and a gel regime. As noted previously, this behavior has also been observed for semi-dilute solutions of flexible polymer chains dissolved in a theta solvent. Under these conditions, the dynamic structure factor,  $S(q,t)$ , exhibits a fast and slow mode (*i.e.* a double exponential form) for wavevectors,  $q$ , such that  $q\xi \ll 1$  where  $\xi$  is the polymer solution correlation length (16-20),

$$S(q,t) = A_F e^{-t/\tau_F} + A_S e^{-t/\tau_S} . \quad (1)$$

Here  $\tau_F$  and  $\tau_S$  are the fast and slow mode relaxation times respectively. Most of the worm-like micelle solutions considered here are in the gel-like regime described by Adam and Delsanti in which the fast relaxation corresponds to the osmotic restoring force owing to the fact that at short times (high frequencies) the worm-like micelle network behaves as a permanent gel (18). This mode is diffusive and as such  $\tau_S \sim q^{-2}$ . Although the results are not shown here, the  $q^2$  dependence of the fast mode observed by others was confirmed for several of the worm-like micelle solutions considered here. The slow mode (long time, low frequency) relaxation time corresponds to the structural relaxation of the worm-like micelle network and as such is closely related to the network terminal stress relaxation time. For the gel-like regime of Adam and Delsanti, the relative amplitudes of the two modes,  $A_F$  and  $A_S$ , are related to the bulk elastic and osmotic moduli and their sum is equal to unity.

It is believed that cetyltrimethylammonium bromide, CTAB, a cationic surfactant forms long, entangled micelles in the presence of sodium salicylate (NaSal) salt (2-11). A series of experimental investigations carried out by Shikata *et al.* (2,4-6,11) and Nemoto *et al.* (8-10) has helped to clarify differences in the dynamical behavior between CTAB/NaSal micelle networks and semi-dilute solutions of high molecular weight flexible polymer chains. These

measurements indicate that the gel diffusion coefficient associated with the fast mode,  $D_G$ , and the hydrodynamic correlation length,  $\zeta_H$ , corresponding to this diffusion coefficient depend in a complicated manner on both the NaSal:CTAB mole ratio at fixed CTAB concentration,  $C_{CTAB} = 0.1 \text{ M}$ , and also on  $C_{CTAB}$  at a fixed NaSal:CTAB mole ratio of unity.

The objective of the present experimental study was to carry out a more comprehensive examination of the effect of the NaSal:CTAB mole ratio and the total CTAB concentration,  $C_{CTAB}$ , on the concentration fluctuation spectrum of CTAB/NaSal systems. This chapter reports the results of an extensive dynamic light scattering study carried out on a series of CTAB/NaSal solutions in which the CTAB concentration was varied from 0.01M to 0.50 M while the NaSal:CTAB mole ratio was varied from 0.4 to 6.0 at room temperature, 23 °C. The DLS section of the chapter focuses on the hydrodynamic correlation length, the slow mode relaxation time and the relative amplitudes of the fast and slow modes. The dynamical properties are used in combination with the zero angle static structure factor and osmotic compressibilities determined from an extensive static light scattering study of the CTAB/NaSal system (21, section 2 in current chapter), to further understanding of Brownian probe motion in the system as investigated by tracer microrheology (section 3).

### ***3.3 Materials and Methods***

***Materials.*** Cetyltrimethylammonium bromide (CTAB) and sodium salicylate (NaSal) were obtained from Fluka and Aldrich Chemicals respectively. Both the CTAB and NaSal were used without further purification. Dust free CTAB/NaSal aqueous solutions were prepared with deionized water that had been filtered through a 0.02  $\mu\text{m}$  filter (Whatman-Anotop 25). The CTAB concentration was varied from 0.01 to 0.50 M for each salt: detergent (NaSal:CTAB)

mole ratio considered here. The NaSal:CTAB mole ratio was varied from 0.4 to 6.0. It should be noted that it proved unfeasible to form CTAB/NaSal solutions at CTAB concentrations in excess of 0.3 M for a NaSal:CTAB ratio of 6. The CTAB/NaSal solutions were allowed to equilibrate at 60 °C for a period of seven days. The samples were then further equilibrated at room temperature for three weeks prior to taking measurements. Long equilibration times were utilized because static light scattering measurements indicated incomplete mixing for CTAB concentrations  $\geq 0.2$  M during the first few weeks.

**3.3.1 Dynamic Light Scattering:** The dynamic light scattering (DLS) measurements were conducted with a home built apparatus (23). The fiber optic-based DLS spectrometer utilized a rigid arm attached to a Newport rotational stage, an ALV-SO/SIPD photon detector and an ALV-5000/E Multiple Tau Digital Correlator operating in its normal mode. The light source was a diode pumped solid state (DPSS) Nd-YAG laser operating at a wavelength of 532 nm *in vacuo*. The scattered light was detected by a goniometer mounted multimode optical fiber that was coupled to the ALV-SO/SIPD photon detector. The intensity autocorrelation function  $g_2(q,t)$  was measured for each sample at a scattering angle of 90°. All measurements were taken at 23 °C. The measured intensity autocorrelation function was converted into the electric field autocorrelation function,  $g_1(q,t)$ , using the Siegert relationship:

$$g_2(q,t) = 1 + B|g_1(q,t)|^2 \quad (2)$$

The measured electric field autocorrelation functions were analyzed by two methods: a double exponential fit of the entire electric field autocorrelation function and single exponential fits of the isolated fast and slow relaxations. For the case of the single exponential fit of the fast mode relaxation the slow mode amplitude was taken as a constant background. The

simultaneous double exponential fit, supposedly applicable to semi-dilute polymer solutions under theta conditions, was found to accurately describe only a fraction of the CTAB/NaSal solutions considered here. Those solutions were most likely those truly exhibiting a single slow mode relaxation time or Maxwellian behavior (20). In light of the fact that only a few spectra were well described by a simultaneous, double exponential fit all of the results reported here are the values found from the single exponential fits to the fast and slow relaxation modes. The network cooperative diffusion coefficient,  $D_c$ , was estimated from the fast mode relaxation time,

$$\tau_F^{-1} = q^2 D_c \quad (3)$$

The hydrodynamic correlation length  $\xi_H$  was obtained through use of the Stokes-Einstein relationship as applied to the cooperative diffusion coefficient estimated from the fast mode relaxation time:

$$\xi_H = \frac{kT}{6\eta D_c} \quad (4)$$

where  $k$  is Boltzmann's constant,  $T$  is the absolute temperature and  $\eta$  is the solvent viscosity.

**3.3.2 Static Light Scattering:** The static light scattering measurements were carried out using a DAWN EOS Laser Photometer (Wyatt Technology Inc, Santa Barbara, CA), based on a photodiode array with eighteen fixed detectors at angular positions from 22.5° to 147°. The light source used was a vertically polarized 30mW gallium arsenide laser with a wavelength of 690 nm *in vacuo*. The Rayleigh ratios for each concentration were extracted and then analyzed with a view of obtaining the osmotic compressibilities.

**3.3.3 Tracer Microrheology:** Tracer microrheology measurements were conducted using the multiple light scattering technique, Diffusing Wave Spectroscopy. Experimental details on the

technique have been described in detail previously (chapter on PEO and Pluronic tracer microrheology). A few notable points about the CTAB/NaSal systems must however be mentioned. Ideally in order to ensure multiple light scattering, tracer probe particles are added at 1 vol %. On adding 1 micron size polystyrene tracer particles, it was however observed that the particles were strongly aggregated, as revealed through observation under a microscope. In order to utilize a 1 vol% tracer particle addition, spheres having different surface chemistries were used. However, the aggregation problem could not be solved. Use of silica particles also did not prevent the observed aggregation. The only option which worked was to use the PS spheres at a lower 1 vol %. Although this is not an ideal, it was still within the tracer microrheology requirement of  $L/l^* > 5$ .

### ***3.4 Results and Discussion***

#### ***3.4.1 Phase Behavior:***

The CTAB/NaSal system exhibits a wide variety of visual viscoelastic behavior depending upon the CTAB concentration and the NaSal:CTAB molar ratio. Figure 3.1 illustrates this wide behavior for seven NaSal:CTAB molar ratios.

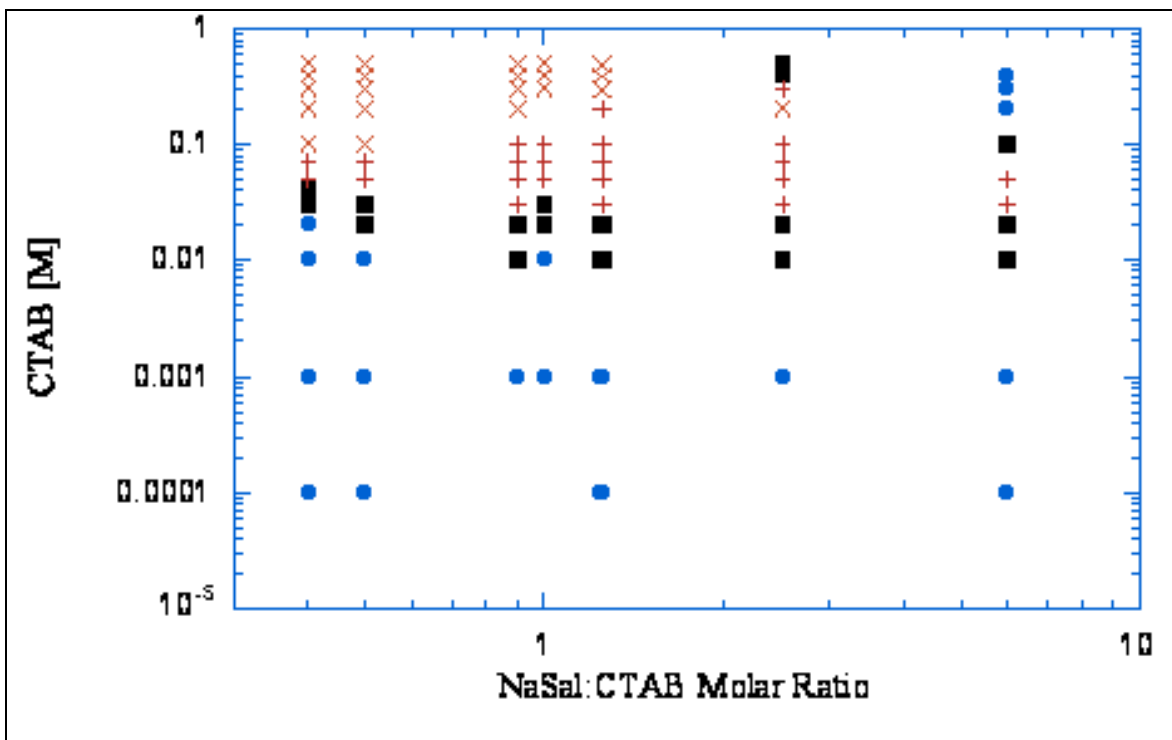


Figure 3.1: Viscoelastic behavior dependence on CTAB concentration and NaSal:CTAB molar ratio. Depending upon the CTAB concentration and the NaSal:CTAB molar ratio four distinct viscoelastic behaviors were exhibited: (●) Viscous-fluid like (■) Viscous-flows but exhibits much more elasticity (+) Gel-like but does flow slightly given long enough time and (X) hard gel-does not flow at all.

It should be noted that the viscoelastic behavior indicated in Figure 3.1 is qualitative and based purely on visual inspection of the samples. The behavior is seen to be predominantly liquid or viscous like at the low CTAB concentrations and low ratio regime and gel-like for the high concentration regime. The onset of the gel-like behavior is however seen to be very sensitive to the NaSal:CTAB molar ratio. The increasing elasticity and gellike behavior is expected as the CTAB concentrations increases since the micelles will grow and become more entangled. The widely varying behavior at high ratios maybe due to changing micellar ionization and/or micellar breakup. This will be discussed further in the context of dynamic and static light scattering measurements on the system.

### 3.4.2 Dynamic Light Scattering:

3.4.2.1 Evolution of the Electric Field Autocorrelation Function with CTAB Concentration. A typical evolution of the electric field autocorrelation function with increasing CTAB

concentration at fixed NaSal:CTAB mole ratio (0.90) is shown in Figure 3.2. It is readily apparent that for the lowest CTAB concentration considered here,  $C_{CTAB} = 0.01$  M, there is no slow mode present. Upon doubling the CTAB concentration to 0.02 M, a slow mode of long relaxation time, albeit of very small amplitude, begins to evolve. The slow mode becomes very prominent for CTAB concentrations  $\geq 0.03$  M. While both the fast and slow mode relaxation times exhibit a monotonic decrease with increasing CTAB concentration for the NaSal:CTAB mole ratio considered in Figure 3.2, there is no doubt that the slow mode amplitude varies in a nonmonotonic manner with CTAB concentration. This latter observation was true for all the NaSal:CTAB mole ratios considered in this study. The CTAB concentration corresponding to the slow mode amplitude maximum was observed to decrease with increasing NaSal:CTAB mole ratio. However, the slow mode relaxation time did not always decrease monotonically with increasing CTAB concentration for different NaSal:CTAB mole ratios.

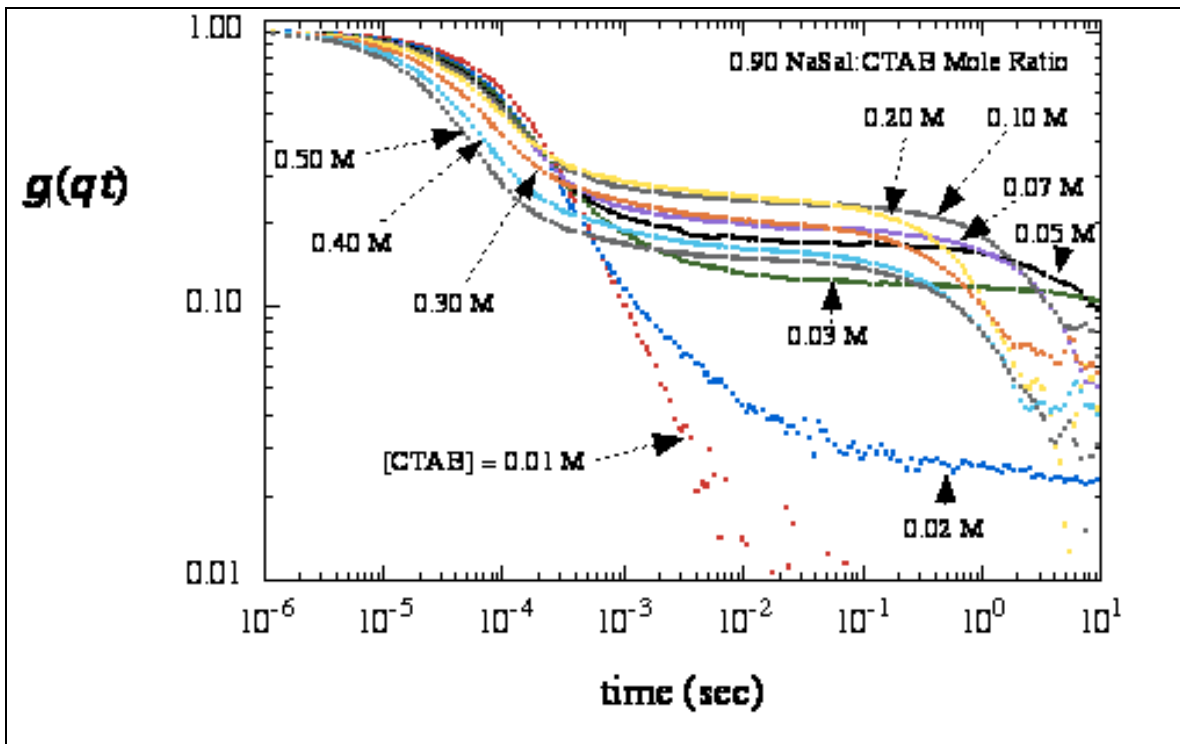


**Figure 3.2.** The variation of the electric field autocorrelation function with CTAB concentration for a NaSal mole ratio of 0.90. Similar behavior was observed at all other NaSal:CTAB mole ratios. The temperature of systems considered here was 23 °C.

3.4.2.2 Effect of NaSal:CTAB Mole Ratio on the Hydrodynamic Correlation Length. Figure 3.3 shows the variation of the hydrodynamic correlation length,  $\xi_H$ , with NaSal:CTAB mole ratio for five CTAB concentrations. The hydrodynamic correlation length exhibited the same qualitative behavior at all the CTAB concentrations considered in this study. Initially  $\xi_H$  increases with increasing NaSal:CTAB mole ratio until reaching a maximum and then decreases to a nearly constant value upon further increase in the NaSal:CTAB mole ratio. The NaSal:CTAB mole ratio at which the maximum  $\xi_H$  value occurred was observed to decrease with increasing CTAB concentration. It is also apparent that the hydrodynamic correlation length decreases with increasing CTAB concentration at fixed NaSal:CTAB mole ratio as expected (24)

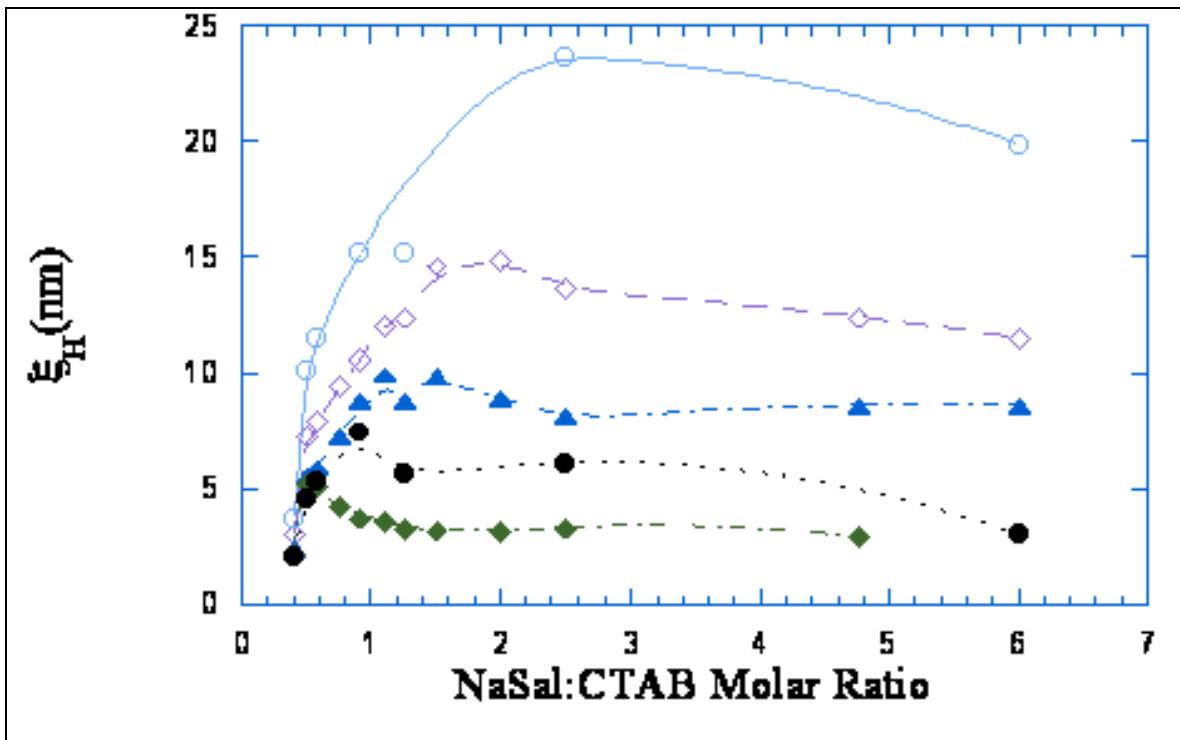


**Figure 3.3.** NaSal:CTAB mole ratio dependence of the hydrodynamic correlation length for five CTAB concentrations: (○) 0.02, (◇) 0.05, (▲) 0.10, (●) 0.20 and (◆) 0.50-M. The NaSal:CTAB mole ratio corresponding to the maximum hydrodynamic correlation length is observed to decrease with increasing CTAB concentration

In the absence of additional observations, one may be inclined to believe that the initial increase in the hydrodynamic correlation length may be attributed to the growth of the CTAB/NaSal micelles with increasing amounts of sodium salicylate. The salicylate ions are believed to insert themselves between the CTAB head groups thereby decreasing the repulsive interactions between  $CTA^+$  headgroups, that in turn reduces the spontaneous curvature of the system. The decrease in spontaneous curvature promotes uniaxial micelle growth owing to the large energetic cost of the hemispherical endcaps. This is the picture one would expect in the absence of a slow relaxation mode wherein the correlation length would grow until the onset of micelle overlap or entanglement. However, two relaxation modes are always observed at the lowest NaSal:CTAB mole ratios considered in this study for CTAB concentrations  $\geq 0.05$  M thereby indicating that these systems are either entangled or at the very least strongly interacting. Therefore, the observed initial increase in the hydrodynamic correlation length with increasing NaSal:CTAB mole ratio observed for CTAB concentrations  $\geq 0.05$  M must be due to enhanced concentration fluctuations and not micelle growth. In the case of the 0.02 M CTAB concentration solution micelle growth is most likely dominating the observed  $\zeta_H$  growth at the lowest NaSal:CTAB mole ratios (0.40-0.57) owing to the single relaxation time spectra observed, but at higher CTAB concentrations the concentration fluctuation spectrum once again indicates the onset of strong micellar interactions.

Ionic worm-like micelle solutions exhibit striking similarities with polyelectrolyte solutions (25). The initial increase in concentration fluctuations observed for NaSal/CTAB solutions with increasing NaSal:CTAB mole ratios is similar to polyelectrolyte gels in which the concentration fluctuations increase with decreasing ionization (26-28). Previous NMR measurements indicate that as the NaSal:CTAB mole ratio is increased the degree of Sal<sup>-</sup>

incorporation into the micelles also increases. This incorporation leads to the micellar charge evolving from negative to positive (29,30). The initial decrease of the micelle net charge at low NaSal:CTAB mole ratios is analogous to the decrease in ionization of charged polyelectrolyte solutions, leading to enhanced concentration fluctuations. The subsequent decrease in concentration fluctuations after the observed maximum can be attributed to the re-increase in the micelle ionization associated with charge reversal. The earlier NMR measurements also indicate that Sal<sup>-</sup> binding increases with increasing CTAB concentration (30). This effect appears to be confirmed by the observed decrease of the NaSal:CTAB mole ratio corresponding to the maximum  $\Delta_H$  value that occurs with increasing CTAB concentration. It should also be noted that similar  $\Delta_H$  behavior has also been observed for polyampholyte solutions at high salt concentrations. In a study of polyampholyte solutions, Nisato et al (31) have reported enhanced light scattering (indicating larger concentration fluctuations and therefore larger  $\Delta_H$ ) at lower salt concentrations. At very high NaSal:CTAB ratios salicylate ions may act as a conventional salt thereby leading to electrostatic screening. Thus, the combination of enhanced screening and increasing ionization may be responsible for the nearly constant  $\Delta_H$  at high NaSal:CTAB ratios.

*3.4.2.3 Effect of CTAB Concentration on Hydrodynamic Correlation Length:* The variation of  $\Delta_H$  with CTAB concentration is shown in Figure 3.4 for three different NaSal:CTAB mole ratios. The hydrodynamic correlation length is observed to decrease monotonically with increasing CTAB concentration for all three NaSal:CTAB mole ratios considered in Figure 3.4. Although not shown here, the same trend was observed, decreasing  $\Delta_H$  with increasing CTAB concentration, for every NaSal:CTAB mole ratio considered in this study. The monotonic decrease of the hydrodynamic correlation length with increasing CTAB concentration at fixed

NaSal:CTAB mole ratio is an indication of strong interactions occurring amongst the micelles either through entanglements or through the formation of cross-links. The  $\xi_H$  CTAB concentration dependence is typically represented in the form of a power law relation

$$\xi_H \sim C_{CTAB}^a \quad (5)$$

In the case of polymer solutions the scaling exponent  $a$  depends only on solvent quality (24). However, electrostatic screening effects (32-33) also influence polyelectrolyte solution hydrodynamic correlation lengths.

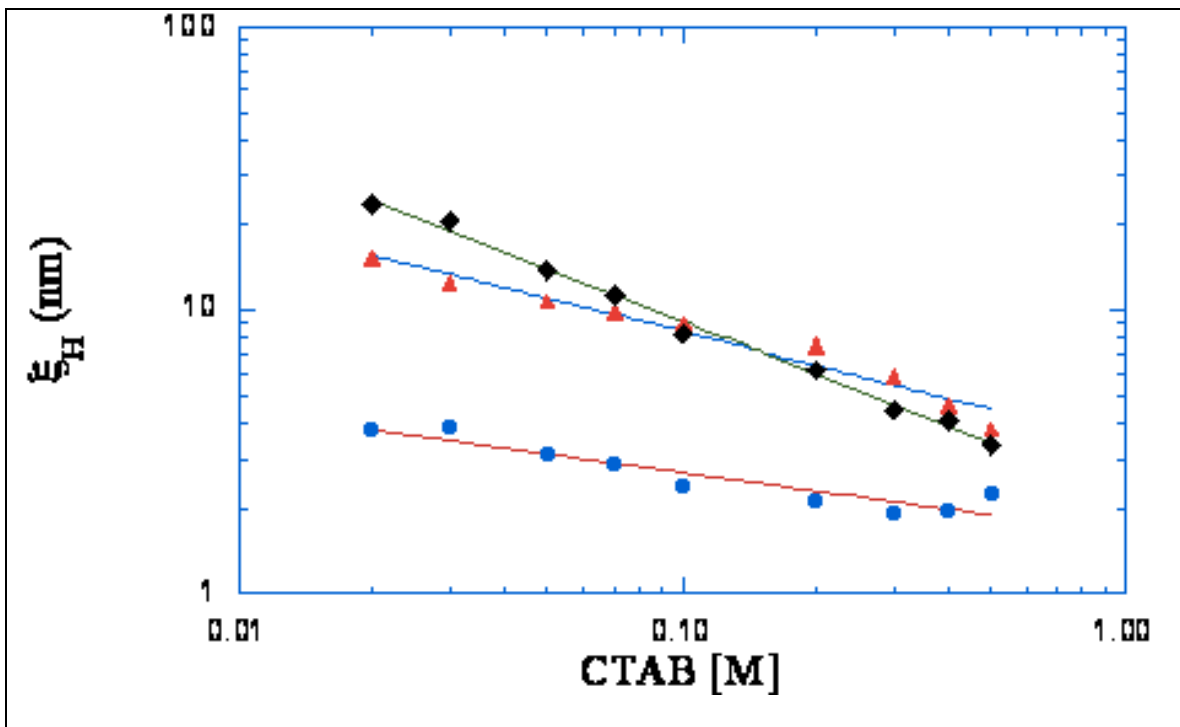


**Figure 3.4.** CTAB concentration dependence of the hydrodynamic correlation length for three NaSal:CTAB ratios: (●) 0.40, (▲) 0.90 and (◆) 2.50. Note the strong variation in concentration dependence at the different NaSal:CTAB mole ratios

For the case of CTAB/NaSal solutions, the scaling exponent  $\alpha$  was found to be strongly dependent on NaSal:CTAB mole ratio as is readily apparent in Figure 3.5. The small magnitude of  $\alpha$  observed at small NaSal:CTAB mole ratios may be indicative of the existence of a charged worm-like micelle network where electrostatic repulsion and network formation are suppressing the observed hydrodynamic correlation length (concentration fluctuations). For NaSal:CTAB mole ratios near 1.5-2.0 the scaling exponent reaches its largest magnitude which is a value near that expected for a semi-dilute polymer solution under good solvent conditions ( $\alpha = -0.77$ ).

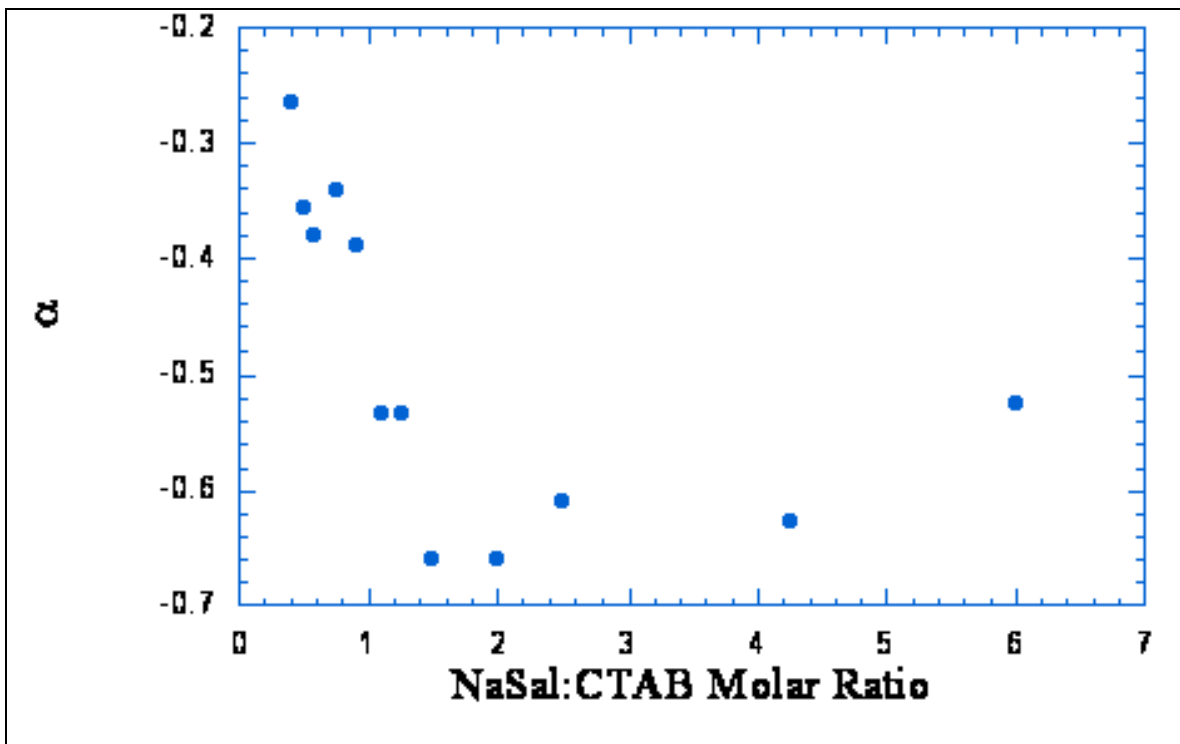


**Figure 3.5.** NaSal:CTAB mole ratio dependence of the hydrodynamic correlation length CTAB concentration scaling exponent  $\alpha$  where  $\xi_H \sim C_{CTAB}^{\alpha}$ . Note the nonmonotonic variation of the scaling exponent with NaSal mole ratio.

This may indicate either near neutral worm-like micelles or a sufficiently high excess NaSal concentration to screen electrostatic interactions between the worm-like micelles if they remain charged. After reaching its maximum value, the magnitude of  $\alpha$  begins to decrease

slightly with increasing NaSal:CTAB mole ratio. This behavior is completely consistent with the charge reversal phenomenon reported by others (29,30).

*3.4.2.4 Effect of NaSal:CTAB Mole Ratio on the Slow Mode Relaxation Time.* The slow mode relaxation time,  $\tau_s$ , exhibits a very complex dependence on NaSal:CTAB mole ratio at fixed CTAB concentration (see Figure 3.6). This slow mode relaxation time NaSal:CTAB mole ratio dependence has been observed previously by both mechanical rheology and dynamic light scattering, albeit at only a few detergent concentrations (4,5,8- 10).

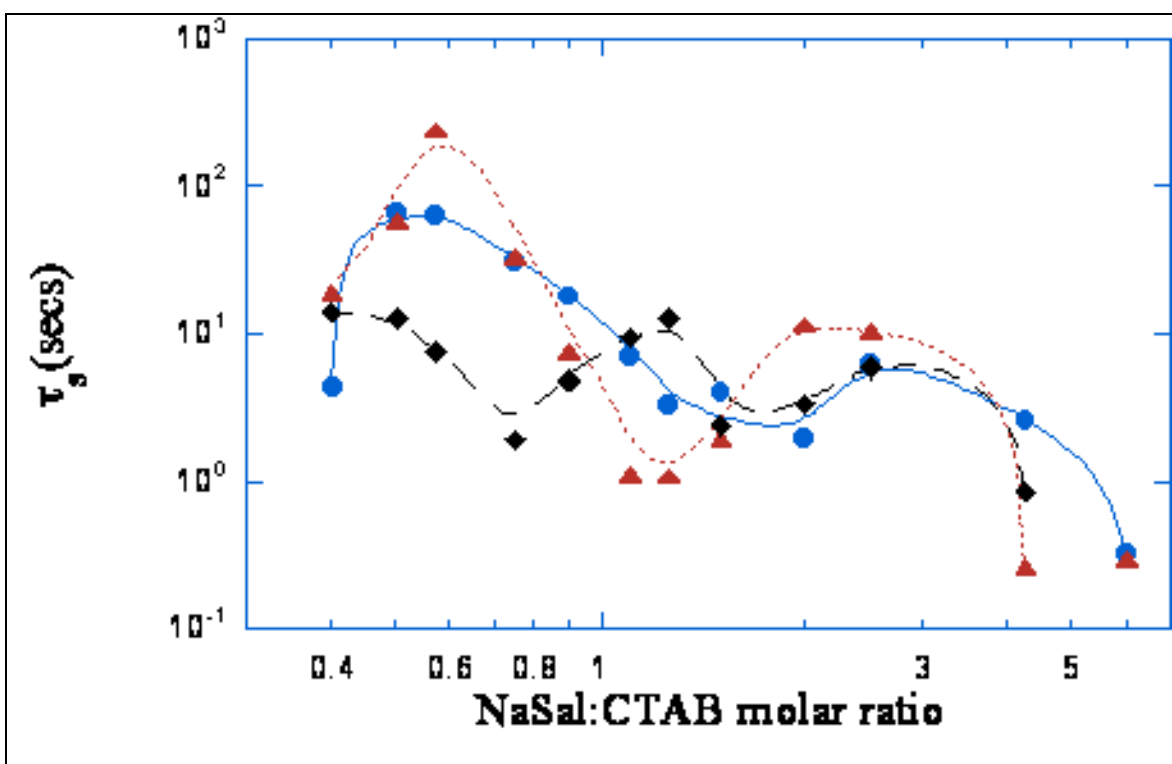


**Figure 3.6.** NaSal:CTAB mole ratio dependence of the slow or terminal relaxation time as measured by dynamic light scattering at three CTAB concentrations: (●) 0.05, (▲) 0.10 and (◆) 0.50 M. This nonmonotonic behavior has been observed by previous investigators with both dynamic light scattering and mechanical rheometry.

The nonmonotonic NaSal:CTAB mole ratio dependence of the slow mode relaxation time owes to the different competing relaxation processes present in CTAB/NaSal worm-like micelle systems.

Stress relaxation in entangled classical polymer solutions is well described via a reptation mechanism in which the polymer chains diffuse along their contour path or tube until they escape at which point the imposed stress is completely relaxed (34). The reptation time,  $\tau_{rep}$ , is the time required for a polymer chain to diffuse along its contour length thereby escaping from the stressed initial tube. For the case of an entangled polymer solution under good solvent conditions the Doi-Edwards tube theory predicts that  $\tau_{rep}$  is given by

$$\tau_{rep} \sim L^3 \phi^{3/2} \quad (6)$$

where  $L$  is the polymer contour length and  $\phi$  is the polymer volume fraction (34). It should be noted that this expression slightly underestimates the experimentally observed length dependence of the reptation time ( $\tau_{rep,exp} \sim L^{3.4}$ ). While equilibrium polymers or worm-like micelles can also relax stress via curvilinear diffusion or reptation, their ability to break and recombine provides another route for stress relaxation. When the worm-like micelle breaking/recombination time is much longer than the worm-like micelle reptation time, stress relaxation is dominated by the reptation process and the stress relaxation behavior of living polymers should be essentially the same as for classical polymers. However, when the worm-like micelle breaking/recombination time is much shorter than the reptation time, the breaking/recombination kinetics dominate the stress relaxation process leading to monoexponential or Maxwellian stress relaxation behavior whose relaxation time,  $\tau_R$ , is simply the geometric mean of the reptation and micelle breaking times (15)

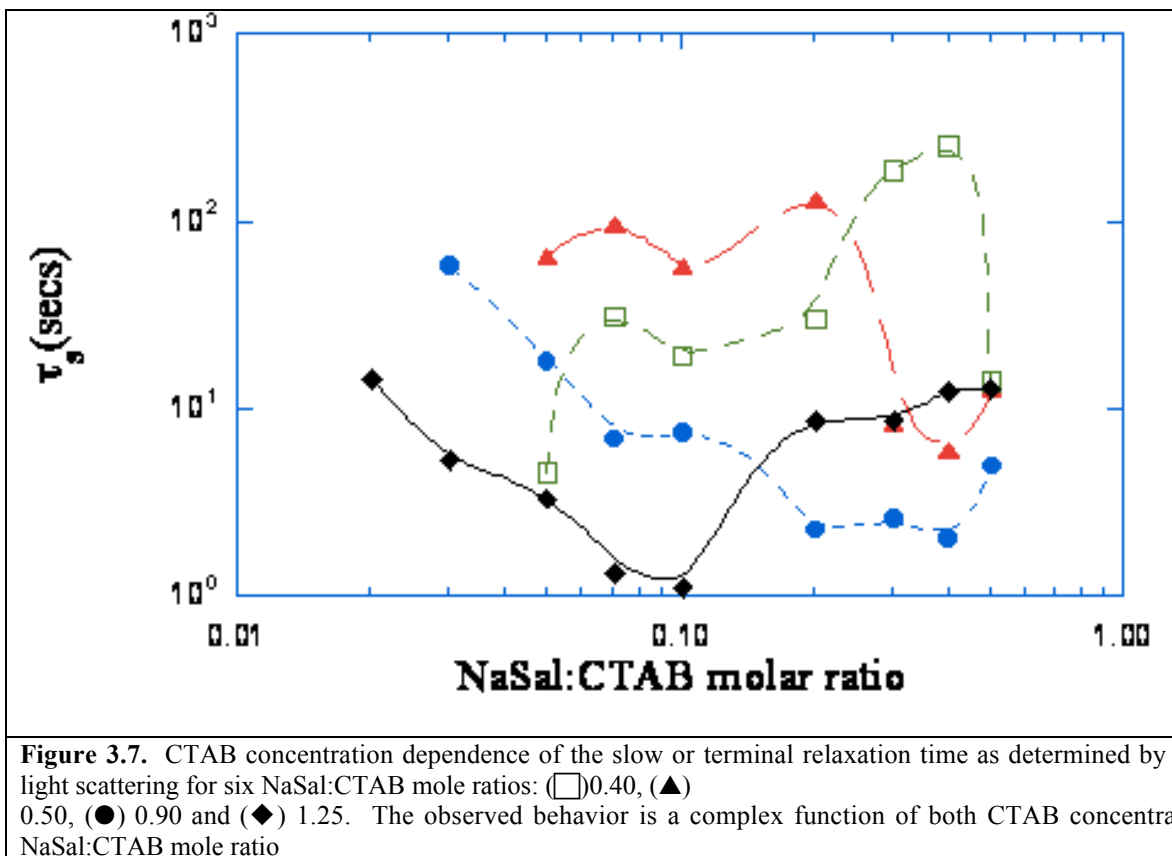
$$\tau_R \sim (\tau_{rep} \tau_{break})^{1/2} \sim L \phi^{3/4}. \quad (7)$$

The micelle breaking time,  $\tau_{break}$ , is simply inversely proportional to the worm-like micelle contour length,  $\tau_{break} \sim 1/L$  and is assumed to be independent of detergent concentration. As the salicylate ion concentration increases at low NaSal:CTAB mole ratio one would expect that both the micelle contour length and volume fraction would increase thereby leading to a concurrent increase in the slow mode relaxation time. However, as noted previously the slow mode relaxation time actually decreases with increasing NaSal:CTAB mole ratio in the low NaSal:CTAB mole ratio region. One possible explanation of this decreasing slow relaxation time with increasing NaSal:CTAB mole ratio may be that the micelle breaking rate increases as the NaSal concentration increases with the NaSal acting as a catalyst for micelle breaking. In this scenario,  $\tau_{break}$  would no longer be simply proportional to  $1/L$ -its value would have a chemical component as well. The strong association between the  $\text{Sal}^-$  ions and the micelles lends credence to this possibility.

The subsequent growth of the relaxation time for intermediate NaSal:CTAB mole ratios may be indicative of electrostatic effects starting to dominate the stress relaxation behavior. With increasing NaSal:CTAB ratios, the micelle ionization decreases. Since charged worm-like micelle solutions are somewhat analogous to polyelectrolyte solutions, a decrease in the micelle ionization will cause the slow relaxation time to increase (32-33). This scenario is consistent with the CTAB concentration dependence of the hydrodynamic correlation length at these intermediate NaSal:CTAB mole ratios, where it was observed that the scaling exponent of the hydrodynamic correlation length with concentration reaches its maximum magnitude for NaSal:CTAB mole ratios near 1.5-2.0. As noted previously, NMR measurements indicate that the slow relaxation time NaSal:CTAB mole ratio variation depends on the CTAB concentration (29,30). This suggests that the charge reversal NaSal:CTAB mole ratio is affected by the CTAB

concentration, thereby leading to the observed shift of the secondary slow relaxation time maximum. This is also consistent with the observed CTAB concentration dependence of the hydrodynamic correlation length variation with NaSal:CTAB mole ratio. The final rapid decrease in the slow mode relaxation time most likely owes to micelle breakup driven by excess NaSal (2,4-6). Micellar break down at large NaSal:CTAB mole ratios has been revealed in recent rheological measurements that indicate a decrease in shear viscosity with increasing excess salicylate ions (35). This viscosity diminution is also readily observed visually.

*3.4.2.5 Effect of CTAB Concentration on the Slow Mode Relaxation Time.* The slow mode relaxation time CTAB concentration dependence is also complex and strongly influenced by the NaSal:CTAB mole ratio (see Figures 3.7 & 3.8). The effect of both the NaSal:CTAB mole ratio and the CTAB concentration was also clearly evident in Figure 3.6, where the first minimum in the slow relaxation time shifted to lower NaSal:CTAB mole ratio with increasing CTAB concentration. Not unexpectedly, it is most likely that interplay between micelle growth, micellar ionization and electrostatic screening is the cause of the complex slow relaxation time variation with CTAB concentration. For small NaSal:CTAB mole ratios, the micelles are still positively charged and the initial increase of the slow mode relaxation time with increasing CTAB concentration is most likely due to micellar growth.



At higher NaSal:CTAB mole ratios the micelles are believed to be nearly neutral (29,30). Therefore, an increase in CTAB concentration should lead to a concurrent increase in the micelle length and the slow relaxation time. However, a decrease in the slow relaxation time with increasing CTAB concentration is actually observed. While it is most likely that the NaSal:CTAB ratio plays the predominant chemical role in affecting the micelle breaking time, it is possible that the micelle breaking time also depends on the CTAB concentration independent of the micelle length effect if one recalls that  $\text{Sal}^-$  binding increases with increasing CTAB concentration at fixed NaSal:CTAB mole ratio.

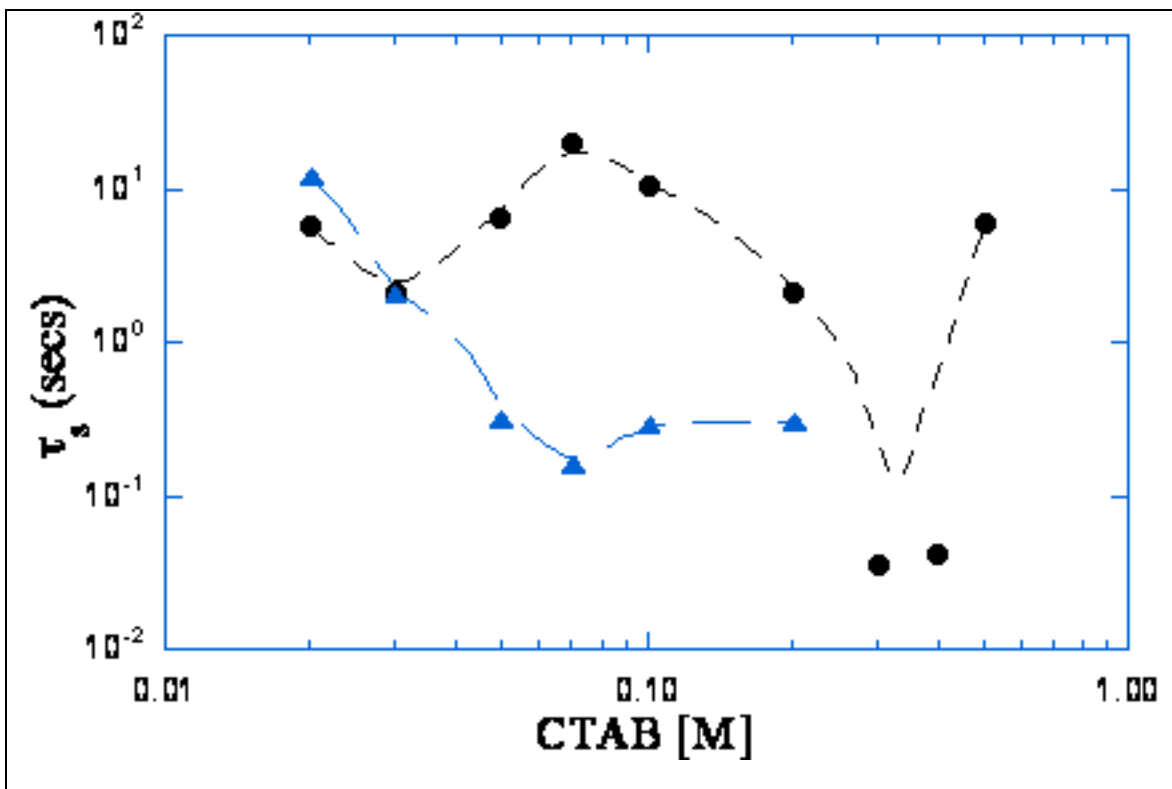


**Figure 3.8.** CTAB concentration dependence of the slow or terminal relaxation time as determined by dynamic light scattering for two NaSal:CTAB mole ratios: (●) 2.50 and (▲) 6.00. The observed behavior is a function of both CTAB concentration and NaSal:CTAB mole ratio.

The enhanced  $\text{Sal}^-$  binding may actually catalyze the micelle breaking process thereby decreasing the slow mode relaxation time. At a NaSal:CTAB mole ratio of 2.5 the behavior is very different. The slow mode relaxation time remains nearly constant at low CTAB concentrations and then begins to decrease at sufficiently high CTAB concentrations. This may be further evidence of micelle overcharging as the observed behavior may be indicative of a competition between electrostatic interaction and  $\text{Sal}^-$  induced chain breaking. At even larger higher NaSal:CTAB mole ratios, the excess  $\text{Sal}^-$  ions lead to a breakdown in the micelle size and the increasing CTAB concentration further drives  $\text{Sal}^-$  uptake thereby catalyzing micellar breakdown.

It would be negligent not to mention the possibility of transient cross-link formation (36-42). The formation of transient cross-links would cause the reptation time to scale with the distance between cross-links,  $\bar{L}_c$ . If cross-links are being formed, this distance should decrease with increasing CTAB concentration thereby leading to a decrease in the slow relaxation time. One group has proposed that small angle light scattering and mechanical rheometry measurements indicate CTAB/NaSal solutions evolve from an entangled system to a cross-linked system at sufficiently large NaSal:CTAB mole ratios (7:1-10:1) for the case of 0.03 M CTAB concentration (37,38). The higher CTAB concentrations considered here may actually promote the formation of cross-links at lower NaSal:CTAB mole ratios as  $\text{Sal}^-$  binding increases with increasing CTAB concentration (29,30). The near constant slow mode relaxation times observed for large CTAB concentrations at large NaSal:CTAB mole ratios may be indicative of network saturation.

*3.4.2.6 Effect of NaSal:CTAB Mole Ratio on the Slow Mode Amplitude.* The slow mode amplitude is strongly influenced by the NaSal:CTAB mole ratio for all CTAB concentrations considered in this study (see Figure 3.9). The slow mode amplitude variation is essentially the same for each detergent concentration. That is, initially increasing with increasing NaSal:CTAB mole ratio until reaching a maximum value after which the amplitude then decreases with further increases in the NaSal:CTAB mole ratio. The NaSal:CTAB mole ratio value at which the slow mode amplitude maximum occurs varies with CTAB concentration is essentially the same as that observed for the hydrodynamic correlation length maximum.

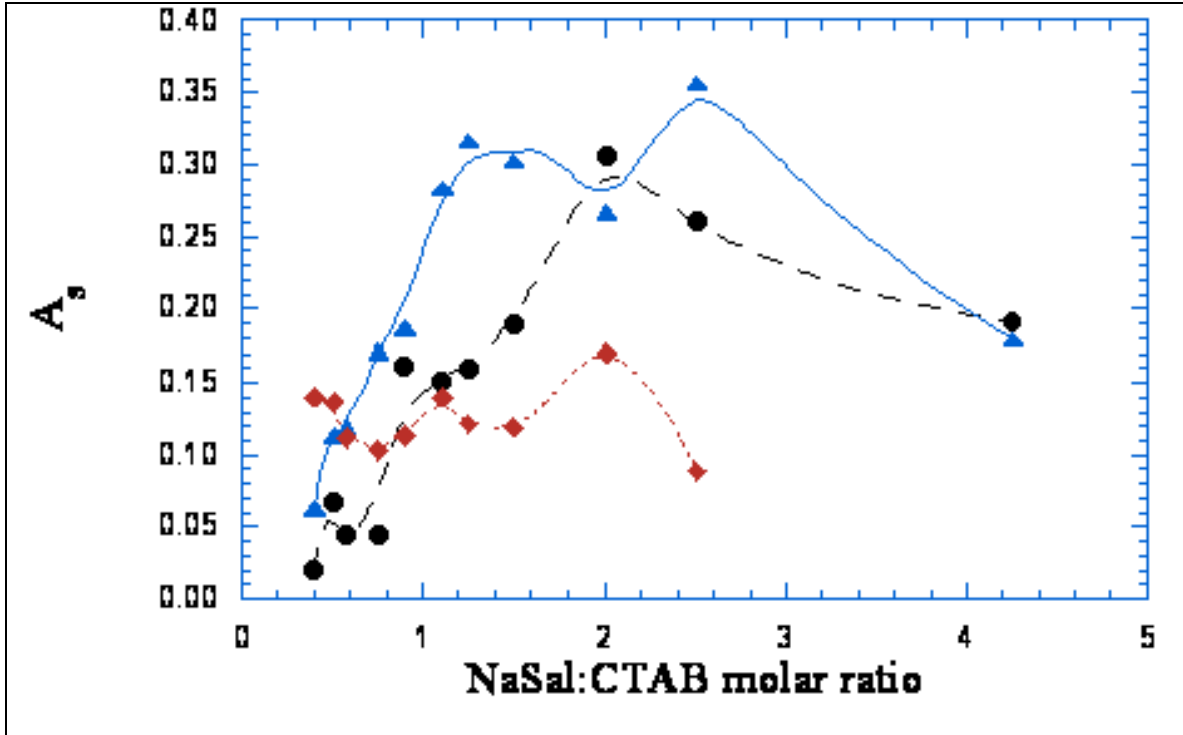


Figure 3.9. NaSal:CTAB mole ratio dependence of the slow mode amplitude at three CTAB concentrations: 0.05 M (●), 0.10 M (▲) and 0.50 M (◆). The NaSal:CTAB mole ratio corresponding to the maximum slow mode amplitude is observed to decrease with increasing CTAB concentration.

The slow mode amplitude is given by the ratio of the elastic modulus,  $M_g$ , of the entanglement network and the bulk osmotic modulus,  $K$ , in the model of Adam and Delsanti (18). For the case of polymer solutions, the elastic modulus and the bulk osmotic modulus are given by

$$M_g \sim \frac{\xi^3}{\xi^2} \quad (8)$$

and

$$K \sim \frac{kT}{\xi} \quad (9)$$

respectively. Here,  $\xi_b$  is the mean distance between two successive binary contact points and  $\xi$  is the static correlation length. These two length scales are proportional to one another for the case

of a semi-dilute polymer solution under good solvent conditions. Since the static correlation length is also proportional to the hydrodynamic correlation length,  $\xi_H$ , the slow mode amplitude and hydrodynamic correlation length should be strongly correlated with one another. Strong correlation between  $A_S$  and  $\xi_H$  was observed at all CTAB concentrations  $\geq 0.05$  M for NaSal:CTAB mole ratios  $\leq 2.0$ . An example of this is shown in Figure 3.10.

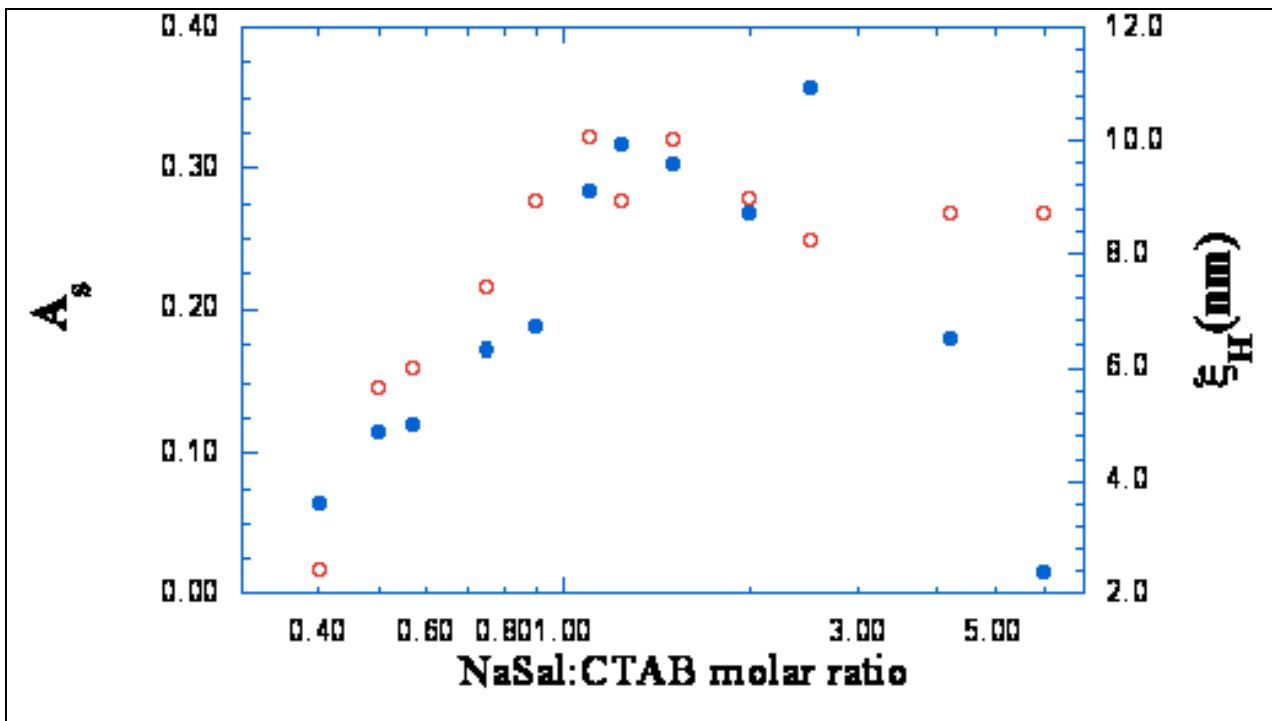


**Figure 3 10.** A strong correlation is observed between the slow mode amplitude (●) and the hydrodynamic correlation length (○). While, the CTAB concentration was 0.10 M in this case, similar behavior was observed for all the solutions exhibiting two distinct relaxation times. This indicates that these CTAB/NaSal solutions are in the gel-like regime defined by Adam and Delsanti

The strong agreement between the hydrodynamic correlation lengths and slow mode amplitude lends credence to the earlier conclusion that the observation of increasing  $\xi_H$ , with increasing NaSal:CTAB mole ratio is primarily due to enhanced concentration fluctuations and not micellar growth. The magnitude of the slow mode amplitude is essentially determined by the micelle ionization. The observation that the strong correlation breaks down at NaSal:CTAB

mole ratios  $> 2.0$  may be indicative of micellar breakdown and electrostatic screening effects at high NaSal:CTAB mole ratios.

*3.4.2.7 Effect of CTAB Concentration on Slow Mode Amplitude.* As shown in Figure 3.11, the slow mode amplitude first increases to a maximum value and then decreases with increasing CTAB concentration at fixed NaSal:CTAB mole ratio. The CTAB concentration value corresponding to the slow mode amplitude maximum increases with increasing NaSal:CTAB mole ratio. The initial increase of the slow mode amplitude with increasing CTAB concentration is the behavior expected based on elastic modulus and correlation length concentration scaling predictions for neutral polymer solutions and polyelectrolyte solutions with excess salt (18,32,33) and the correlation length concentration scaling reported for the first time here. However, the presence of the slow mode amplitude maximum and subsequent slow mode amplitude decrease with further increasing CTAB concentration is unexpected for neutral polymers and polyelectrolytes with fixed charge density and salt:polymer mole ratios. The observed slow mode amplitude maximum may be an indication of subtle micelle charging effects as Sal<sup>-</sup> incorporation into the micelles increases with increasing CTAB concentration. The elastic modulus and static correlation length, and therefore the bulk osmotic modulus, of semidilute polyelectrolyte solutions are predicted to be sensitive to polyelectrolyte concentration, excess salt concentration, polyelectrolyte charge density and counterion condensation (32,33). Therefore, a scenario in which the elastic modulus to bulk osmotic modulus (i.e. the slow mode amplitude) exhibits the observed behavior is not out of the question. Unfortunately, a more detailed understanding of Sal<sup>-</sup> binding as a function of NaSal:CTAB mole ratio *and* CTAB concentration is required to truly evaluate this hypothesis.

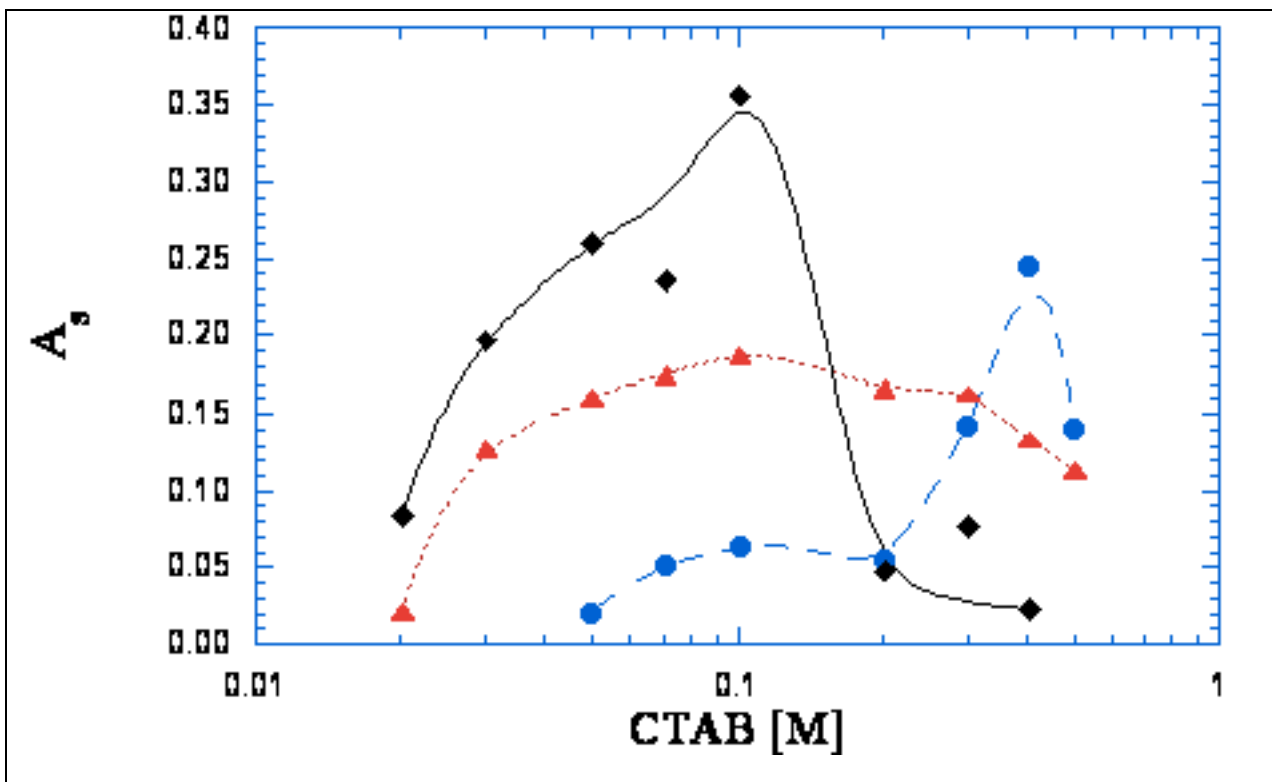


Figure 3.11. CTAB concentration dependence of the slow mode amplitude at three NaSal:CTAB mole ratios: (●) 0.45, (▲) 0.90 and (◆) 2.50 M. The CTAB concentration corresponding to the maximum slow mode amplitude is observed to decrease with increasing NaSal:CTAB mole ratio.

### **3.4.3 Static Light Scattering:**

The investigation of wormlike micelle systems via static light scattering has been very limited. Although there have been a few studies of CTAB/KBr solutions with static light scattering (1,13, 15), similar investigations of CTAB/NaSal solutions have not been reported. Dynamic light scattering investigations of this system have demonstrated the inherent dynamic complexity of the solutions. Dynamic properties such as the hydrodynamic correlation length, the slow relaxation time and the slow mode amplitude have been seen to be very sensitive to both the NaSal/CTAB molar ratio as well as the CTAB concentration. This is primarily due to effects these parameters have on the micellar charge and electrostatic screening effects. An investigation of the static properties of this system is interesting in that it should provide insight into the influence of these parameters on the osmotic pressure and static correlation length.

**3.4.3.1 The Rayleigh Ratio Behavior:** The static light scattering measurements were carried out over the same concentration and NaSal/CTAB molar ratios as the dynamic light scattering measurements. Figure 3 12 illustrates the wide variation in the Rayleigh Ratio for different CTAB concentrations at fixed NaSal/CTAB molar ratio. The observed behavior is typical for all NaSal/CTAB molar ratios. The Rayleigh ratio  $R(\square)$  initially increases with increasing CTAB concentration until reaching a maximum value and then begins to decrease with further increasing CTAB concentration. For the 0.90 NaSal:CTAB molar ratio the apparent maximum is reached at a CTAB concentration of 0.2M. The Rayleigh ratio maximum is observed to shift to lower CTAB concentrations with increasing NaSal/CTAB molar ratios.

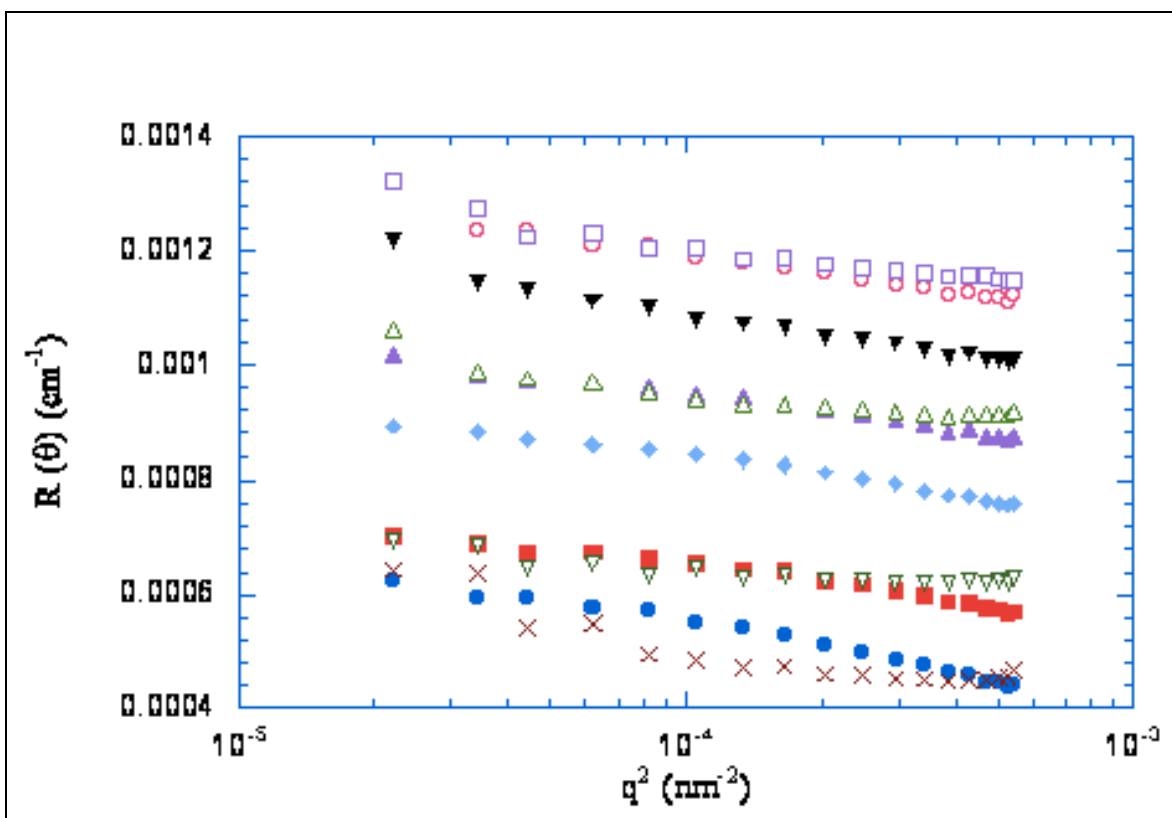


Figure 3.12: Variation of the Rayleigh Ratio with  $q^2$  for solutions in which the NaSal:CTAB molar ratio is kept constant at 0.90 and the CTAB concentration is varied: (●) 0.01M (■) 0.02M (◆) 0.03M (▲) 0.05M (▼) 0.07 M (○) 0.1M (□) 0.2M (Δ) 0.3M (◻) 0.4M and (X) 0.5M. The  $R(\square)$  shows a clear maximum at 0.2M. The presence of a peak is typically seen in all NaSal:CTAB molar ratios investigated.

This behavior is indicative of a change in micellar interactions with varying CTAB concentration and molar ratio. A better appreciation of this variation in  $R(\square)$  can be obtained through consideration of the zero angle Rayleigh Ratio,  $R(0)$ , as illustrated in figure 3.13. The figure clearly illustrates the movement of the maximum  $R(0)$  to lower CTAB concentrations with increasing NaSal/CTAB molar ratio. This behavior is reminiscent of the behavior of some of the dynamic parameters which showed a shift in the maximum with both the CTAB concentration and the NaSal/CTAB molar ratio. The shift in the  $R(0)$  peak with varying CTAB concentration observed at constant molar ratio is also observed for samples having a constant CTAB molar

concentration, but in which the NaSal/CTAB molar ratio is varied. This behavior is illustrated in figure 3.14.

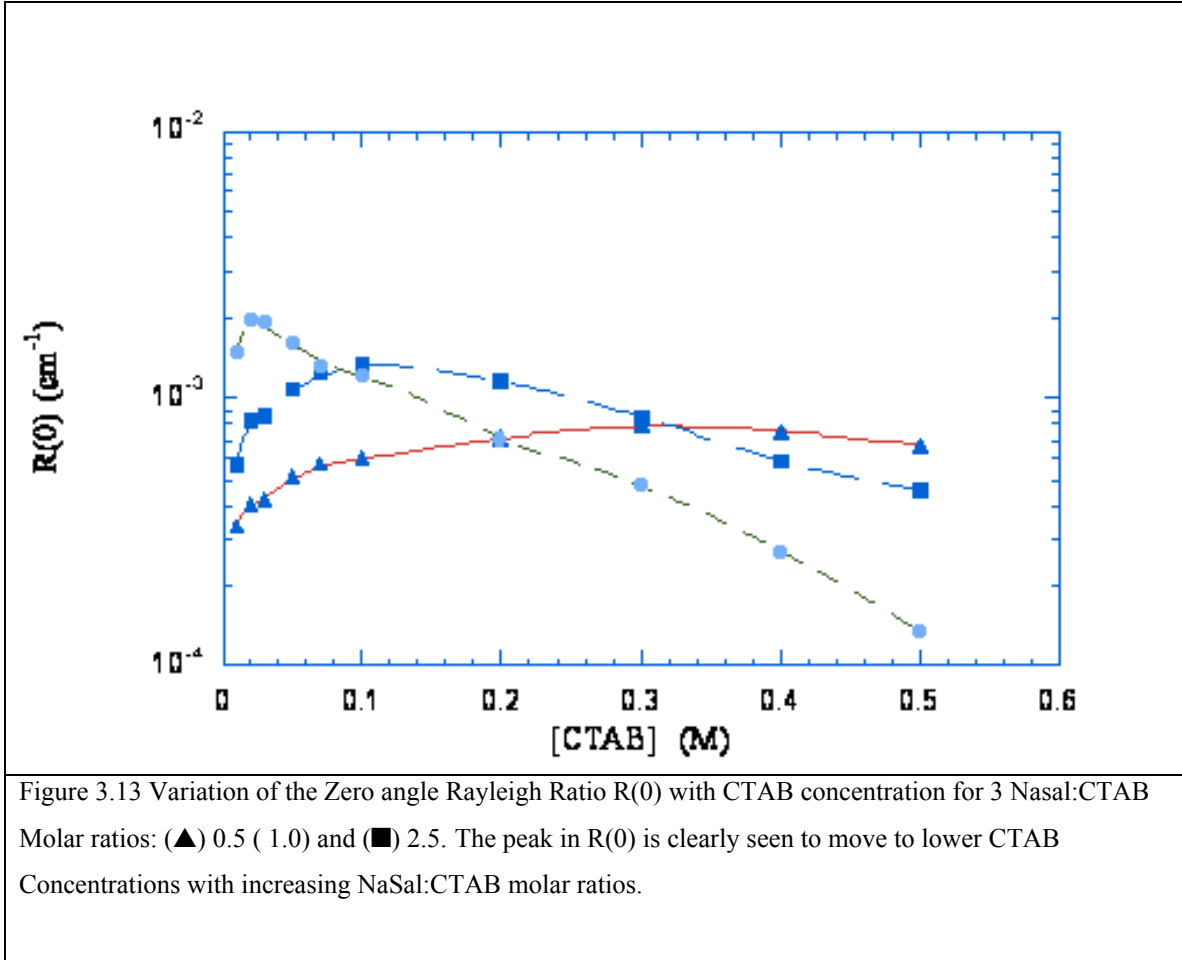


Figure 3.14 illustrates the variation of the zero angle Rayleigh Ratio,  $R(0)$  with the NaSal/CTAB molar ratio for different CTAB molar concentrations. The  $R(0)$  maximum moves to lower NaSal/CTAB molar ratios with with increasing CTAB concentrations. The zero angle Rayleigh Ratio for identical micellar particles can be written as (43),

$$\square R_{\square} = K(C \square CMC)MP(q)S(q), \quad (10)$$

where,  $K$  is an optical constant,  $CMC$  is the critical micellar concentration and  $M$  is the molar mass of the micelles.  $P(q)$  is the particle form factor and  $S(q)$  is the static structure factor. As a

note it should be mentioned that in order to calculate the optical constant a knowledge of the change in refractive index with concentration,  $dn/dc$ , is required. This parameter was therefore measured and its dependence on the NaSal:CTAB molar ratio is illustrated in Figure 3.15.

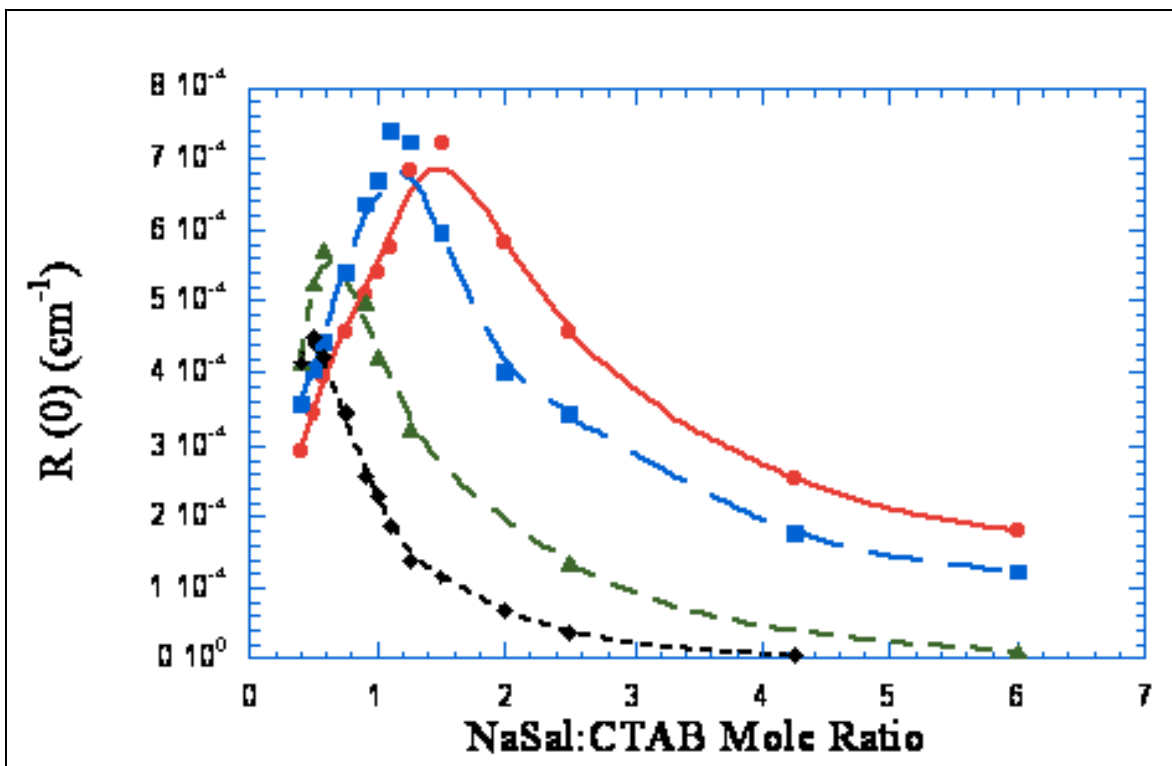


Figure 3.14 Variation of  $R(0)$  with NaSal:CTAB molar ratios for CTAB concentrations: (●) 0.05M (■) 0.1M (▲) 0.3M and (◆) 0.5M. The peak is seen to shift to lower ratios with increasing CTAB concentrations.

The  $dn/dc$  behavior exhibits an interesting behavior showing a maximum near 2.2.5. Interestingly this is the NaSal:CTAB molar range where many of the solutions show a marked change in the static and dynamic parameters. This has been discussed in the context of the dynamic and static parameters as being caused by a micellar charge reversal effect.

The zero angle Rayleigh Ratio is effected by both the micellar concentration and the intermicellar interactions. In fact it is very difficult to de-couple these effects and isolate the main contributing factor to the  $R(0)$  behavior.

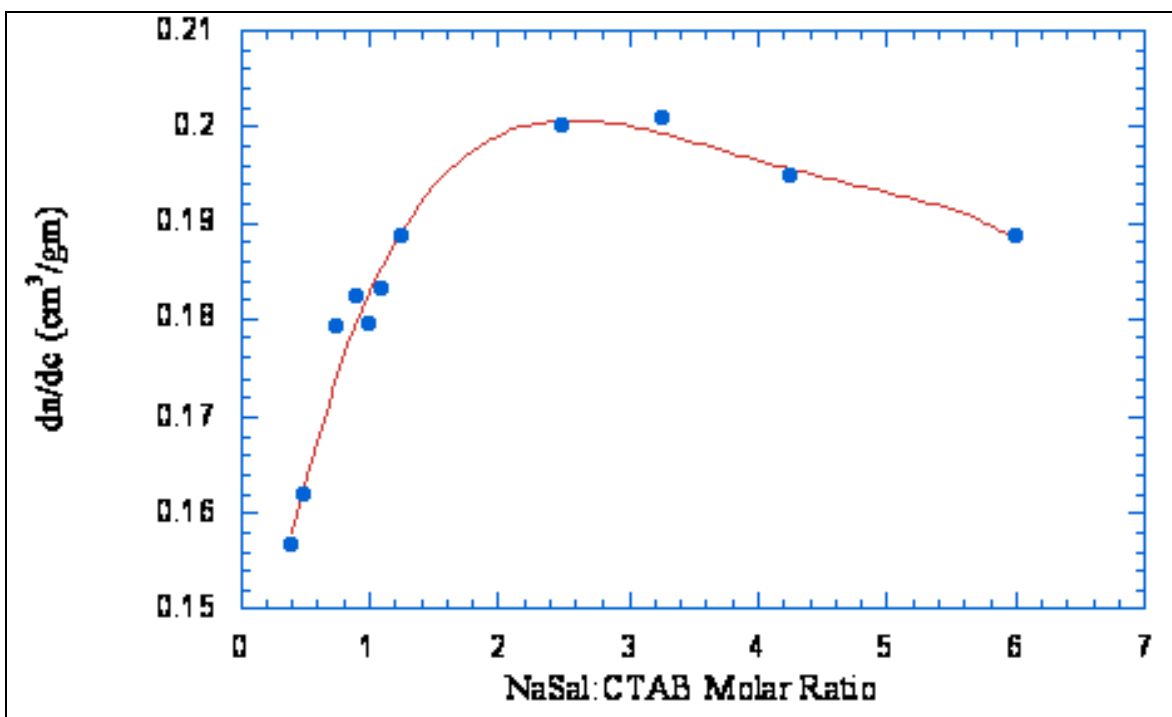


Figure 3.15: Variation of the  $dn/dc$  with the NaSal:CTAB molar ratio. The  $dn/dc$  exhibits a near Maximum at a molar ratio about 2-2.5.

The increase in  $\Delta R_0$  that is observed at low CTAB (and constant NaSal:CTAB molar ratio) and at low NaSal:CTAB molar ratio (constant CTAB concentration) maybe due to increasing concentration, however since there is a peak, this is indicative that micellar interactions are also playing a role.

Previous NMR studies on the CTAB/NaSal system (29,30) indicate that the micellar charge is affected by the NaSal/CTAB molar ratio. The micelle is initially positively charged, but with increasing NaSal/CTAB molar ratio it becomes neutral and eventually undergoes charge reversal at higher salt:detergent ratios. These previous NMR studies have also shown that the NaSal:CTAB charge reversal ratio is dependent on the CTAB concentration. The charge reversal phenomena was also seen to adequately support the trends that were observed in the behavior of the dynamic parameters. Here the observed peak in the  $\Delta R_0$  and its dependence on

both the NaSal/CTAB molar ratio and on the CTAB concentration is again indicative of this charge reversal phenomena. At low NaSal/CTAB molar ratios the micelle is positively charged and electrostatic interactions give rise to the lower scattered intensity.

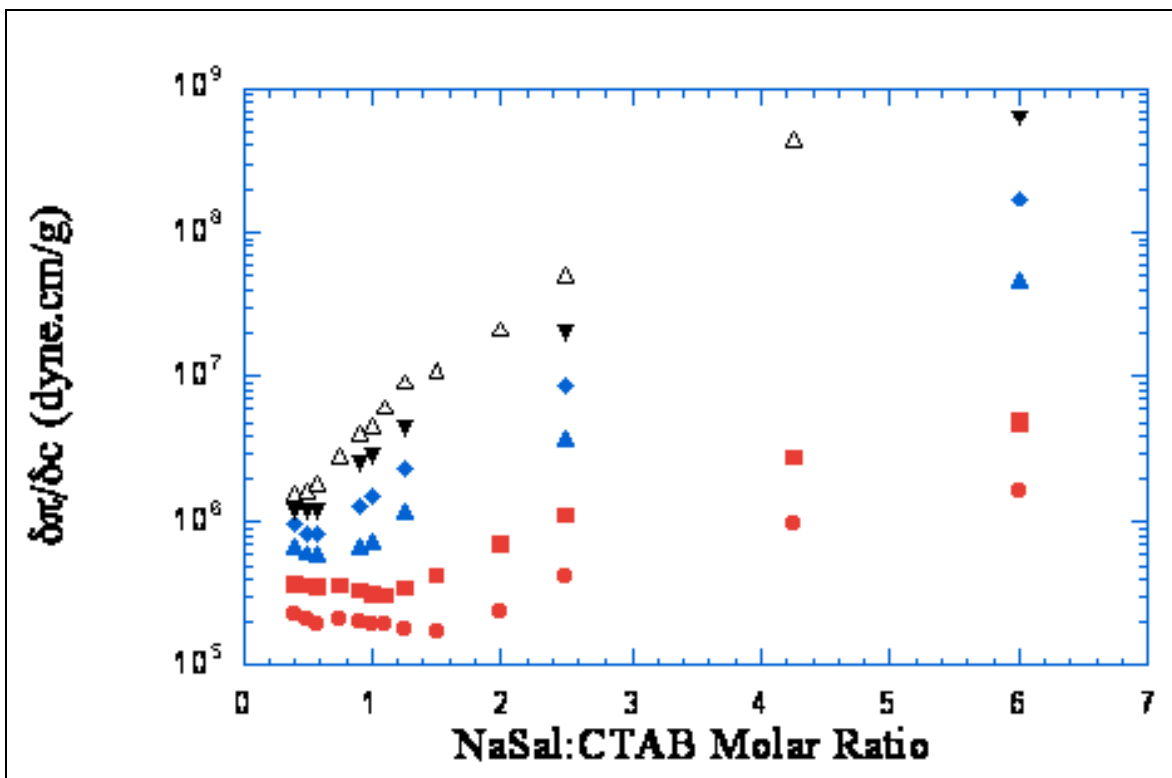


Figure 3.16 :Variation of the osmotic compressibility with the NaSal:CTAB molar ratio for CTAB concentrations:(●) 0.05M (■) 0.1M (▲)0.2M (◆) 0.3M (▼) 0.4 M and (Δ) 0.5M . All the CTAB concentrations exhibit a slight kink after which the osmotic compressibility increases sharply with NaSal:CTAB molar ratio. This kink is seen to move to lower NaSal:CTAB molar ratio values with increasing CTAB concentration.

With increasing neutralization, these interactions are suppressed causing the  $\square R_0$  to increase to a peak when the micelle is essentially neutral. With further increase in the NaSal/CTAB molar ratio, the micelle undergoes a charge reversal leading to increasing electrostatic interactions and decreasing  $\square R_0$  . The behavior that is exhibited here is very similar to polyelectrolyte gels in which the concentration fluctuations increase with decreasing ionization (26-28).

**3.4.3.2 Osmotic Compressibility dependence on CTAB and NaSal:CTAB molar ratio:** The charge reversal phenomena can be clearly identified in the osmotic compressibility behavior. Figure 3.16, illustrates the variation of the osmotic compressibility with the NaSal/CTAB molar ratio for six representative CTAB concentrations. It should be noted that for this CTAB concentration and NaSal:CTAB molar ratio range, the total concentration variation was from 0.004 g/ml to 0.54 g/ml. The osmotic compressibility can be extracted from the zero angle Rayleigh Ratio through:

$$\square R_0 = KCRT \left[ \frac{\partial \square}{\partial c} \right] \square \quad (11)$$

The osmotic compressibilities exhibit a very interesting behavior. They tend to decrease with increasing molar ratio and then exhibit a sharp transition and begin to increase monotonically.

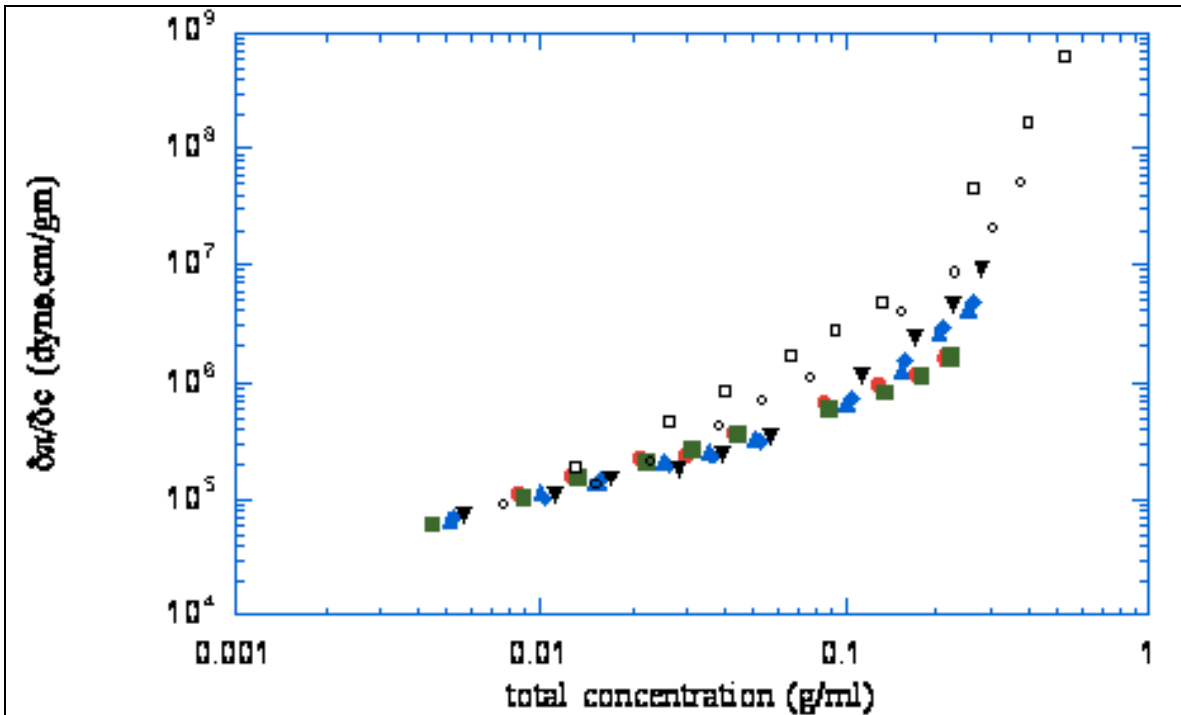


Figure 3.17: Osmotic compressibility variation with total concentration for solutions having molar ratios: (●) 0.40 (■) 0.50 (▲) 0.90 (◆) 1.0 (▼) 1.25 (○) 2.5 and (□) 6.0. The largest increases in osmotic compressibility are seen for ratios of 2.5 and 6.0.

The location of the change in slope is clearly seen to move to lower NaSal/CTAB molar ratios with increasing CTAB concentration. This again can be explained from the charge reversal phenomena. Decreasing interactions associated with increasing micellar neutrality would cause the initial decrease in the osmotic compressibilities.

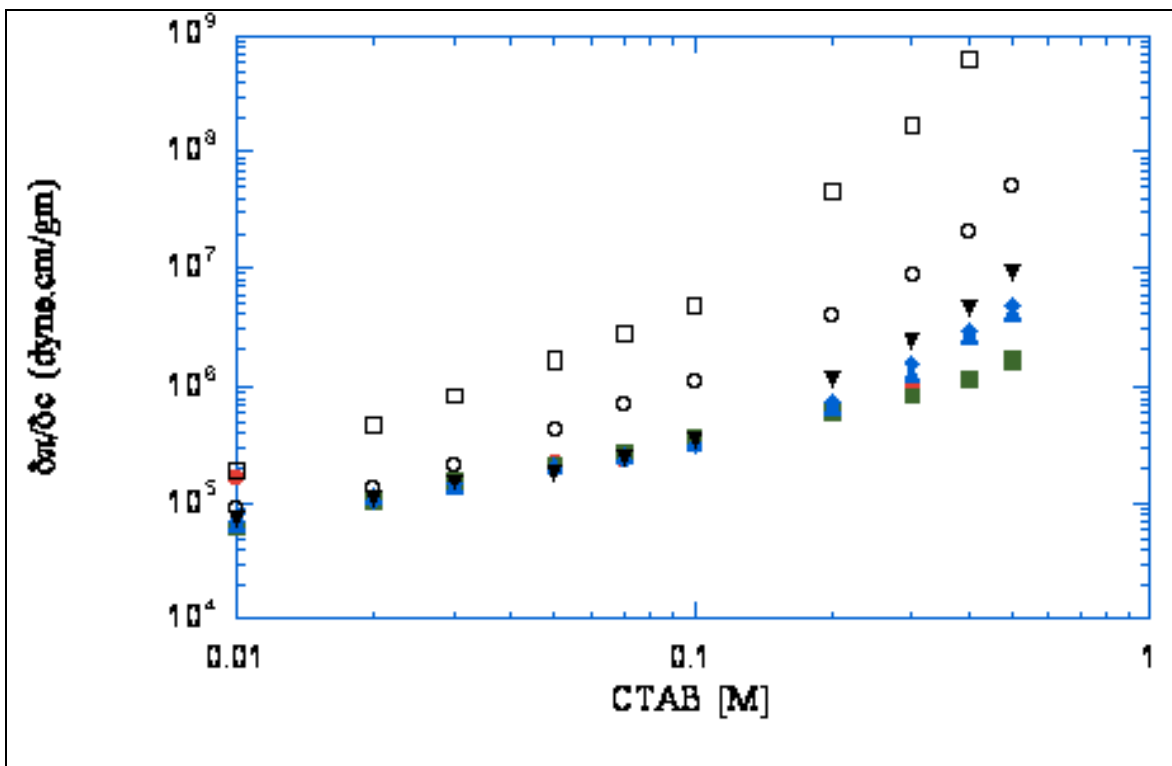


Figure3.18: Osmotic compressibility variation with CTAB concentration for solutions having molar ratios: (●) 0.40 (■) 0.50 (▲)0.90 (◆) 1.0 (▼) 1.25 (○) 2.5 and (□) 6.0.

Once the micelle reaches neutrality, increasing the ratio causes the onset of charge reversal causing the interactions to increase leading to an increase in the osmotic compressibility. Since the charge reversal ratio is affected by the CTAB concentration, the change of slope moves to lower ratios with increasing CTAB. This change in the slope magnitude may be attributed to increasing interaction associated with increasing concentrations.

The osmotic compressibility also exhibits a strong dependence on the total concentration and the CTAB concentration as illustrated in figures 3.17 and 3.18. Figure 3.17 illustrates that the osmotic compressibility increases with total concentration. However the extent of the increase is seen to be very sensitive on the NaSal:CTAB molar ratio. The increase is not seen to be significantly different for the low NaSal:CTAB molar ratios. However, the osmotic compressibility is seen to increase dramatically with concentration at the high NaSal:CTAB molar ratios of 2.5 and 6.0. This again illustrates the sensitivity of the osmotic compressibility on the NaSal:CTAB molar ratio. Figure 3.18 illustrates the dependence when plotted as a function of the CTAB concentration. It increases with both CTAB concentration and NaSal:CTAB molar ratio.

**3.4.3.3 Osmotic Pressure dependence on concentration:** The osmotic pressure was extracted from the osmotic compressibility and is illustrated in figure 3.19. The osmotic pressure exhibits a clearly monotonic increase with increasing CTAB concentrations. The osmotic pressure follows a power law relationship with the total concentration. For each NaSal:CTAB molar ratio the power law dependence is seen to exhibit two distinct regimes depending upon the concentration. The lower concentration regime is seen to exhibit a power law scaling 1.35 for a NaSal:CTAB molar ratio of 0.40 to a value of 2.29 for a NaSal:CTAB molar ratio of 6.0. The power law exponent for the lower concentration regime is seen to increase between NaSal:CTAB molar ratio of 1.25 to 6.0. For the lower ratios its behavior is nonmonotonic. The high concentration regime value of the power law exponent is seen to increase monotonically from 1.82 at a ratio of 0.40 to 4.27 at a ratio of 6. The existence of two regimes corresponds well with the change of the solutions from exhibiting a viscous behavior to a strong gel-like behavior. The lower concentration regime especially for the lower and intermediate ratios is a viscous solution

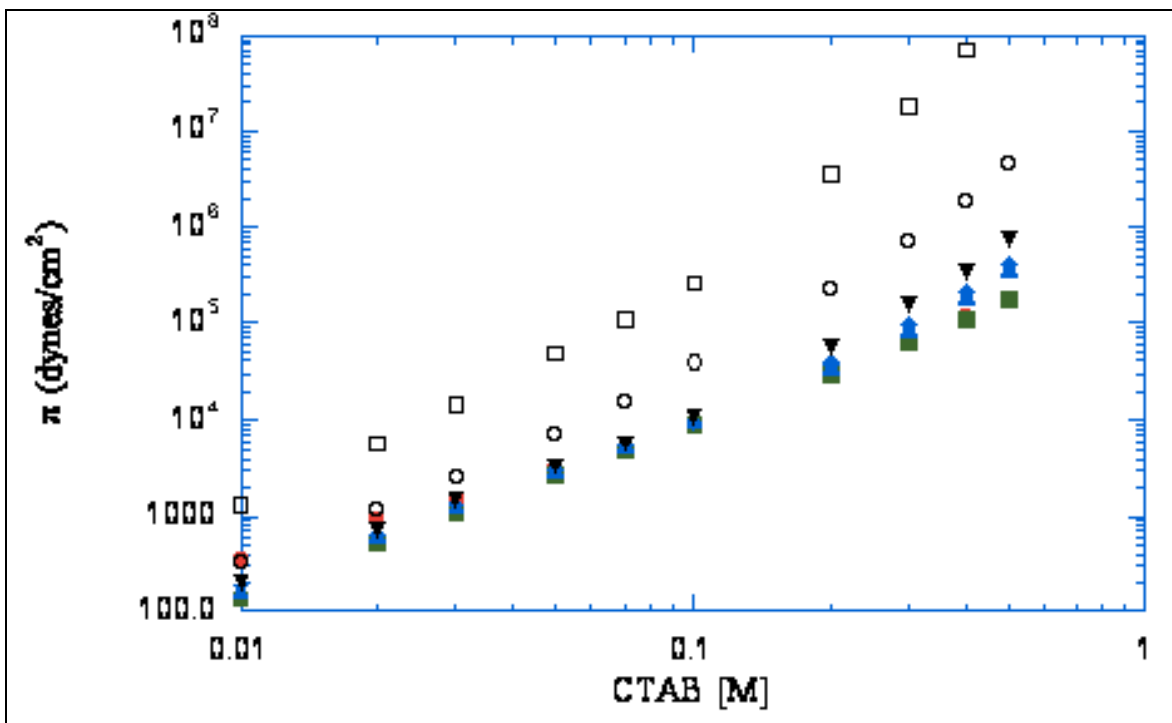


Figure 3.19: Osmotic Pressure variation with CTAB concentration for solutions having molar ratios: (●) 0.40 (■) 0.50 (▲) 0.90 (◆) 1.0 (▼) 1.25 (○) 2.5 and (□) 6.0. The osmotic pressure is seen to increase monotonically with CTAB concentration. The osmotic pressure is seen not to be affected by the NaSal:CTAB molar ratio as the slight increments that can be observed are attributable to higher total concentrations associated with higher ratios.

Since the micelles are charged at these low ratios, their behavior is most likely to resemble that of a polyelectrolyte. It does, however, become neutral at a ratio of about 2-2.5. Here the power law exponent takes on a value of 2.04. Theoretical and simulation (46) studies on the osmotic pressure of equilibrium polymers in the semi-dilute regime and under good solvent conditions have revealed a power law scaling exponent of 2.3. This value is close to the scaling exponent at a NaSal:CTAB molar ratio of 2.5. The observation of a scaling exponent close to the theoretical prediction for excluded volume equilibrium polymers may be attributable to the near-neutral entangled micelles that exist near these NaSal:CTAB molar ratios. For the high concentration regime, the solutions essentially exhibit a gel-like behavior. The osmotic pressure behavior should therefore resemble a behavior close to the behavior of a polyelectrolyte gel.

According to Rubinstein et al (32), the osmotic compressibility in polyelectrolyte gels exhibits a number of different power law dependencies depending upon the polymer concentration and the salt content. The behavior which is most like being exhibited here is the low salt limit, which is similar to highly charged micelles with little screening,  $\chi \sim c$ , while for highly screened polyelectrolytes at low concentration,  $\chi \sim c^2$ . For highly screened polyelectrolyte gels at high concentrations,  $\chi \sim c^{2.25}$ . Since the micelles undergo decreasing ionization and then become neutral, the exhibited power law dependency change is similar to the polyelectrolyte power law dependency change. The very high exponent at a ratio of 6 may be indicative of micellar break up at these high ratios and high concentrations. The solutions at these very high ratios and concentrations are not gel-like but essentially exhibit a viscous behavior.

**3.4.3.4 Effect of NaSal:CTAB molar ratio and CTAB concentration on the static correlation length:** Dynamic light scattering studies on the system provided a better understanding of the concentration fluctuation spectrum through extraction of the hydrodynamic correlation lengths. The hydrodynamic correlation lengths exhibited a strong dependence on both the NaSal/CTAB molar ratio and the CTAB concentration. Static light scattering also provides insight into the concentration fluctuations in the system through the static correlation length. Under good solvent conditions the two correlation lengths are identical. However, under poor solvent conditions, enhanced concentration fluctuations cause the two correlation lengths to vary. Figure 20 illustrates the behavior of the static correlation length with the NaSal/CTAB molar ratio for several CTAB concentrations. The behavior that is observed here is somewhat reminiscent of the behavior observed for the hydrodynamic correlation length CTAB concentration variation, especially for the low and intermediate CTAB concentration range. For the CTAB concentration

range (0.01M-0.2M) the static correlation length increases with increasing NaSal:CTAB molar ratio until reaching a maximum and then decreases slightly to an almost constant value.

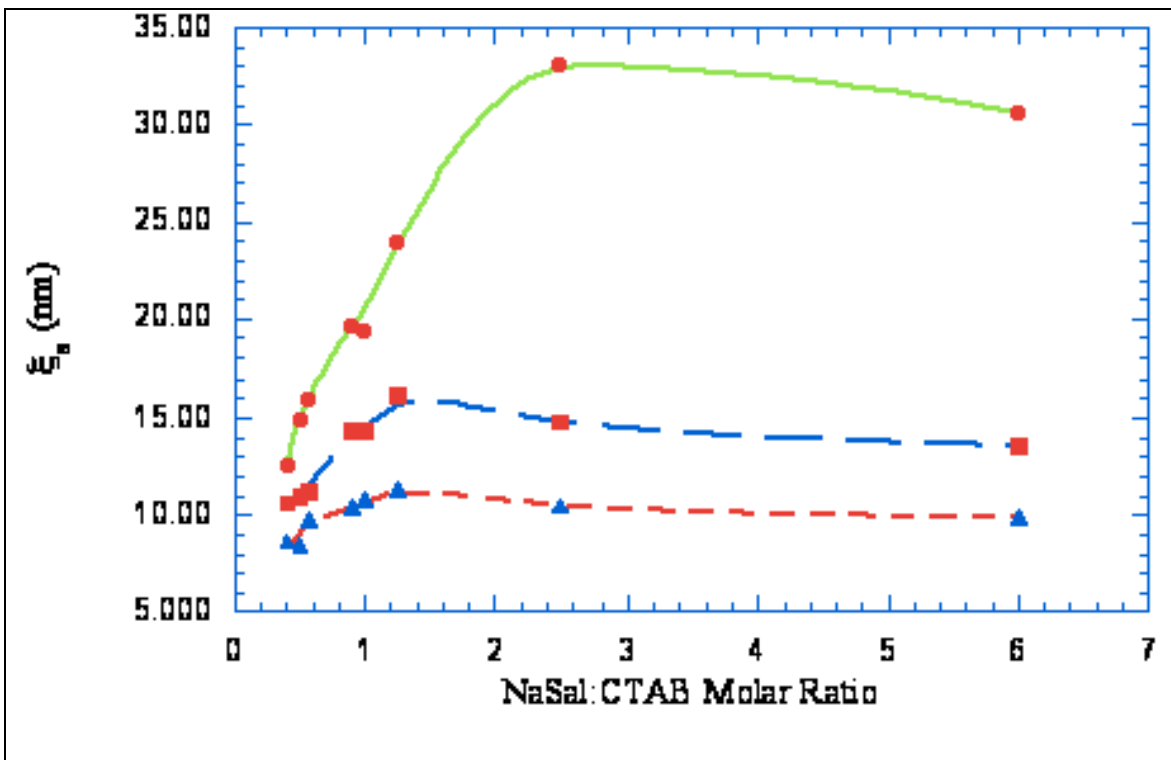


Figure 3. 20: Variation of static correlation length with NaSal:CTAB molar ratio for CTAB (●) 0.02M (■) 0.07M (▲)0.2M. The peak tends to shift to lower NaSal:CTAB molar ratios with increasing CTAB concentrations. This behavior is however limited to the low and intermediate CTAB concentrations. More complicated non monotonic behavior is seen for CTAB concentrations-0.3M -0.5M

The initial increase may be attributed to increasing concentration fluctuations associated with decreasing micellar ionization. This behavior is analogous to polyelectrolyte behavior (27-28) The peak occurs at the apparent charge reversal NaSal:CTAB molar ratio and since this is affected by the CTAB concentration a shift in the peak is observed to lower ratios with increasing CTAB concentrations as observed for the case of R(0). As was discussed for the hydrodynamic correlation length, the slight decrease to a near constant value at higher ratios may be attributed to the re-increase in the micellar ionization and the probable onset of electrostatic

repulsions at these higher ratios. This behavior was typical for the hydrodynamic correlation length NaSal:CTAB molar ratio dependence for all the CTAB concentrations investigated. However for the static correlation lengths, this behavior was limited to the low to intermediate CTAB concentration (0.01M to 0.2M). Ideally both the hydrodynamic and static correlation lengths should exhibit the same behavior, especially under good solvent conditions. However, the influence of micellar breakup at the high concentrations and high ratios may be the cause of the deviation between the two parameters. The static correlation length dependence on CTAB concentration is very similar to that observed for the hydrodynamic correlation length, in that the static correlation length decreases monotonically with increasing CTAB concentration. The static correlation length variation with concentration relationship follows a power law dependence of the form

:

$$\xi_S \sim C_{CTAB}^{\alpha} \quad (12)$$

The behavior is illustrated in figure 3.21 For comparative purposes the hydrodynamic correlation length scaling exponent is also shown in Figure 3.21. The behavior is similar to the hydrodynamic correlation length scaling exponent behavior in that the value becomes more negative with increasing NaSal:CTAB molar ratio at small ratios but the subsequent increase of the exponent is not observed. As was discussed in the case of the hydrodynamic correlation length scaling exponent, electrostatic repulsions at low ratios are most likely suppressing concentration fluctuations leading to low magnitude scaling exponent values.

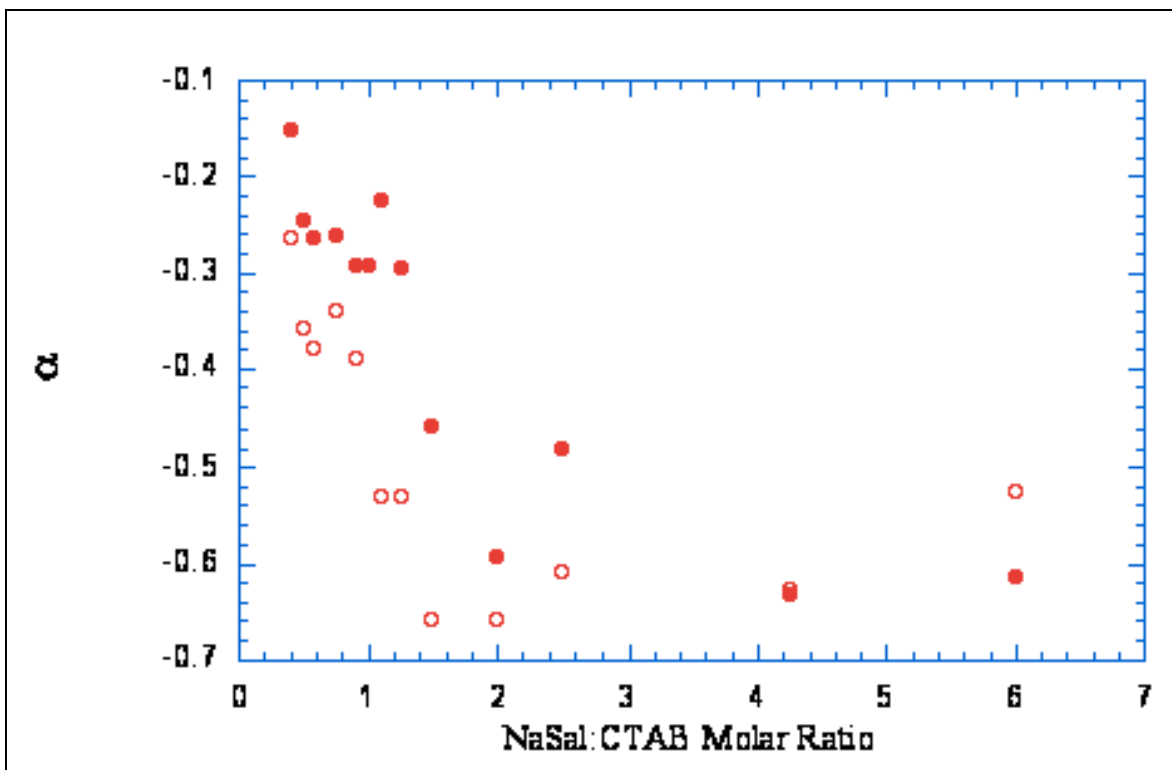


Figure 3.21: The static correlation concentration scaling exponent (●) variation with NaSal:CTAB molar ratio. The behavior is similar to that seen for the scaling exponent of the hydrodynamic correlation length(○). However a clear minima in the value followed by a subsequent re-increase as seen in hydrodynamic correlation length scaling exponent behavior is not seen here.

With decreasing micellar ionization concentration fluctuations will increase leading to more negative  $\alpha$  parameter values. Finally the reversal of charge causes the concentration fluctuations to be suppressed again to a certain extent. However, unlike the hydrodynamic correlation length scaling exponent, the static correlation length scaling exponent exhibits a decrease until high NaSal:CTAB molar ratios, indicating the reversal to take place at really high ratios. This is not however supported by other studies on this system. The deviation may also be attributable to possible dissolution problems at these very high concentrations

#### ***3.4.4 Tracer Microrheology:***

The dynamic and static light scattering measurements of the CTAB/NaSal worm-like micellar system have revealed very interesting static and dynamic properties. The complex dependence of the various static and dynamic parameters on both the NaSal:CTAB molar ratio and the CTAB concentration has been seen to be primarily driven by the changes in micellar ionization and electrostatic screening associated with changes in the NaSal:CTAB molar ratio and the CTAB concentration. The system also exhibits interesting osmotic compressibility behavior particularly with respect to NaSal:CTAB molar ratio variations at fixed CTAB concentration. The inherent complexity of this system coupled with its similarities with polymer solutions and its expected Maxwell fluid like behavior make it an interesting candidate to investigate with tracer microrheology techniques.

It has already been mentioned that tracer microrheology measurements to date have primarily focused on simple polymeric and biopolymeric materials such as DNA solutions and actin filament networks (47). Recently however, additional systems have been investigated (22,48). Notable and most pertinent to the current study is a recent tracer microrheology/mechanical rheometry study on a giant worm-like micellar system carried out by Cardinaux et al (48) on the micellar system  $C_{16}E_6$ . Under certain conditions this system self assembles to form large worm-like aggregates. The most significant finding from this comparable study was the existence of a scaling or correction factor for the tracer microrheology data. It was observed that in order for the complex viscoelastic moduli  $G^*$  from the tracer microrheology and from mechanical rheometry measurements to quantitatively agree, the tracer microrheology data had to be multiplied by a factor of 1.5-2.0.

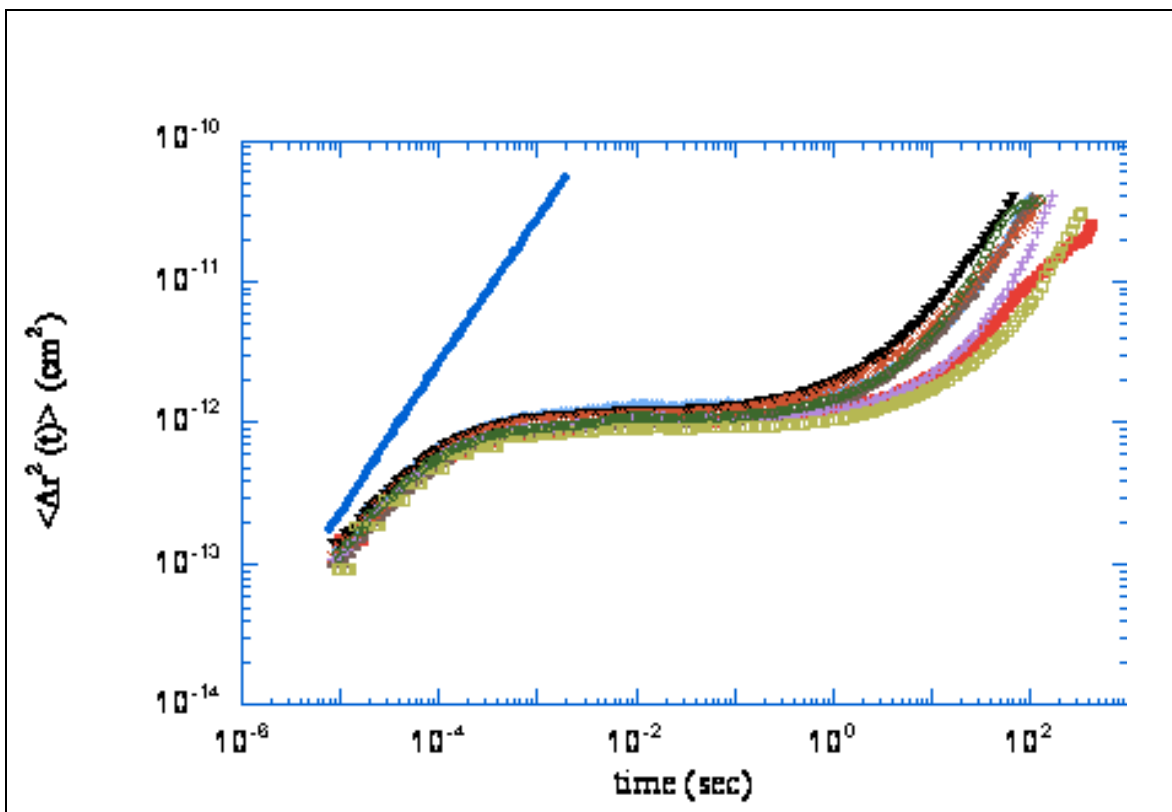


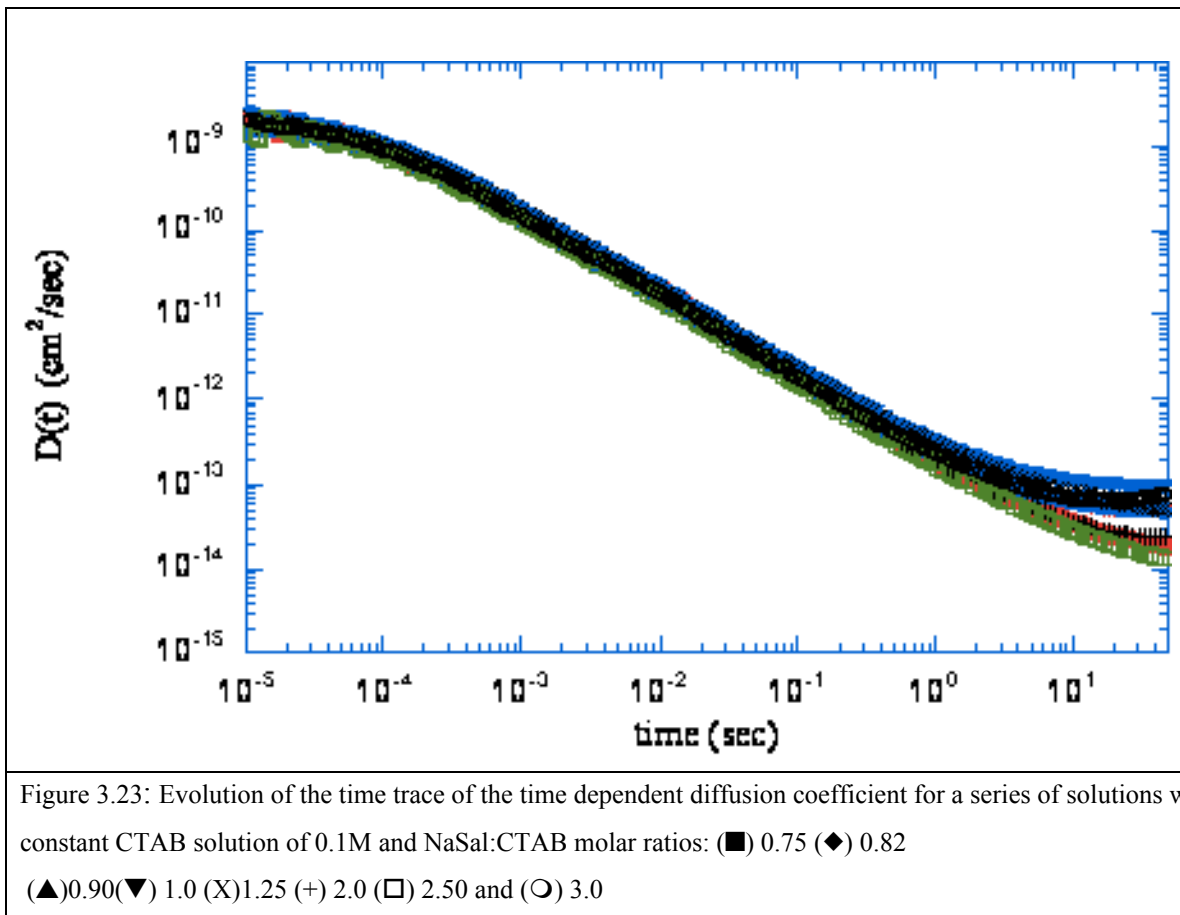
Figure 3.22: Evolution of the mean square displacement time trace for a series of solutions with a constant CTAB solution of 0.1M and NaSal:CTAB molar ratios: (■) 0.75 (◆) 0.82 (▲) 0.90 (▼) 1.0 (X) 1.25 (+) 2.0 (□) 2.50 and (○) 3.0. The  $\langle \Delta r^2(t) \rangle$  for water (●) is included in order to form a basis for comparison. All the molar ratios exhibit very similar behavior. The main difference shows up extensively in the long time behavior.

**3.4.4.1 Evolution of the Mean Squared Displacement:** In the present study, the CTAB molar concentration was kept constant at 0.1M eight NaSal:CTAB molar ratios varying from 0.75 to 3.0 were considered. As was mentioned in the materials and methods section of this chapter, tracer microrheology experiments on this system presented significant experimental challenges. First and foremost of these was the aggregation of the probe sphere at 1 vol%. In order to alleviate this, experiments were finally conducted at a probe sphere concentration of 0.1 vol%.

Figure 3. 22 illustrates the time evolution of the mean square displacement,  $\langle \Delta r^2(t) \rangle$ , for seven CTAB NaSal solutions in which the CTAB concentration was kept fixed at 0.1M,

while the NaSal:CTAB molar ratio was varied from 0.75 to 3.0. All the samples exhibit nearly identical behavior.  $\langle r^2(t) \rangle$  rises monotonically to a near constant plateau and finally exhibits diffusive behavior at long times.. The major difference between the time traces for the different ratios is the significant variation in the  $\langle r^2(t) \rangle$  escape or terminal time.

**3.4.4.2 Evolution of the Time Dependent Diffusion coefficient:** A better appreciation of the late stage brownian motion in these solutions can be observed via the time dependent diffusion coefficient  $D(t)$ , as illustrated in figure 3.23.



As expected,  $D(t)$  also exhibits almost similar behavior for all the investigated NaSal:CTAB molar ratios, the main difference again being the long time behavior.

On examining the behavior of both  $\langle \Delta r^2(t) \rangle$  and  $D(t)$ , it is clearly seen that for the time scales in question the behavior is significantly different than the low and intermediate concentrations of the two other investigated systems, the flexible polymer PEO and the triblock™ copolymer F108. The behavior is reminiscent of the  $\langle \Delta r^2(t) \rangle$  behavior for Pluronic™ F108 samples in the FCC soft crystal phase with an initial increase followed by a plateau region and a subsequent re-increase to diffusive escape (chapter 5). The main feature that emerges is that this system exhibits strong viscoelasticity for all the ratios investigated, as manifested by the plateau region. There is essentially no time independent region in  $D(t)$  except at the longest times when one would expect diffusive escape. The  $D(T)$  begins at a value which is slightly lower than the probe diffusion in water value of about  $4.5 \times 10^{-9} \text{ cm}^2/\text{sec}$  and then decreases monotonically. From the  $\langle \Delta r^2(t) \rangle$  time trace, what can be inferred is that the probes move subdiffusively at short times causing the  $\langle \Delta r^2(t) \rangle$  to increase monotonically. At intermediate times they 'feel' the elastic structures in the system and they move slowly as if in a 'cage' formed by the entanglements. Eventually at long enough times, when the system has relaxed completely, the probes 'escape' from the 'cage'. As the relaxation times are strongly influenced by the NaSal:CTAB molar ratios, this causes the final time trace to vary with NaSal:CTAB molar ratios.

**3.4.4.3 Complex Viscoelastic Modulus Frequency Dependence:** In order to order to investigate the viscoelastic response of the system in more familiar rheological terms, the complex viscoelastic moduli were extracted through use of the generalized Stokes -Einstein equation and conversion of the creep compliance  $J(t)$ . The complex viscoelastic modulus variation with frequency for the series of NaSal:CTAB molar ratios investigated is illustrated in figure 24. The behavior is that expected from the  $\langle \Delta r^2(t) \rangle$  time trace. At lower frequencies (longer times) a

variation in the frequency trace is observed due to different relaxation times associated with different NaSal:CTAB molar ratios. The plateau modulus varies in a non monotonic manner with the NaSal:CTAB molar ratios. These plateau values vary from 170-280 dynes/cm<sup>2</sup>.

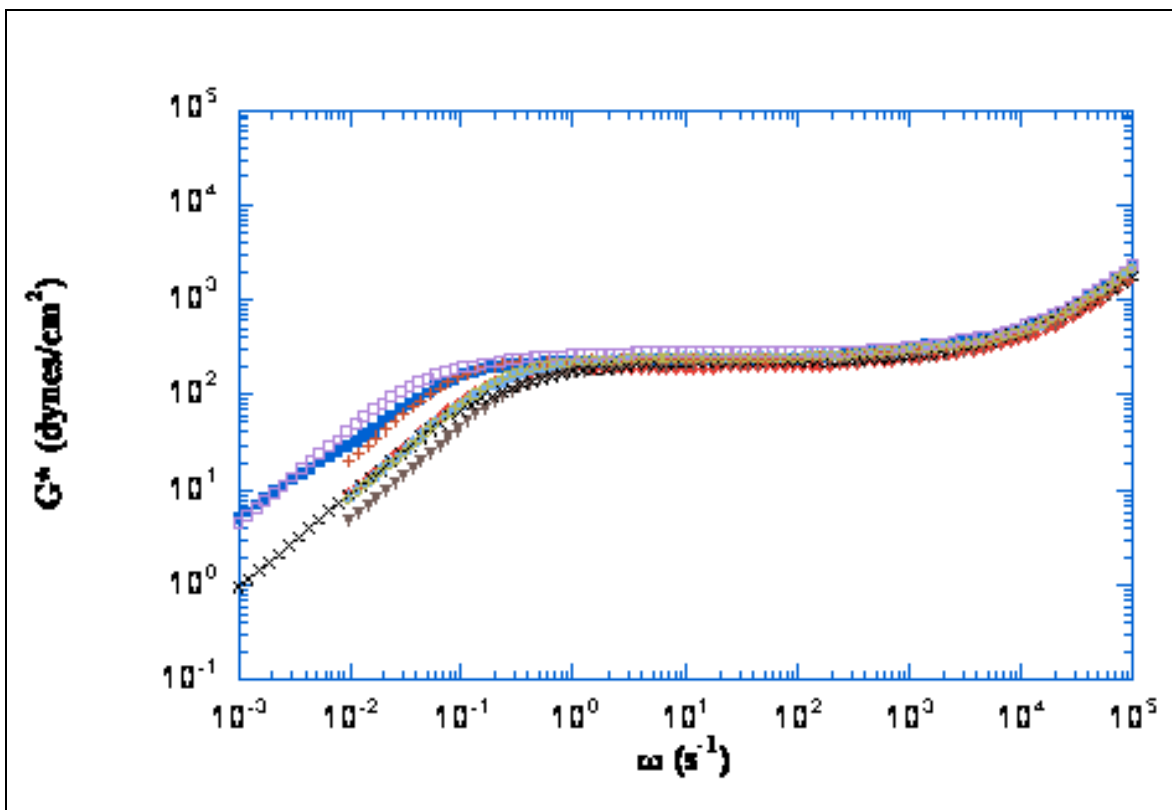


Figure 3.24: Frequency dependence of the complex viscoelastic moduli  $G^*$  for a series of solutions with a constant CTAB solution of 0.1M and NaSal:CTAB molar ratios: (■) 0.75 (◆) 0.82 (▲) 0.90 (▼) 1.0 (X) 1.25 (+) 2.0 (□) 2.50 and (○) 3.0. All the molar ratios exhibit significant viscoelasticity and show a nonmonotonic dependence of the plateau modulus on the NaSal:CTAB molar ratio.

The final frequency traces at higher frequencies are very similar for almost all the ratios, as the probes begin to 'feel' the elastic structures at essentially the same time.

#### 3.4.4.4 Maxwellian Fluid Analysis:

Wormlike micellar systems like CTAB:NaSal are interesting systems to investigate through tracer microrheology as they can be considered as being representative Maxwell fluids. As

mentioned before wormlike micelles have the ability to break and recombine. This provides an additional stress relaxation mechanism. When the wormlike micelle breaking/recombination kinetics dominate the stress relaxation process a monoexponential or Maxwellian stress relaxation behavior is observed. Since the CTAB:NaSal system falls into the class of wormlike micelles it was pertinent to carry out a Maxwellian scaling analysis of the tracer microrheology data.

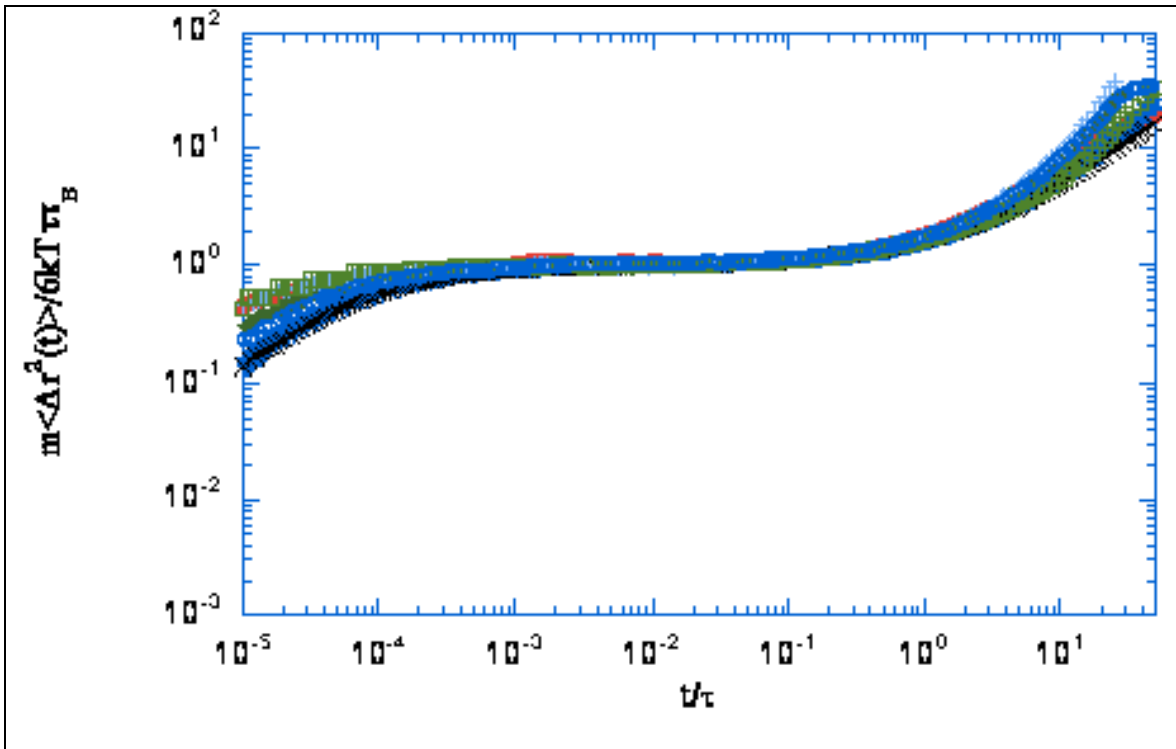


Figure 3.25: Probe diffusion rescaled with respect to the terminal relaxation time and plateau mean square for series of CTAB:NaSal solutions having a CTAB concentration of 0.1M and in which the NaSal:CTAB molar varies as: (■) 0.75 (◆) 0.82(▲)0.90(▼) 1.0 (X)1.25 (+) 2.0 (□) 2.50 and (○) 3.0. The collapse of the data c the near maxwellian behavior of these solutions.

As illustrated by van Zanten et al (22) the applicability of the Maxwell model to the late

time diffusion can be tested through a late time rescaling representation,  $\frac{m\langle r^2(t) \rangle}{6kT\tau_B}$  vs  $t/\tau$  where

$m$  is the mass of the particle,  $\tau$  is the relaxation time and  $\tau_B$  is the Brownian time, defined as  $m/\zeta$ .

Details of the Maxwellian scaling argument are given in ref 22. Figure 3.25 illustrates the

collapse of the data after  $t/\tau_B > 10^{-3}$  for the CTAB:NaSal samples investigated in the current study after carrying out the long time Maxwellian rescaling. The collapse at long times is however not as good as that seen for the CTAB/KBr system. This indicates that the Maxwell model may not be the best representation of the long time or low frequency dynamics in this system for some of the NaSal:CTAB molar ratios. The Maxwell scaling relationship is however not expected to work at short times (high frequencies) due to the presence of other relaxation modes, such as rouse modes or breathing modes at these short times. In order to test this a short time maxwellian rescaling was carried out on the NaSal:CTAB system and it is illustrated in figure 3.26:

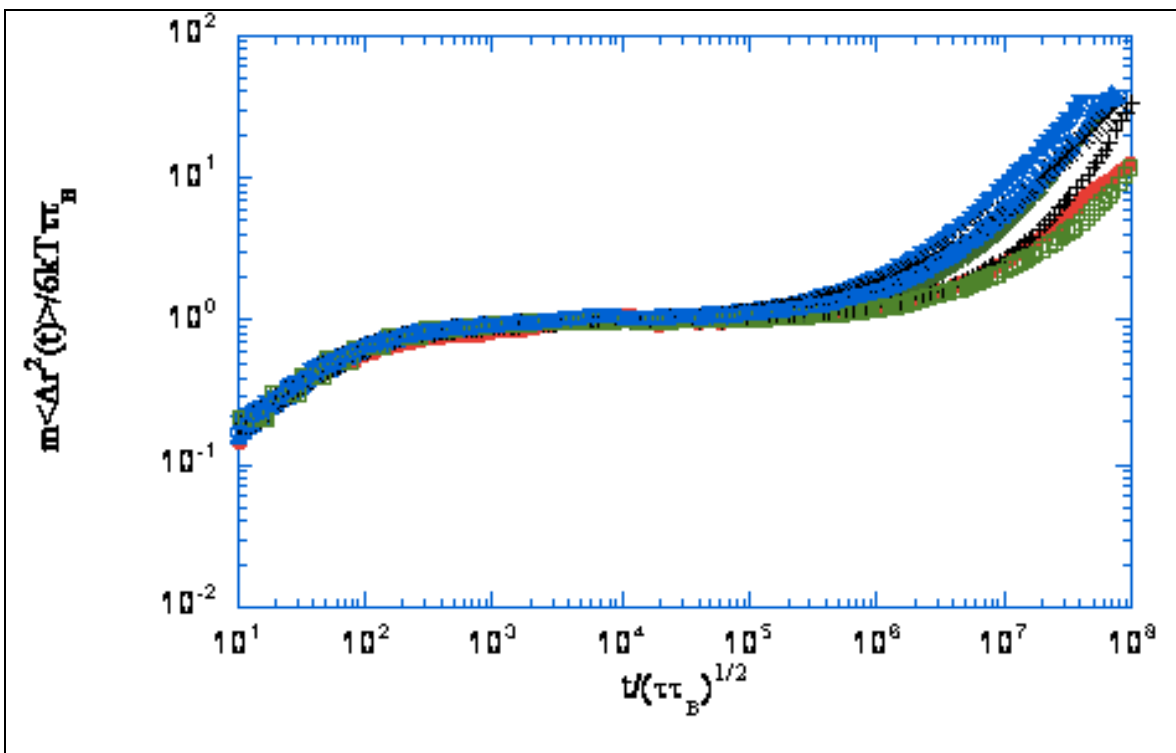


Figure 3.26: Probe diffusion rescaled with respect to the plateau onset time predicted for a single relaxation maxwell fluid and the plateau mean-square displacement for a series of CTAB:NaSal solutions having a concentration of 0.1M and in which the NaSal:CTAB molar ratio varies as: (■) 0.75 (◆) 0.82 (▲) 0.90 (X) 1.25 (+) 2.0 (□) 2.50 and (○) 3.0. The collapse of the data confirm the near maxwellian behavior of these solutions.

Surprisingly the data do seem to collapse for the short time rescaling. This result is very similar to the CTAB/KBr system (22) in which the data was also seen to collapse neatly when the short

time Maxwellian rescaling was carried out. Similar to the CTAB/KBr system, the plateau onset occurs at  $t/(\tau_B)^{1/2} \sim 10^2-10^3$  and not unity. This is indicating that this result is fortuitous with respect to Maxwellian dynamics. The inapplicability of the Maxwell model at short times (high frequencies) can be further illustrated through use Cole-Cole plots. A distinctive signature of fluids exhibiting a single monoexponential decay or Maxwellian dynamics is a semi-circular  $G''$  vs  $G'$  plot (a Cole-Cole) plot. Figure 27 illustrates Cole-Cole plots for three NaSal:CTAB molar ratios:

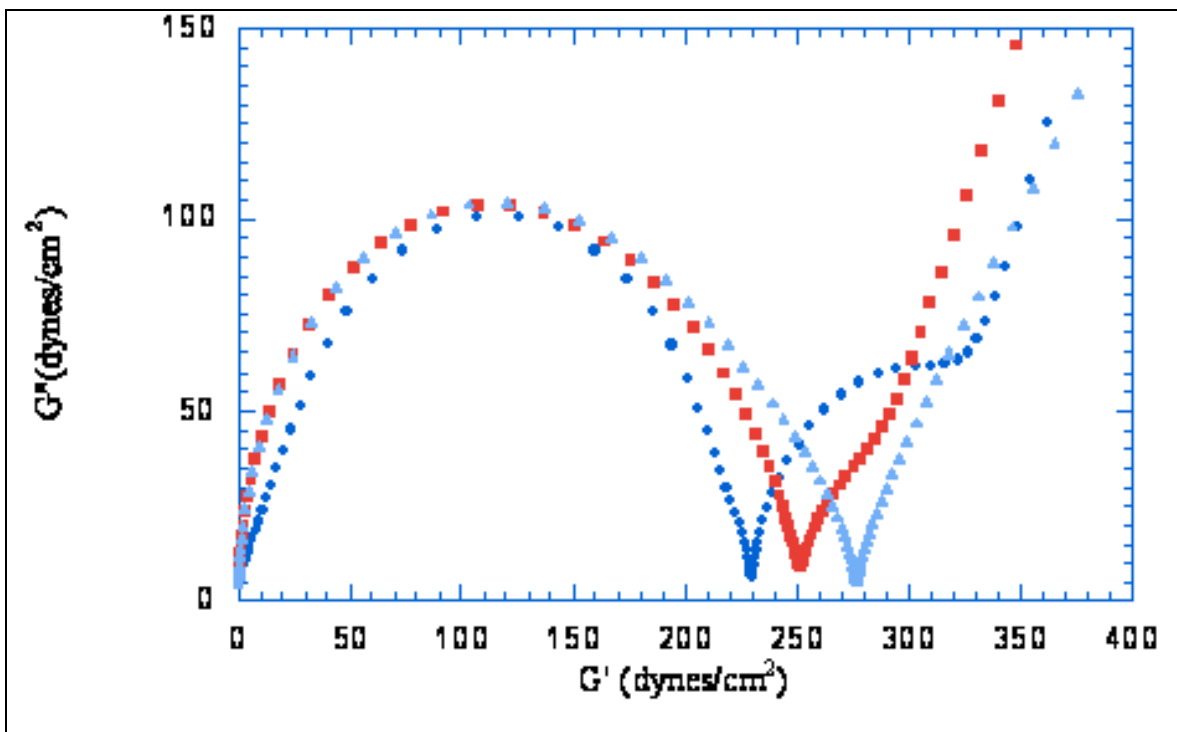


Figure 3.27: Cole-Cole plot for three NaSal:CTAB molar ratios: (●) 0.75 (■) 0.90 and (▲)2.50. The semi-circular shape of the Cole-Cole plot at low to intermediate frequencies and deviations at high frequencies indicate applicability of the Maxwell model only for the low to the intermediate frequencies.

The Figure illustrates Maxwell fluid behavior at long times and deviation at short times or high frequencies. As mentioned before other relaxation mechanisms which are present at these short times may be the possible reason for this deviation. An interesting point to note is that the deviation from the semi-circular shape is seen to be sensitive to the NaSal:CTAB molar ratio. This is however not unexpected. The static and dynamic light scattering measurements have

shown the sensitivity of the relaxation times and mechanisms on the NaSal:CTAB molar ratio. It is therefore not unexpected that the same parameters would also influence the short time relaxation mechanisms.

The applicability of the model as illustrated via the long time Maxwellian rescaling and the semi-circular shape of the Cole-Cole plots provided a means to fit the experimental tracer microrheology data to extract parameters of interest.

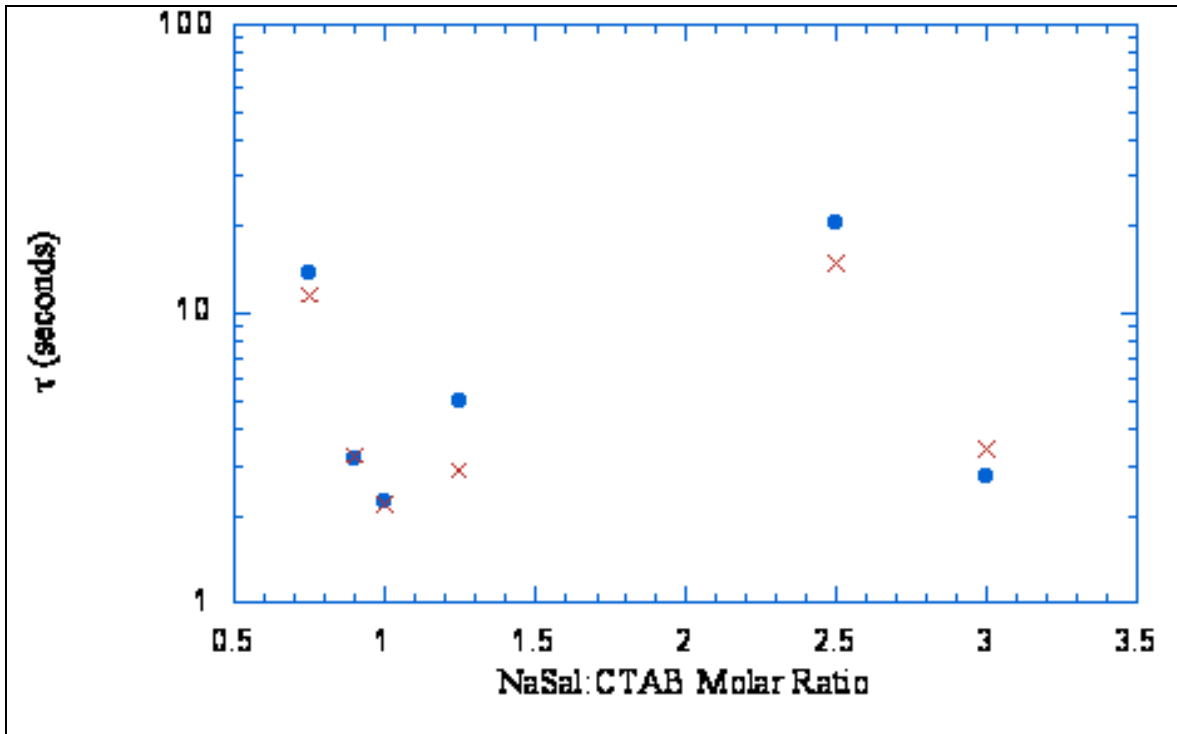


Figure 3.28: Variation of the slow relaxation time with the NaSal:CTAB molar ratio. The relaxation times were extracted through: (●) Tracer -Maxwell Fit of  $\langle \square r^2(t) \rangle$  (X) Tracer-maxwell fit of  $G'G''$  (X). Both fits exhibit good qualitative agreement.

As illustrated by van Zanten and Rufenner (22), for a single relaxation time Maxwell fluid, at very long times, the  $\langle \square r^2(t) \rangle$  can be described by the inertialess Maxwell model for Brownian motion:

$$\langle \square r^2(t) \rangle = \frac{6kT}{\square} (t + \square) \quad (14)$$

This provided an excellent description of the  $\langle r^2(t) \rangle$  plateau behavior and provided a method of estimating the relaxation times and modulus  $G_0$ . The Maxwell model was also utilized to extract relaxation times from the tracer microrheology  $G'$  and  $G''$  data. A comparison of the relaxation times obtained from these two fits is illustrated in figure 28:

The plot illustrates that there is a discrepancy between the magnitudes of the relaxation times between the two estimation techniques. However, this may be attributable to the difference in goodness of the fits as well as slight error due to estimating the  $G'$  and  $G''$  moduli from the creep compliance  $J(t)$ . The qualitative trends are however seen to agree very well.

#### ***3.4.4.5 Mechanical Rheometry Tracer Microrheology Comparison:***

One of the main objectives of this experimental investigation was to carry out a comparative study of tracer microrheology and mechanical rheometry measurements on this system in order to investigate any discrepancies and to corroborate those with the static and dynamic properties if possible. Mechanical rheometry measurements were conducted on the same series of NaSal:CTAB molar ratio solutions. Both creep measurements and dynamic frequency sweeps were conducted in order to extract the creep compliance,  $J(t)$  and the complex viscoelastic moduli  $G^*$ . Figure 3.29 illustrates the comparative results. The plot illustrates the comparison between the viscoelastic parameters extracted from tracer microrheology and those extracted from mechanical rheometry for four NaSal:CTAB molar ratios. The comparative behavior is seen to be extremely sensitive to the NaSal:CTAB molar ratio. From the  $G^*$  comparison, it is



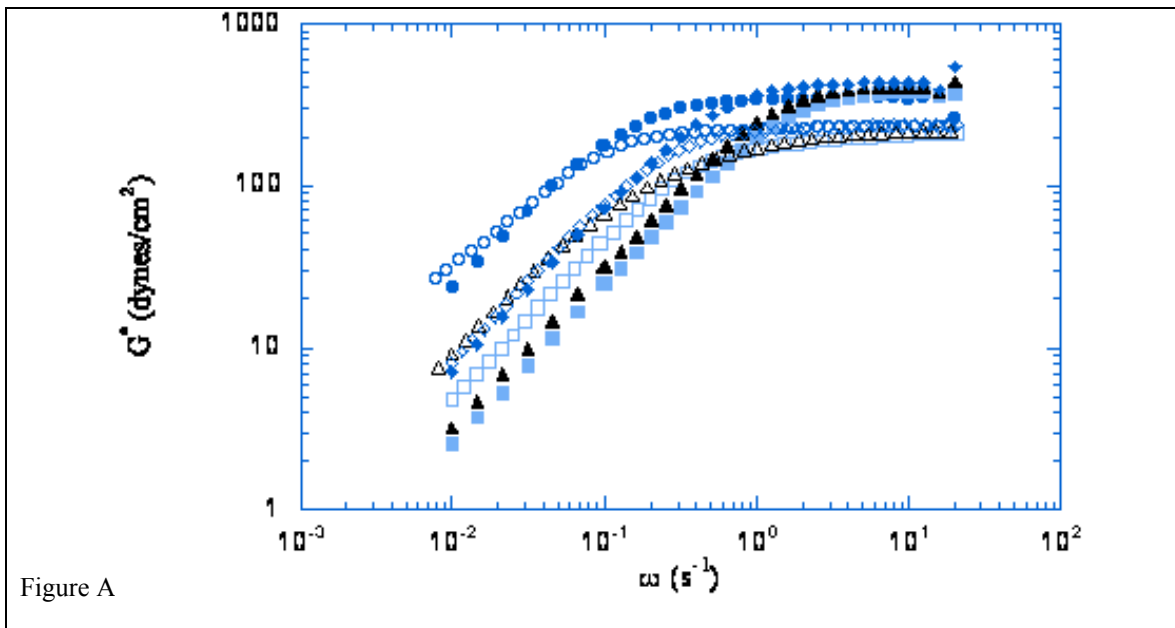


Figure A

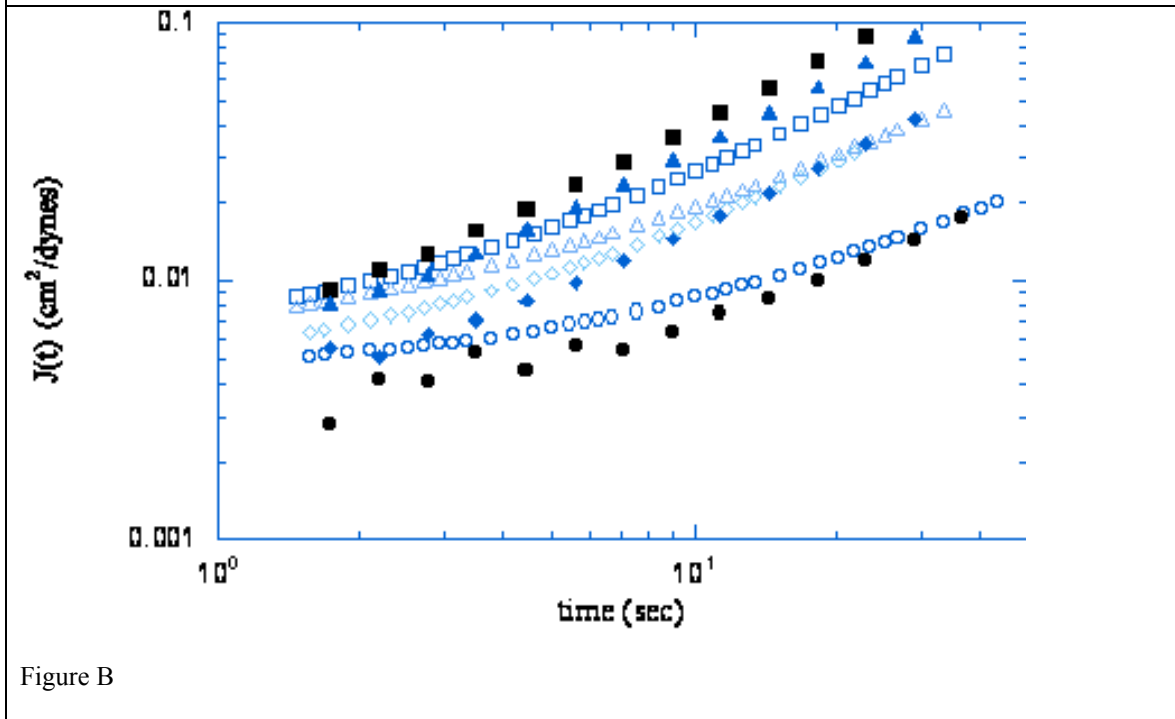


Figure B

Figure 3.29: Comparison between viscoelastic parameters obtained from tracer microrheology and mechanical rheometry. Figure a above illustrates the comparison for the complex viscoelastic moduli  $G^*$  and figure b illustrates the comparison for the creep compliance. The agreement in the two techniques is seen to be highly dependent on the frequency and the NaSal:CTAB molar ratio. Four ratios: (●) 0.75 (■) 1.0 (▲) 1.25 and (◆) 3.0. are shown in the figure. Closed symbols represent mechanical rheometry and open symbols represent tracer microrheology measurements.

observed that the highest and lowest molar ratios, 0.75 and 3.0 exhibit very similar behavior.

The tracer microrheology and mechanical rheometry  $G^*$  values agree very well in the low

frequency (long time) limit. However, after a certain frequency, the mechanical rheometry  $G^*$  begins to surpass the tracer microrheology data for these two ratios and eventually what is observed is that the tracer microrheology underestimates the plateau modulus in the high frequency (short time) limit. The intermediate ratios, 1 and 1.25 exhibit very different comparative behaviors. The tracer microrheology  $G^*$  is significantly higher than the mechanical rheometry data in the low frequency (long time) limit but then at a certain intermediate frequency the mechanical rheometry  $G^*$  overtakes it and this also results in an underestimation of the plateau modulus by tracer microrheology. The creep compliance measurements agree well with this same trend. For the lowest and highest ratios of 0.75 and 3.0 there is good comparative agreement at long times and overestimation (as creep and  $G^*$  are inversely related) of the creep compliance by tracer microrheology at high times. For the intermediate concentrations of 1 and 1.25 the tracer microrheology data underestimates the mechanical data at long times and a crossover can be seen at the shorter times. Since the crossover takes place at higher frequencies for these ratios, the overestimation by the tracer microrheology could not be adequately picked up due to scatter in the data at these short times. A notable point in this comparative study was that the deviations in the final plateau values ranged from 1.5 to 2, a correction factor also obtained by Cardinaux et al (48) on another worm like micellar system. A straight multiplication of the data by a factor of 1.5 to 2 however does not bring about a quantitative agreement in the investigated system due to the dependence of the deviation on the frequency (figure 3.30).

The deviations between the two techniques is further illustrated on considering some of the extracted parameters. One parameter which is seen to be strongly dependent on NaSal:CTAB molar ratio and provides an insight into the relaxation mechanisms is the terminal relaxation time. Figure 31 illustrates the variation between the relaxation times obtained

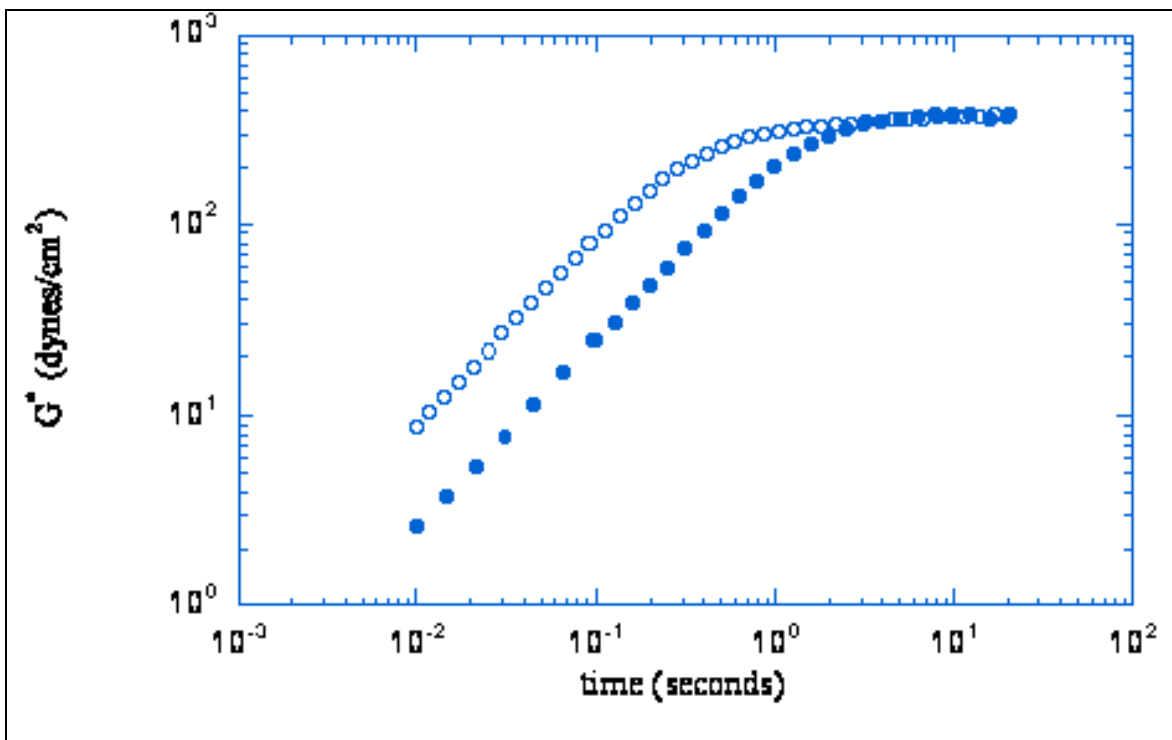


Figure 3.30:  $G^*$  frequency variation for a CTAB =0.1 M, NaSal:CTAB Molar Ratio=1 solution . The deviation of the (○) tracer microrheology and (●)mechanical rheometry data is frequency dependent. As a result a multiplication of the tracer microrheology data by a number equivalent to the plateau deviation does not collapse the data.

from tracer microrheology, mechanical rheometry and dynamic light scattering. The most notable point from the figure is the excellent agreement in the qualitative trends between all three techniques. Quantitatively, the tracer microrheology terminal relaxation times are seen to consistently overestimate the relaxation times determined from mechanical rheometry. This may be attributable to the effect of longitudinal compression modes on the extracted viscoelastic parameters as will be discussed in detail later. Except for the two lowest ratios investigated, the tracer microrheology data is also seen to overestimate the relaxation times as estimated through dynamic light scattering.

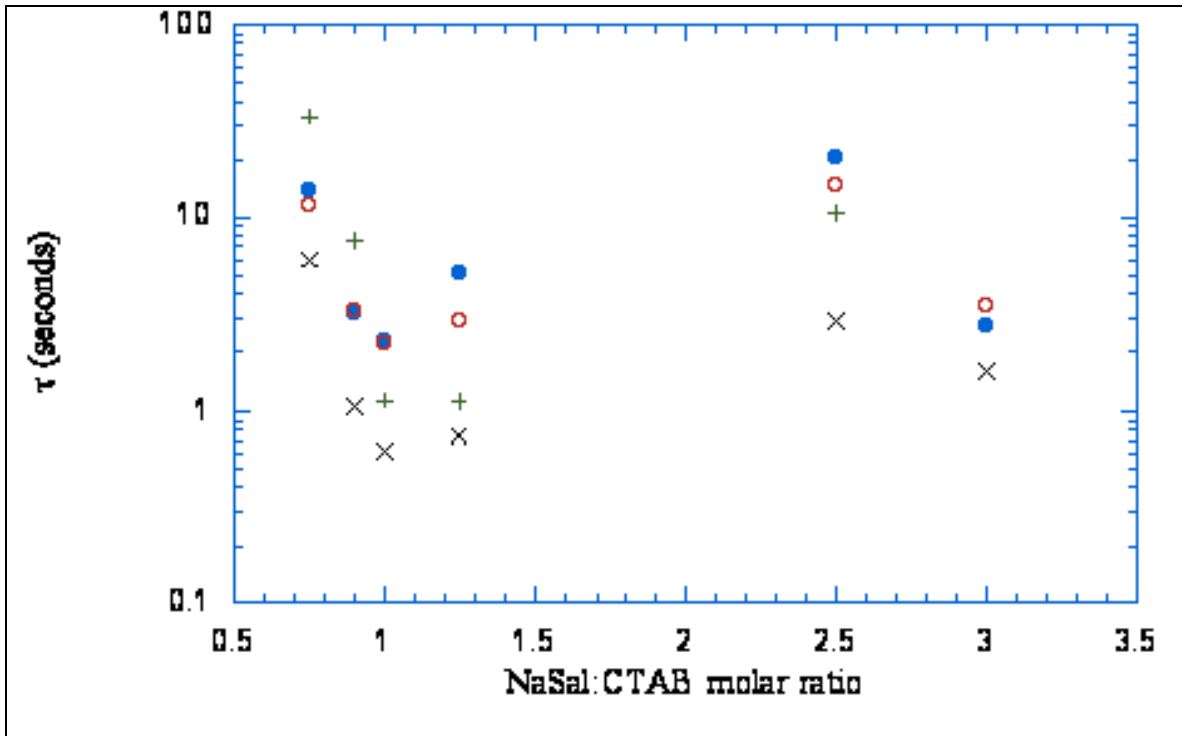


Figure 3.31: Relaxation time variation with NaSal:CTAB molar ratio. Relaxation times extracted from: (●) Tracer -Maxwell Fit of  $\langle r^2(t) \rangle$  (○) Tracer-maxwell fit of G'G'' (X) Mechanical-Maxwell Fit of G' DLS. The most notable point is the good qualitative agreement in the relaxation time-NaSal:CTAB molar ratio variation trend.

Quantitative discrepancies between the values in the three techniques may also arise due to goodness of the fits used to estimate this parameter.

The zero shear viscosity variation with the NaSal:CTAB molar ratio was estimated from the tracer microrheology measurements and from mechanical rheometry measurements and is illustrated in figure 3.32. It is seen that for all ratios the tracer microrheology zero shear viscosity overestimates the mechanical rheometry zero shear viscosity. From the comparison of the relaxation times and zero shear viscosity for the two techniques it is seen that for both the parameters, the tracer microrheology overestimates the mechanical rheometry. In the case of the plateau modulus, it is however seen that the tracer microrheology underestimates the mechanical rheometry. The plateau modulus is related to the zero shear viscosity and the relaxation time

through,  $G_0 = \frac{\eta_0}{\lambda}$ . Since the tracer microrheology terminal relaxation time is overestimating the mechanical rheometry terminal relaxation time, this may be the parameter which is leading to an underestimation of the plateau modulus. It is however difficult to draw definitive conclusions from this analysis alone. The overestimation of the zero shear viscosity is reminiscent of the positive deviation away from Stokes-Einstein (SE) behavior seen in dynamic light scattering experiments and discussed in chapter 1 (references 31-48 in chapter 1).

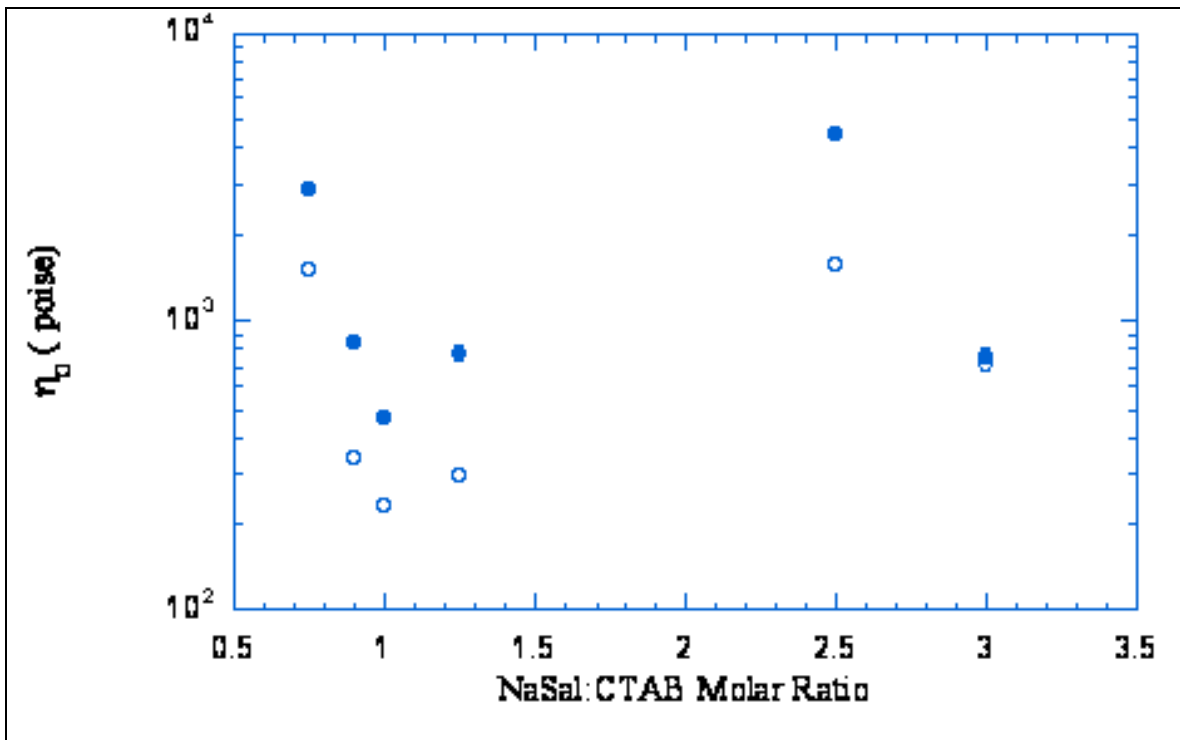


Figure:3.32 Variation of zero shear viscosity with the NaSal:CTAB molar ratio for (●) Tracer microrheology (○) mechanical rheometry measurements. The tracer viscosity is seen to be consistently higher than the mechanical rheometry viscosity. Qualitative agreement is seen to be good

The deviations between the tracer microrheology and mechanical rheometry data observed here brings into focus the ability of the generalized Stokes-Einstein relation to adequately describe the connection between the Brownian motion of the tracer particles and the viscoelastic response of the fluid.

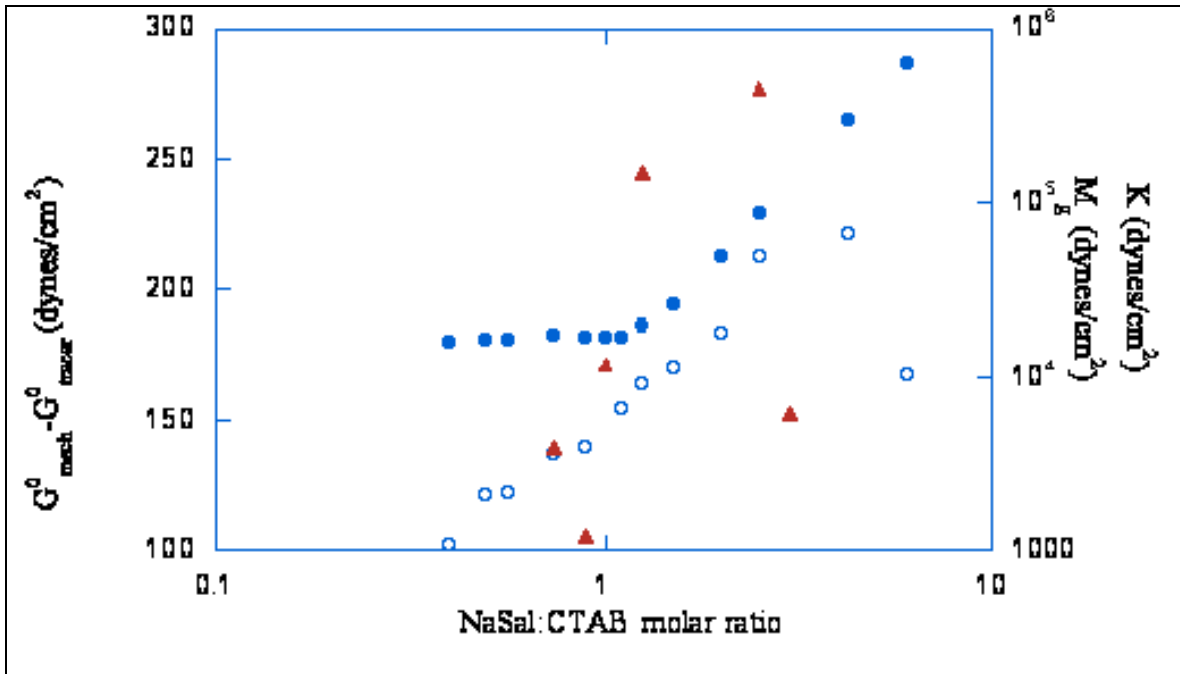


Figure 3.33: Variation of the deviation in the (▲) plateau modulus, the (●) bulk osmotic modulus and the (○) bulk longitudinal elastic modulus with the NaSal:CTAB molar ratio. Increases in the plateau modulus deviation is seen to track to a certain extent with  $M_G$ .

As was discussed previously the theoretical developments by Levine and Lubensky (49-51) have identified a characteristic frequency below which the longitudinal dynamical modes may play a role in affecting the extracted viscoelastic moduli. The static light scattering measurements on the system, discussed earlier have shown the sensitivity of the osmotic compressibility on the NaSal:CTAB molar ratio. It is therefore clearly apparent that the bulk osmotic modulus  $K$  and the bulk longitudinal elastic modulus,  $M_G$  will also exhibit a strong sensitivity to the NaSal:CTAB molar ratio. In order to observe the dependence of these parameters on the the NaSal:CTAB molar ratio they were extracted and they are plotted together with the deviation in the plateau modulus, as a function of the NaSal:CTAB molar ratio. The bulk osmotic modulus was computed from

$K = c \frac{\partial \square}{\partial c}$ , and the bulk longitudinal elastic modulus was computed from  $\frac{M_g}{K} = \frac{A_f}{A_s}$ , where  $A_f$

and  $A_s$  are the fast and slow mode amplitudes obtained from dynamic light scattering measurements. From figure 3.32 it seems that the deviations in the plateau modulus do tend to track with the longitudinal bulk elastic modulus. However, the peak occurs at lower NaSal:CTAB molar ratios for the deviations. Therefore it is difficult to make any definitive conclusions at this stage.

Another test of the longitudinal dynamical mode effects can be further investigated on carrying out a sphere size sweep on the CTAB:NaSal system.

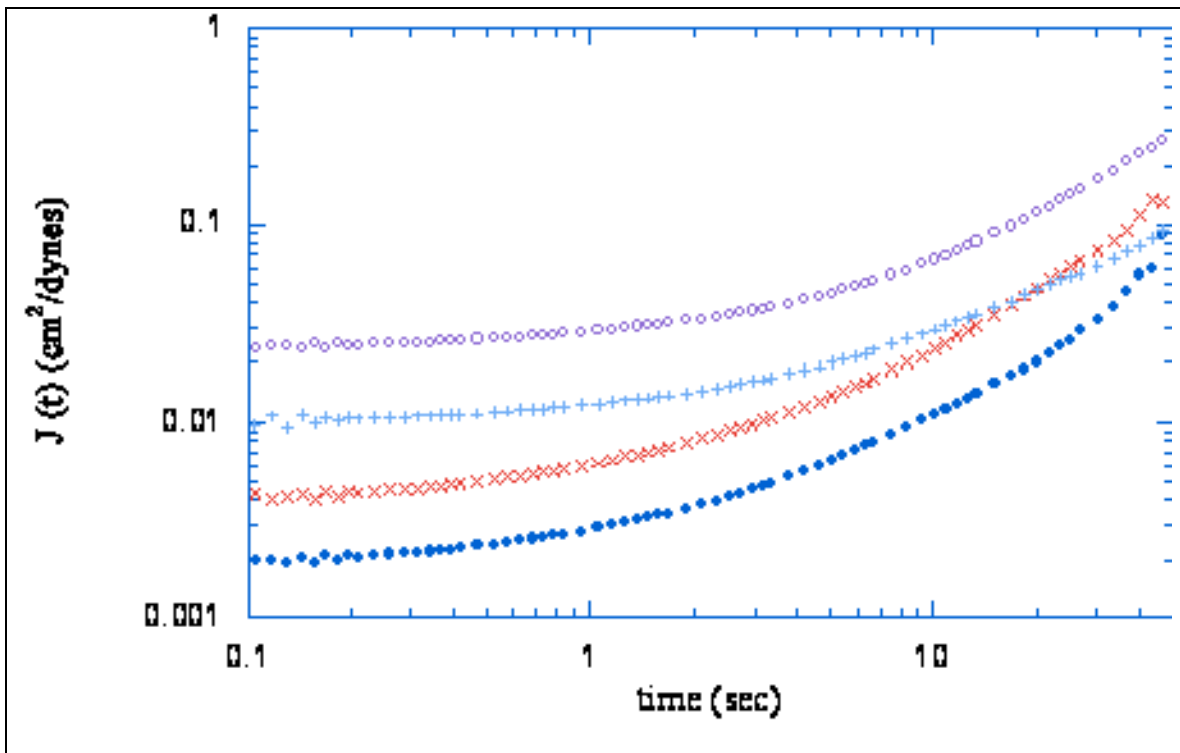


Figure 3.34: Creep compliance for a 0.1M CTAB concentration NaSal:CTAB solution having a NaSal:CTAB ratio of 1.0 and in which the tracer probe size was varied. The probe sizes were:(●)0.195 microns (×) 0.358 microns, (+) 0.739 microns and (○) 1.55 microns. As is clearly seen the data did not collapse into a single curve. This is indicative that the longitudinal compression modes may be playing a role in affecting the viscoelastic parameters.

This is clearly apparent as the Levine and Lubensky cutoff frequency is affected by the radius of the probe particle ( $\omega_c \sim a^D$ , where  $a$  is the probe radius). In order to test this a sphere size sweep was carried out on a series of 0.1M CTAB, NaSal/CTAB R=1.0 solutions in which the sphere size was varied from 0.195 microns to 1.55 microns. As seen in figure 33, the creep compliance data do not collapse at all when the correct radii are used to extract the data from the mean square displacement data indicating that the longitudinal compression modes are playing a role. Also note worthy is the change in terminal times associated with different sphere sizes.

### **3.5 Conclusions**

This chapter has detailed a tracer microrheology/ dynamic light scattering and static light scattering investigation of CTAB/NaSal solutions over a wide range of CTAB concentration and NaSal:CTAB mole ratio. The conclusions that can be drawn can be summarized as follows:

*1) Dynamic Light Scattering Measurements:* From the DLS measurements two distinct relaxation times were observed for CTAB concentration  $\geq 0.02$  M. The hydrodynamic correlation length,  $\zeta_H$ , associated with the fast relaxation mode was found to depend on both the CTAB concentration and NaSal:CTAB mole ratio. In particular, the CTAB concentration scaling of  $\zeta_H$  was shown to vary in a nonmonotonic manner with the NaSal:CTAB mole ratio. The scaling exponent was found to range from  $-0.25$  to  $-0.67$  where its minimum value was found for NaSal:CTAB mole ratios near 1.5-2.0. This is in strong support of the decreasing micellar ionization picture associated with increasing NaSal:CTAB molar ratio. The distinct minimum of the scaling exponent followed by a re-increase is indicative of micellar neutrality followed by a charge reversal at higher NaSal:CTAB molar ratios. The amplitude of the slow relaxation mode

was observed to be strongly correlated with the hydrodynamic correlation length for NaSal:CTAB mole ratios less than or equal to 2 thereby strongly suggesting polymer/polyelectrolyte solution behavior at these conditions. The behavior of the hydrodynamic correlation length and slow mode amplitude were described quite well within a framework of micelle ionization and electrostatic screening effects. However, the NaSal:CTAB mole ratio and CTAB concentration dependence of the slow relaxation time could not be entirely explained within the context of electrostatic interactions. In order to account for the observed slow relaxation time behavior it was hypothesized that the micelle breaking time is influenced by bound salicylate ions whose degree of binding depends on both the NaSal:CTAB mole ratio and CTAB concentration.

2) *Static Light Scattering Measurements:* Most of the static parameters of interest corroborated the results of the dynamic light scattering measurements. The static correlation length showed a similar dependence on the NaSal:CTAB molar ratio as the hydrodynamic correlation length did, in that it increased to a maximum and then decreased to an almost constant value. The behavior however was limited to concentrations below 0.3M. The  $\zeta$  parameter exhibited a similar monotonically decreasing behavior with the NaSal:CTAB molar ratio. Supporting the decreasing micellar ionization picture associated with increasing NaSal:CTAB molar ratio. The distinct minimum followed by a re-increase to indicate neutrality and a charge reversal was however not observed in this case. One of the main results obtained from the static light scattering measurements was the extraction of the osmotic compressibility. The osmotic compressibility dependence on the NaSal:CTAB molar ratio exhibited a very interesting sharp transition at a particular NaSal:CTAB molar ratio after which the osmotic compressibility exhibited a much stronger dependence on the ratio. The ratio at which the sharp transition

occurred was highly dependent on the CTAB concentration. This again supports the idea of charge reversal and its dependence on both the CTAB concentration and the NaSal:CTAB molar ratio. The osmotic pressure exhibited a power law dependence on the total concentration for each NaSal:CTAB ratio examined. The power law behavior was however divided into two concentration regimes for each NaSal:CTAB molar ratio. The low concentration regime corresponded with viscous samples and at high ratios showed behavior similar to the theoretical behavior exhibited by equilibrium polymers. The high concentration regime corresponded with mostly gellike samples and exhibited a behavior similar to polyelectrolyte gels.

The overall picture that emerged from the static and dynamic light scattering measurements on CTAB/NaSal system was that of a system where the competition between micellar charge, electrostatic screening and micelle breaking controls the system dynamics.

*3)Tracer Microrheology and Mechanical Rheometry:*The tracer microrheology measurements on this system have revealed the viscoelastic response of the system over a wide frequency range, not accessible through mechanical rheometry. A series of solutions having a constant CTAB concentration [0.1M] and varying NaSal:CTAB molar ratios were observed to exhibit very similar viscoelasticity. The major difference showing up in the long time behavior after the system has relaxed. The plateau modulus exhibited a nonmonotonic dependence on the NaSal:CTAB molar ratio. The tracer microrheology and mechanical rheometry comparisons were also very interesting. The agreement between the two techniques was highly dependent on the frequency and the NaSal:CTAB molar ratio. The best agreement which was seen at lower frequencies or longer times was for the highest and lowest ratios examined. Sphere size sweeps also revealed that the creep compliance data could not be collapsed onto a single master curve. This is indicative that longitudinal dynamical modes or structural features may be affecting the

extracted viscoelastic parameters. The deviations in the tracer microrheology and mechanical rheometry plateau moduli were also seen to track with the bulk longitudinal elastic modulus,  $M_G$ . However, the location of maximum deviation seems to occur at lower NaSal:CTAB molar ratios than that of the longitudinal elastic modulus. Therefore it is difficult to make any definitive conclusions at this stage.

## **References**

1. Cates, M. E. and Candau, S. J.; *J.Phys:Condens. Matter* ,1990, 2, 6869.
2. Shikata,T., Sakaiguchi, Y., Uragami, H., Tamura, A.; and Hirata, H.; *J. Coll.Interface Sci.* **1987**, 119, 291.
3. Imae, T., Abe, A. and Ikeda, S.; *J. Phys. Chem.* **1988**, 92, 1548.
4. Shikata, T. and Hirata, H.; *Langmuir* ,**1988**, 4, 354.
5. Shikata, T., Hirata, H. and Kotaka, T.; *Langmuir*, **1989**, 5, 398.
6. Shikata, T. and Kotaka, T.; *J of Non-Crystalline Solids*, **1991**, 131, 831.
7. Nemoto, N., Yamamura, T. and Osaki, K.; *Langmuir*,**1991**,7,2607.
8. Koike, A., Yamamura, T. and Nemoto, N.; *Coll. Polym. Sci.* **1994**, 272, 955.
9. Nemoto, N. and Kuwahara, M.; *Coll. Polym. Sci.* **1994** ,272, 846.
10. Nemoto, N., Kuwahara, M., Yao, M. and Osaki, K.; *Langmuir*,**1995**, 11, 30.
11. Shikata, T., Imai, S. and Morishima, Y.; *Langmuir*, **1997**, 13, 5229.
12. Brown, W., Johansson K. and Almgren, M.; *J. Phys. Chem.* **1989**,93, 5888.
13. Buhler, E.,Munch J. and Candau, S.; *J. Phys. II* ,France 1995, **5**, 765.
14. Cates, M.E.; *Macromolecules* **1987**, 20, 2289.
15. Candau, S. J.; In *Theoretical Challenges in the Dynamics of Complex Fluids (NATO ASI Series: Series E. Applied Sciences)*; McLeish, T., Ed.; Kluwer Academic Publishers: New York, 1997; Vol. 339, p 53
16. Brochard, F. and de Gennes, P.G.; *Macromolecules* ,**1977**, 10, 1157.
17. Brochard, F.; *J. Physique*, **1983**, 44, 39.
18. Adam, M. and Delsanti, M.; *Macromolecules*, **1985**,18,1760.
19. Semenov, A.; *Physica A*, **1990**,166, 263.

20. Doi, M. and Onuki, A.; *J. Phys. II (France)* ,**1992**, 2, 1631.
21. van Zanten, J.H., Amin, S., van Zanten, R.M. and Dees, S.J.; *In preparation*.
22. van Zanten, J.H. and Rufener, K.P.; *Phys. Rev. E*, **2000**, 62, 5389.
23. Kermis, T.W., McHugh, M.A. and van Zanten, J.H.; *In preparation*.
24. de Gennes, P.G.; *Scaling Concepts in Polymer Physics*; Cornell University Press: New York, **1979**.
25. Magid, L.J. ; *J. Phys. Chem, B* **1998**, 102, 4046.
26. Shibayama , M., Ikkai, F., Shiwa, Y. and Rabin, Y.; *J Chem Phys*, **1997**, 107, 5227
27. Shiwa, Y.; *The European Physical Journal B*, **1998**, 345
28. Travas-Sejdic, J. and Eastal, A.; *Polymer*, **2000**, 41, 2535
29. Rehage, H. and Hoffman, H.; *Molecular Physics*, **1991**, 74, 5, 933
30. Olsson, U., Soderman, O and Guering, P.; *J. Phys. Chem.*, **1986**, 90, 5223
31. Nisato, G., Munch, J. and Candau, S.; *Langmuir*, **1999**, 15, 4236
32. Rubenstein, M., Colby, R.H., Dobrynin, A.V. and Joanny, J.-F.; *Macromolecules*, **1996**, 29, 398.
33. Rubinstein, M., Colby, R.H. and Dobrynin, A.V.; *Phys. Rev. Lett.* **1994**, 73, 2776
34. Doi, M. and Edwards, S.F. ; *The Theory of Polymer Dynamics*; Oxford University Press: Oxford, **1986**.
35. Kim, W. and Yang, S.; *J. Coll.Interface Sci.* **2000**, 232, 225.
36. Lequex, F.; *Europhys. Lett.*, **1992**, 19, 675
37. Kadoma, I. A. and van Egmond, J. W.; *Langmuir*, **1997**, 13, 4551
38. Kadoma, I. A., Ylitalo, C.M. and van Egmond, J. W.; *Rheol. Acta*, **1997**, 36, 1
39. Lin, Z.; *Langmuir*, **1996**, 12, 1729

40. Khatory, A., Lequeux, F., Kern, F. and Candau, J.; *Langmuir*, **1993**, 9, 1456
41. Khatory, A., Kern, F., Lequeux, F., Appell, J., Porte, G., Morie, N., Ott, A. and Urbach, W.;  
*Langmuir*, **1993**, 9, 933
42. Drye, T. J. and Cates, M. E.; *J. Phys. Chem.*, **1992**, 96, 1367
43. Schurtenberger, P.; in Light Scattering, Brown B (ed)
44. Young, R.J. and Lovell, P.A.; *Introduction to Polymers*, **1981**, Chapman & Hall
45. Russel, W.B., Saville, D.A. and Schowalter, W.R.; *Colloidal Dispersions*, **1989**, UK,  
Cambridge University Press
46. Milchev, A., Wittmer, J. P., van Der Schoot, P. and Landau, D.; *Europhysics Letters*,  
**2001**, 54, 58
47. References 4-13, 21-29 in chapter 1
48. Cardinaux, F., Cipelletti, L., Scheffold, F. and Schurtenberger, P.; *Europhysics Letters*,  
**2002**, 57, 738
49. Levine, A. J. and Lubensky, T. C.; *Phys Rev E*, **2002**, 65, 011501/1.
50. Levine, A.J. and Lubensky, T.C.; *Phys. Rev. Lett.*, **2000**, 85, 1774
51. Levine, A.J. and Lubensky, T.C.; *Phys Rev E*, **2001**, 63,4, 1510

## Chapter 4

### Micellar Soft Crystal Rheology

---

#### *4.1 Abstract*

Pluronic™ F108 FCC soft crystal linear viscoelasticity properties are investigated via mechanical rheometry for a number of concentrations above the disordered micelle-FCC soft crystal transition concentration. The viscoelastic moduli  $G'$  and  $G''$  are essentially frequency independent especially at the higher concentrations. This is the expected predominantly elastic behavior generally observed for solids and strongly gelled systems. The concentration dependence of the elastic modulus is stronger than the linear dependence typically observed for hard sphere dispersions. This deviation away from hard sphere behavior is attributed to a longer ranged intermicellar interaction potential and the potential coexistence of dispersed micellar and FCC soft crystal phases. The near constant values of  $G'$  at higher concentrations are attributed to the weaker concentration dependence of the interparticle separations due to compression and interpenetration of coronal layers due to increased packing. The observed rheological behavior indicates that micellar packing and the intermicellar interaction potential plays a dominant role- this is most clear in the context of the observed viscosity behavior. The viscosity frequency dependence indicates that the interparticle interactions are becoming more hard sphere in nature with increasing concentration due to compression and interpenetration of the coronal layers under tight packing conditions.

## 4.2 Introduction

The colloidal dispersion rheology has attracted widespread interest because of their use in a plethora of technological applications. In particular, the dynamics and rheology of polystyrene latex dispersions have been studied quite extensively (1-5). Typically, the dynamics in disordered systems have been described with theoretical models based on hard sphere and electrostatic interactions (6-10). These theories have also been extended to the case of colloidal systems at high concentrations, where the colloidal particles may order into a crystal lattice forming either a face centered cubic (FCC) or body centered cubic (BCC) structure, depending upon the 'softness' of the interaction potential (11-13). For the case of polystyrene lattices this ordering has been largely attributed to the electrostatic repulsion present between the spheres (10). For the case of uncharged spheres whether the dispersion ultimately forms a FCC or a BCC structure depends on the interparticle interaction potential. Hamley *et al.* (11-13) and Pople *et al.* (14), have shown that sharp, short range interactions, which are typical of hard spheres, favor FCC structures, while softer, longer ranged repulsive interactions favor the formation of BCC structures.

An interesting class of materials that form FCC and BCC structures similar to those found for concentrated polystyrene lattices are the so-called soft crystals composed of block copolymer micelles in a selective solvent. One such class of materials that order into soft crystals at sufficiently high concentrations and temperatures in aqueous solution are the triblock copolymers known commercially as Pluronic<sup>TM</sup> or Polaxamers<sup>TM</sup>. These triblock copolymers have the structure  $(\text{PEO})_n-(\text{PPO})_m-(\text{PEO})_n$ . The PEO and PPO chains are both soluble in aqueous solution at temperatures  $\leq 5^\circ\text{C}$ . However, as the temperature is raised above  $5^\circ\text{C}$ , water becomes an increasingly poor solvent for the PPO block, while the PEO chains remain

essentially unaffected. The low affinity of water for the PPO chains causes the PPO blocks to associate with one another thereby forming micelles in which the core consists of water free PPO surrounded by a highly hydrated PEO corona. These block copolymer micelles are very similar in structure to so-called 'hairy' or polymer-stabilized colloidal particles. This structure leads to interparticle interaction potentials that are longer ranged than those found for hard spheres. The softness of the interparticle interaction potentials, along with the solvated nature of the PEO corona, provides the mechanism for these triblock copolymers to form ordered soft crystals at relatively small volume fractions (15).

One such system is Pluronic™ F108 commercially available from BASF. This triblock copolymer has the structure  $(\text{PEO})_{127}\text{-(PPO)}_{48}\text{-(PEO)}_{127}$ . Phase behavior studies of aqueous solutions of Pluronic™ F108 (16) indicate that the equilibrium between triblock copolymer unimers and micelles is largely temperature dependent with micelle formation occurring at 2wt% at a temperature of 25°C. As the Pluronic™F108 concentration increases, the micelle interactions increase until these interactions eventually drive a phase transition between a disordered and ordered micellar dispersion. While previous studies indicate that this phase transition occurs at about 27 wt% (16), in progress tracer microrheology studies indicate the onset of gel-like behavior at much lower concentrations of ~ 22.7 wt% (17). Both of these observations are consistent with a reported dispersed phase-ordered phase coexistence region between approximately 22 and 27 wt% at 25 °C(15,18-19). Small angle x-ray scattering investigations indicate that a 35 wt% Pluronic™ F108 aqueous solution at 25 °C forms a polycrystalline FCC crystal. This FCC crystal is composed of 120 Å radius micelles (corresponding to an aggregation number of approximately 50) and exhibits a lattice parameter of 294 Å and a nearest neighbor separation of 208 Å (15,18-19).

While the structure and rheological response of several soft crystal forming Pluronic aqueous solutions have been investigated previously, the vast majority of these studies have considered the connection between crystal structure, shear rate and steady shear viscosity (15,18-19). Here we report a study of the linear viscoelastic behavior of aqueous Pluronic™ F108 soft FCC crystals at 25 °C for Pluronic™ F108 concentrations ranging from 23 to 40wt%. The measured viscoelastic properties are described within the context of colloidal dispersion dynamics in the linear viscoelastic regime (6,8,10)

### ***4.3 Materials and Methods***

#### ***Materials***

Pluronic™ F108 was obtained from BASF Corporation and used without further purification. All samples were prepared at room temperature and then cooled down to 5°C to ensure complete dispersion of the polymer. Samples were prepared for rheometry measurements in which the concentration was varied from 23 to 40 wt %. All samples were allowed to equilibrate for two weeks at 5 °C prior to making measurements.

#### ***Mechanical Rheometry***

Linear viscoelastic moduli were determined with a Rheometrics controlled stress rheometer (DSR). Measurements were conducted in a serrated 40 mm parallel plate geometry. The plate temperature was fixed at 5°C and the liquid samples immediately transferred. In order to eliminate edge effects the top plate was brought down a certain distance close to the final gap width and the sides were cleaned off. The plate temperature was then raised to 25° C. The sample was allowed to equilibrate for one hour and then the top plate was brought down to the final width. In order to prevent evaporation effects, the serrated parallel plates were enclosed in

a custom made vapor trap. Both creep and dynamic measurements were carried out on each sample. It should be remarked that measurements were also carried out using a 40 mm cone and plate geometry. However, as this geometry showed reproducibility problems because of sample slippage, no results are reported for measurements carried out in this geometry.

#### 4.3.1 Determination of the linear viscoelastic regime.

In order to determine the stress range corresponding to the linear viscoelastic regime a dynamic stress sweep was carried out for each sample. Figure 4.1 illustrates a stress sweep for a 24 wt% sample where the stress was varied from 1-300 dyn/cm<sup>2</sup>. The near constant value of the elastic modulus  $G'$  over the entire range indicates that the system is within the linear viscoelastic regime at the applied stresses. As a cross check for the linear viscoelastic regime, creep experiments were carried out on each sample at different stresses.

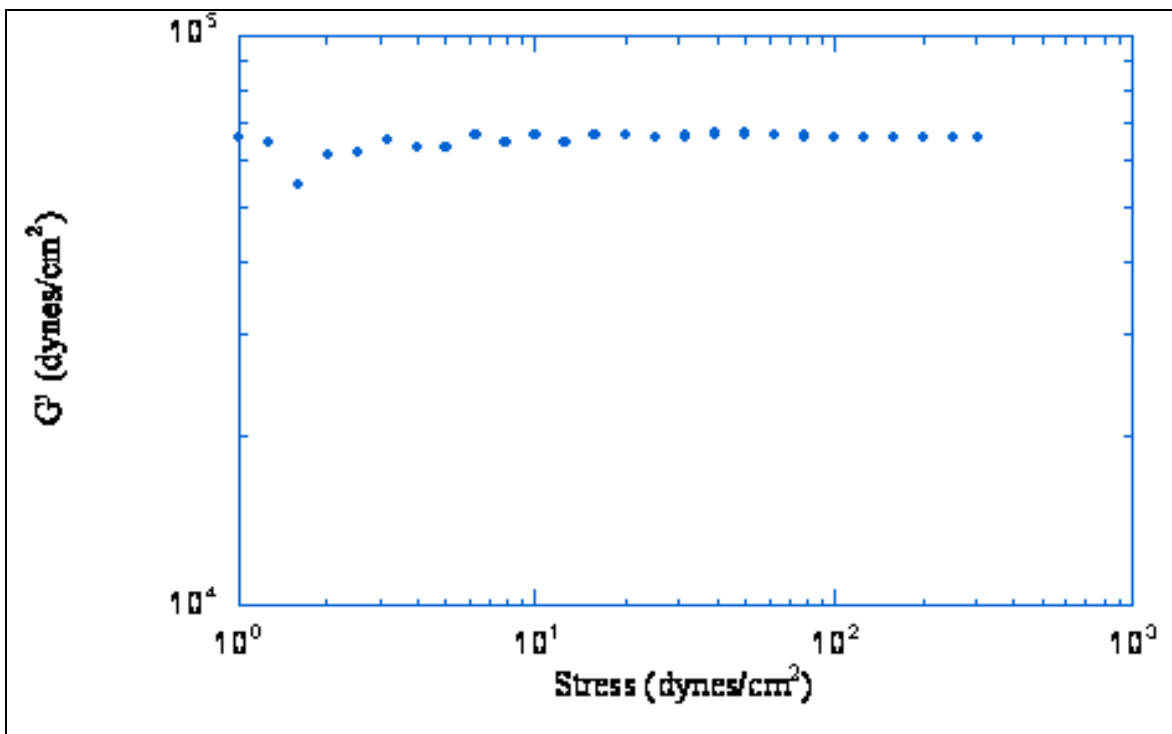


Figure 4.1: Stress dependence of the elastic modulus for a 24 wt % F108 sample. The near constant value for  $G'$  indicates that the system is within the linear viscoelastic regime at the applied stresses. This test for linear viscoelasticity was carried out on all F108 samples prior to choosing an appropriate stress to carry out the measurements

Figure 4.2 displays the creep compliance for the 24 wt% sample measured at a several stresses. The creep compliance should not vary with the stress if the system is within the linear viscoelastic regime.

Although this was true for the creep compliance at the lowest stresses, 50 and 70 dyn/cm<sup>2</sup>, deviations arise as the stress is increased above these values. For instance, significant deviation is observed for a 250 dyn/cm<sup>2</sup> stress while major deviation occurs in the 500 dyn/cm<sup>2</sup> case. Although the stress sweep indicated a linear viscoelastic regime up to 300 dyn/cm<sup>2</sup>, the onset of the nonlinear regime actually appears to take place at somewhat lower stresses. In order to ensure that all measurements were in the linear regime both stress sweeps and creep compliance measurements at varying stresses were carried out for all samples.

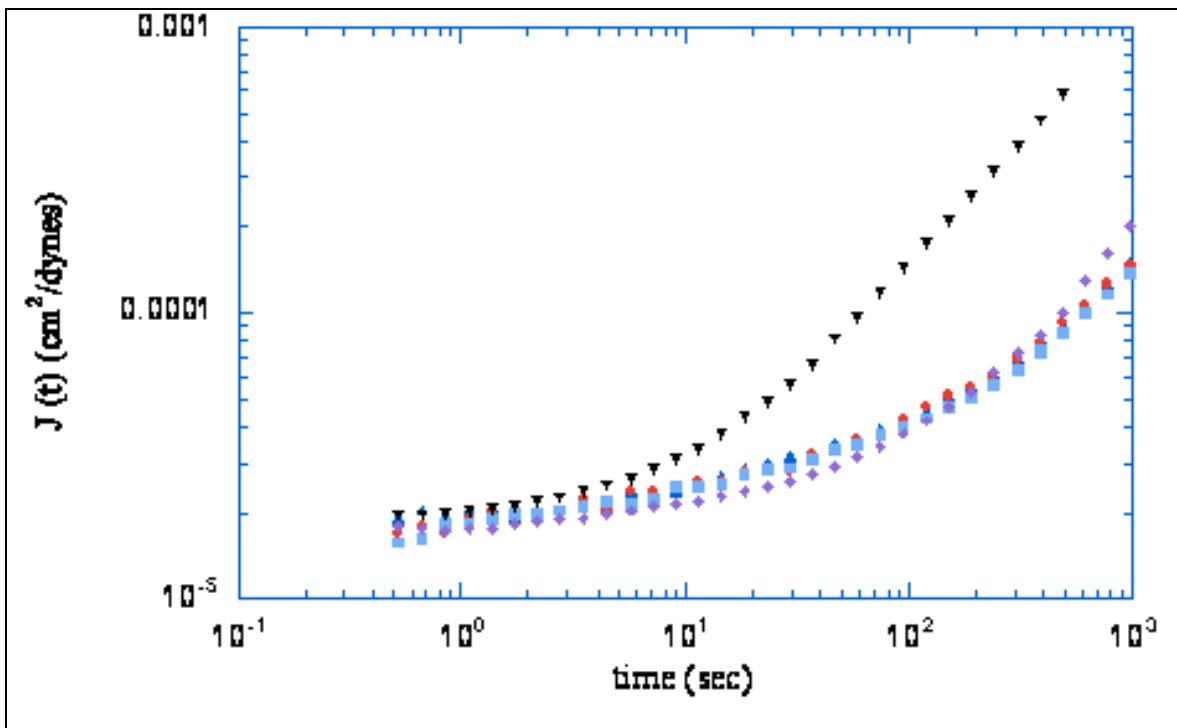


Figure 4.2: Creep compliance for a 24wt% F108 sample for five different stresses: (▲) 50 dynes/cm<sup>2</sup>, (●) 70 dynes/cm<sup>2</sup>, (■) 150 dynes/cm<sup>2</sup>, (◆) 250 dynes/cm<sup>2</sup>, and (▼) 500 dynes/cm<sup>2</sup>. The deviation of the creep compliance at the higher stresses indicates that for these stresses the system is not within the linear viscoelastic regime.

#### 4.4 Results and Discussion

The main objective of this experimental study was to determine the frequency dependent linear viscoelastic moduli of aqueous Pluronic™ F108 solutions in the soft FCC crystal phase. In an attempt to observe the change in viscoelastic properties for samples ranging from the disordered micellar phase to the FCC phase aqueous Pluronic™ F108 solutions were prepared at concentration ranging from 21 to 40 wt %. However, due to torque limitations of the rheometer reliable data was not obtained for the liquid-like disordered micellar solutions having concentrations of 21 and 22 wt%. This report therefore focuses on the concentration range from 23 to 40 wt %. According to the phase diagram reported by Molino *et al.*(15), only the 30, 35 and 40 wt % solutions are purely FCC soft crystals. As noted previously the reported phase diagram indicates a coexistence of disordered micelle-FCC soft crystal phases over the concentration range ~22 to 27 wt%. Also, in progress tracer microrheology (17) indicate that the disordered micelle-FCC crystal phase transition actually takes place at a lower concentration of 22.7 wt%.

##### 4.4.1 Frequency Dependence of $G'$ , $G''$ .

Figure 4.3 shows the storage and loss moduli frequency dependence for three representative Pluronic™ F108 concentrations: 24, 27.5 and 40 wt%. The storage modulus is observed to dominate the viscous modulus by at least an order of magnitude at all frequencies. This observation was true for every Pluronic™ F108 concentration considered. The storage modulus also increases monotonically with increasing Pluronic™ F108 concentration as expected. The storage moduli of the two lowest Pluronic™ F108 concentration solutions, 23 and 24 wt%, exhibit some frequency dependence at the lowest frequencies probed but eventually the observed storage modulus becomes essentially constant at higher frequencies.

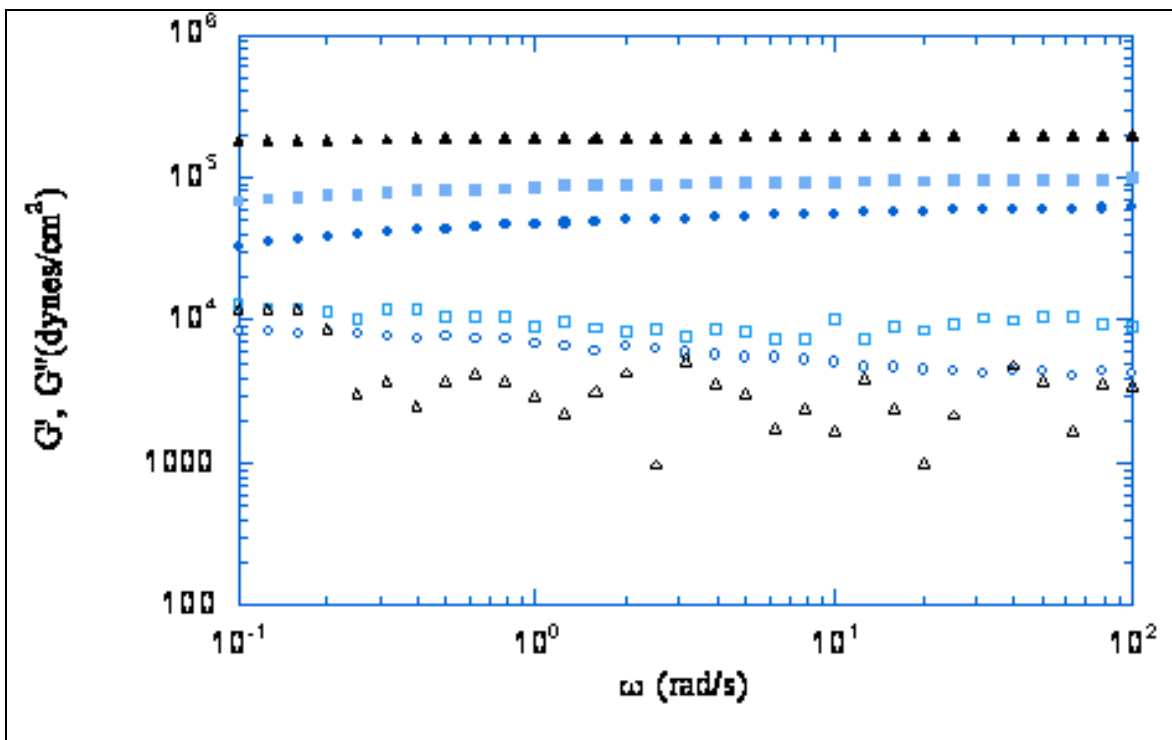


Figure 4.3: Frequency dependence of the storage and loss moduli,  $G'$  and  $G''$ , for three F108 concentrations: (●) 24%, (■) 27.5% and (▲) 40%. Filled symbols represent the storage modulus  $G'$  and open symbols represent the loss modulus  $G''$ . The storage modulus  $G'$  increases monotonically with F108 concentration and dominates the viscous moduli  $G''$  by at least two orders of magnitude.

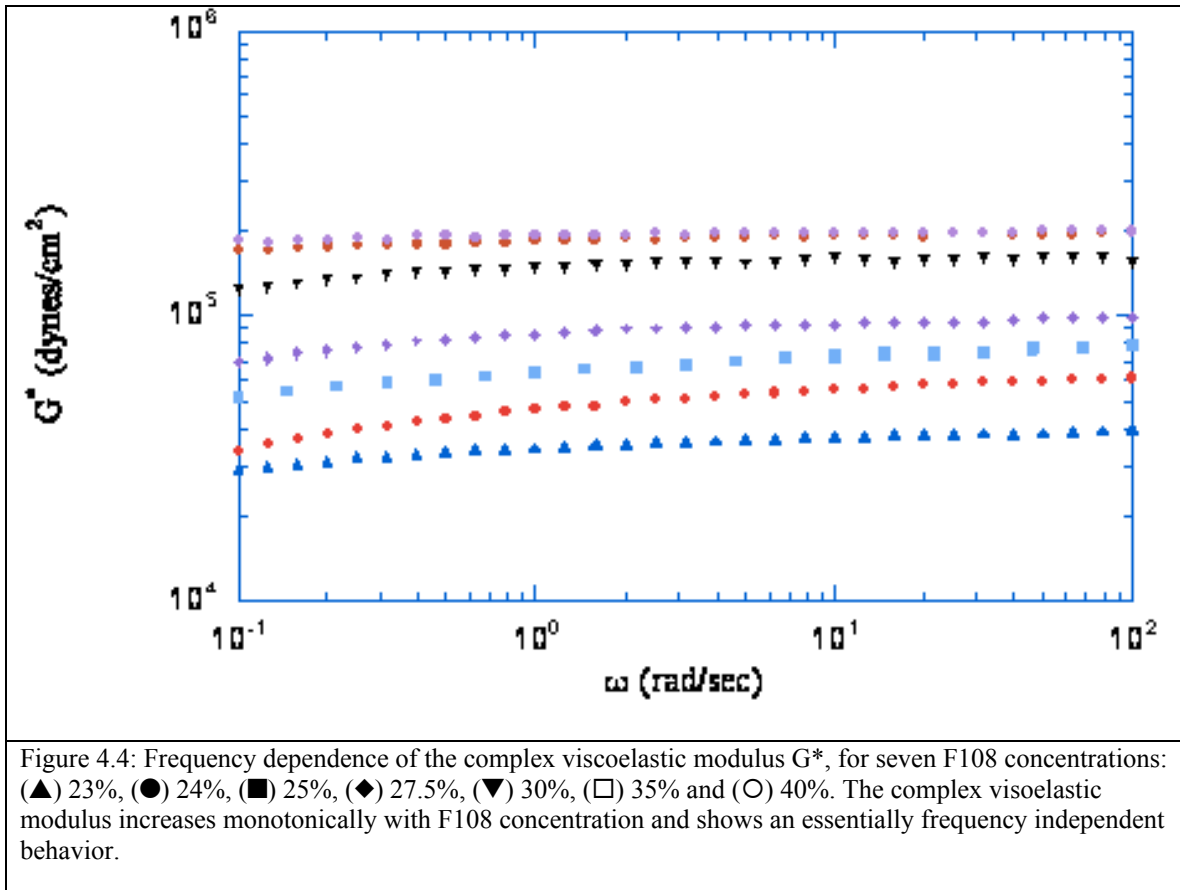
All of the higher Pluronic™ F108 concentration solutions, 25%-40 wt%, display essentially frequency independent storage moduli over the investigated frequency range. The loss moduli exhibit a slight decrease with increasing concentration. The lowest Pluronic™ F108 concentrations, 23 to 27.5 wt%, exhibit a slight decrease of the loss modulus with increasing frequency. At the higher concentrations the measured viscous moduli exhibit frequency independent behavior. This observed behavior is expected as with increasing elasticity, associated with increasing Pluronic™ F108 concentrations, the storage moduli should increase monotonically and the loss moduli should decrease monotonically with concentration. The observed frequency dependence of  $G'$  and  $G''$  at high concentrations is the expected predominantly elastic behavior typically seen for strong gels and solids (20).

The storage and loss moduli frequency dependence has been investigated, both theoretically and experimentally, for a number of ordered lattice systems (2,6,8,11-13,18,19). For the case of a soft interparticle interaction potential based on hard sphere and electrostatic interactions, Dennemann *et al* (6) have shown that the storage modulus  $G'(\omega)$  is nearly frequency independent for high and intermediate frequencies and proportional to  $\omega^2$  at lower frequencies while the loss modulus  $G''(\omega)$  is equal to  $\omega \eta$  at sufficiently high frequencies and varies as  $\omega^{-1/2}$  and  $\omega$  for intermediate and low frequencies respectively. According to this theoretical prediction, for the frequency range that is probed here, a constant  $G'(\omega)$  and a decreasing  $G''(\omega)$  should be observed. However, as has already been noted, this prediction is based on a combination of hard sphere and electrostatic interactions. Elliott and Russel (8) have developed a more applicable theoretical description based on an interparticle interaction potential model for polymerically stabilized colloids. However, this model focuses solely on the high frequency shear modulus rather than the overall frequency dependence of the storage and loss moduli. To date experimental investigations of block copolymer micellar soft crystal linear viscoelastic moduli have been extremely limited (11-13,18-20). The linear viscoelastic moduli have been observed to vary considerably with the crystal structure. Previous measurements of an aqueous BCC soft crystal formed from a (PEO)-(PBO) diblock copolymer at 40 wt% (11-13), indicate that  $G''$  is independent of frequency over 4 decades,  $G'$  is larger than  $G''$  and  $G'$  increases weakly with increasing frequency. A BCC soft crystal forming triblock copolymer, Pluronic™ (18-19), exhibits significantly different  $G'$  and  $G''$  frequency dependence. In this system  $G'$  increases and  $G''$  decreases with increasing frequency. Similar behavior was also observed for a single 35 wt% Pluronic™ F108 soft FCC crystal (18-19). Such strong frequency dependence was not observed for the linear viscoelastic moduli reported here. The behavior that is observed here is

very similar to the  $G'$ ,  $G''$  frequency dependence observed for a polystyrene-polyvinylpyridine diblock system investigated above the liquid-solid transition concentration (20). The wide variation in the linear viscoelastic behavior for these different systems may be attributable to the different crystal structures and more likely the difficulty associated with correctly measuring the linear viscoelasticity as discussed in the materials and methods section.

#### 4.4.2 Behavior of the complex viscoelastic modulus, $G^*$ .

Figure 4.4 illustrates the frequency dependence of the complex viscoelastic modulus,  $G^*$ , for all the concentrations considered. It is seen that although there is a slight frequency dependence at the low frequency end for the lowest concentrations, the complex viscoelastic modulus essentially exhibits a frequency independent behavior for almost the entire frequency range for a majority of the concentrations that have been investigated.



The complex viscoelastic modulus is also seen to increase monotonically with increasing concentration. This is expected as the storage or elastic modulus is dominating the complex viscoelastic modulus,  $G^*$ . For the case of hard sphere dispersions the elasticity scales as  $k_B T/a^3$ , where  $a$  is the lattice parameter (5). Since the lattice parameter decreases with increasing concentration ( $a^3 \sim c^{-1}$ ), the elasticity, and in turn  $G^*$ , should increase with increasing concentration. The concentration dependence of the plateau modulus is illustrated in Figure 4.5. The observed concentration dependence is much stronger than linear which may be indicative of the increasing formation of the FCC soft crystal phase as the coexistence region is traversed.

The complex modulus  $G^*$  remains essentially unchanged at the highest concentrations considered (*i.e* 35 and 40 wt%). This may be attributable to the concentration dependence of the interparticle separation.

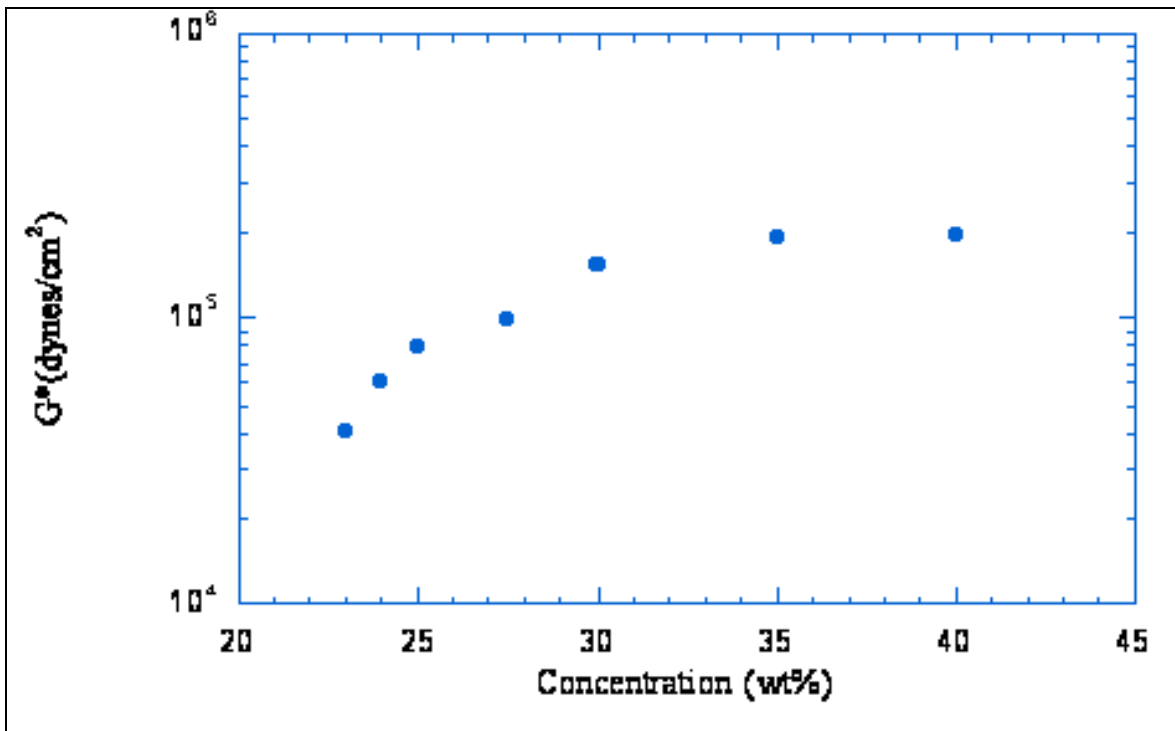


Figure 4.5: Concentration dependence of the plateau modulus. The plateau modulus shows an almost constant value for the highest concentrations probed.

Hairy particle dispersions simulations have shown that concentration dependence of the interparticle distance is considerably different for concentrations above and below the freezing concentration (7). Although the tracer microrheology studies (17) indicate a disorder-FCC transition at 22.7 %, this may indicate only an initial onset of FCC such that there are a few FCC crystal domains in an essentially disordered micellar phase. With increasing concentration the number of FCC crystal domains increases such that the true freezing concentration may be above 30 wt %. As such the interparticle concentration scaling would be different for the 35 wt% and 40 wt% concentrations. The different concentration dependence of the interparticle separation distance can be appreciated also from a packing consideration. At very high concentrations the spheres would pack more tightly, since they are deformable soft spheres, causing the hairy corona layers to compress and also to interpenetrate considerably. This tight packing would cause a weaker concentration dependence of the interparticle separation distance than that is observed at lower concentrations. A weaker concentration dependence of the interparticle separation distance would imply an essentially constant  $G'$  and hence a nearly constant value for  $G^*$ .

#### *4.4.3 Behavior of the Creep Compliance, $J(t)$ .*

Figure 4.6 illustrates the behavior of the creep compliance. At long times the creep compliance increases considerably, especially for the low concentrations (23 to 25%). The creep compliance temporal variation is somewhat diminished at the higher concentrations illustrating their greater resistance to deformation and thereby greater elasticity. At longer times the FCC soft crystal structure responds to the imposed stress by configurational rearrangement of the constitutive micellar spheres. This causes the creep compliance to increase with increasing time. The higher the concentration is, the more difficult these rearrangements become thereby causing

the creep compliance to be both lower in magnitude and to exhibit less temporal variation than the lower concentration gels (*i.e.* a much slower relaxation time). Ideally the same behavior for the creep compliance and complex viscoelastic modulus should be observed, as  $J^* = 1/G^*$ . However, it is seen that this is not observed in the concentration range considered. Although the qualitative trends are the same, quantitatively different behavior is observed. This may be attributable to the slightly different flow behaviors being accessed through the different measurements. It is seen that the  $G^*$  data exhibits a more flat profile than the creep compliance data. This indicates that the constant stress measurement carried out for measuring the creep compliance is causing the samples to flow slightly more than the dynamic sweep measurements.

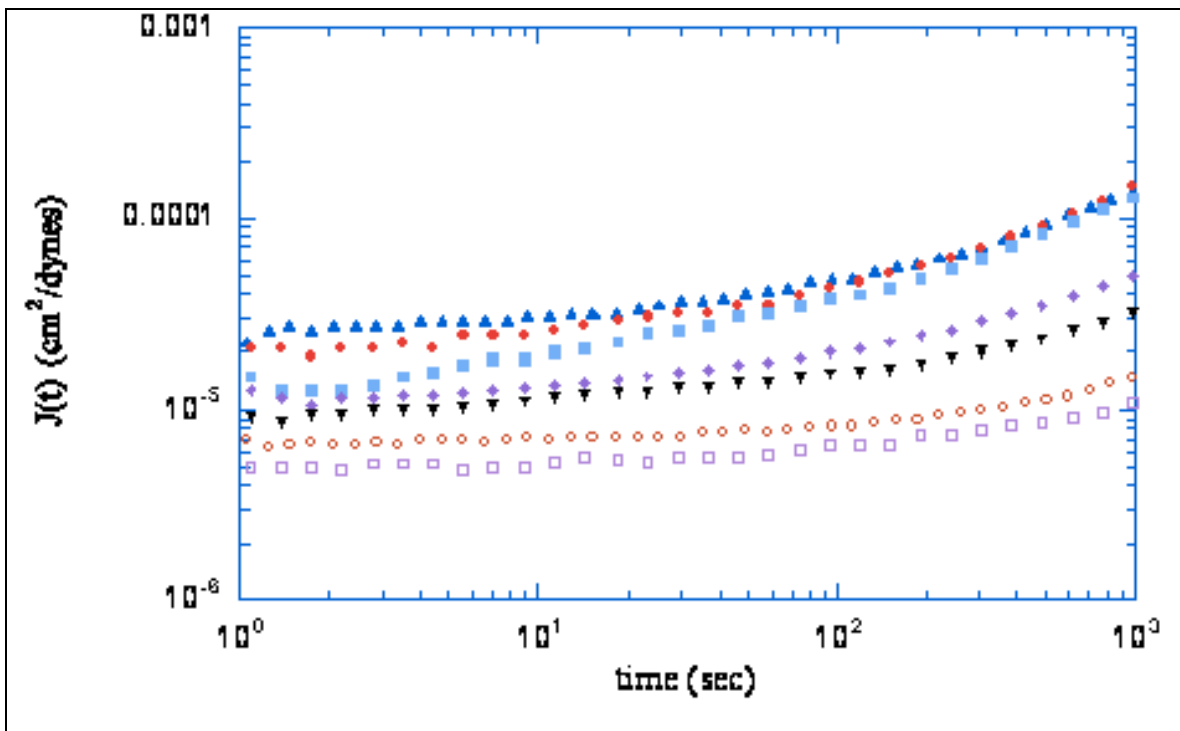


Figure 4.6: Creep compliance behavior for seven F108 concentrations: (▲) 23%, (●) 24%, (■) 25%, (◆) 27.5%, (▼) 30%, (□) 35% and (○) 40%. The creep compliance shows the same qualitative trends as the  $G^*$  behavior with concentration but does not show good quantitative agreement.

#### 4.4.4 Dynamic Viscosity Concentration Dependence.

The viscosity frequency dependence is shown in Figure 4.7 for three concentrations 24%, 27.5% and 30%. The viscosity exhibits a monotonic decrease with increasing frequency and

increases with increasing Pluronic™ F108 concentration. This behavior is qualitatively similar to the theoretical and experimental viscosity behavior observed for dense hard sphere dispersions (21).

The viscosity frequency dependence was fit with a power law (i.e.  $G''/\omega \sim \omega^\alpha$ ) in order to extract the scaling exponent  $\alpha$ . Figure 4.8 illustrates the scaling exponent concentration dependence. The scaling exponent becomes increasingly larger (less negative) with increasing concentration. Experimental Investigations on dense hard sphere dispersions have shown that both  $\alpha'(\omega)$  and  $\alpha''(\omega)$  decay as  $\omega^{-1/2}$ . Although the scaling increase observed here never reaches the  $-1/2$  value predicted for hard spheres, the intermicellar interaction potential maybe switching to a harder potential with increasing concentration.

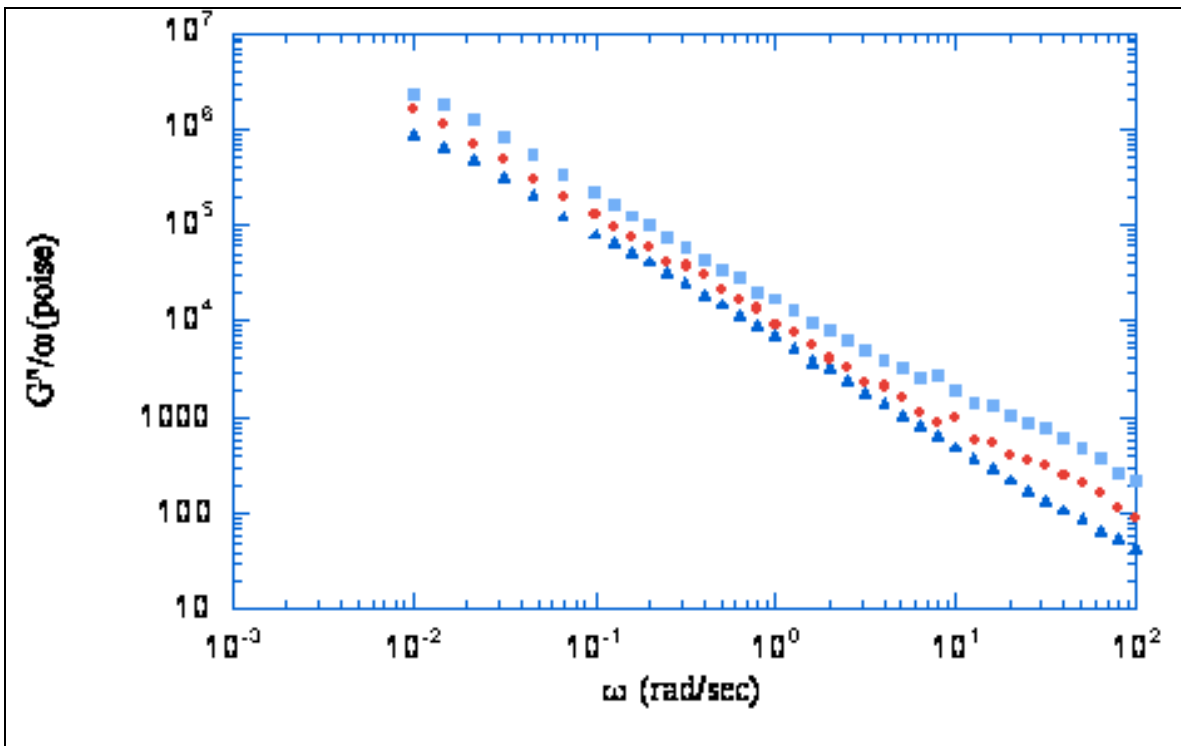


Figure 4.7: Frequency dependence of the viscosity for three F108 concentrations: (▲) 24%, (●) 27.5% and (■) 30%. The monotonically decreasing viscosity at higher concentrations is similar to the behavior observed for hard sphere dispersions.

Particle softness is related to the inverse of the interparticle interaction potential gradient  $\left[ \frac{du(r)}{dr} \right]$  (22). This local softness is of the order  $\left[ \frac{du(r)}{dr} \right] \sim \frac{k_B T}{\xi}$ , where  $\xi$  is the blob size or mean particle radius (20).

Since the mean radius is comprised of both the core radius and the corona thickness, the corona compression that occurs with increasing concentration will lead to a decrease in the mean radius and therefore  $\xi$ . The corona compression will lead to an increasing interparticle interaction potential gradient thereby yielding increasingly hard sphere like behavior.

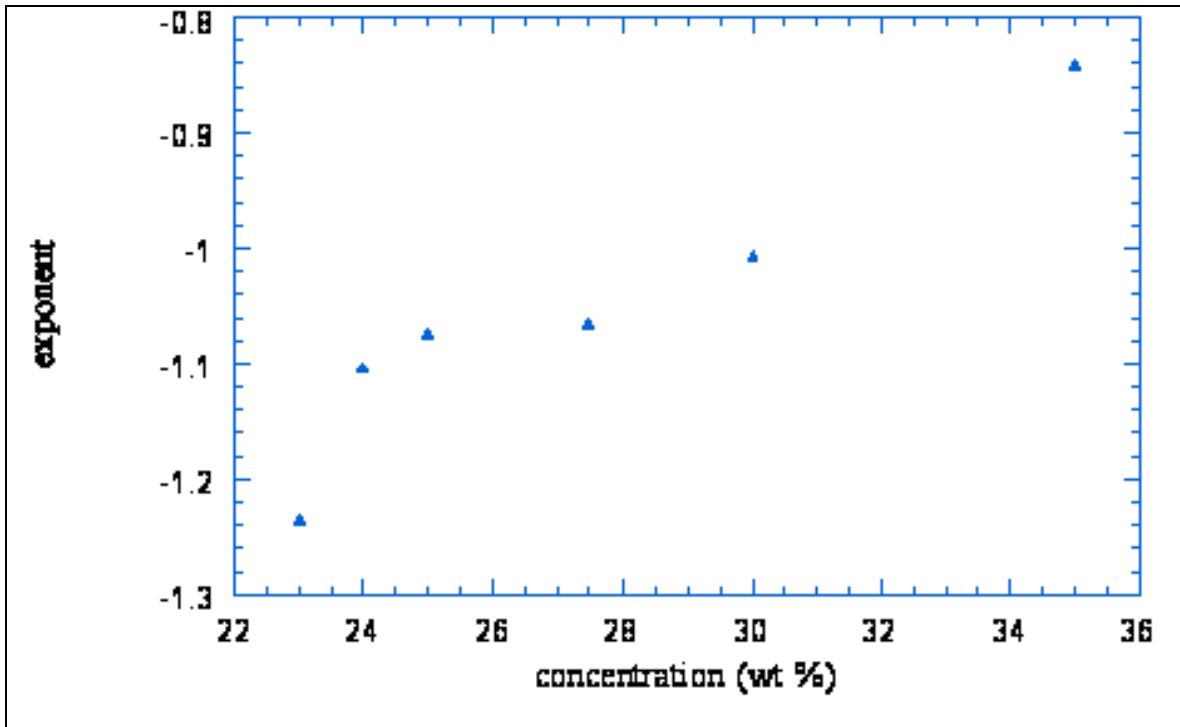


Figure 4 8: Concentration dependence of the frequency scaling exponent of the viscosity. The scaling exponent becomes increasingly larger (less negative) with increasing concentration and tends towards the hard sphere value of  $-1/2$  at the high concentrations.

#### 4.5 Conclusion

The linear viscoelasticity of aqueous Pluronic™ F108 FCC soft crystals was investigated via mechanical rheometry for a number of concentrations above the disordered micelle-FCC soft

crystal transition concentration. It was observed that the viscoelastic moduli  $G'$  and  $G''$  showed essentially a frequency independent behavior especially at the higher concentrations. This is the expected predominantly elastic behavior generally observed for solids and strongly gelled systems. The complex viscoelastic moduli  $G^*$ , which was primarily dominated by the elastic moduli, showed increasing plateau values with increasing concentrations and essentially constant values at the highest concentrations that were probed. The concentration dependence of the  $G^*$  plateau was stronger than the linear dependence typically observed for hard sphere dispersions. This deviation away from hard sphere behavior was attributed to the longer range potential present in FCC crystalline structures. The near constant values of  $G^*$  at higher concentrations was attributed to the weaker concentration dependence of the interparticle separations due to compression and interpenetration of coronal layers due to increased packing. The complex viscoelastic moduli  $G^*$  showed qualitative agreement with the creep compliance which was obtained through constant stress measurements. The quantitative disagreement was attributed to the different flow behavior accessed in the two different measurements. The observed rheological behavior indicates that micellar packing and the intermicellar interaction potential plays a dominant role-this is most clear when discussed in the context of the viscosity behavior. The viscosity frequency dependence indicates that the interparticle interactions were becoming more hard sphere in nature with increasing concentration due to compression and interpenetration of the coronal layers under tight packing conditions.

## ***References***

1. Ackerson, B.J. and Clark, N.A.; *Phys Rev A*, **1984**, 30, 806
2. Benzing D.W. and Russel W.B.; *J Colloid Interface Sci*, **1981**,83, 178
3. Chen, L.B , Ackerson, B.J. and Zukoski, C.F.; *J.Rheol*, **1994**, 38, 193
4. Lindsay, H.M. and Chaikin, P.M.; *J.Chem.Phys*, **1982**, 76, 3774
5. Mason, T.G. and Weitz, D.A. ; *Phys Rev Lett* , **1995**,75,2770
6. Denneman, A.I., Jongschapp, R.J. and Mellema, J.; *J of Chem Phys*, **1999**, 111,8182
7. Duits, M.H. Nommensen, P.A. ,van den Ende, D. and Mellema, J.;*Colloids and Surf*,  
**2001**, A183, 335
8. Elliott, S.L. and Russel, W.B.; *J.Rheol* ,**1998**, 42, 361
9. Wagner, N.J.; *J of Colloid and Interface Sci*,**1993**, 161,169
10. Van der Vorst, B., van den Ende, D. and Mellema, J.; *J. Rheol*,**1995**, 39, 1183  
Hamley, I.W., Mortensen, K., Yu, G.E. and Booth, C.; *Macromolecules*,**1998**,  
31,6958  
Hamley, I.W., Pople, J.A., Fairclough, J.P., Ryan, A.J., Booth, C. and Yang, Y.W.;  
*Macromolecules*,**1998**, 31,3906
13. Hamley, I.W., Daniel, C. and Mingvanish, W.; *Langmuir*, **2000**,16, 2508
14. Pople, J.A., Hamley, I.W., Fairclough, J.P. and et al.; *Macromolecules*,**1997**, 30,5721
15. Molino, F.R., Berret, J.-F., Porte, G., Diat, O. and Lindner, P.; *Eur. Phys.*  
*J.B*,**1998**,3:59
16. Alexandridis, P., Nivaggioli, T. and Hatton, A.T.; *Langmuir*,**1995**,11, 1468
17. Amin, S. and van Zanten, J.H.; (*in preparation*)
18. Eiser, E., Molino, F. and Porte, G.; *The European Physical Journal*,**2000**,E 2,39

19. Eiser, E., Molino, F., Porte, G. and Pithon, X.; *Rheol Acta*, **2000**,39,201
20. Buitenhuis, J. and Forster, S.; *J Chem Phys*,**1997**, 107,262
21. Van der Werff ,J.C., de Kruif, C.G., Blom, C. and Mellema, J.; **1989**,
22. Hensen, J.P., and McDonald, I.R.; *Theory of Simple Liquids*, London **1986**

## Chapter 5

### A Tracer microrheology study of a Triblock Copolymer in the Cubic Crystalline Phase

---

#### *5.1 Abstract*

This chapter details a comprehensive tracer microrheology investigation of the triblock copolymer Pluronic™ F108, which forms an FCC crystalline phase at high concentrations and at room temperature. In order to investigate the changes in the viscoelastic response of the system associated with changes in microstructure, tracer microrheology measurements are carried out over a wide range of Pluronic F108 concentrations varying from 3 to 35 wt %. As the technique allows observation of the viscoelastic behavior over a wide frequency range, a wide variety of interesting dynamical behavior is observed with changing microstructure, advocating the utility of the technique as a sensitive probe of microstructural changes. The mean squared displacements exhibits a dramatic change in the temporal variation at about 22.7wt% indicating the probable onset of the FCC crystalline phase. The complex viscoelastic modulus indicates that the system is essentially viscous when in the isotropic micellar solution phase and increasingly elastic with increasing order in the FCC soft crystalline phase. Tracer microrheology underestimates the complex viscoelastic modulus plateau modulus (overestimates the creep compliance) compared with mechanical measurements for all the concentrations investigated. Sphere size sweeps conducted on three different concentrations exhibits increasing disagreement between the creep compliance extracted with different sphere sizes as the Pluronic™ concentration is increased. This is indicative that either longitudinal dynamic modes or

structural heterogeneities may be causing the tracer microrheology data to underestimate the complex viscoelastic modulus plateau modulus (overestimate the creep compliance)

## **5.2 Introduction:**

The utility of tracer microrheology has already been discussed in the context of polyethylene oxide solutions. To re-iterate, tracer microrheology techniques are gaining wide recognition due to the ability of such methods to probe the viscoelastic properties of complex fluids over a wide frequency range and through the application of very small strains. As a result a large number of tracer microrheology studies have been undertaken (1-29). As discussed previously these studies have primarily focused on simple polymeric systems, namely biopolymers such as DNA and actin filament solutions. The investigations provided deeper insight into the short time dynamics of these systems. These actin filament studies were particularly interesting as actin filaments can be treated as model semi-flexible polymers.

The most notable feature which emerged from these earlier investigations was the ability to accurately extract the viscoelastic moduli through use of the generalized Stokes-Einstein equation (1):

$$J(t) = \frac{a}{k_B T} \langle \Delta r^2(t) \rangle \quad (1)$$

This was evidenced through good quantitative agreement between the viscoelastic modulus extracted from the tracer microrheology technique and that obtained from the mechanical rheometry measurements. Levine and Lubensky (15-17) have shown that the longitudinal compression modes affect the extracted viscoelastic parameters below a certain characteristic

frequency. Aqueous PEO solutions behave as good solvent systems at room temperature. This indicates that the osmotic modulus for the system should be very high, thus diminishing the influence, if any, of concentration fluctuation induced longitudinal modes on the Brownian motion and any extracted dynamical moduli. Osmotic compressibility is also not expected to play a role in the case of the actin filament network.

It has been noted previously that one of the main objectives of this experimental study was to gain a better understanding of Brownian motion in viscoelastic media. As such, one aim was to carry out tracer microrheology studies of a system exhibiting widely varying microstructure. The Pluronic™ class of triblock copolymers was chosen as it exhibits interesting microstructural changes with ranging concentration, sometimes changing from an isotropic micellar solution to a soft micellar crystal. From an experimental standpoint it was chosen because it was not expected to pose significant experimental complexities. Since the Pluronic™ triblock copolymer consists of a PEO block on each end and the PEO system by itself did not exhibit any experimental complexities, it was expected that the PEO-PPO-PEO system should not also present any experimental complexities, such as tracer aggregation.

### ***5.3 Materials and Methods:***

Pluronic™ F108 was obtained from BASF Corporation and used without further purification. Dust free Pluronic™ F108 aqueous solutions were prepared with deionized water that had been filtered through a 0.02  $\mu\text{m}$  filter (Whatman-Anotop 25). Polystyrene latex spheres having sulfate groups on the surface and ranging in size from 0.195 to 1.55  $\mu\text{m}$  in diameter were utilized as optical probes (Duke Scientific, Palo Alto, CA). The optical probes were typically dispersed in the Pluronic™ solutions at about 1 vol%. All of the tracer microrheology samples

were examined with optical microscopy to ensure that the optical probes were not aggregated. All samples were prepared at room temperature (25 °C) and then cooled down to 5°C and then transferred to flat sided 10 mm thick spectrophotometric cells for diffusing wave spectroscopy measurements (Spectrocell, Oreland, Pa). All samples were allowed to equilibrate for two weeks prior to taking measurements.

### 5.3.1 Diffusing Wave Spectroscopy

Point-point transmission mode diffusing wave spectroscopy (DWS) was utilized to monitor the tracer probe motion (30). The beam from a diode pumped solid state (DPSS) Nd-YAG laser operating at a wavelength of 532 nm *in vacuo* was incident upon a flat scattering cell, containing the Pluronic™ F108 solution and spherical optical probes. An ALV SI/SIPD photon detector collects the multiply scattered light via a single mode optical fiber. In order to ensure point-point geometry, the single mode optical fiber has a gradient refractive index (GRIN) lens, with a very narrow angle of acceptance, attached to it. In addition, a polarizer with horizontal acceptance is placed before the optical fiber to ensure that only multiply scattered light is detected from the vertically polarized incident beam. The ALV SI/SIPD photon detector signal is fed into a ALV fast digital correlator operating in the cross correlation mode to minimize the effects of afterpulsing and deadtime correction.

The measured intensity auto correlation function was converted into the electric field autocorrelation function via the Siegert relationship. The electric field autocorrelation function obtained from a DWS measurement can be related to the mean square displacement through:

(30)

$$g_1(t) = \int_0^{\infty} P(s) \exp\left[-\frac{1}{3} k_0^2 \langle r^2(t) \rangle \frac{s}{l^*}\right] ds \quad (2)$$

where  $g_1(t)$  is the electric field autocorrelation function,  $P(s)$  is the scattering path length distribution function,  $k_0$  is the wave vector,  $\langle \square r^2(t) \rangle$  is the particle mean squared displacement and  $l^*$  is the distance over which light becomes completely randomized. The mean squared displacement of the spherical tracer probes was extracted pointwise from the electric field autocorrelation function through a bisection root searching algorithm. It should be noted that while in DLS the length scale over which particle motion is probed can be adjusted by varying the scattering angle, in DWS the length scale over which the motion is probed is primarily adjusted by varying the cell thickness  $L$ . Most importantly, owing to multiple scattering nature of DWS the technique is capable of resolving *angstrom*-scale particle motions and, therefore, short time dynamics.

In tracer microrheology the viscoelastic shear modulus of the fluid is typically obtained from the mean squared displacement through use of the generalized Stokes Einstein relation (GSER) equation (1)

$$\langle \tilde{r}^2(s) \rangle = \frac{k_B T}{\square s a \tilde{G}(s)} \quad (3)$$

where  $\langle \tilde{r}^2(s) \rangle$  is the Laplace transform of the tracer particle mean squared displacement,  $a$  is the tracer particle radius and  $\tilde{G}(s)$  is the viscoelastic shear modulus. The generalized Stokes-Einstein equation is based on the assumption that the complex fluid can be treated as a continuum around the tracer sphere (1). The GSE equation also assumes that the Stokes relation for viscous fluids can be extended to describe the viscoelastic drag on a sphere at all frequencies. The GSE equation was utilized to extract the creep compliance data. The creep compliance is extracted from:

The creep compliance is utilized as its calculation does not involve any transformation from the time domain to the frequency domain. The complex viscoelastic modulus was obtained by fitting the creep data to a modified Voigt model allowing for purely viscous dissipation at very long times and obtaining a retardation spectrum from it.

### ***5.3.2 Mechanical Rheometry:***

Details of the mechanical rheometry measurements on the Pluronic™ F108 system are presented in Chapter 2 (Mechanical Rheology of a Triblock copolymer in the cubic crystalline phase).

## ***5.4 Results and Discussion:***

### ***5.4.1 Evolution of the Mean Squared Displacement:***

It was noted previously that small angle x-ray scattering and phase behavior studies of the F108 system have shown that the system passes from a fluid isotropic micellar solution into a solid like FCC cubic crystalline phase at sufficiently high concentrations (31 to 33). In order to observe the microstructural transitions and viscoelastic response associated with this phase change, tracer microrheology measurements were carried out in which the Pluronic™ F108 concentration was varied from 3 to 35 wt %. However, since the main objective of the study was to focus on the FCC cubic crystalline phase, mechanical rheometry measurements were limited to Pluronic™ concentrations that were in the crystalline phase. Another reason for limiting the comparative study to the crystalline region was due to the limitations of the available mechanical rheometers to accurately measure viscoelastic properties of fluids exhibiting sufficiently low viscosities.

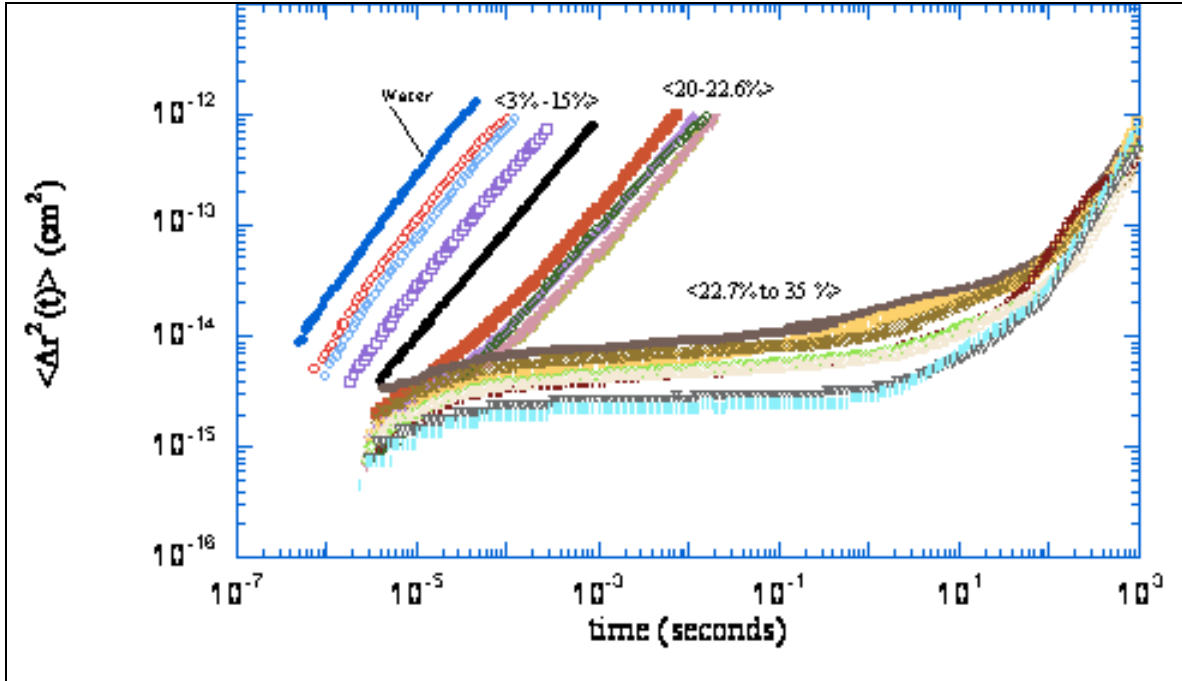


Figure 5.1: Evolution of the  $\langle \Delta r^2(t) \rangle$  time trace for a series of pluric concentrations: (⊙) 3% (-) 5% (□) 10% (●) 15% (■) 20% (◆) 21% (▲) 22% (▼) 22.5% (○) 22.6% (○) 22.7% (□) 23% (X) 23.5% (+) 23.7% (□) 24% (Δ) 25% (□) 30% and (l) 35%. The evolution of the  $\langle \Delta r^2(t) \rangle$  time trace indicates a microstructural change at about 22.7%.

Probe motion becomes slower with increasing Pluronic™ F108 concentration as seen from the  $\langle \Delta r^2(t) \rangle$  temporal variation. This is expected as the solutions are becoming more viscous with increasing concentration. The lowest F108 concentrations probed 3%-15% have essentially the same shape as the water  $\langle \Delta r^2(t) \rangle$  time trace and shows an essentially diffusive behavior. The  $\langle \Delta r^2(t) \rangle$  temporal variation however starts to change significantly at 20 wt% deviating from purely diffusive behavior. All the samples from 20 to 35wt% exhibit a very similar power law dependence at short times. In this concentration range,  $\langle \Delta r^2(t) \rangle \sim t^{0.6}$ , for  $t \leq 10^{-5}$  s. This indicates that at these short times the probes are sampling the same dynamics regardless of Pluronic™ F108 concentration. Since the plateau onset has not occurred at these short times, this subdiffusive behavior can be attributed to the probes sensing either dynamics

intrinsic to individual micelles themselves. The probe radius  $R$  to intermicellar distance  $d$ ,  $R/d > 1$  for all Pluronic solutions having concentrations greater than 20%. This short time behavior can be further explored on rescaling  $\langle \square r^2(t) \rangle$  with concentration. The  $\langle \square r^2(t) \rangle$  was rescaled with the Pluronic™ F108 concentration dependence of the high frequency modulus. Figure 5.2 (a) illustrates the re-scaled behavior. Although the rescaling does tend to collapse the 20 to 22.6% and 22.7 to 35% separately, a complete collapse of the data is not observed in each of these two concentration regimes. This can be attributed to the re-scaling concentration exponent utilized. The high frequency data, as will be discussed later, cannot adequately be described with a good power law fit due to the limited number of experimental points and the concentration dependence. The re-scaled  $\langle \square r^2(t) \rangle$  at very short time scales ranging from  $10^{06} < t < 10^{04}$  however does seem to collapse considerably at the very short time scales (figure 5.2b), again giving credence to the fact that the probes are experiencing essentially the same dynamical phenomena at these very short time scales.

A dramatic change in  $\langle \square r^2(t) \rangle$  temporal variation is observed for concentrations  $\geq 22.7\%$ . The mean squared displacement exhibits subdiffusive motion at the earliest times, followed by an almost time independent plateau and finally final diffusive escape. This behavior indicates that the FCC soft crystal begins forming at 22.7 wt% Visual inspection of the samples at these concentrations also indicates their essentially solid like character.  $\langle \square r^2(t) \rangle$  temporal variation reflects the microstructural state of the suspending media. For the low concentrations, from 3 to about 15 wt%, the solutions consists of essentially disordered micelles (CMC is 2 wt% at 25°C (34)). As such the  $\langle \square r^2(t) \rangle$  behaves as if the probes are dispersed in a viscous liquid, giving rise to the nearly linear time dependence of  $\langle \square r^2(t) \rangle$ . Upon increasing concentration to

22.6 wt%, the micelles begin to interact much more strongly and at short times  $\langle \Delta r^2(t) \rangle$  reflects the increasingly elastic nature of the micellar dispersion. Finally at sufficiently large concentrations, the micellar dispersion orders into an FCC soft crystal. Under these conditions,  $\langle \Delta r^2(t) \rangle$  increases sub diffusively at short times, begins to 'feel' the elastic structure, thereby exhibiting a plateau and eventually at sufficiently long times, the probe 'escapes' from the micellar cage and begins to diffuse as the soft crystal has relaxed completely by micellar rearrangement.

#### ***5.4.2 Zero shear viscosity concentration dependence***

The state of the suspending media can be further understood on extracting the zero shear viscosity from the tracer microrheology data. Since the complex viscoelastic moduli is extracted from the creep compliance through use of a Voight model, the linear portion of the model fit contains the zero shear viscosity. The concentration dependence of the zero shear viscosity is illustrated in Figure 5.3. The viscosity concentration dependence exhibits the qualitative behavior expected for colloidal dispersions. The viscosity increases up to a concentration of 22 wt% where it begins to increase sharply at the onset of the FCC soft crystal phase. From 3 to 15 wt% it appears that the viscosity can be modeled as a virial expansion in the concentration (36).

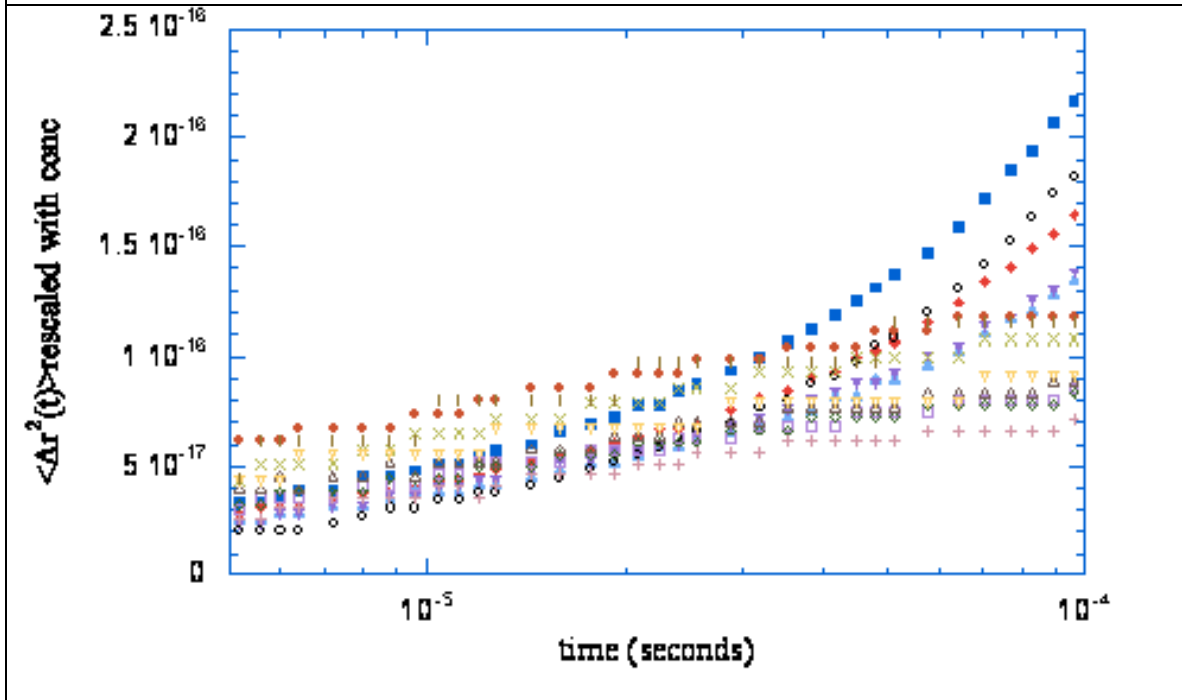
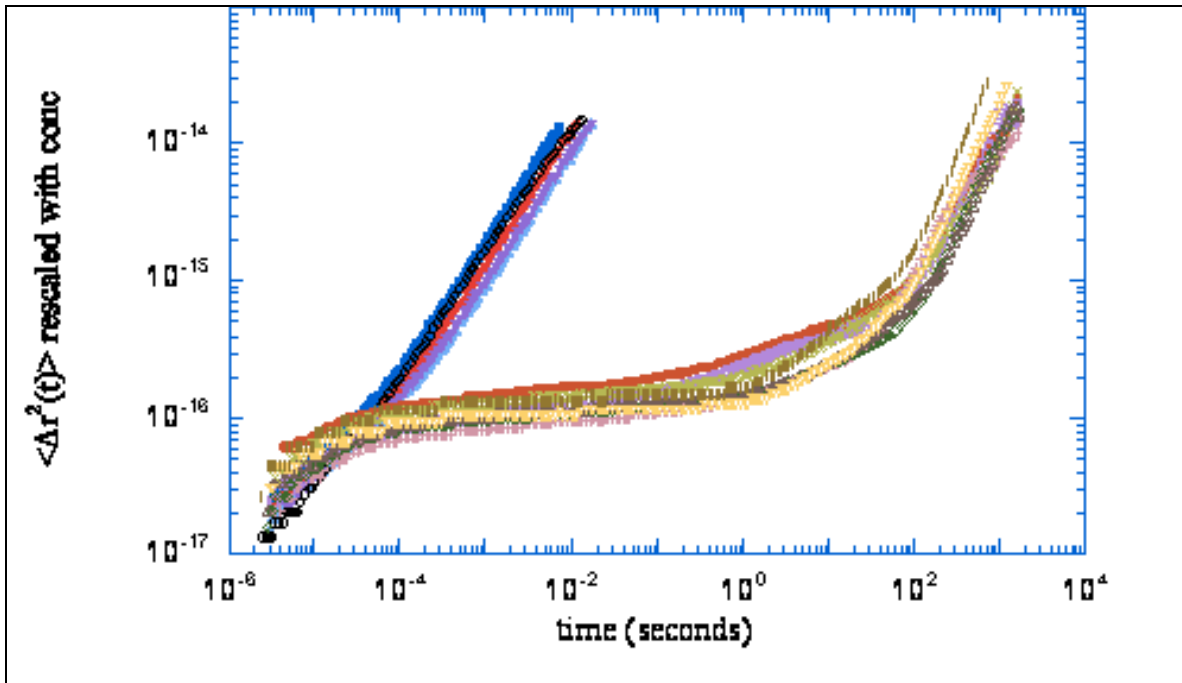


Figure 5.2: (a) Variation of the rescaled  $\langle \Delta r^2(t) \rangle$  with time. The  $\langle \Delta r^2(t) \rangle$  was re-scaled with concentration in order to explore a possible collapse of the data. Although a certain degree of collapse is observed a complete collapse is not. Figure b shows the rescaled behavior at very short time scales. Concentrations shown: (■) 20% (◆) 21% (▲) 22% (▼) 22.5% (○) 22.6% (●) 22.7% (□) 23% (X) 23.5% (+) 23.7% (◻) 24.5% (◻) 30% and (l) 35%.

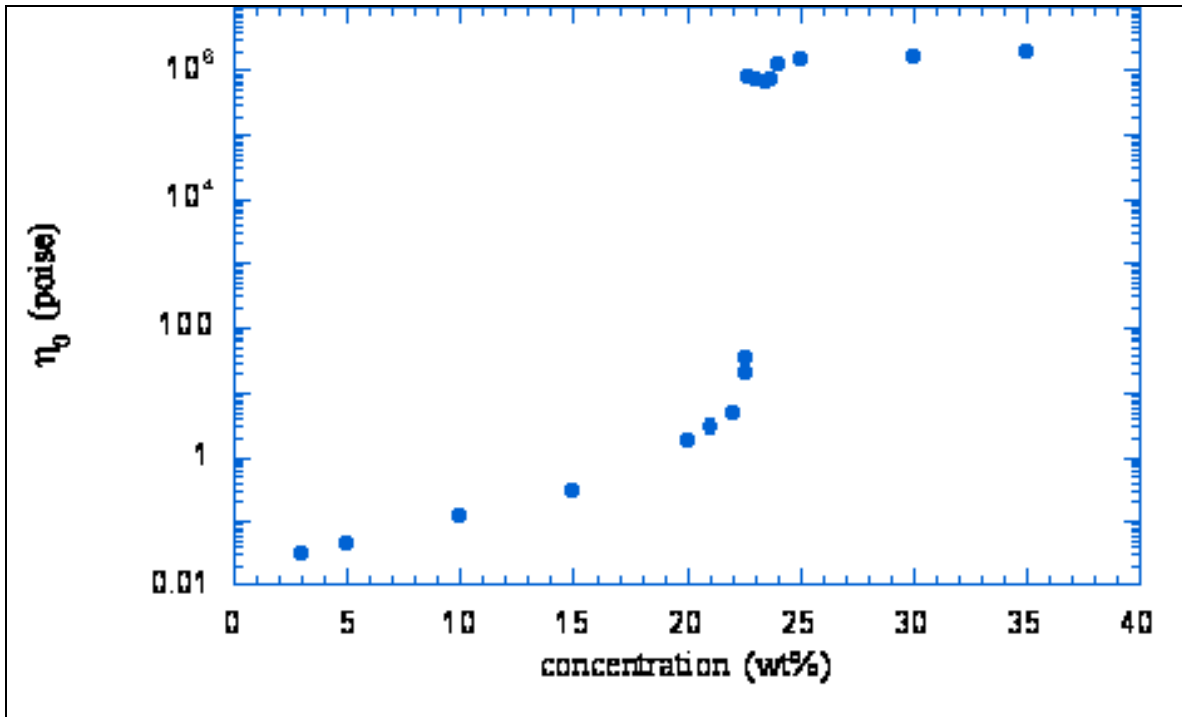


Figure 5.3: variation of the (●) zero shear viscosity with Pluronic F108 concentration. The zero shear viscosity increases upto 22wt%, where it begins to increase sharply at the onset of the FCC soft crystal phase.

However upon observing the overall behavior from 3 to 22 wt%, it was believed that the zero shear viscosity could be modeled by the following form of the Krieger-Dougherty equation (37):

$$\frac{\eta_0}{\eta} = \frac{\eta_0}{\eta_c} \left( \frac{\eta_c}{\eta} \right)^{\frac{[\eta]_0}{[\eta]_c}} \quad (4)$$

where  $\eta$  is the dispersion volume fraction  $\eta_c$  is the critical packing volume fraction. This relationship is supposed to be valid for the entire concentration range. However, this does not describe the zero shear viscosity data from 3 to 22 wt%. This maybe attributable to the fact that the above relationship is valid for purely hard sphere dispersions. As has been discussed previously it is believed that the interparticle interaction potential in this system is probably intermediate between hard and soft sphere potentials.

The initial increase with concentration up to 22 wt% is due to an increase in the number of micelles. This causes an increasing disturbance of flow, leading to a subsequent viscosity increase. At 22.5-22.6% the micellar dispersion begins to change from an isotropic solution to a FCC soft crystal, thereby causing a sharp increase in the viscosity. Finally at the highest concentrations probed, the micell coronas are further compressed with increased concentration leading to a slowly increasing viscosity.

#### **5.4.3 Evolution of the time dependent diffusion coefficient $D(t)$ :**

The nature of the suspending micellar dispersion can be further further explored via the time dependent diffusion coefficient  $D(t)$ , as illustrated in Figure 5.4. The time dependent diffusion coefficient is defined as:

$$D(t) \equiv \frac{\langle \Delta r^2(t) \rangle}{6t} \quad (5)$$

$D(t)$  provides a measure of the deviation away from purely diffusive behavior. The lowest concentrations probed, ranging from 3 to 15 wt% exhibit nearly the same behavior.  $D(t)$  is essentially time independent and becomes smaller with increasing concentration as the viscosity increases. The lowest concentration of 3 wt% has a  $D(t)$  value which is lower than  $D_0$  of water,  $4.5 \times 10^{-9}$  cm<sup>2</sup>/sec. This is due to the increased viscosity as originally described by Einstein. Since the probe size is much larger than the micelle size and intermicellar separation distance, its motion is hindered with respect to that expected for pure water. As the concentration increases,  $D(t)$  decreases further due to the viscosity increase resulting from increased micelle interactions. At early times, subdiffusive motion is observed for the more concentrated 20-22.6% solutions owing to the onset of elasticity, with the diffusion coefficient eventually becoming time independent  $D(t)$  is very temporal in nature for the case of FCC soft crystal phase ( $\geq 22.7\%$ ). The probes now become elastically bound by a 'cage' formed by the

micelles. In order to gain an understanding of the relationship between the time dependent diffusion coefficient and the local displacement of the microsphere,  $D(t)$  is plotted as a function of  $\langle \Delta r^2(t) \rangle$  (Figure 5.5) It is seen that for the lowest concentration regime of 3 to 15 wt%,  $D(t)$  remains essentially unchanged. This indicates that the probes essentially feel the same resistance at all displacements. For the intermediate concentration regime of 20 to 22.6 wt%,  $D(t)$  decreases progressively with time and comes to an almost constant value

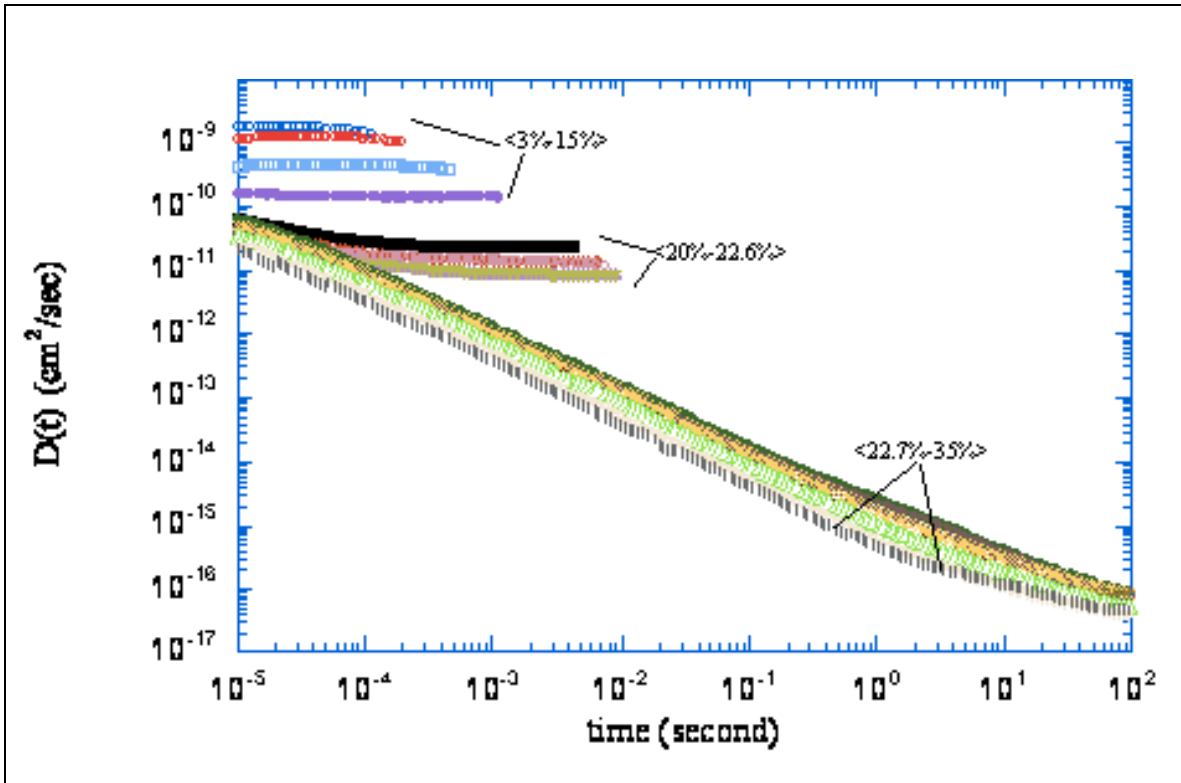
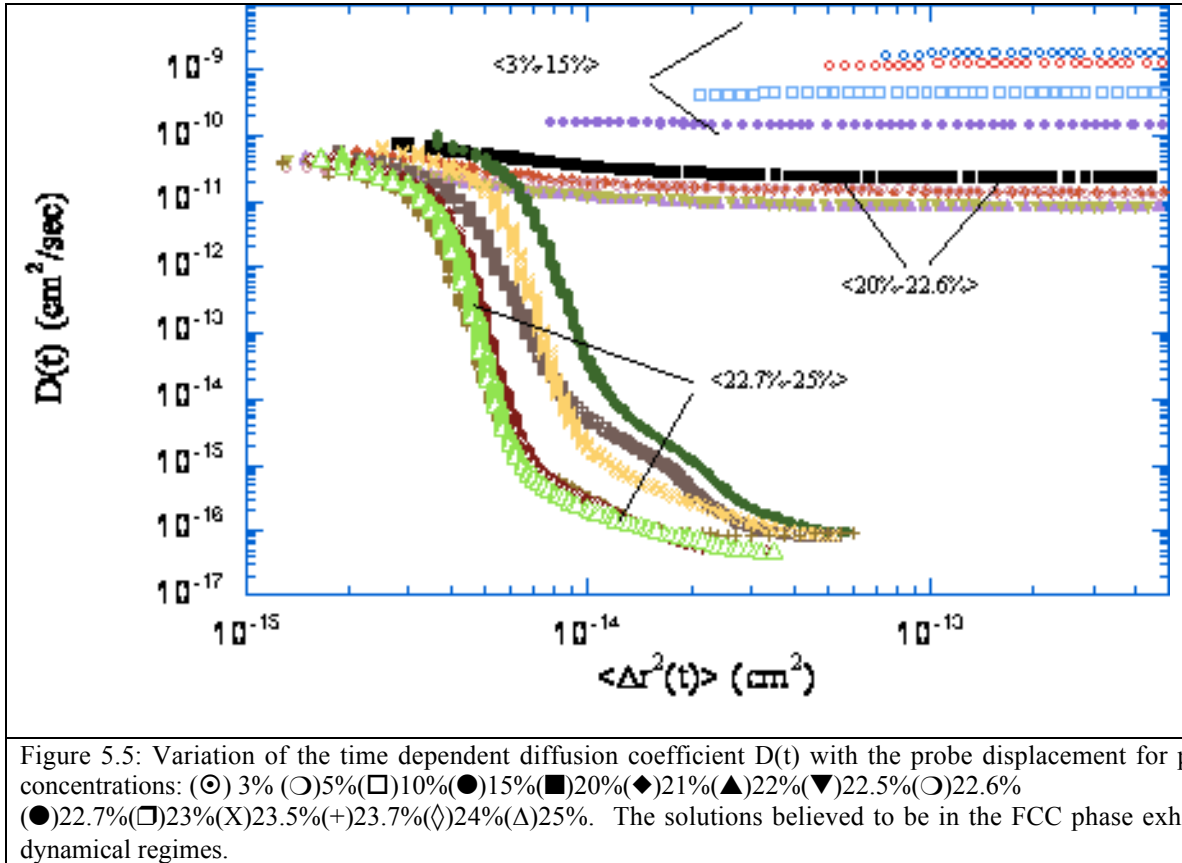


Figure 5.4: Evolution of the time dependent diffusion coefficient  $D(t)$  for Pluronic F108 samples having Concentrations : (⊙) 3% (○) 5% (□) 10% (●) 15% (■) 20% (◆) 21% (▲) 22% (▼) 22.5% (○) 22.6% (●) 22.7% (□) 23% (X) 23.5% (+) 23.7% (□) 24% (Δ) 25% (□) 30% and (l) 35% The diffusion coefficients shows time traces for isotropic micellar solutions and for samples in the FCC cubic phase

This indicates that the increasing micellar crowding gives rise to a certain degree of elastic trapping of the probes. The most striking behavior is observed for the highest concentration regime from 22.7 wt% onwards when the system is believed to be in the FCC soft crystalline phase. Two distinct dynamical regimes can be observed. A sort near-plateau at short

length scales, and then a sharp downward transition past a characteristic crossover length scale. This is due to the probes experiencing the caging effect of the micelles. The crossover length scale is seen to shift to shorter lengths with increasing concentration. This is probably due to the probes beginning to feel the caging effects at smaller displacement with increasing concentration



**5.4.4 Complex viscoelastic modulus frequency dependence:** The complex viscoelastic modulus was obtained from the creep compliance using a procedure introduced by Mason and coworkers in which the creep data were fitted to a Voigt model and the retardation spectrum was obtained (9). Through use of the retardation spectrum the complex viscoelastic moduli is computed (see Figure 5.6). The lowest concentrations exhibit an essentially viscous response having nearly a linear frequency dependence for the entire frequency range. The concentrations 20 to 22.5 wt%

have an almost linear frequency dependence but not over the entire frequency range. They do exhibit some elasticity at high frequencies. This indicates once again that for these intermediate concentrations the probes essentially experience two types of viscoelasticity. At low frequencies,  $G^*$  reflects the overall micellar dispersion viscosity and at higher frequencies  $G^*$  shows signs of an elastic component. After the onset of the FCC soft crystal phase almost all the samples exhibit a very similar behavior, in that at very low frequencies (up to  $10^{-2} \text{ s}^{-1}$ )  $G^*$  is essentially lossy followed by an elastic plateau at higher frequencies. The plateau modulus increases essentially monotonically with increasing concentration. This is expected as the storage or elastic modulus is dominating the complex viscoelastic modulus,  $G^*$ .

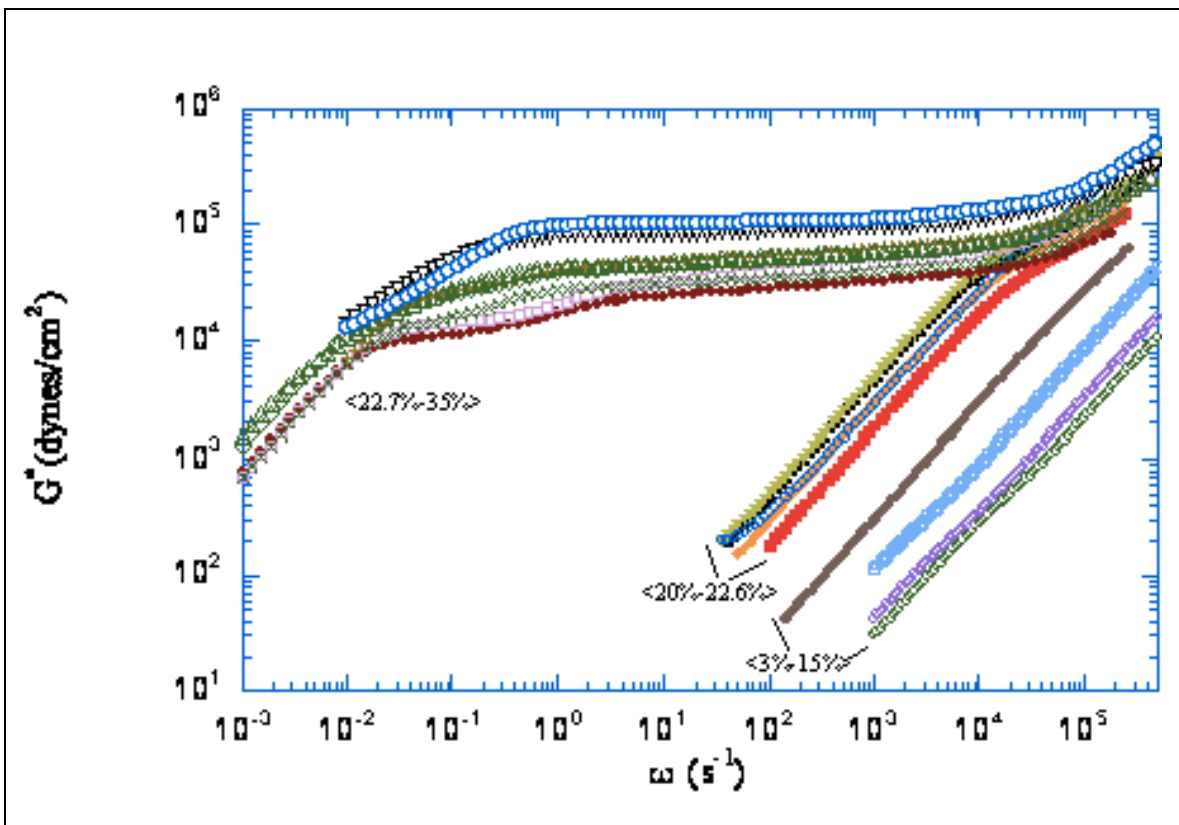


Figure 5.6: Frequency dependence of the Complex viscoelastic modulus for pluronic F108 samples having concentrations: : (⊙) 3% (○) 5% (□) 10% (●) 15% (■) 20% (◆) 21% (▲) 22% (▼) 22.5% (○) 22.6% (●) 22.7% (□) 23% (X) 23.5% (+) 23.7% (□) 24% (Δ) 25% (□) 30% and (l) 35% The samples in the FCC phase tend to exhibit high elasticity.

For hard spheres, the elasticity is predicted to scale as  $k_B T/a^3$ , where  $a$  is the lattice parameter (35). Since the lattice parameter decreases with increasing concentration ( $a^3 \sim c^{-1}$ ), the elasticity, and in turn  $G^*$ , should increase with increasing concentration. It should however be pointed out at this stage, that on examining the concentration dependence of the high frequency elastic modulus, it was seen that the elastic modulus actually has a much stronger concentration dependence than that predicted for hard spheres. The high and intermediate frequency dependence has been discussed extensively in the context of possible intermicellar interaction potentials (chapters on Pluronic high frequency behavior and mechanical rheometry). The reader is referred to these chapters for an in depth look at the frequency dependence. The  $\langle r^2(t) \rangle \sim t^{0.6}$  scaling observed in the mean squared displacement for samples having concentrations ranging from 20 to 35 wt% manifests itself as  $G^* \sim \phi^{0.6}$ . As the elasticity is increasing with concentration, it is expected that the terminal time should be affected by concentration. It is actually observed that the terminal times do move to longer times with increasing concentration. The largest difference is seen to be for the two highest concentrations of 30 and 35 wt%. This may be because the system is purely in the FCC soft crystal phase, while for lower concentrations it may be in the two phase region.

**5.4.5 Viscosity Frequency Dependence:** The zero shear viscosity concentration dependence further illustrates the microstructural transitions the Pluronic™ F108 system undergoes. In order to observe the viscosity frequency dependence,  $G''/\omega$  was extracted for each investigated concentration and plotted versus frequency (Figure 5.7). As expected, at the lowest concentrations, viscous liquid like samples exhibit frequency independent behavior. The intermediate concentrations (20 to 22.5 wt%) indicate the

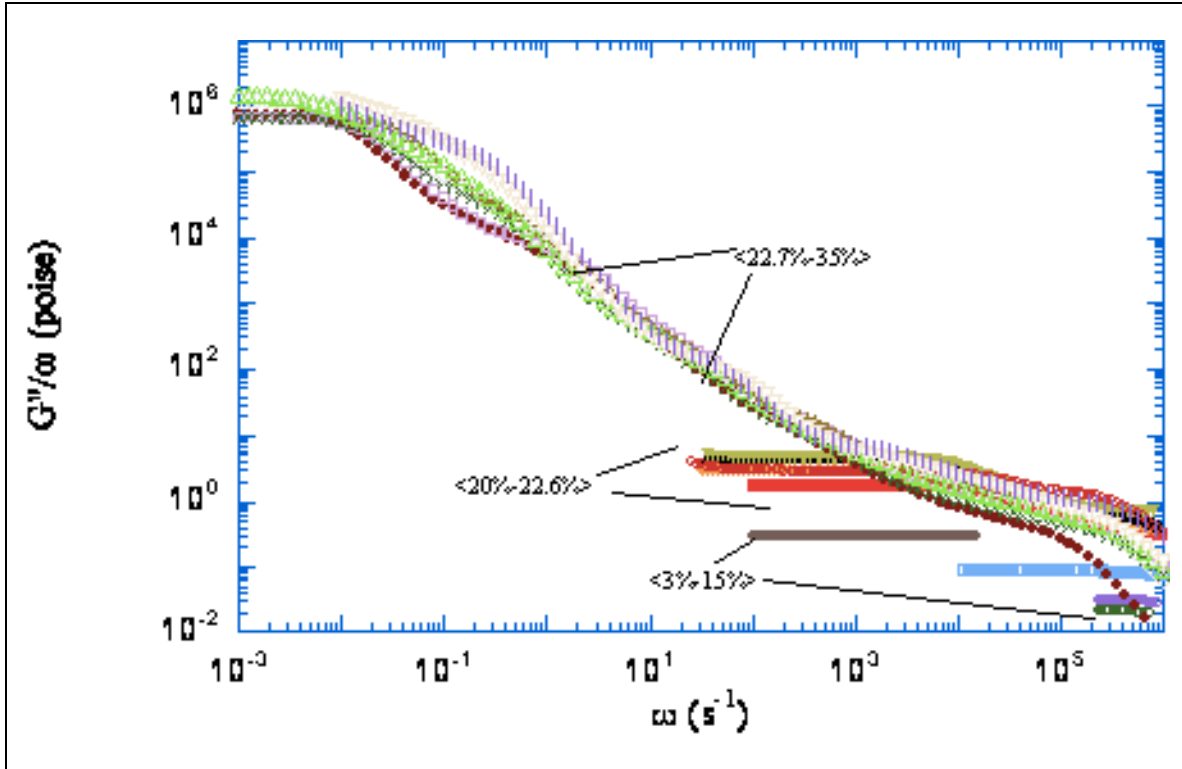


Figure 5.7: Frequency dependence of the viscosity for a series of Pluronic F108 samples in which the concentrations were: (⊙) 3% (○) 5% (□) 10% (●) 15% (■) 20% (◆) 21% (▲) 22% (▼) 22.5% (○) 22.6% (●) 22.7% (□) 23% (X) 23.5% (+) 23.7% (□) 24% (Δ) 25% (□) 30% and (l) 35%. The viscosity value is higher than the viscosity value even at the highest concentration.

onset of elasticity via a slight frequency dependence at high frequencies. The FCC soft crystal phase samples all essentially exhibit the same frequency dependency. A notable point about the frequency dependent viscosity is its high frequency behavior. It is observed that the viscosity is always larger than the water viscosity value. Ideally systems, at very short times, should exhibit a viscosity value close to that of water. However, this may occur at frequencies  $> 10^6$ .

The drastic changes in the viscoelastic response of the Pluronic™ F108 system as the microstructure changes from an isotropic micellar solution to a FCC soft crystal can be further appreciated on examining the frequency dependence of the storage and loss moduli,  $G'$  and  $G''$ . Figure 5.8 illustrates the viscoelastic moduli behavior for three Pluronic concentrations, 15, 20

and 35 wt%. At 15 wt% the solution is an isotropic micellar solution. The behavior is that typically observed for a viscous liquid. The system is dissipating more energy than it is storing, causing the loss modulus to dominate over the storage modulus the entire frequency range examined. The 20 wt% solution exhibits more elasticity. At the higher frequencies  $G'$  approaches  $G''$  and eventually slightly surpass  $G''$  at the highest frequencies probed. At these very short times, the system has not relaxed and is exhibiting an essentially elastic behavior. The 35 wt% solution exhibits the most interesting behavior. The viscolastic moduli frequency dependence is very similar to that observed for entangled polymers in that it consists of three distinct zones, a transition zone, a plateau zone and a terminal zone. Although this behavior has been observed in polymer melts via time-temperature superposition, it has not previously been observed for colloidal dispersions. At very high frequencies  $G''$  is close in magnitude to  $G'$ . This indicates that at these very short time scales mechanisms are active that are dissipating energy. In polymeric systems, this is usually attributed to 'breathing' or Rouse modes. Here these modes may be active in the micellar coronas. In the plateau region the behavior is nearly perfectly elastic, hence comparatively little energy is dissipated in periodic deformations.  $G''$  is therefore considerably less than  $G'$  in this region. The minima in the  $G''$  observed here for the plateau region is a feature which is typically observed in the plateau region of entangled polymers.

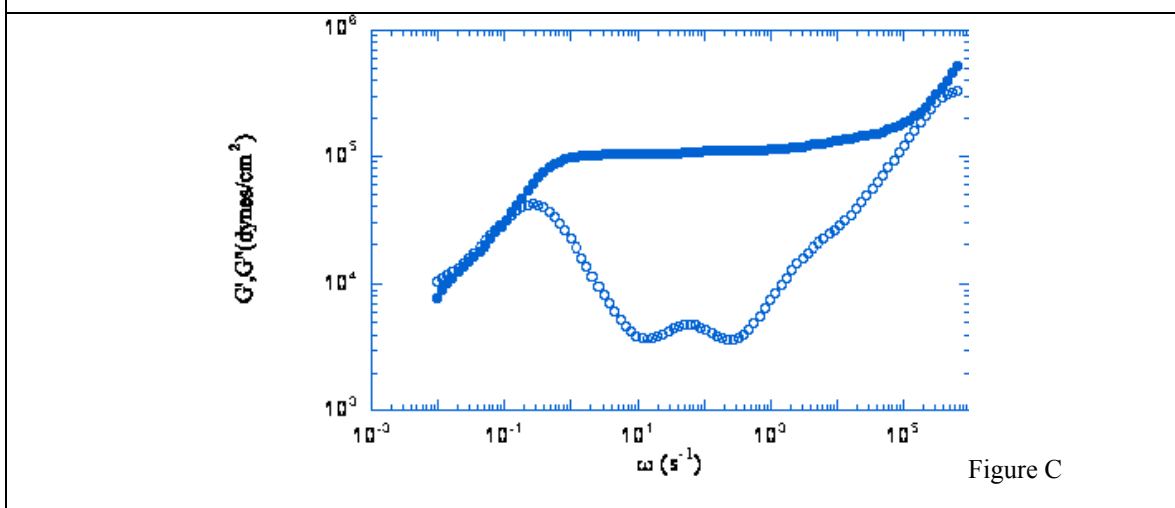
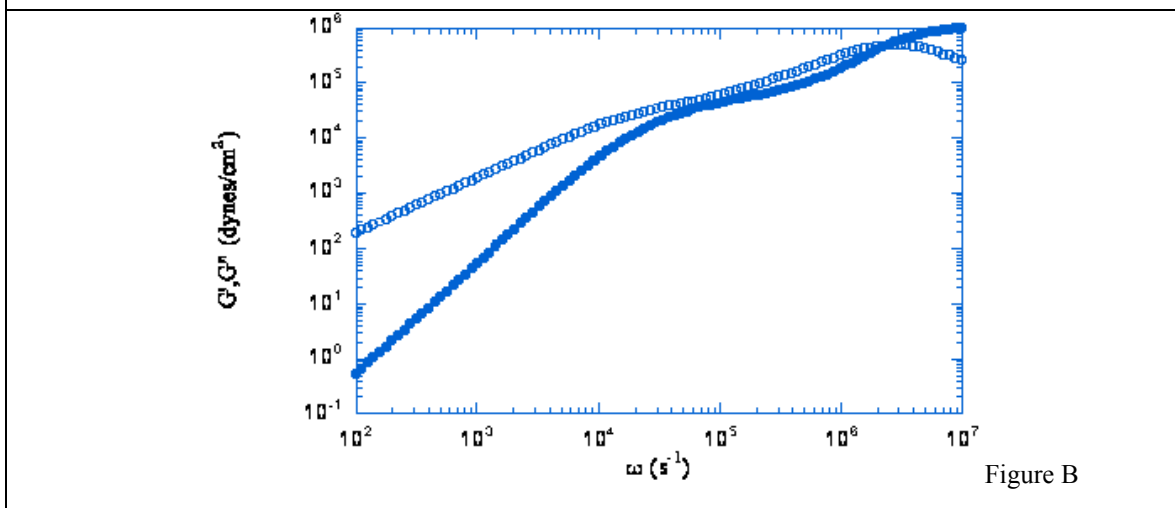
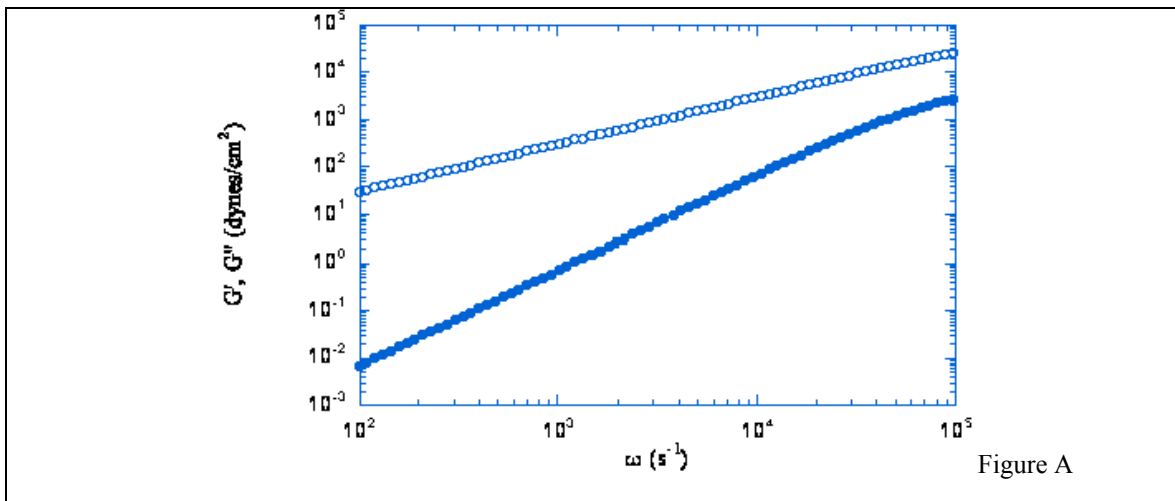


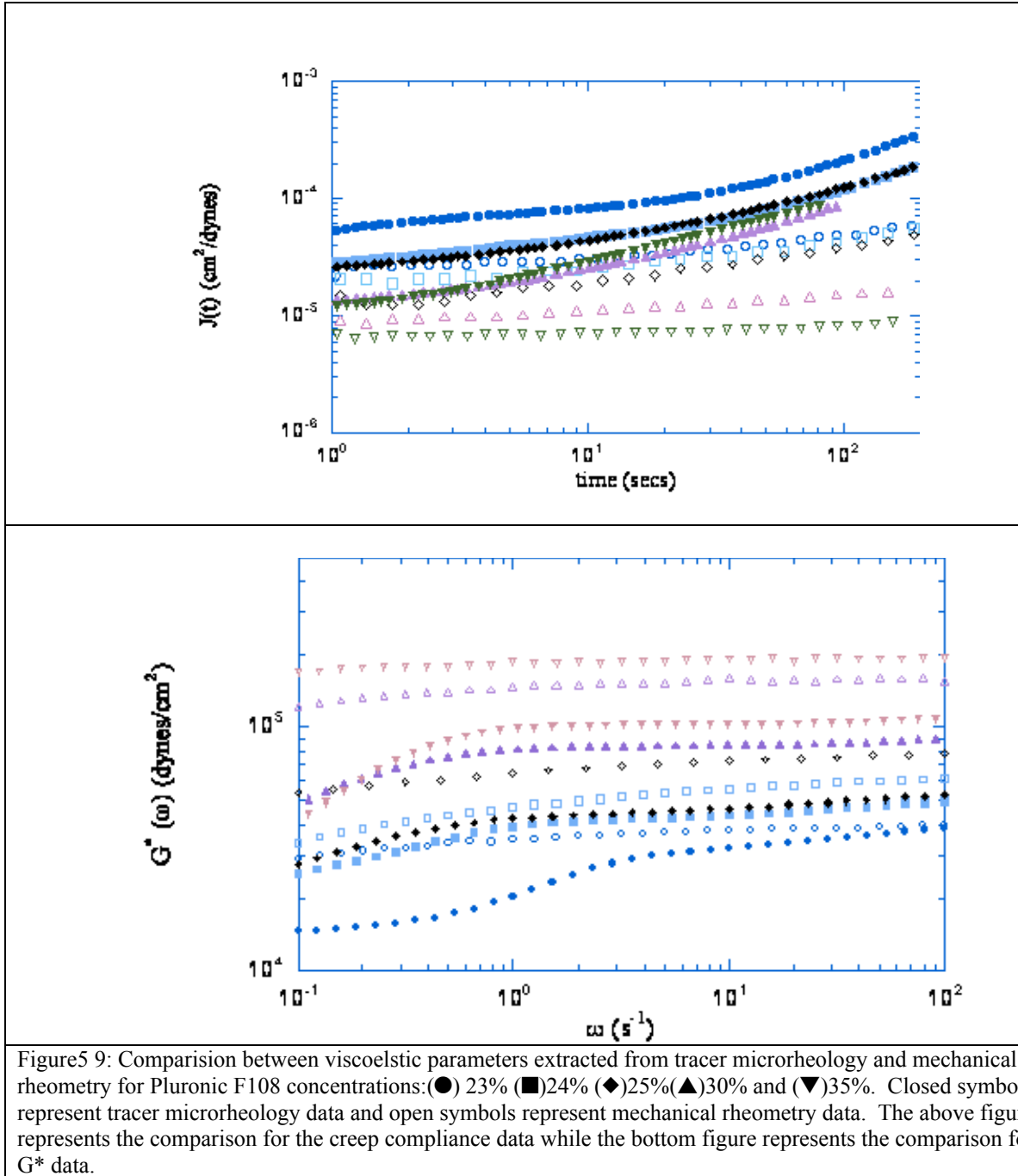
Figure 5.8: Frequency dependence of (●) storage modulus  $G'$  and (○) loss modulus  $G''$  for three Pluronic F108 concentrations (a) 15 wt%, (b) 20 wt% and (c) 35 wt%. The  $G'G''$  exhibits widely varying behavior illustrating the widely varying microstructure of the system.

Finally at long enough times the FCC soft crystalline structure relaxes completely causing  $G'$  to decrease and  $G''$  to increase in this region. For entangled flexible polymers, the predicted high frequency  $G' \sim \omega^{1/2}$ . As discussed earlier for the Pluronic™ F108 system the high frequency scaling has been observed to be  $G' \sim \omega^{0.6}$ . The high frequency scaling for colloidal dispersions has exhibited a number of different behaviors and these are discussed in detail in chapter 6. To summarize, the sterically stabilized colloidal dispersions investigated by van der Werff *et al* exhibit  $\omega^{1/2}$  scaling of the elastic modulus at high frequencies (ref 3 in chapter 6). While measurements of hard sphere dispersions carried out by Shikata and Pearson (ref 5 in chapter 6) show an essentially frequency independent behavior of the high frequency elastic modulus. However, this is in stark contrast with the experimental finding of a frequency dependence  $G_{\infty}' \sim \omega^{0.59 \pm 0.17}$  for hard spheres as obtained by Fritz *et al* (ref 2 in chapter 6). The Pluronic™ F108 system is however not expected to exhibit a purely hard sphere behavior as its interaction potential is expected to be softer than a purely hard sphere potential.

Tracer microrheology experiments on the Pluronic™ F108 system have revealed a wide variety of interesting behavior. It has been observed that the overall viscoelastic response is very sensitive to microstructural changes and the inherent strength of tracer microrheology experiment lies in the fact that the technique is a very sensitive probe of these microstructural changes and their associated dynamics. It allows the viscoelastic response of the medium to be probed over a wide frequency range, thus allowing deeper insight into the short time dynamics present in these systems. As has been discussed previously the Brownian motion of the probes is believed to be related to the viscoelastic response of the suspending media through the generalized Stokes-Einstein relationship (GSER) (1). Therefore in order to better understand probe motion in viscoelastic media it is necessary to take a deeper look at the validity of the

GSER. This has been done in detail theoretically, by Levine and Lubensky(15-17). The approach that was undertaken in this study was purely an experimental one. The procedure was to carry out both tracer microrheology and mechanical rheometry on the system.

**5.4.6 Tracer microrheology and mechanical rheometry comparison** The most direct method of comparing the viscoelastic responses obtained through tracer microrheology and mechanical rheometry is via the creep compliance,  $J(t)$ . The creep compliance was obtained for the measured tracer microrheology mean squared displacement,  $\langle \Delta r^2(t) \rangle$ , through use of the GSER.  $J(t)$  for the mechanical rheometry measurements were obtained from creep experiments (details in the chapter on mechanical rheometry). Figure 5.9a illustrates the comparison of the creep compliance,  $J(t)$  obtained from the two techniques. The figure clearly illustrates the considerable discrepancy in the  $J(t)$  obtained from the two techniques. It is observed that in both cases the creep compliance decreased with increasing concentrations as expected, since the elasticity is increasing. The most notable points with regard to the discrepancy are, (1) the tracer microrheology  $J(t)$  in all cases overestimates the mechanical rheometry  $J(t)$  and (2) the tracer microrheology data show a stronger time dependence than the mechanical rheometry data. Figure 5.9b illustrates the comparison with regard to the complex viscoelastic modulus. As mentioned earlier, for the tracer microrheology experiments, the complex viscoelastic modulus was obtained from the creep compliance using a procedure introduced by Mason and coworkers in which the creep data was fitted to a modified Voigt model allowing for purely viscous dissipation at very long times and the retardation spectrum was obtained.



The complex viscoelastic modulus measurements for mechanical rheometry were dynamic frequency sweep measurements. The comparison again illustrates the discrepancy in the viscoelastic parameters obtained from the two techniques. The notable points with regard to the discrepancies are again, (1) the tracer microrheology  $G^*$  in all cases underestimates the

mechanical rheometry  $G^*$  and (2) the tracer microrheology  $G^*$  exhibit a stronger frequency dependence than the mechanical rheometry data.

The viscoelastic modulus underestimation does not agree quantitatively with the magnitude of the creep compliance overestimation. This may be attributable to the inherent difficulty associated with reproducibility of the mechanical rheometry data due to loading effects etc. The overestimation in the case of  $J(t)$  and the underestimation in the case of  $G^*(\omega)$  both correspond to the same experimental fact. The mean square displacement,  $\langle \Delta r^2(t) \rangle$ , being measured in the tracer microrheology experiments is reflecting a smaller  $G^*$  (larger  $J^*$ ) than the mechanical rheometry  $G^*$  (or  $J^*$ ). One possible reason for this may be attributable to the longitudinal modes whereby  $\langle \Delta r^2(t) \rangle$  is not just determined by  $G^*$ .

**5.4.7 Sphere size sweep:** In order to gain a better understanding of the possible longitudinal mode effects, a sphere size sweep was carried out on three different Pluronic™ F108 concentration solutions. The concentrations that were chosen were, 15, 25 and 35 wt%. Four different sphere sizes were chosen varying from 0.195 to 0.966 microns. Figure 5.10 illustrates the evolution of  $\langle \Delta r^2(t) \rangle$  for the three concentrations.  $\langle \Delta r^2(t) \rangle$  exhibits a monotonic increase with decreasing sphere size. This is expected since smaller spheres are expected to move greater distances in a given time. An anomalous behavior is observed for the highest concentration (35 wt %) in that  $\langle \Delta r^2(t) \rangle$  for the two highest sphere sizes is reversed. This may however be attributable to the extremely small probe motion in these samples at very short times. The poor resolution of these two data sets makes normalization of the data exceedingly difficult owing to correlator resolution. One possible alternative may be to utilize thicker cells. Since better resolution depends upon  $(L/l^*)$ , the cells will have to be significantly thicker. The problem

associated with thicker cells is that the transmitted multiply scattered light may be drastically reduced, thereby hindering detection, and increasing measurement times.

If the longitudinal dynamical modes do not play a significant role in affecting the extracted viscoelastic parameters then the creep compliance data for the sphere size sweep for each concentration should collapse into a single creep master curve. Figure 5.11 illustrates the creep compliance for each of the concentrations. It is seen that the agreement is good at all time scales for the 15 wt% Pluronic™ solution but gets poorer for the larger Pluronic™ F108 concentration samples. The agreement or deviation is seen to be very sensitive to probe sphere size. Specifically for 25 wt% concentration it is seen that the agreement is very good at the short times (or high frequencies) but tends to get poorer at longer times for the two intermediate sphere sizes, 0.195 and 0.511 microns. The agreement between the largest sphere sizes ( *ie* 0.739 and 0.966 microns) is excellent through the entire time range. For the 35% sample the collapse is very poor. It should be noted that due to the poor correlator resolution for the 0.739 and 0.966 micron sphere case for  $\langle \square r^2(t) \rangle$  in 35 wt % Pluronic™ F108, not too much credence will be given to the behavior of these two sphere sizes. Within the context of a two fluid polymer network model Levine and Lubensky (15-17) have defined a characteristic frequency at which longitudinal modes may become important:

$$\square = \frac{2\square + \square}{a^2 \square} \quad (6)$$

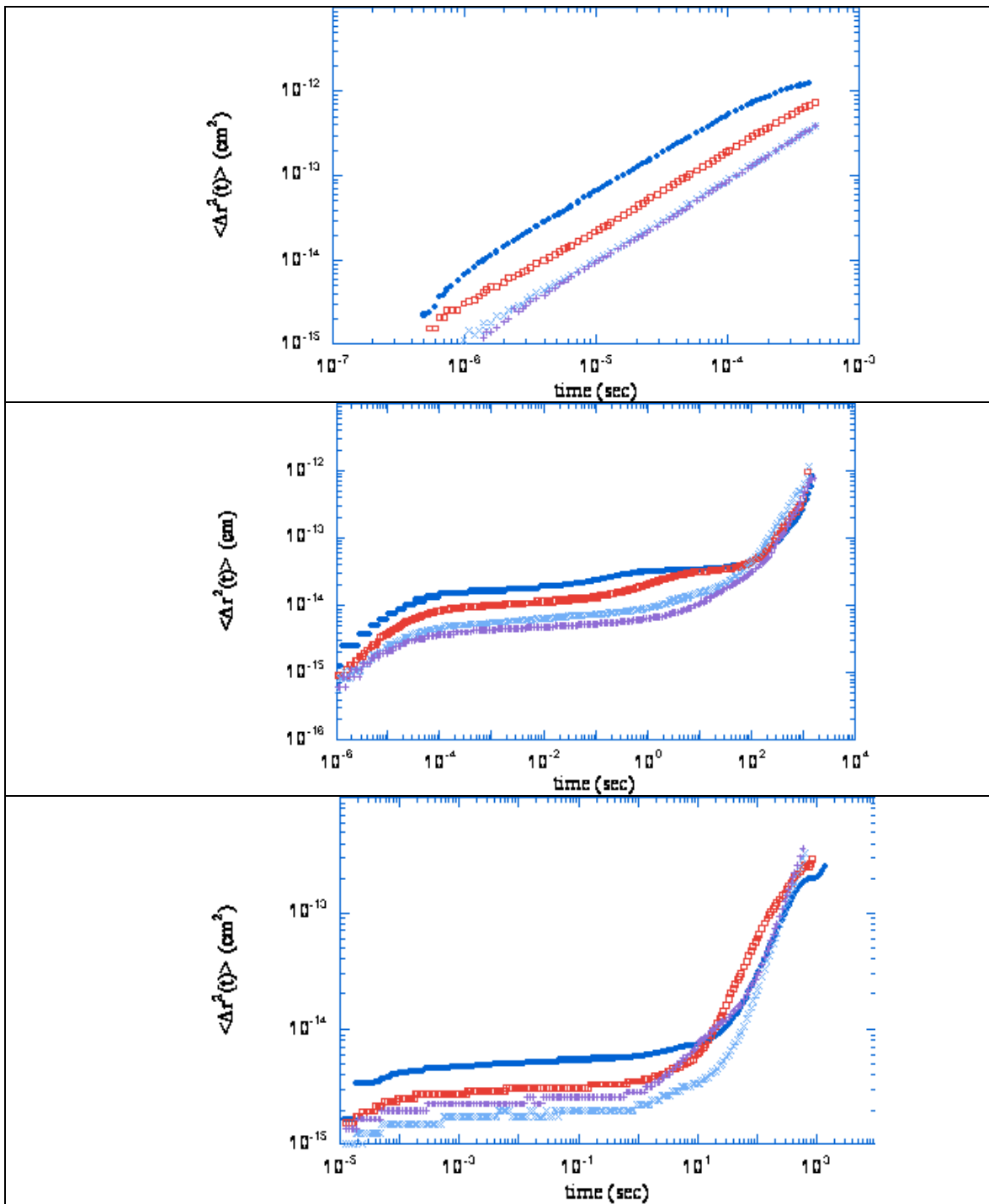
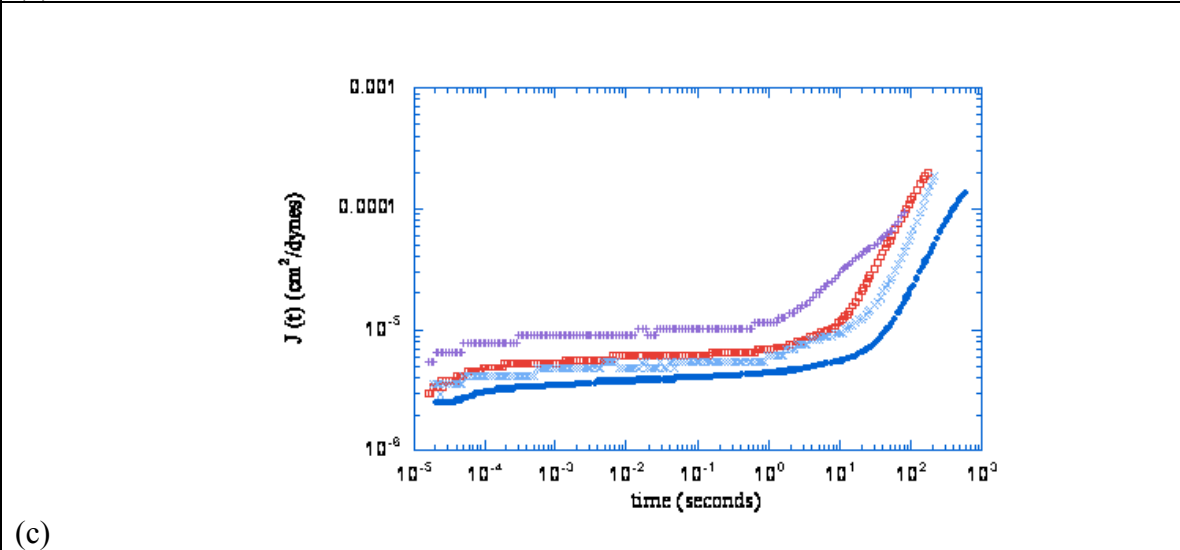
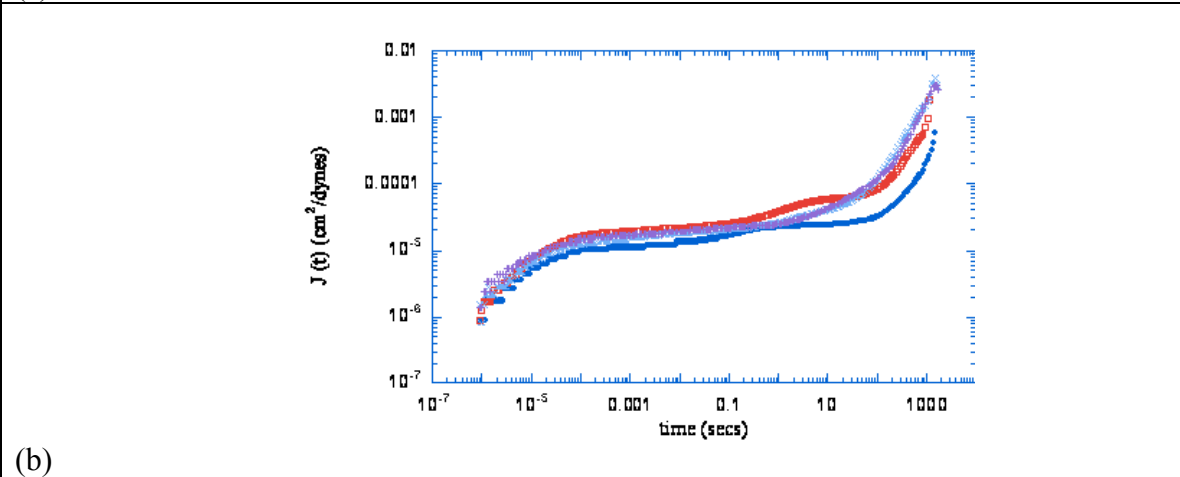
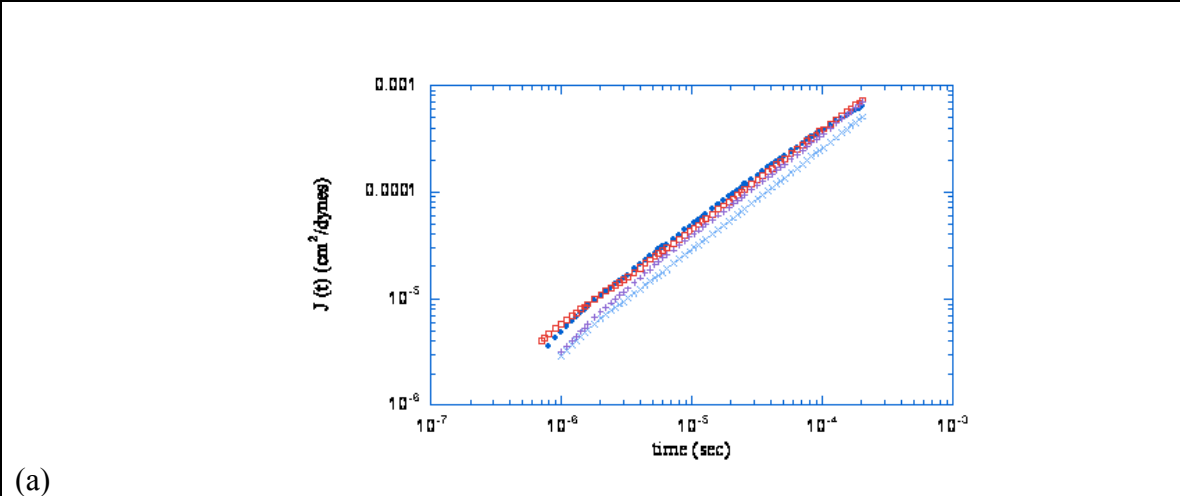


Figure 5.10:  $\langle \Delta r^2(t) \rangle$  data for a sphere size sweep carried out on (a) 15% (b) 25% and (c) 35% Pluronic F108 solution. In each case four different sphere sizes: (●) 0.195 microns (□) 0.511 microns (X) 0.739 microns and (+) 0.966 microns were used. The  $\langle \Delta r^2(t) \rangle$  exhibits a monotonic increase with decreasing sphere size as expected except for the highest 35% concentrations.



(a) Figure 5.11: Creep compliance data for a sphere size sweep carried out on (a) 15% (b) 25% and (c) 35% Pluronic F108 solution. In each case four different sphere sizes: (●) 0.195 microns (□) 0.511 microns (X) 0.739 microns and (+) 0.966 microns were used. The creep compliance agreement is seen to be very sensitive on both the frequency and the Pluronic concentration.

where  $\nu$  and  $\lambda$  are the network Lamé coefficients  $a$  is the bead size and  $\Delta$  is the network mesh. At frequencies below this characteristic frequency the network and the fluid become de-coupled and longitudinal compression modes may cause a draining effect in the network. Although the micellar system is not a network, the characteristic frequency may be thought of in an analogous manner. The equivalent length to the network mesh size is the intermicellar distance. Increasing micellar crowding will lead to decreasing intermicellar distance, causing the characteristic frequency to shift to higher values. Decreasing probe size also leads to an increase in the critical frequency. In the FCC soft crystal phase, the coronas are also getting compressed leading to significant decreases in the intermicellar separation (31-33). Increasing concentration and decreasing probe size will increase the potential influence of the longitudinal modes. This effect may be apparent in the sphere size sweep results on the Pluronic™ F108 system. For the sphere size sweep on the 15 wt% solution, the creep data collapses neatly. This indicates that the concentration is low enough here, such that the longitudinal modes do not play a significant role. Most likely because of the lack of elasticity (*i.e.* “structure formation”) The 25 wt% solution sphere size sweep shows excellent collapse of the data for the 0.739 and 0.966 micron sphere sizes and poor agreement for the 0.195 and 0.511 micron spheres. This may indicate that at this higher concentration decreasing sphere size leads to an increase in longitudinal mode contributions.

The grain boundary size in this inherently polycrystalline FCC soft crystal may also play a role. While initial investigations of these solutions with static light scattering are in their infancy, it appears that they contain structures whose length scales are on the order of 100s nm. This may play an important role as the probes also lie in this size range. An upcoming x-ray

scattering study of these solutions will however provide a better insight into the actual change of intermicellar separation distance with changing concentrations.

### ***5.5 Conclusions:***

This chapter detailed a comprehensive tracer microrheology investigation of aqueous triblock copolymer Pluronic™ F108 solutions, which form an FCC crystalline phase at high concentrations and at room temperature. In order to investigate the changes in the viscoelastic response of the system associated with changes in microstructure, tracer microrheology measurements were carried out over a wide range of Pluronic F108 concentrations varying from 3 to 35 wt %. As the technique allowed the observation of the viscoelastic behavior over a wide frequency range, a wide variety of interesting dynamical behavior was observed with changing microstructure, advocating the utility of the technique as a sensitive probe of microstructural and dynamical changes. The mean squared displacement exhibited a dramatic change in the temporal variation at about 22.7 wt% indicating the probable onset of the FCC crystalline phase. The complex viscoelastic modulus also indicated that the system is essentially viscous when in the isotropic micellar solution phase and increasing elastic with increasing order in the FCC soft crystalline phase. Tracer microrheology underestimated the complex viscoelastic modulus plateau modulus (overestimated the creep compliance) compared with mechanical measurements for all the concentrations investigated. Sphere size sweep conducted on three different concentrations showed increasing disagreement between the creep compliance extracted with different sphere sizes as the Pluronic™ concentration was increased. This was indicative that either the longitudinal dynamic modes or structural heterogeneities are causing the tracer

microrheology data to underestimate the complex viscoelastic modulus plateau modulus  
(overestimate the creep compliance)

## ***References***

1. Mason, T. and Weitz, D.; *Phys. Rev. Lett.*, **1995**, *74*, 1250
2. van Zanten, J. and Rufener K.; *Phys. Rev. E*, **2000**, *62*, 5389
3. Mason, T., Ganesan, K., van Zanten, J., Wirtz, D. and Kuo, S.; *Phys. Rev. Lett.*, **1997**, *79*, 3282
4. Palmer, A., Xu, J. and Wirtz, D.; *Rheol. Acta*, **1998**, *37*, 97
5. Palmer, A., Mason, T., Xu, J., Kuo, S. and Wirtz, D.; *Biophysical Journal*, **1999**, *76*, 1063
6. Palmer, A., Cha, B. and Wirtz, D.; *J. Polym. Sci., Part B: Polym. Phys*, **1998**, *36(17)*, 3007.
7. Xu, J., Palmer, A. and Wirtz, D.; *Macromolecules*, **1998**, *31*, 6486.
8. Rufener, K., Palmer, A., Xu, J. and Wirtz, D.; *Journal of Non-Newtonian Fluid Mechanics* **1999**, *82*, 303
9. Mason, T., Gisler, T., Kroy, K., Frey, E. and Weitz, D.; *J of Rheol.*, **2000**, *44*, 917
10. Mason, T.; *Rheol. Acta*, **2000**, *39*, 371
11. Mason, T.G., Dhople, A. and Wirtz, D.; *Mater. Res. Soc. Symp. Proc.*, **1997**, *463*, 153
12. Gittes, F., Schnurr, B., Olmsted, P.D., MacKintosh, F.C. and Schmidt, C.F.; *Phys. Rev. Lett* **1997**, *79*, 3286
13. Schnurr, B., Gittes, F., MacKintosh, F.C. and Schmidt, F.C. *Macromolecules*, **1997**, *30*, 7781
14. Crocker, J., Valentine, M., Weeks, E., Gisler, T., Kaplan, P., Yodh, A. and Weitz, D.; *Phys. Rev. Lett.*, **2000**, *85*, 888
15. Levine, A. J. and Lubensky, T. C.; *Phys Rev E*, **2002**, *65*, 011501/1.
16. Levine, A.J. and Lubensky, T.C. ;*Phys. Rev. Lett.*, **2000**, *85*, 1774
17. Levine, A.J. and Lubensky, T.C.; *Phys Rev E*, **2001**, *63*, 1510
18. Gittes, F. and MacKintosh, F.C.; *Phys Rev E*, **1998**, *58*, R1241

19. MacKintosh, F. C. and Schmidt, C. F.; *Current Opinion in Colloid & Interface Science*, **1999**, *4*, 300.
20. Gisler, T. and Weitz, D. A.; *Phys. Rev. Lett*, **1999**, *82*, 1606.
21. Xu, J., Tseng, Y., Carriere, C. J., Wirtz, D.; *Biomacromolecules*, **2002**, *3*, 92.
22. Tseng, Y. and Wirtz, D.; *Biophys Journal*, **2001**, *81*, 1643
23. Yamada, S., Wirtz, D., Kuo, S. C.; *Biophys. J.*; **2000**, *78*, 1736
24. Harden, J. L. and Viasnoff, V.; *Current Opinion in Colloid & Interface Science*, **2001**, *6*, 438
25. Narita, T., Knaebel, A., Munch, J.-P., Candau, S. J.; *Macromolecules*, **2001**, *34*, 8224
26. Stradner, A., Romer, S., Urban, C., Schurtenberger, P.; *Progress in Colloid & Polymer Science*, **2001**, *118*, 136
27. Knaebel, A., Bellour, M., Munch, J.-P., Viasnoff, V., Lequeux, F., Harden, J. L.; *Europhys Letters*, **2000**, *52*, 73.
28. Urban, C., Romer, S., Scheffold, F., Schurtenberger, P.; *Progress in Colloid & Polymer Science*, **2000**, *115*, 270.
29. Nisato, G., Hebraud, P., Munch, J.-P., Candau, S. J.; *Physical Review E*, **2000**, *6*, 2879
30. Weitz, D., Pine, D.; *Diffusing Wave Spectroscopy-in Dynamic Light Scattering-the method and some applications* (Clarendon Press 1993)
31. Eiser E., Molino F., and Porte, G.; *Euro Phys Jour E*, **2000**, *2*, 39
32. Eiser E., Molino F., Porte, G. and Pithon, X.; *Rheol Acta*, **2000**, *39*, 201
33. Molino, F. R., Berret, J. -F., Porte, G., Diat, O. and Lindner, P.; *Eur. Phys. Jour B*, **1998**, *3*, 59
34. Alexandridis, P., Nivaggioli, T. and Hatton, A. T.; *Langmuir*, **1995**, *11*, 1468
35. Mason, T.G., and Weitz, D.A.; *Phys Rev Lett*, **1995**, *75*, 2770

36. de Kruif, C.G., van Iersel, E.M.F., Vrij, A and Russel, W.B.; *J.Chem.Phys*, **1986**, 83, 4717

37. Kreiger, I. M.; *Adv Colloid Interface Sci*, **1972**, 3, 111

## Chapter 6

# High Frequency Elastic Modulus of Triblock Copolymer Soft Crystals

---

### ***6.1 Abstract:***

This chapter details the first experimental investigation of the high frequency elastic modulus of aqueous Pluronic™ F108 solutions in the cubic crystalline phase via diffusing wave spectroscopy based tracer microrheology. The high frequency elastic modulus is one of the most direct probes of interparticle interaction potentials at short distances. The dependence of the high frequency elastic modulus on the intermicellar separation distance is studied as a means of investigating interparticle interactions in the soft crystals. It is observed that there is a strong dependence of the high frequency elastic modulus on the intermicellar separation distance. On attempting to model this dependence with a host of different interparticle interaction potentials, it is observed that the actual interaction potential exhibited a behavior that was intermediate to the hard and soft sphere type associated with similar systems. A definitive conclusion however cannot be drawn at this stage due to the accuracy of the estimated structural parameters and the use of a perfect crystal structure factor in model calculations. The high frequency elastic modulus, as determined through tracer microrheology studies, exhibits a slight frequency dependence that diminished with increasing Pluronic™ F108 concentration. This is most likely due to the formation of stronger gels with increasing concentration. The frequency dependence observed here is weaker than that expected for a purely hard sphere dispersion. This may be a consequence of the softer intermicellar interactions in this system.

## 6.2 Introduction

The rheological behavior observed for dense colloidal systems is the result of complex interplay between particle configuration, pair potential and hydrodynamics (1-12). A thorough understanding of dense colloidal dispersion rheology especially requires deep insight into the interparticle and hydrodynamic interactions at small separations. A direct measure of these interactions at small separations is contained in the high frequency elastic or storage modulus,  $G'$  (1-12).

The high frequency elastic modulus,  $G'$ , has been the subject of extensive theoretical study for hard sphere, charge stabilized and polymerically stabilized colloidal dispersions (1,6, 8-10). A key aspect of these high frequency elastic modulus models is the need to correctly account for the role of the hydrodynamic interactions and accurately estimate the pair interaction potential. The approach of Lionberger and Russell (1) indicates that hydrodynamic interactions have a profound influence on  $G'$ . The role of hydrodynamic interactions is much less prominent for charged colloidal systems as shown by Wagner (8) and Bergenholtz (6). Hydrodynamic interactions have also been predicted to have little effect on the high frequency elastic modulus for polymerically stabilized colloids systems above the close packing concentration (9-10). Above the close packing concentration, the most significant factor in accurately modeling  $G'$  is the dispersion structure (10).

Experimental investigations of colloidal dispersion high frequency rheological behavior have been somewhat limited by the experimental difficulty in accessing sufficiently large frequencies (2-7, 10-12). Most of these experimental investigations have focused on hard sphere and charged colloidal systems with polymerically stabilized colloids being the subject of a limited number of studies (9-13). As a result the applicability of the various theoretical models has not

been investigated from an optimal experimental perspective. In an attempt to alleviate this, we have investigated the high frequency rheological behavior face centered cubic (FCC) soft crystals.

One class of materials that order into soft crystals at sufficiently high concentrations and temperatures in aqueous solution are the triblock copolymers known commercially as Pluronics<sup>TM</sup> or Polaxamers<sup>TM</sup>. These triblock copolymers contain polyethylene oxide (PEO) and polypropylene oxide (PPO) segments with the structure (PEO)<sub>n</sub>-(PPO)<sub>m</sub>-(PEO)<sub>n</sub>. The PEO and PPO chains are both soluble in aqueous solution at temperatures  $\leq 5^{\circ}\text{C}$ . However, as the temperature is raised above  $5^{\circ}\text{C}$ , water becomes an increasingly poor solvent for the PPO block, while the PEO chains remain essentially unaffected. The decreasing water affinity of the PPO blocks leads to their association (segregation) yielding micelles whose core consists of water free PPO surrounded by a highly hydrated PEO corona. These block copolymer micelles are very similar in structure to so-called ‘hairy’ or polymer-stabilized colloidal particles. This structure leads to interparticle potentials that are longer ranged than those found for hard spheres. The softness of the interparticle potentials, along with the solvated nature of the PEO corona, provides the mechanism for these triblock copolymers to form ordered soft crystals at relatively small volume fractions [15-17]. Here a tracer microrheology and mechanical rheology study of aqueous Pluronic<sup>TM</sup> F108 soft crystals is reported.

### ***6.3 Materials and Methods***

#### ***Materials***

Pluronic<sup>TM</sup> F108 was obtained from BASF Corporation and used without further purification. Dust free Pluronic<sup>TM</sup> F108 aqueous solutions were prepared with deionized water

that had been filtered through a 0.02  $\mu\text{m}$  filter (Whatman-Anotop 25). Polystyrene latex spheres ranging in size from 0.195 to 1.55  $\mu\text{m}$  in diameter were utilized as optical probes (Duke Scientific, Palo Alto, CA). The optical probes were dispersed in the Pluronic solutions at about 1 vol%. All samples were first prepared at room temperature (spheres/water + Pluronic F108), then cooled to 5°C to enhance mixing in the liquid state, transferred at 5 °C to flat sided 10 mm thick spectrophotometric cells for diffusing wave spectroscopy measurements (Spectrocell, Orelan, Pa) and then allowed to warm to 25 °C. The samples were allowed to equilibrate for two weeks prior to taking measurements. All of the tracer microrheology samples were examined via optical microscopy to ensure that the optical probes were not aggregated prior to measurement.

### ***6.3.1 Diffusing Wave Spectroscopy***

Point-point transmission mode diffusing wave spectroscopy (DWS) was utilized to monitor the tracer probe motion. The beam from a diode pumped solid state (DPSS) Nd-YAG laser operating at a wavelength of 532 nm *in vacuo* was incident upon a flat scattering cell, containing the Pluronic F108 solution and spherical optical probes. An ALV SI/SIPD photon detector collects the multiply scattered light via a single mode optical fiber. In order to ensure point-point geometry, the single mode optical fiber has a gradient refractive index (GRIN) lens, with a very narrow angle of acceptance, attached to it. In addition, a polarizer with horizontal acceptance is placed before the optical fiber to ensure that only multiply scattered light is detected from the vertically polarized incident beam. The ALV SI/SIPD photon detector signal is fed into a ALV fast digital correlator operating in the cross correlation mode to minimize the effects of afterpulsing and deadtime correction. The measured intensity auto correlation function

was converted into the electric field autocorrelation function via the Siegert relationship. The electric field autocorrelation function obtained from a DWS measurement can be related to the mean square displacement through: (18)

$$g_1(t) = \int_0^L P(s) \exp\left[-\frac{1}{3} k_0^2 \langle r^2(t) \rangle \frac{s}{l^*}\right] ds \quad (1)$$

where  $g_1(t)$  is the electric field autocorrelation function,  $P(s)$  is the scattering path length distribution function,  $k_0$  is the wave vector,  $\langle r^2(t) \rangle$  is the particle mean squared displacement and  $l^*$  is the distance over which light becomes completely randomized. The mean squared displacement of the spherical tracer probes was extracted pointwise from the electric field autocorrelation function through a bisection root searching algorithm. It should be noted that while in DLS the length scale over which particle motion is probed can be adjusted by varying the scattering angle, in DWS the length scale over which the motion is probed is primarily adjusted by varying the cell thickness  $L$ . Most importantly, owing to multiple scattering nature of DWS the technique is capable of resolving *angstrom*-scale particle motions and, therefore, short time dynamics.

In tracer microrheology the viscoelastic shear modulus of the fluid is typically obtained from the mean squared displacement through use of the generalized Stokes Einstein relation (GSER) equation (19)

$$\langle \tilde{r}^2(s) \rangle = \frac{k_B T}{\zeta s a \tilde{G}(s)} \quad (2)$$

where  $\langle \tilde{r}^2(s) \rangle$  is the Laplace transform of the tracer particle mean squared displacement,  $a$  is the tracer particle radius and  $\tilde{G}(s)$  is the viscoelastic shear modulus. The generalized Stokes-Einstein equation is based on the assumption that the complex fluid can be treated as a continuum around the tracer sphere (19). The GSE equation also assumes that the Stokes relation for viscous fluids can be extended to describe the viscoelastic drag on a sphere at all frequencies. The GSE equation was utilized to extract the creep compliance data. The creep compliance is extracted from:

$$(3)$$

The creep compliance is utilized as its calculation does not involve any transformation from the time domain to the frequency domain. The complex viscoelastic modulus was obtained by fitting the creep data to a modified Voigt model allowing for purely viscous dissipation at very long times and obtaining a retardation spectrum from it.

### **6.3.2 Mechanical Rheometry:**

Linear viscoelastic moduli were determined with a Rheometrics DSR controlled stress rheometer. Measurements were carried out using a serrated 40 mm parallel plate geometry. The plate temperature was fixed at 5°C and the liquid samples immediately transferred. In order to eliminate edge effects the top plate was brought down a certain distance close to the final gap width and the sides were cleaned off. The plate temperature was then raised to 25° C. The sample was allowed to equilibrate for one hour and then the top plate was brought down to the final width. In order to prevent evaporation effects, the serrated parallel plates were enclosed in a custom made vapor trap. Both creep measurements and dynamic measurements were carried out on each Pluronic concentration. It is to be noted that measurements were also carried out using a

40 mm cone and plate geometry. However, since this geometry exhibited reproducibility problems, due to sample slippage, no results are reported for measurements carried out utilizing this geometry. In order to determine the stress range corresponding to the linear viscoelastic regime a dynamic stress sweep was carried out for each sample. As a cross check for the linear viscoelastic regime creep experiments were carried out on each sample for different stresses. In order to ensure that all measurements were in the linear regime both stress sweeps and creep compliance measurements at varying stresses were carried out (20).

## ***6.4 Results and Discussion:***

### ***6.4.1 Determination of High Frequency $G'$ :***

The aim of this study was to develop an understanding of the interparticle and hydrodynamic interactions at small separations for the Pluronic™ F108 system through investigating the behavior of the high frequency elastic modulus,  $G'$ . Figure 6.1 a and b illustrates the frequency dependence of the storage modulus for tracer microrheology and mechanical rheometry measurements on the Pluronic™ F108 system. It is seen that for the mechanical rheometry measurements, the storage modulus reaches a distinct plateau. It is therefore relatively straightforward to extract the high frequency elastic modulus.

A number of theoretical models of the high frequency elastic modulus have been developed in an effort to gain insight into interparticle interactions at small separation distances.

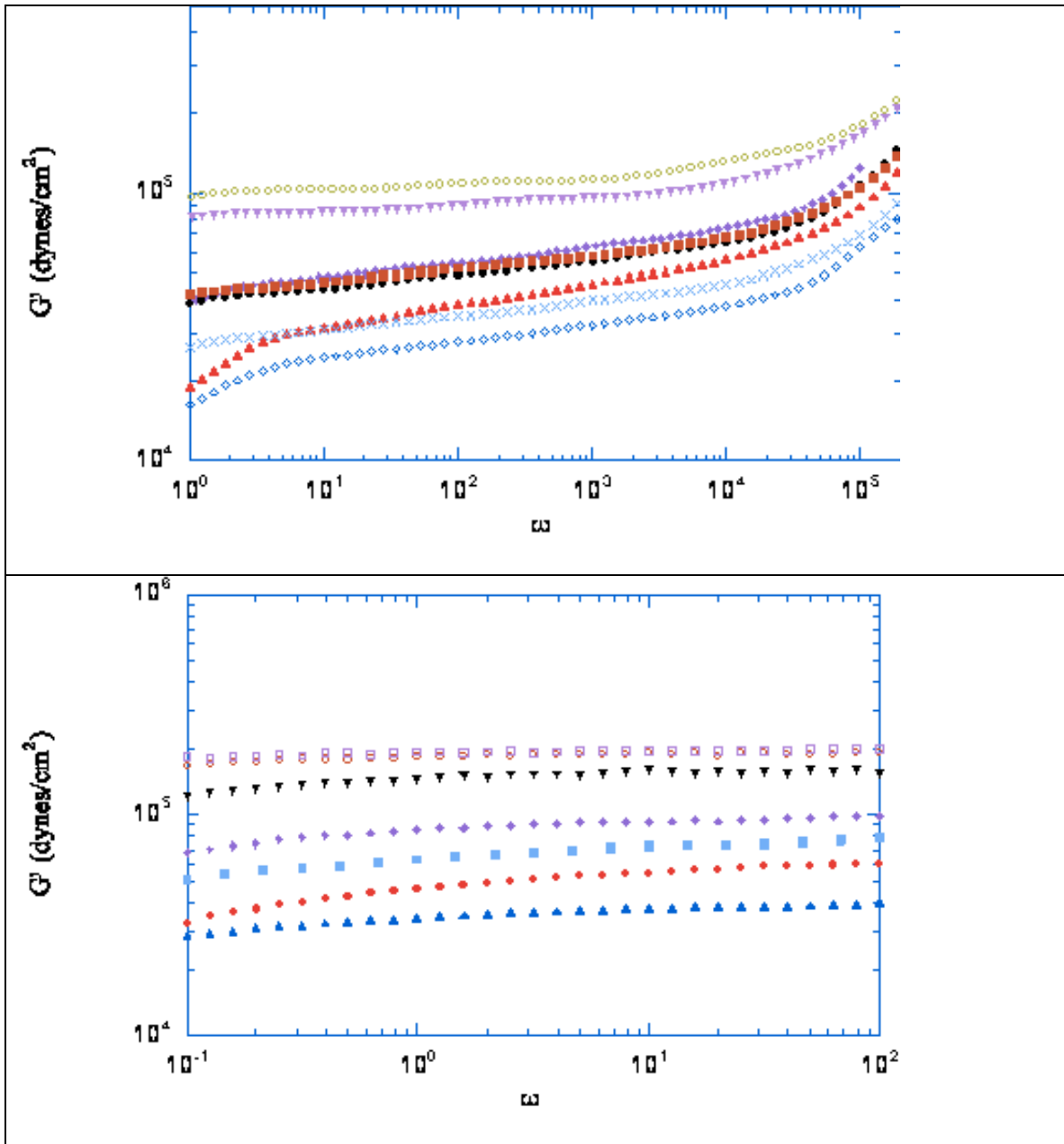


Figure 6.1: Frequency dependence of elastic modulus  $G'$  obtained from (fig a) tracer microrheology and (fig b) mechanical rheometry for Pluronic F108 solutions having concentrations: ( $\square$ ) 22.7% ( $\blacktriangle$ ) 23% ( $\times$ ) 23.5% ( $\blacklozenge$ ) 23.7% ( $\bullet$ ) 24% ( $\blacksquare$ ) 25% ( $\blacktriangledown$ ) 30% ( $\circ$ ) 35% and ( $\square$ ) 40%. The tracer microrheology  $G'$  always exhibits a frequency dependence

The plateau value close to the highest frequency probed was chosen as the high frequency  $G'$ . Since the plateau value was independent of frequency in the plateau region there was no error inherent in estimating this. The storage modulus obtained from tracer microrheology measurements did not exhibit a completely frequency independent region.  $G'$  always exhibited a

slight frequency dependence and then at the highest frequencies probed it exhibited a strong dependence. In order to estimate the high frequency storage modulus a high enough frequency was required and at the same time an almost frequency independent region was required. A frequency of  $10^3 \text{ s}^{-1}$  seemed to satisfy this criteria and the  $G'$  values corresponding to this frequency was chosen as the high frequency  $G'$  for the tracer microrheology measurements.

#### ***6.4.2 High Frequency Elastic Modulus Behavior Modelling:***

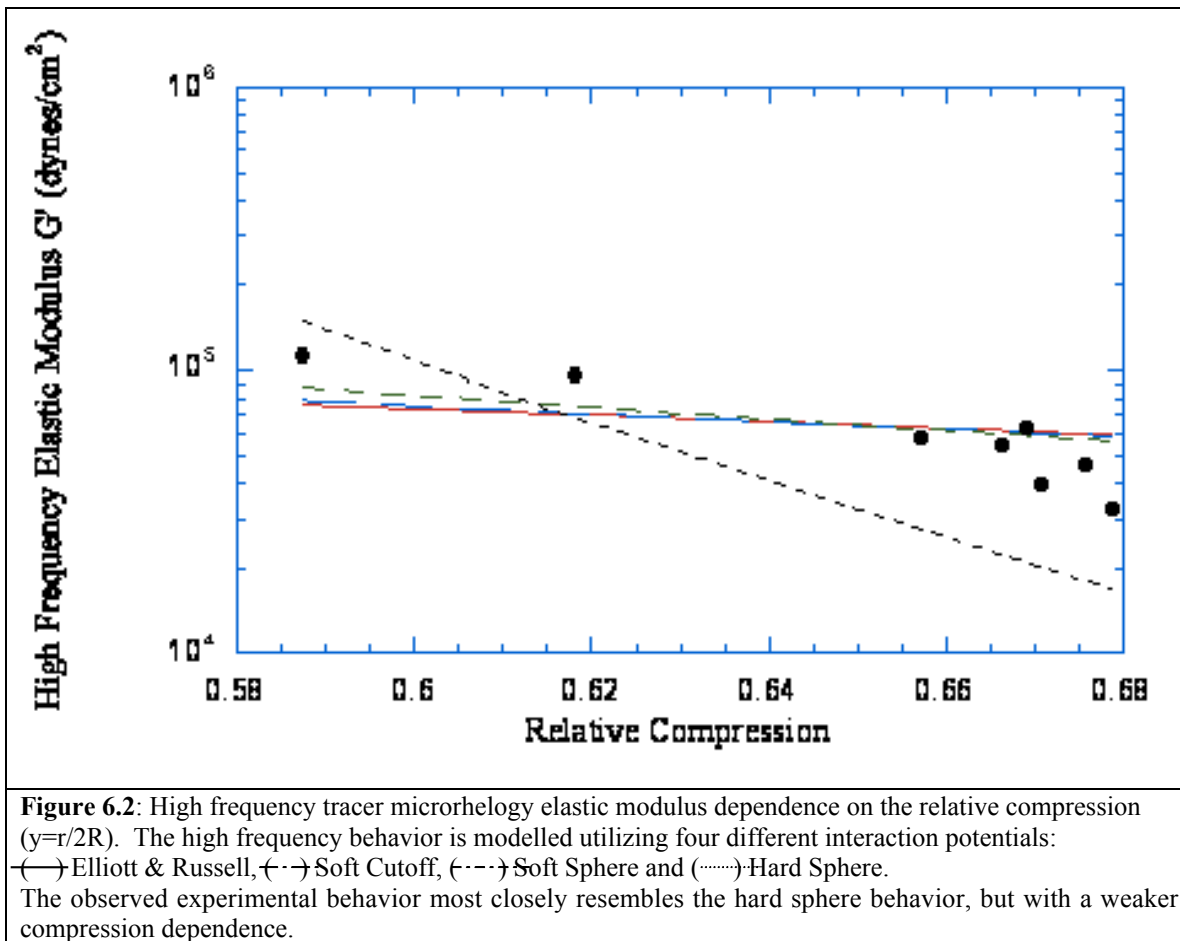
The main theoretical developments have been for hard sphere dispersions (1), charged colloidal dispersions (6-8), polymerically stabilized colloidal dispersions (9-11) and soft spheres (12-13). Pluronic F108 soft crystals are expected to have an interaction potential that is longer ranged (softer) than a hard sphere potential, similar to that found for polymerically stabilized colloids as the Pluronic™ F108 micelles consist of a corona of highly hydrated PEO chains surrounding a core of melt of PPO. The model of Elliott and Russel (9) based on the interaction potential between a pair of polymerically stabilized colloids may provide a description of the high frequency behavior. However, it must be kept in mind that the system under consideration here is a micellar dispersions wherein the micelle core is deformable. One of the key parameters determining the magnitude of the interparticle (intermicellar) interactions is the relative compression of the corona or hairy polymer layer. The relative compression is defined as  $y = r/2R$ , where  $r$  is the interparticle separation (center-to-center) and  $R$  is the overall particle radius which is the sum of the core radius and the corona (hairy layer) equilibrium thickness. The FCC crystal structural parameters have only been determined for the 35 wt% concentration case by small angle x-ray scattering (SAXS). Geometric scaling has been used to estimate the lattice

parameters at other concentrations. The overall particle radius consists of the core and the corona. The core radius was approximated through (23):

$$R_c = \left[ \frac{3}{4} a n v_{po} \right]^{1/3} \quad (4)$$

where,  $n$  is the number of  $po$  units per surfactant,  $v_{po}$  is the volume per  $PO$  molecule and  $a$  is the aggregation number, which was determined previously from SAXS measurements. The corona thickness was estimated using the brush model (23).

Figures 6.2 and 6.3 represent the variation of the high frequency elastic modulus with relative compression for tracer microrheology (figure 6.2) and mechanical rheometry measurements (figure 6.3).



Both the tracer microrheology and mechanical rheometry show similar trends for the high frequency behavior in that high frequency elastic modulus increases with increasing concentration (lower relative compression values). This is expected as higher elasticity is associated with smaller interparticle separations.

The relationship between the high frequency elastic modulus and the interparticle potential has been derived by Zwanzig and Mountain (21) and is given by:

$$G' = \rho kT + \frac{2\rho}{15} \rho^2 \int_0^\infty g(r) \frac{\partial}{\partial r} \left[ r^4 \frac{\partial u(r)}{\partial r} \right] dr \quad (5)$$

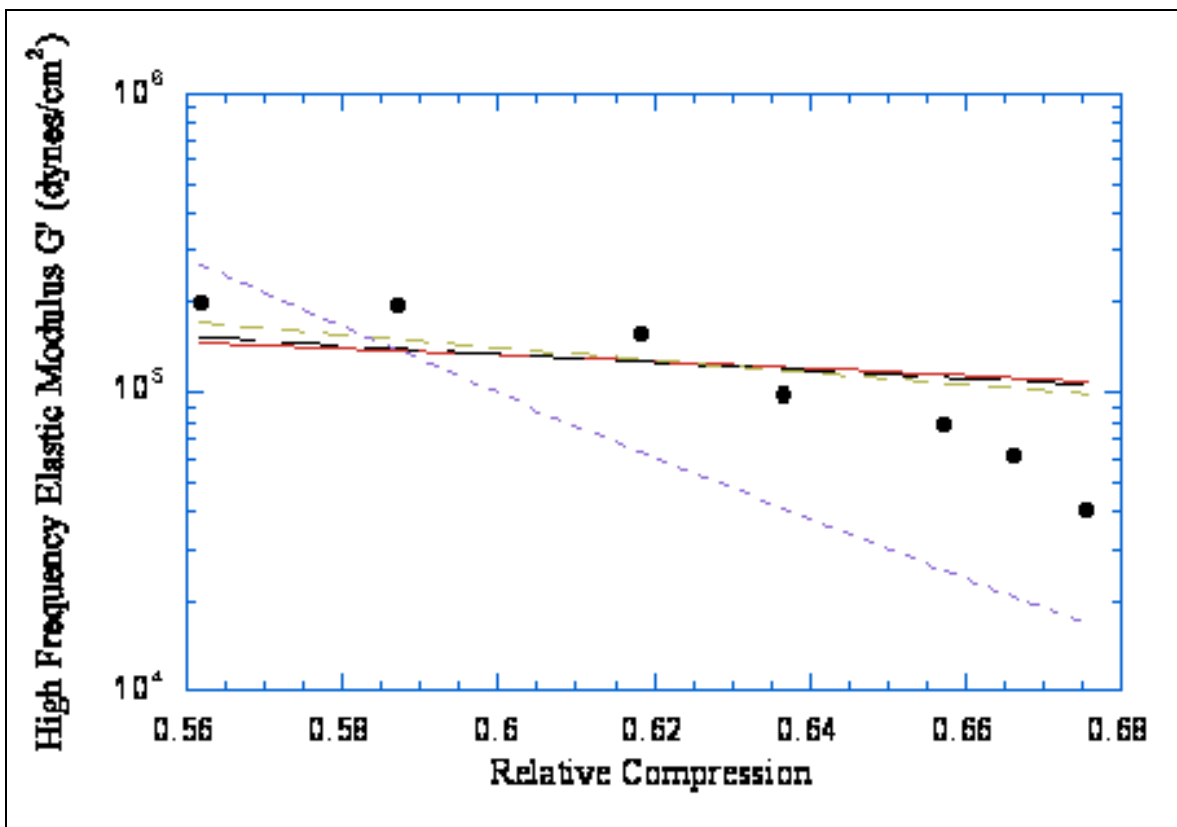


**Figure 6.3:** High frequency rheometry elastic modulus dependence on the relative compression ( $\gamma=r/2R$ ). The high frequency behavior is modelled utilizing four different interaction potentials: (—) Elliott & Russell, (- - -) Soft Cutoff, (· · · · ·) Soft Sphere and (- · - · -) Hard Sphere. The mechanical rheometry data also show a stronger agreement with the hard sphere potential, however the dependence on the relative compression is weaker.

where  $u(r)$  is the intermolecular potential and  $g(r)$  is the radial distribution function. For a crystalline system the radial distribution function is given by a series of delta functions thereby simplifying the expression for the high frequency elastic modulus (22):

$$G' = bp_m(r) \left[ \frac{\partial^2 u(r)}{\partial r^2} \right] \quad (6)$$

where,  $p_m(r)$  is a prefactor that depends on the type of lattice and can be calculated from a knowledge of the maximum packing fraction and the coordination number and  $b$  is a constant with a value  $1/5$ . The derivative is evaluated at the interparticle separation distance. Since the Pluronic™ F108 soft crystal system is analogous to polymerically stabilized colloidal dispersions and is expected to have a longer range (softer) potential than a hard sphere dispersion, a number of interaction potentials were considered: (1) the polymerically stabilized hard core colloid potential of Elliott and Russel (9), (2) the soft sphere potential of Witten and Pincus (13), (3) a soft sphere potential with an exponential cutoff as described by Buitenhuis and Forster (12) and (4) the hard sphere potential (12).

Figures 6.2 and 6.3 illustrate that none of the chosen interaction potentials adequately model the experimental data. The high frequency elastic modulus exhibits a stronger dependence on the relative compression than predicted by the Elliott-Russell and Witten-Pincus potentials. It has been previously demonstrated that the Elliott and Russell model describes the high frequency behavior of polymerically stabilized spheres quite adequately (9). For the investigated system, the inability of this model may be attributable to the fact that the micellar core is soft and potentially deformable. The observed high frequency elastic moduli relative compression dependence indicates that the micellar interaction potential is in between those expected for soft and hard spheres. Further supporting evidence in favor of a harder potential is the FCC soft

crystal structure formed by Pluronic™ F108 under the experimental conditions (15-17). The interaction potential for FCC crystal forming micellar dispersions is believed to be relatively short ranged (harder), while softer intermicellar potentials yield body centered cubic (BCC) soft crystals (12).

It should be noted that the above analysis is potentially limited by two factors. First, it is assumed that the structure of the FCC soft crystals under consideration can be described as perfect crystals in order to utilize equation (4). The FCC crystal structural parameters have only been determined for the 35 wt% concentration case by small angle x-ray scattering (SAXS) (15-17). Geometric scaling has been used to estimate the lattice parameters at other concentrations. Future SAXS measurements are scheduled at which time the full static structure factor will be determined for Pluronic™ F108 solutions ranging from 3-40 wt%. The second factor is the micelle radius estimate. The only available literature value is a 120 Å radius of gyration. The radius of gyration provides a measure of the scattering power (mass) distribution within the micelle, while the models under consideration require both the core radius and corona thickness. The core radius and corona equilibrium thickness can be estimated from theoretical considerations (12, 23) with the largest potential error being the corona thickness. In order to take this into account, the high frequency elastic modulus variation with the interparticle separation was modeled with the equilibrium layer thickness as a free parameter (see Figure 6.4). The ability of any of the intermicellar potentials under consideration to model the observed rheological behavior is essentially unaffected by lifting this restriction.

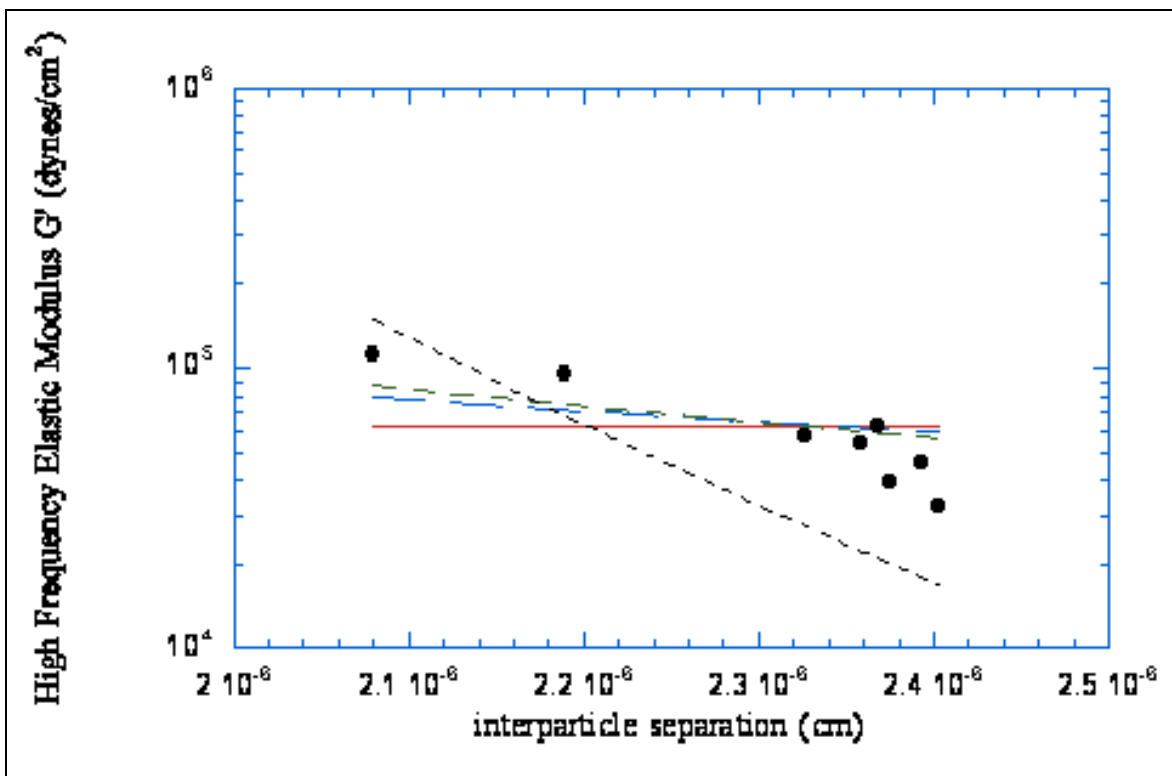


**Figure 6.4:** High frequency tracer microrheology elastic modulus dependence on the interparticle separation. The high frequency behavior is modelled utilizing four different interaction potentials: —(—) Elliott & Russell, ( - - ) Soft cutoff, ( - . - ) Soft Sphere and ( ..... ) Hard Sphere.

From the above analysis and the slopes of the hard sphere and soft sphere fits, it seems that an interaction potential in between a soft sphere and hard sphere fit would be a better choice of the probable interaction potential acting in the system. A definitive conclusion about the inability of the chosen potentials to model the high frequency behavior however cannot be drawn at this stage. This is primarily due to two factors. The first being the accurate determination of the structural parameters which was discussed in the previous paragraph and the other being the accuracy of the radial distribution function being estimated by a series of delta functions. In reality it is expected that the actual  $g(r)$  will actually exhibit broadening of the peaks. Future x-ray scattering studies on the system will aid in a more accurate estimation of both  $g(r)$  and the

structural parameters. This will help in carrying out a more accurate modelling of the high frequency elastic modulus behavior.

#### **6.4.3 High Frequency Elastic Modulus Frequency Dependence:**

The high frequency elastic modulus determined from the tracer microrheology exhibits a small frequency dependence. The variation this frequency dependence  $\square$  (*i.e.*  $G_{\infty}' \sim \square^{\square}$ ) with concentration is illustrated in figure 6.5. The elastic modulus frequency dependence diminishes with increasing concentration. This most likely due to the formation of stronger gels with increasing concentration. This high frequency behavior, as obtained from tracer microrheology studies, is in contrast to the high frequency behavior obtained from the mechanical rheometry measurements which show an essentially frequency independent behavior. Prior experimental investigations of colloidal dispersion high frequency dynamics, while limited, have yielded widely varying observations (2,3,5). The sterically stabilized colloidal dispersions investigated by van der Werff *et al* exhibit  $\square^{1/2}$  scaling of the elastic modulus at high frequencies (3). While measurements of hard sphere dispersions carried out by Shikata and Pearson (5) show an essentially frequency independent behavior of the high frequency elastic modulus. However, this is in stark contrast with the experimental finding of a frequency dependence  $G_{\infty}' \sim \square^{0.59 \pm 0.17}$  for hard spheres as obtained by Fritz *et al* (2). The weaker frequency dependence observed here may be a consequence of the softer intermicellar interactions in this system. The difference that is observed between the frequency dependence of the elastic modulus extracted from tracer microrheology measurements and from mechanical rheometry is reminiscent of the behavior observed for hard sphere dispersions (2). In the hard sphere case, the observation of a high

frequency plateau was attributable to the measurement limitations of conventional rheometers and the large magnitude of the viscous modulus,  $G''$ , at high frequency.

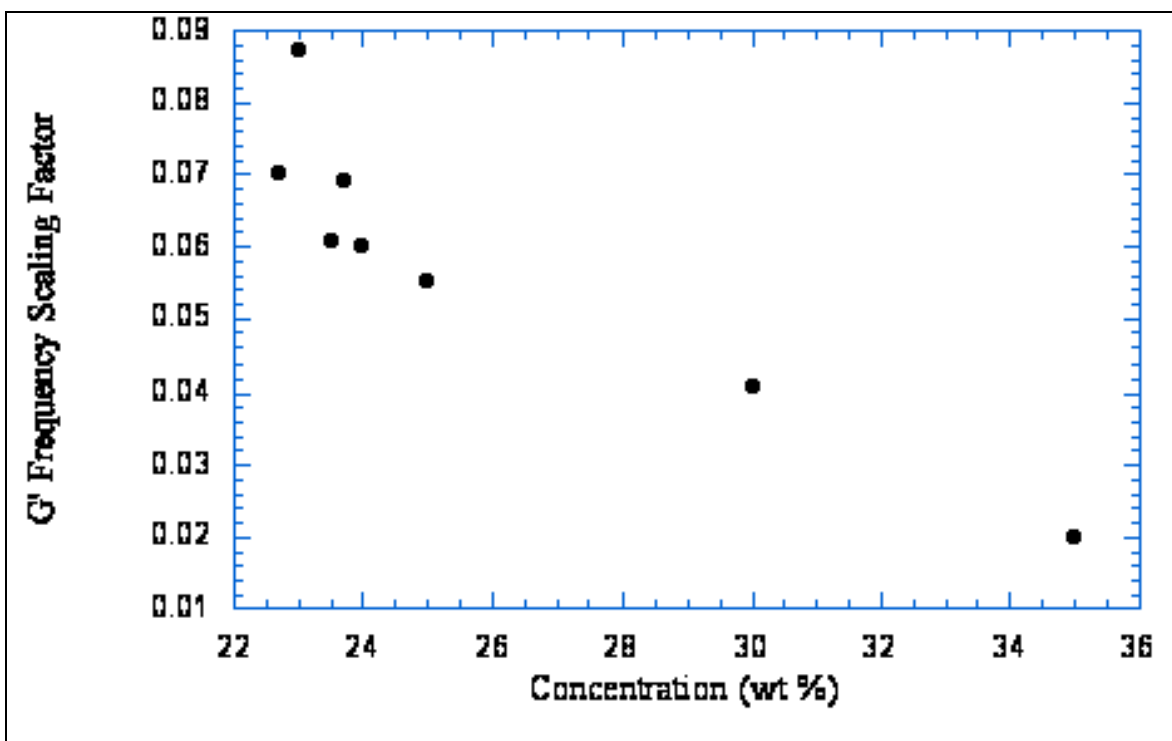
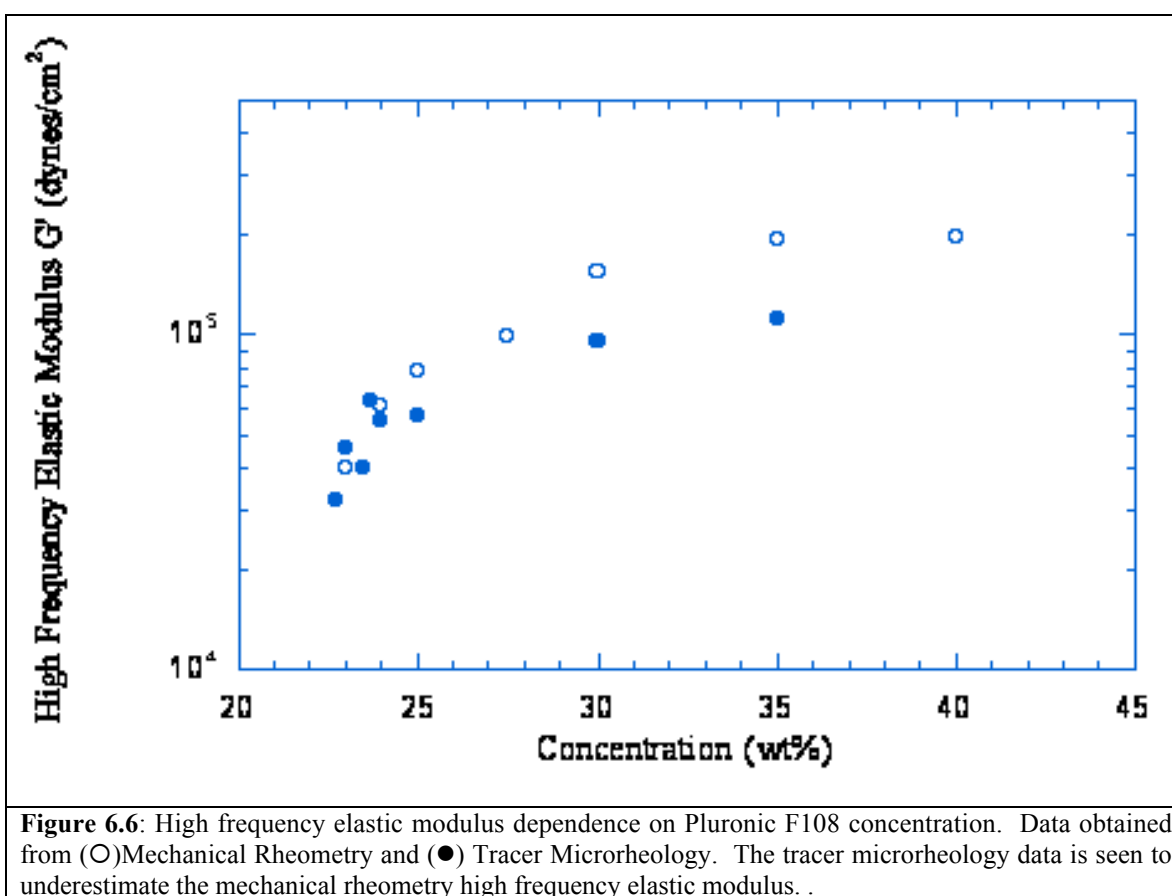


**Figure 6.5:** High frequency elastic modulus frequency scaling factor dependence on the concentration. The frequency dependence gets weaker with increasing concentration, due to the formation of a stronger gel at higher concentration.

The high frequency plateau observed by Shikata and Pearson (5), in contrast to the frequency dependent behavior predicted theoretically (1) and observed experimentally (2), was not seen at all concentrations examined by them and those that did seem to limit to a plateau did not demonstrate a definitive plateau over a broad frequency range. The observation of a high frequency plateau for the mechanical rheometry measurements in the present study may be attributable to the limited frequency range that was investigated. Unfortunately, time temperature superposition is not an option owing to the temperature dependent phase behavior of the Pluronic™ F108 system.

#### 6.4.4 Concentration Dependence of High Frequency Modulus:

Figure 6.6 illustrates the concentration dependence of the high frequency elastic modulus extracted from tracer microrheology and mechanical rheometry. The high frequency tracer microrheology is seen to underestimate the high frequency elastic modulus determined from mechanical rheometry for the high concentration samples. The agreement is seen to be reasonable for lowest two mechanical rheometry concentrations of 23 and 24 wt%.



The mechanical rheometry and the tracer microrheology data both exhibit a stronger than linear dependence. If the system was behaving as a hard sphere dispersion a close to linear dependence should have been observed. However as mentioned earlier the system should exhibit a potential

which is softer than a perfectly hard sphere potential. Therefore a linear dependence on the concentration is not expected. A power law fit of the data was attempted. However, the observed concentration dependence and limited number of data points did not allow a good power law fit of the data. Slight differences in the concentration dependence observed for the mechanical rheometry and the tracer microrheology data may be attributable to the frequency range probed in the two techniques. The tracer microrheology technique provides access to much higher frequencies than mechanical rheometry. The limited frequency range available in mechanical rheometry may not be sufficient to measure true "high frequency" behavior in that highest frequency probed may still be lower than that required to exceed the time scale for micellar Brownian motion. The high frequency elastic modulus is strongly dependent on near contact intermicellar interactions and is therefore the most direct probe of the interparticle interaction potentials. However, the most basic requirement for utilizing rheological measurements in this manner is that the elastic modulus must be measured at frequencies that are above the onset of the true "high frequency" behavior. As noted earlier, these frequencies are usually not accessible through mechanical rheometry without the use of time-temperature superposition, an option not feasible for the temperature sensitive Pluronic F108 system. Diffusing wave spectroscopy based tracer microrheology provides access to these frequencies.

### ***6.5 Conclusions:***

This chapter detailed the first experimental investigation of the high frequency elastic modulus of aqueous Pluronic™ F108 solutions in the cubic crystalline phase via diffusing wave spectroscopy based tracer microrheology. The high frequency elastic modulus is one of the most

direct probes of interparticle interaction potentials at short distances. The dependence of the high frequency elastic modulus on the intermicellar separation distance was studied as a means of investigating interparticle interactions in the soft crystals. It was observed that there is a strong dependence of the high frequency elastic modulus on the intermicellar separation distance. On attempting to model this dependence with a host of different interparticle interaction potentials, it was observed that the actual interaction potential exhibited a behavior that was intermediate to the hard and soft sphere type associated with similar systems. A definitive conclusion however cannot be drawn at this stage due to the accuracy of the estimated structural parameters and the use of a perfect crystal structure factor in model calculations. The high frequency elastic modulus, as determined through tracer microrheology studies, exhibited a slight frequency dependence that diminished with increasing Pluronic™ F108 concentration. This is most likely due to the formation of stronger gels with increasing concentration. The frequency dependence observed here was weaker than that expected for a purely hard sphere dispersion. This may be a consequence of the softer intermicellar interactions in this system.

## References

1. Lionberger ,R.A. and Russell,W.B.; *J.Rheol*, **1994**, 38, 1885
2. Fritz,G. B., Maranzano,J., Wagner ,N. J. and Willenbacher, N.; *J of Non Newtonian Fluid Mech*, **2002** 102, 149
3. van der Werff, J. C., de Kruif, C. G., Blom, C. and Mellema,; *J.Phys Rev A*, **1989**,39, 795
4. Mason, T. G. and Weitz, D. A.; *Phys Rev Lett*, **1995**,75, 2770
5. Shikata, T. and Pearson, D.S.;*J. Rheol* , **1994**,38, 601
6. Bergenholtz, J., Willenbacher, N., Wagner, N. J., Morrison, B., van den Ende, D. and Mellema, J. ; *J of Coll and Inter Sci*, **1998**, 202, 430
7. Horn, F. M., Richtering, W., Bergenholtz, J. , Willenbacher, N. and Wagner, N. J.;*J of Coll and Inter Sci*, **2000**, 225, 166
8. Wagner, N. J. ; *J of Coll and Inter Sci*, **1993**,161, 169
9. Elliott, S. L. and Russel, W. B.; *J.Rheol*, **1998**,42,361
10. Duits, M. H., Nommensen, P. A, van den Ende, D. and Mellema, J.;*Colloids and Surf A*, **2001**,183,335
11. Nommensen, P.A., Duits, M. H., van den Ende, D. and Mellema, J.; *Langmuir*, 2000,16, 1902
12. Buitenhuis, J. and Forster, S.; *J. Chem. Phys*, **1997**,107, 262
13. Witten ,T.A. and Pincus, P.A.; *Macromolecules*, **1986**,19, 2509
14. Alexandridis, P. , Nivaggioli, T. and Hatton, A. T.; *Langmuir*,**1995** ,11, 1468
15. Eiser, E., Molino, F. and Porte G.; *Euro Phys Jour E*, **2000**, 2,39 ()
16. Eiser, E., Molino, F., Porte, G. and Pithon, X.; *Rheol Acta*, **2000**, 39, 201

17. Molino, F. R., Berret, J. -F., Porte, G., Diat O. and Lindner, P.; *Eur. Phys. Jour B*, **1998**, 3, 59
18. Weitz, D.A. and Pine, D.J.; *Diffusing Wave Spectroscopy in Dynamic Light Scattering- the method and some applications* (Clarendon Press 1993)
19. Mason, T.G. and Weitz, D.A.; *Phys. Rev. Lett*, **1995**, 74, 1250
20. Amin, S. and van Zanten, J.H.; *manuscript in preparation*
21. Zwanzig, R. and Mountain, R.D.; *J. Chem Phys*, **1965**, 43, 44
22. Mewis, J. and 'Haene, P.D.; *Makromol. Chem., Macromol. Symp*, **1993**, 68, 213
23. Nolan, S.L., Phillips, R.J., Cotts, P.M. and Dungan, S.R.; *J of Coll and Inter Sci*, **1997**, 191, 291

# Chapter 7

## Static Light Scattering Measurements Of Micellar Soft Crystals

---

### 7.1 Abstract:

This chapter reports on a detailed static light scattering investigation into the Pluronic™ F108 system. Concentrations are chosen such that the entire phase range from isotropic micellar solution to an ordered FCC cubic phase can be investigated. The scattered intensity as investigated through the extracted zero angle Rayleigh Ratio shows an essentially monotonic increase with concentration until reaching the highest concentrations where it remains essentially unchanged. The zero angle Rayleigh ratio increase can primarily be attributed to increasing concentrations. A major concern was the strong angular dependence of the scattered intensity at low  $q$  wavevectors. An Ornstein-Zernicke fit of the high concentration regime indicates that the correlations lengths are extremely large. This indicates that  $R_{\square}(q) \sim q^{-2}$  which means  $q^2 \lambda^2 \gg 1$ . This makes the accuracy of the  $\square R_0$  values questionable. Although the magnitudes may vary, the qualitative trends in the data are however not expected to change dramatically. The osmotic compressibility and osmotic pressures are therefore extracted in order to gain a qualitative understanding of the behavior. It is observed that the osmotic compressibility increased up to 6wt% after which it remains essentially constant and then decreased at the higher concentrations. It is expected that  $\square \square / \square c$  should increase with increasing concentration, due to the increasing micellar interactions associated with increasing concentrations, thereby indicating that the extrapolated  $\square R_0$  values are not accurate, especially at high concentrations.

## ***7.2Introduction:***

Pluronics<sup>TM</sup> or Polaxomers<sup>TM</sup> are a commercially important class of triblock copolymers, consisting of polyethylene oxide-polypropylene oxide-polyethylene oxide (PEO-PPO-PEO) repeat units. They are interesting from a microstructure-property perspective as they are amphiphilic and in the presence of a selective solvent tend to form thermodynamically stable micelles as well as an array of lyotropic liquid crystalline mesophases of varying morphologies(1). Recent experimental investigations on these systems have therefore focused on identification of the different morphologies, delineation of the composition temperature ranges where the morphologies occur and the structural characterization of the different morphologies (1-29).

An interesting feature of this class of amphiphilic triblock copolymers is that they can form 'gels'. It must be noted that these 'gels' are different from typical polymer, gels which occur as a result of physical or chemical cross links. In this case, the term 'gel' refers to the strong elastic properties that these materials exhibit at high concentrations in an appropriate temperature range. Here, it is the packing of triblock copolymer micelles into a crystalline lattice which gives rise to the structural integrity of the gels. Structural characterization of these materials both in the cubic crystalline phase and in the isotropic micellar phase, has been carried out primarily through use of small angle neutron scattering (SANS), small angle x-ray scattering (SAXS) and light scattering (14-29). The focus of the scattering studies was to extract structural information from the scattered intensity profiles through use of various structural models. SANS data have been analyzed for these systems using several form factors, such as, core-shell concentric spheres (17), a spherical core coated with gaussian chains (19) and a sticky hard-sphere core-shell model (20). Static light scattering studies (25-28) have also been conducted on di and

triblock micellar systems and were typically analyzed assuming a hard sphere interaction potential (26,28).

The majority of structural characterization studies carried out on Pluronic™ systems have been focused on determining structural parameters such as the aggregation number, the micelle radius, etc. Osmotic compressibility measurements on triblock copolymer systems as it goes from an isotropic micellar system to a cubic crystalline structure have not been reported till date. The osmotic compressibility concentration variation is essential from a number of different perspectives. First of all it provides insight into the micellar interactions underlying the soft crystal formation. Second the osmotic compressibility information may aid the interpretation of Brownian motion of probe particles in these systems. Tracer microrheology experiments conducted in our laboratory (Pluronic™ Chapter on Tracer Microrheology) have shown a discrepancy between the rheological parameters extracted from probe motion experiments and those from mechanical rheometry. Recent theoretical developments have indicated that the longitudinal modes may affect the extracted rheological parameters. With a view to gaining deeper insight into the changes in the osmotic compressibility with concentration, a comprehensive static light scattering experiment was conducted on the Pluronic™ F108. This triblock copolymer has the structure  $(\text{PEO})_{127}\text{-(PPO)}_{48}\text{-(PEO)}_{127}$ . Phase behavior studies of aqueous solutions of Pluronic™ F108 indicate that the equilibrium between triblock copolymer unimers and micelles is largely temperature dependent with micelle formation occurring at 2wt% for a temperature of 25°C (9). As the Pluronic™ F108 concentration increases, the micelle interactions increase with these interactions eventually leading to a phase transition from a disordered to an ordered micellar dispersion. While previous studies indicate that this phase transition occurs at about 27 wt% (9), in progress tracer microrheology studies indicate the onset

of gel-like behavior at much lower concentrations of  $\sim 22.7$  wt% (Pluronic Chapter on Tracer Microrheology). Both of these observations are consistent with a reported coexistence region between approximately 22 and 27 wt% at 25 °C (22-24). Small angle x-ray scattering investigations indicate that a 35 wt% Pluronic™ F108 aqueous solution at 25 °C forms a polycrystalline FCC soft crystal. This FCC soft crystal is composed of micelles with a radius of gyration of 120 Å (corresponding to an aggregation number of approximately 50) exhibiting a lattice parameter of 294 Å and a nearest neighbor separation of 208 Å (22-24).

### ***7.3 Materials and Methods:***

Pluronic™ F108 was obtained from BASF Corporation and used without further purification. Dust free Pluronic F108 aqueous solutions were prepared with deionized water that had been filtered thrice through a 0.02  $\mu$ m filter (Whatman-Anotop 25). All samples were prepared at room temperature (25 °C) and then cooled down to 5°C. All samples were allowed to equilibrate for two weeks prior to taking measurements. Samples were prepared in which the Pluronic™ concentration was varied from 0.1 to 40 wt%.

The static light scattering measurements were performed with a DAWN EOS Laser Photometer (Wyatt Technology Inc, Santa Barbara, CA), based on a photodiode array with eighteen fixed detectors at angular positions ranging from 22.5° to 147°. The light source was a vertically polarized 30mW gallium arsenide laser with a wavelength of 690 nm *in vacuo*. The Rayleigh ratios for each concentration were extracted and then analyzed with a view of obtaining the osmotic compressibilities.

### ***7.4 Results and Discussion:***

***7.4.1 Variation of the zero angle Rayleigh Ratio:*** To gain insight into the osmotic compressibility variation associated with the change from a disordered micellar dispersion to an

ordered micellar FCC cubic lattice, static light scattering experiments were conducted over a wide range of Pluronic™ F108 concentrations. Figure 7.1 illustrates the variation of the Rayleigh Ratio with the wavevector  $q$ , for a few of the concentrations examined. It is clearly seen that there is hardly any angular dependence of the scattered intensity at the low concentrations. This is expected as there should be very little interactions between the micelles in this dilute concentration regime. The onset of micellar interactions appears to take place at about 6-8 wt %. The scattered intensity angular dependence is also observed to become stronger as the Pluronic™ concentration increases from 6% to 40% (the highest concentration examined)

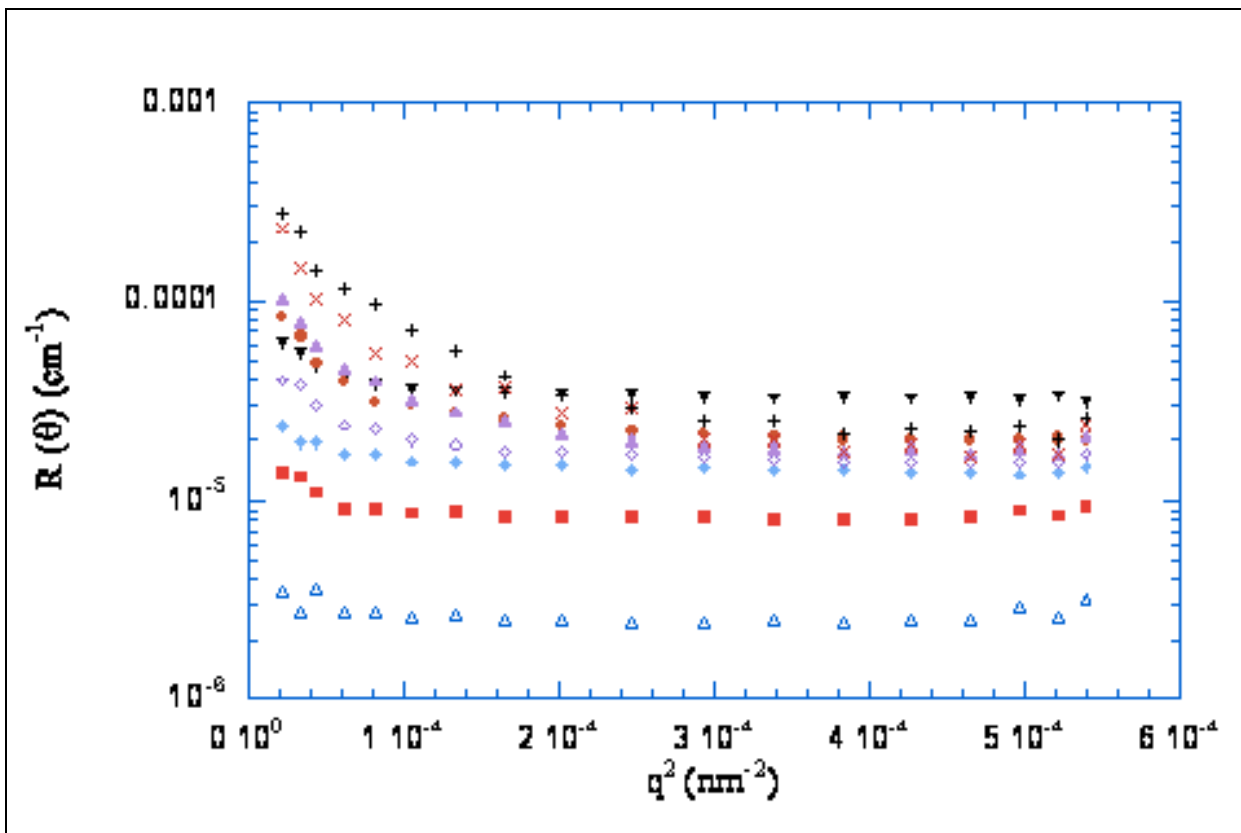


Figure 7.1: Variation of the Rayleigh Ratio with  $q^2$ . The concentrations shown here are ( $\Delta$ )0.2% ( $\blacksquare$ )1.0% ( $\blacklozenge$ )6.0% ( $\square$ )8.0% ( $\blacktriangledown$ ) 14.0% ( $\bullet$ ) 18.0% ( $\blacktriangle$ ) 22.0% ( $\times$ )30.0% and ( $+$ )40.0%. The angular dependence is observed to increase with increasing concentration.

Another notable feature about the scattered intensity seems to be the nearly monotonic increase of the Rayleigh Ratio magnitude with increasing concentration at small  $q$ . Only at the highest

concentrations there seems to be no further increase in the value. The nearly monotonic increase is more clearly observed when the Rayleigh Ratio extrapolated to zero  $q$  is plotted versus the concentration (Figure 7.2). One point that must be noted is that in order to extrapolate the Rayleigh Ratio values to zero  $q$ , the  $q$  dependence data was fit with a polynomial in  $q^2$  and the extrapolation carried out such that a best fit was obtained especially for the low  $q$  data.

The concentration dependence of the zero angle Rayleigh Ratio shows an essentially monotonic increase as illustrated in figure 7.2. The most notable feature of the  $R(0)$  concentration dependence is that the slope of the dependence is seen to change at about 6wt%. The slope change actually occurs between 2 and 6% as the  $R(0)$  is seen to be not changing appreciably between 2% to 6%. This may be indicative of the onset of micellization. Although the reported CMC value of the Pluronic™ F108 system is 2wt%, this may actually not be a sharp CMC.

The zero angle Rayleigh Ratio concentration dependence can be written as (30),

$$\square R_{\square} = KCMP(q)S(q), \quad (1)$$

where,  $K$  is an optical constant,  $C$  is the concentration and  $M$  is the molar mass.  $P(q)$  is the particle form factor and  $S(q)$  is the static structure factor. Since the Pluronic™ micelles have a radius of gyration of about 120 Å, which is at the limit of the spatial resolution of a light scattering experiment,  $P(q)$  can be set equal to 1. After the onset of micellization, this expression may be written as:

$$\square R_0 = K(C - CMC)M_{mic}S(q) + K(CMC)M_{fp}S(q) \quad (2)$$

This equation indicates that the total scattered intensity as reflected through the Rayleigh ratio has contributions from both the micelles and unimers (referred to as free polymer, fp, in the equation). Small angle x-ray scattering investigations indicate that the Pluronic™ F108 micelles

have an aggregation number of 50, implying,  $\frac{M_{mic}}{M_{fp}} \approx 50$  (22-24). This would explain the sharp

change in the slope. In order to explore this change in the zero angle Rayleigh Ratio concentration dependence slope change, the  $\square R_0$  is plotted with the viscosity as a function of concentration. The behavior is illustrated in figure 7.3.

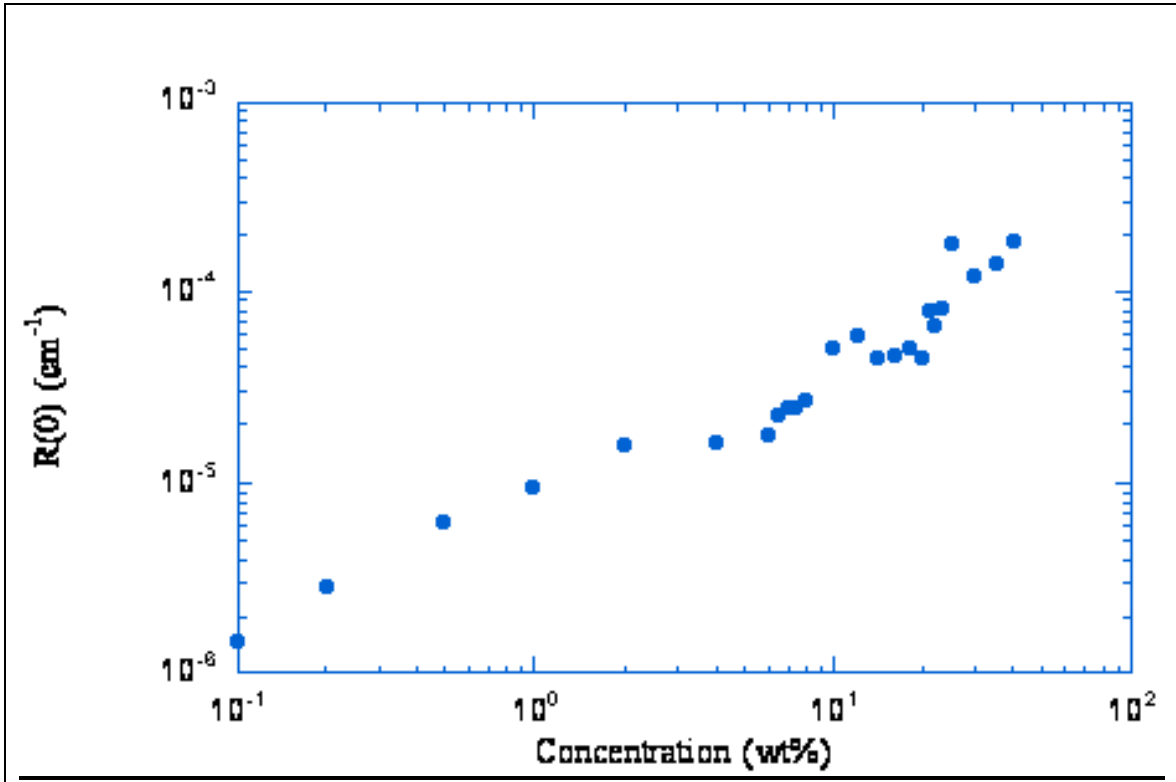
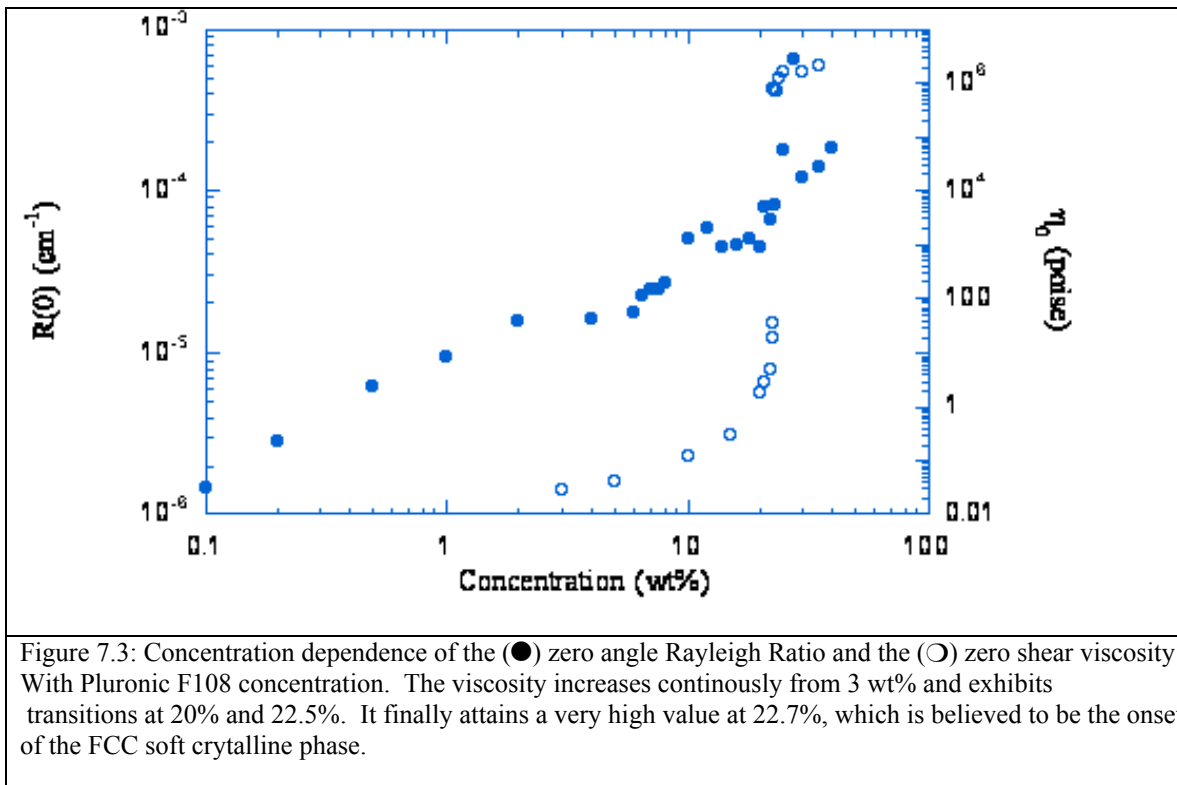


**Figure 7.2:** Variation of Zero Angle Rayleigh Ratio with Pluronic Concentration. The behavior is essentially a monotonic growth. A distinct change in slope is however observed at 6%.

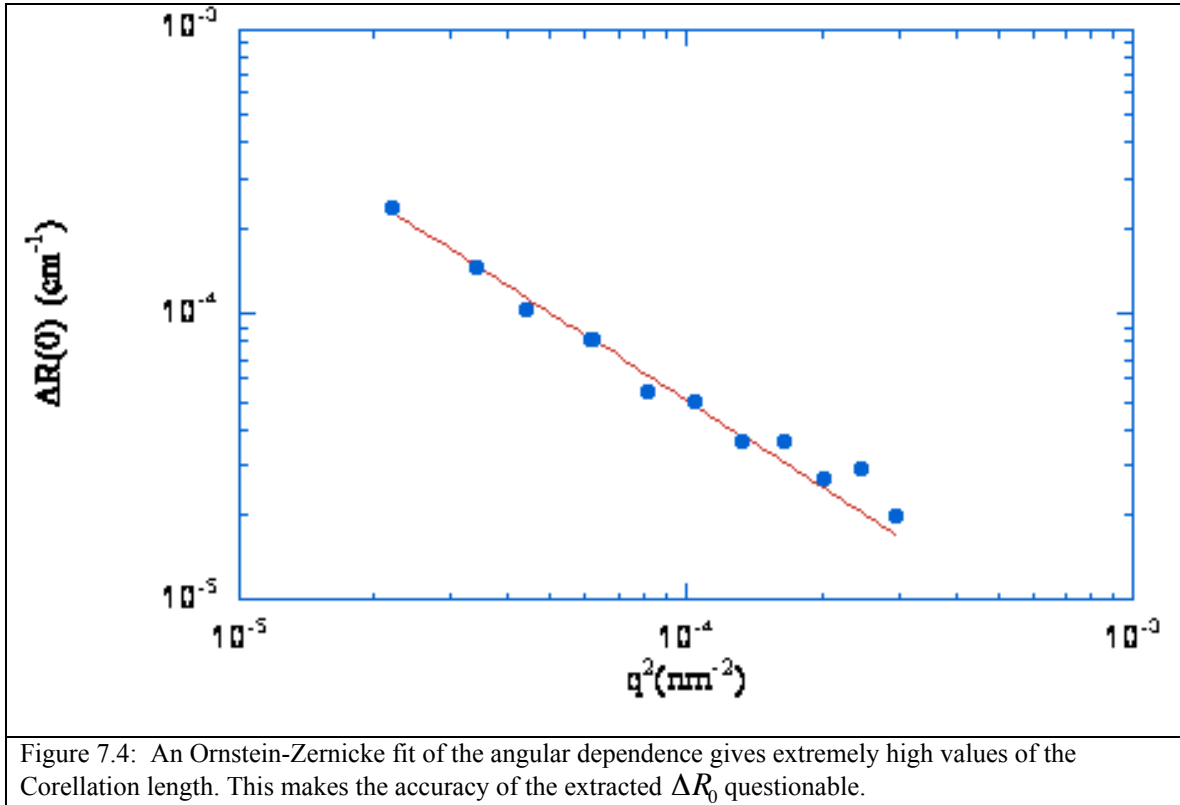
The zero shear viscosity increases continuously with the concentration. The behavior is typically that found for close packing. There are no abrupt changes except at 20 to 22.7 wt%. This is due to increasing micellar crowding and the transition to a FCC soft crystal. The  $\square R_0$  increases continuously and exhibits a change in the slope at 6 wt%. The dramatic change in the zero shear viscosity indicating a transition into a FCC soft crystal does not seem to be reflected in the  $\square R_0$  behavior, thereby indicating that the  $\square R_0$  transition is simply due to micelle formation.

Tracer microrheology studies (Pluronic™ Chapter on Tracer Microrheology) of the Pluronic™ F108 system do tend to indicate that the initial onset of the cubic phase takes place between 22.5% and 22.7%. A notable feature of the zero angle Rayleigh Ratio is that a maximum is not observed for the range of concentrations investigated, unlike the case of hard sphere dispersions.



The zero angle Rayleigh Ratio is affected by both the micellar concentration and interactions. In fact it is very difficult to decouple these effects and isolate the main contributing factor to the  $\square R_0$  behavior. The increase in  $\square R_0$  which is observed in figure 7.2 may be due to increasing micellar growth due to mass action effects, especially at the low concentration regime and simply due to increasing interactions at the high concentration regime. Hard sphere interaction would cause the  $\square R_0$  to decrease with increasing concentration, this however is not the case as

seen through figure 7.1. The behavior illustrated in figure is most likely due to the formation of FCC soft crystals gains that strongly forward scatter light.



7.4.2 *Ornstein-Zernicke fit of data:* Low  $q$  scattering from the micelles is seen to increase considerably with increasing concentration. The strong angular dependence at low  $q$  prompted a more detailed examination of the data. One way to check the reliability of the technique as a method for investigating the zero wavevector static properties of the system was to apply the Ornstein-Zernicke equation to model the scattered intensity angular dependence. The Ornstein Zernicke (O-Z) expression is given by:

$$\square R(q) = \frac{\square R(0)}{(1 + q^2 \square^2)} \quad (3)$$

Where  $\xi$  is the solution correlation length. To accurately isolate the zero angle Rayleigh Ratio, it is best to have,  $q\xi < 1$ . Figure 4 represents an (O-Z) fit to the 30 wt% data. From the fit the correlation length was extracted (here this probably represents the size of the FCC crystalline grains). The correlation length was found to be about 400 nm for the high concentration samples. This makes the extraction of the zero angle Rayleigh Ratio unreliable to a certain extent. This is apparent from figure 7.4 which indicates that  $R_{\theta}(q) \sim q^{-2}$  which means  $q^2\xi^2 \gg 1$ . Since the strong low q dependence is seen also in the intermediate samples, this raises the question about the reliability of the zero angle extrapolation for a large number of samples. Although the samples were prepared very carefully, this could be an artifact of dust contamination. In order to check for the possibility of dust contamination and to homogenize the samples, they have been filtered through a 0.1 micron filter and will be measured in the near future. In the event that the data still exhibit very high correlation lengths, this will indicate that the samples cannot be accurately characterized by the available static light scattering instrument. Much lower q values will then be required in order to access the low q behavior adequately (i.e.  $q\xi \ll 1$ ). It should be mentioned that a detailed x-ray scattering investigation will be undertaken which will also give additional structural information on the system at larger wavevector

*7.4.3 Osmotic compressibility behavior:* Although the extrapolated zero angle Rayleigh Ratios may not be entirely accurate for the high and intermediate concentration range, the overall behavior is not expected to change dramatically. The osmotic compressibility was extracted from the zero angle Rayleigh Ratio through:

$$\xi R_0 = KCRT \left[ \frac{\partial \xi}{\partial c} \right]^{-1} \quad (4)$$

From the figure it is seen that the osmotic compressibility goes through a maximum at 6 wt% and then the value almost tends to stay the same until finally decreasing at very high concentrations. The data does show a considerable amount of scatter. This can be attributed to the accuracy of the  $\Delta R_0$  extrapolation at the intermediate and high concentrations.

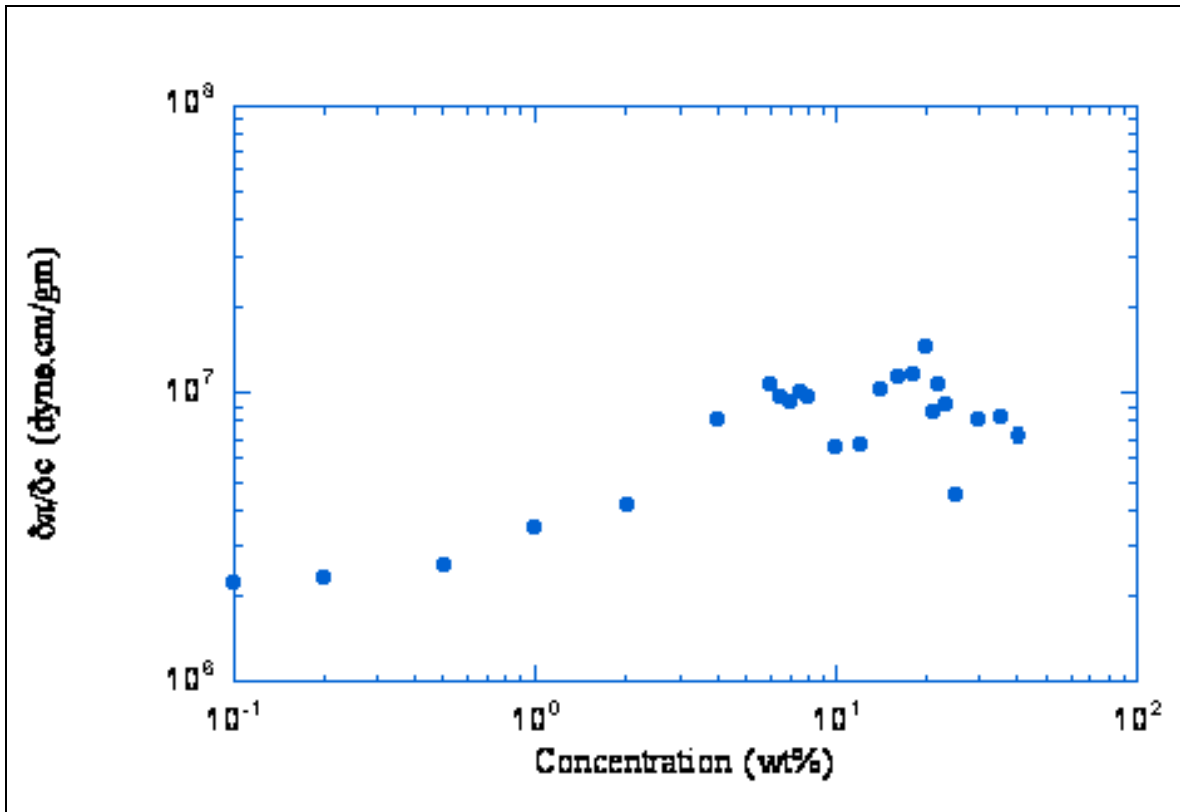


**Figure 7.5:** Variation of the osmotic compressibility with concentration. The osmotic compressibility exhibits a clear peak at 6 wt% remains essentially unchanged and finally decreases.

The osmotic compressibility is directly affected by intermicellar interactions. The osmotic compressibility suggests that  $\Delta R_0$  is being underestimated for concentrations  $\geq 10\text{wt}\%$  as  $\Delta R_0/\Delta c$  should increase with increasing concentration since the increasing micellar interactions associated with increasing concentration is not reflected in the osmotic compressibility data. The osmotic compressibility is an indicator of the interparticle interaction potentials acting in the system. The osmotic pressure is directly related to the radial distribution function through (32):

$$\Pi = nkT \left[ \frac{2\beta}{3} n^2 \int_0^{\infty} r^3 g(r) \frac{d\beta}{dr} dr \right] \quad (5)$$

where  $\beta$  is the interaction potential, and  $g(r)$  is the radial distribution function. Depending upon the system being investigated an appropriate form for the interaction potential can be chosen and the osmotic compressibility behavior modeled. For the vast majority of studies, the hard sphere potential has been the predominant interaction potential used to interpret scattering studies of small molecular surfactant micelles. However the peak in  $\Pi/R_0$  expected near Pluronic F 108 concentrations of 10-15 wt% is not observed.

**7.4.4 Osmotic Pressure Behavior** As was mentioned earlier the osmotic pressure is essentially determined by the microstructure and interactions present in the complex fluid system. As was seen earlier interactions in the Pluronic™ F108 system are not well described by a hard sphere potential but rather by a potential that is in between a hard and soft sphere. Unlike hard spheres, the Pluronic™ micelles are deformable to a certain extent when they are compressed. Qualitatively, the osmotic pressure concentration dependence that is observed here is reminiscent to a certain extent of the osmotic pressure concentration dependence seen in emulsions (36). From a structural perspective emulsion droplets are to a certain extent similar to the Pluronic micelles as both are somewhat deformable. Theoretical and experimental investigations of emulsions have shown that the droplet response to compression has three characteristic regimes in three dimensions- 1) a regime corresponding to when the droplets are infinitesimally deformed, 2) a region which consists of deformation that follows contact and 3) a third regime in which the droplet response to compression sharply rises due to volume conservation effects. The behavior that is seen here is probably indicative of an osmotic pressure behavior that is similar to

the behavior in the 1<sup>st</sup> and 2<sup>nd</sup> regimes. Inferences drawn from the SAXS scattering data indicate that solutions in the FCC phase are compressed so the behavior at the highest concentration range is probably similar to a emulsion regime 2 behavior. From the extracted osmotic compressibility behavior, it can be inferred that a final rapid increase in the osmotic pressure typical of emulsion regime 3 behavior was not observed here.

### **7.5 Conclusions:**

This chapter has reported on a detailed static light scattering investigation into the Pluronic™ F108 system. Concentrations were chosen such that the entire phase range from isotropic micellar solution to an ordered FCC cubic phase could be investigated. The scattered intensity as investigated through the extracted zero angle Rayleigh Ratio showed an essentially monotonic increase with concentration until reaching the highest concentrations where it remains essentially unchanged. The zero angle Rayleigh ratio increase could primarily be attributed to increasing concentrations. A major concern was the strong angular dependence of the scattered intensity at low  $q$  wavevectors. An Ornstein-Zernicke fit of the high concentration regime indicated that the correlations lengths are extremely large. This indicates that  $R_{\square}(q) \sim q^{-\square}$  which means  $q^2 \square^2 \gg 1$ . This makes the accuracy of the  $\square R_0$  values questionable. Although the magnitudes may vary, the qualitative trends in the data are however not expected to change dramatically. The osmotic compressibility and osmotic pressures were therefore extracted in order to gain a qualitative understanding of the behavior. It was observed that the osmotic compressibility increased up to 6wt% after which it remained essentially constant and then decreased at the higher concentrations. It is expected that  $\square \square / \square c$  should increase with increasing concentration, due to the increasing micellar interactions associated with increasing

concentrations, thereby indicating that the extrapolated  $\square R_0$  values are not accurate, especially at high concentrations.

## ***References:***

1. Alexandridis, P.; *Current Opinion in Colloid and Interface Science*, **1997**, 2, 478
2. Alexandridis, P., Hatton, T. A.; *Colloids Surf A*, **1995**, 96, 1
3. Almgren, M., Brown, W., Hvidt, S.; *Colloid Polym Sci*, **1995**, 273, 2
4. Nace, V.M. (ed.); *Nonionic Surfactants: Polyoxyalkylene Block Copolymers*. **1996**, New York Mercel Dekker Inc.
5. Chu, B.; *Langmuir*, **1995**, 11, 414
6. Chu, B.; Zhou, Z.; *Surf Sci Ser*, **1996**, 60, 31
7. Nace, V. M.; *Surf Sci Ser*, **1996**, 60, 145
8. Alexandridis, P., Lindman, B. (Eds.); *Amphiphilic Block-Copolymers Self Assembly and Applications*, **1997**, Amsterdam, Elsevier Science BV.
9. Alexandridis, P., Nivaggioli, T. and Hatton, A. T.; *Langmuir*, **1995**, 11, 1468
10. Alexandridis, P., Nivaggioli, T. and Hatton, A. T.; *Macromolecules*, **1994**, 27, 2414
11. Wanka, G., Hoffmann, H., Ulbricht, W.; *Colloid Polym Sci*, **1990**, 268, 101
12. Hvidt, S.; *Colloids Surf A*. **1996**, 112, 201
13. Armstrong, J., Chowdhury, B. O., O'Brien, R., Beezer, A., Mitchel, J., Leharne, S.; *J. Phys Chem*, **1995**, 99, 4590
14. Mortensen, K.; *J Phys: Condens Matter*, **1996**, 8, A103
15. Alexandridis, P., Zhou, D., Khan, A.; *Langmuir* **1996**, 12, 2690
16. Prud'homme, R. K., Wu, G., Schneider, D.K.; *Langmuir*, **1996**, 12, 4651
17. Mortensen, K., Pedersen, J. S.; *Macromolecules*, **1993**, 26, 805
18. Wu, G., Chu, B., Schneider, D. K.; *J Phys Chem*, **1995**, 99, 5094
19. Pedersen, J. S., Gerstenberg, M. C.; *Macromolecules*, **1996**, 29, 1363
20. Liu, Y. C., Chen, S. H., Huang, J.S.; *Phys Rev E*, **1996**, 54, 1698

21. Berret, J-F., Molino, F., Porte, G., Diat, O., Lindner, P.; *J Phys Condens Matter*, **1996**, *8*, 9513
22. Eiser, E., Molino, F., and Porte, G.; *Euro Phys Jour E*, **2000**, *2*,39
23. Eiser, E., Molino, F., Porte, G. and Pithon, X.; *Rheol Acta*, **2000**,*39*, 201
24. Molino, F. R., Berret, J –F., Porte, G., Diat, O. and Lindner, P.; *Eur. Phys. Jour B*,**1998**, *3*, 59
25. Schadler, V., Nardin, C., Wiesner, U., and Mendes, E.; *J.Phys Chem B*, **2000**, *104*, 5049
26. Kelarakis, A., Havredaki, V., Viras, K., Mingvanish, W., Heatly, F., Booth, C., Mai, S-M.; *J Phys Chem B* , **2001**, *105*, 7384
27. Mingvanish, W., Chaibundit, C., Booth, C.; *Phys Chem Chem Phys*, **2002**, *4*, 778
28. Nolan, S. L., Philips, R. J., Cotts, P. M., Dungan, S. R.; *J of Colloid and Interface Sci*, **1997**, *191*, 291
29. Hamley, I. W., Castelletp ,V., and Fundin, J.; *Langmuir*, **2002**, *18*, 1051
30. Schurtenberger, P.; in *Light Scattering*, Brown B (ed)
31. Young, R.J. and Lovell, P.A.; *Introduction to Polymers*, **1981**, Chapman & Hall
32. Russel, W.B., Saville, D.A., and Schowalter, W.R.; *Colloidal Dispersions*, **1989**, UK, Cambridge University Press
33. Carnahan, N.F. and Starling, K.E.; *J.Chem Phys*, **1969**, *51*, 635
34. Pusey, P.N. and van Megen, W.; *Complex and Supramolecular Fluids* (Safran S.A. and Clark N.A. eds), **1987**, 673, Wiley-Interscience
35. Woodcock, L.V.; *Ann. New York Acad Sci*, **1981**, *371*, 274
36. Mason, T.G., Lacasse, M-D., Grest, G.S., Levine, D., Bibette, J. and Weitz, D.A.; *Phys Rev E*, **1997**, *56*, 3150

## Chapter 8

### Conclusions and Recommendations for Future Work

---

#### ***8.1: Conclusions:***

The motivation of this experimental research project was to gain a better understanding of the potential connection between the Brownian motion of a probe particle and the viscoelastic response of the suspending media. In order to achieve this objective, tracer microrheology and mechanical rheometry study were conducted on three representative viscoelastic systems having widely varying dynamic properties and microstructure. The systems that were chosen were, (1) aqueous poly ethylene oxide (PEO) solution, (2) cetyltrimethylammonium bromide/ sodium salicylate worm like micelle solutions and (3) a poly ethylene oxide-poly propylene oxide-polyethylene oxide (PEO-PPO-PEO) triblock copolymer, Pluronic™ F108 in an aqueous solution. The objective was to study the dynamic response in these systems, as revealed through tracer probe motions and to try to gain an understanding of the effects of longitudinal and transverse modes on the extracted viscoelastic parameters. The PEO system was chosen as a representative flexible polymer, where the longitudinal modes should not play a significant role on the extracted parameters. The Pluronic™ system was chosen as it was expected that tracer microrheology experiments should reveal interesting high frequency behavior and the system should not be challenging from a tracer microrheology experimental standpoint. The wormlike micellar system was chosen as it was expected to exhibit Maxwellian fluid behavior, the simplest form of viscoelasticity.

**8.1.1 Poly ethylene oxide (PEO) aqueous solutions:** This work was a detailed tracer microrheology and mechanical rheometry study of aqueous solutions of the flexible polymer polyethylene oxide (PEO). The study was carried out on PEO solutions in which the concentration was varied from 0.2 to 15 wt%. This ensured the examination of the viscoelastic properties as the polymer solution progressed from the unentangled to the entangled regime. PEO solutions having concentrations greater than 1 wt% exhibited considerable elasticity, as manifested through development of a plateau in the evolution of the mean square displacement. The tracer microrheology measurements showed excellent agreement with the mechanical rheometry measurements especially for the higher concentrations as manifested by the excellent agreement of the creep compliance measured from the two techniques. A sphere size sweep on a 7 wt% PEO solution exhibited that the creep compliance was independent of probe size. This was indicative that neither structural effects nor longitudinal dynamical modes are playing a role in affecting the extracted viscoelastic properties.

. The terminal relaxation times and the zero shear viscosity extracted from the long time mean squared displacement behavior and from mechanical rheometry measurements exhibited deviations in quantitative agreement at low concentration, but excellent agreement at high concentrations. Power law fits of the zero shear viscosity and the terminal relaxation time concentration dependence exhibited stronger variations with concentration than expected for semi dilute polymer solutions. The time dependent diffusion coefficient exhibited the expected behavior of increasing time dependency and decreasing magnitude with increasing PEO concentration. This is due to the particle diffusion becoming highly restricted by the increasingly entangled PEO network.

### **8.1.2 CTAB/NaSal Wormlike Micellar Solution**

*8.1.2.1 Dynamic Light Scattering Measurements:* From the DLS measurements two distinct relaxation times were observed for CTAB concentration  $\geq 0.02$  M. The hydrodynamic correlation length,  $\zeta_H$ , associated with the fast relaxation mode was found to depend on both the CTAB concentration and NaSal:CTAB mole ratio. In particular, the CTAB concentration scaling of  $\zeta_H$  was shown to vary in a nonmonotonic manner with the NaSal:CTAB mole ratio. The scaling exponent was found to range from  $-0.25$  to  $-0.67$  where its minimum value was found for NaSal:CTAB mole ratios near 1.5-2.0. This is in strong support of the decreasing micellar ionization picture associated with increasing NaSal:CTAB molar ratio. The distinct minimum of the scaling exponent followed by a re-increase is indicative of micellar neutrality followed by a charge reversal at higher NaSal:CTAB molar ratios. The amplitude of the slow relaxation mode was observed to be strongly correlated with the hydrodynamic correlation length for NaSal:CTAB mole ratios less than or equal to 2 thereby strongly suggesting polymer/polyelectrolyte solution behavior at these conditions. The behavior of the hydrodynamic correlation length and slow mode amplitude were described quite well within a framework of micelle ionization and electrostatic screening effects. However, the NaSal:CTAB mole ratio and CTAB concentration dependence of the slow relaxation time could not be entirely explained within the context of electrostatic interactions. In order to account for the observed slow relaxation time behavior it was hypothesized that the micelle breaking time is influenced by bound salicylate ions whose degree of binding depends on both the NaSal:CTAB mole ratio and CTAB concentration.

*8.1.2.2 Static Light Scattering Measurements:* Most of the static parameters of interest corroborated the results of the dynamic light scattering measurements. The static correlation

length showed a similar dependence on the NaSal:CTAB molar ratio as the hydrodynamic correlation length did, in that it increased to a maximum and then decreased to an almost constant value. The behavior however was limited to concentrations below 0.3M. The  $\xi$  parameter exhibited a similar monotonically decreasing behavior with the NaSal:CTAB molar ratio. Supporting the decreasing micellar ionization picture associated with increasing NaSal:CTAB molar ratio. The distinct minimum followed by a re-increase to indicate neutrality and a charge reversal was however not observed in this case. One of the main results obtained from the static light scattering measurements was the extraction of the osmotic compressibility. The osmotic compressibility dependence on the NaSal:CTAB molar ratio exhibited a very interesting sharp transition at a particular NaSal:CTAB molar ratio after which the osmotic compressibility exhibited a much stronger dependence on the ratio. The ratio at which the sharp transition occurred was highly dependent on the CTAB concentration. This again supports the idea of charge reversal and its dependence on both the CTAB concentration and the NaSal:CTAB molar ratio. The osmotic pressure exhibited a power law dependence on the total concentration for each NaSal:CTAB ratio examined. The power law behavior was however divided into two concentration regimes for each NaSal:CTAB molar ratio. The low concentration regime corresponded with viscous samples and at high ratios showed behavior similar to the theoretical behavior exhibited by equilibrium polymers. The high concentration regime corresponded with mostly gellike samples and exhibited a behavior similar to polyelectrolyte gels.

The overall picture that emerged from the static and dynamic light scattering measurements on CTAB/NaSal system was that of a system where the competition between micellar charge, electrostatic screening and micelle breaking controls the system dynamics.

*8.1.2.3 Tracer Microrheology and Mechanical Rheometry:* The tracer microrheology measurements on this system have revealed the viscoelastic response of the system over a wide frequency range, not accessible through mechanical rheometry. A series of solutions having a constant CTAB concentration [0.1M] and varying NaSal:CTAB molar ratios were observed to exhibit very similar viscoelasticity. The major difference showing up in the long time behavior after the system has relaxed. The plateau modulus exhibited a nonmonotonic dependence on the NaSal:CTAB molar ratio. The tracer microrheology and mechanical rheometry comparisons were also very interesting. The agreement between the two techniques was highly dependent on the frequency and the NaSal:CTAB molar ratio. The best agreement which was seen at lower frequencies or longer times was for the highest and lowest ratios examined. Sphere size sweeps also revealed that the creep compliance data could not be collapsed onto a single master curve. This is indicative that longitudinal dynamical modes or structural features may be affecting the extracted viscoelastic parameters. The deviations in the tracer microrheology and mechanical rheometry plateau moduli were also seen to track with the bulk longitudinal elastic modulus,  $M_G$ . However, the location of maximum deviation seems to occur at lower NaSal:CTAB molar ratios than that of the longitudinal elastic modulus. Therefore it is difficult to make any definitive conclusions at this stage.

### ***8.1.3 Pluronic<sup>TM</sup> F108 Triblock Copolymer:***

*8.1.3.1 Mechanical Rheometry:* The linear viscoelasticity of aqueous Pluronic<sup>TM</sup> F108 FCC soft crystals was investigated via mechanical rheometry for a number of concentrations above the disordered micelle-FCC soft crystal transition concentration. It was observed that the viscoelastic moduli  $G'$  and  $G''$  showed essentially a frequency independent behavior especially at the higher concentrations. This is the expected predominantly elastic behavior generally

observed for solids and strongly gelled systems. The complex viscoelastic moduli  $G^*$ , which was primarily dominated by the elastic moduli, showed increasing plateau values with increasing concentrations and essentially constant values at the highest concentrations that were probed. The concentration dependence of the  $G^*$  plateau was stronger than the linear dependence typically observed for hard sphere dispersions. This deviation away from hard sphere behavior was attributed to the longer range potential present in FCC crystalline structures. The near constant values of  $G^*$  at higher concentrations was attributed to the weaker concentration dependence of the interparticle separations due to compression and interpenetration of coronal layers due to increased packing. The complex viscoelastic moduli  $G^*$  showed qualitative agreement with the creep compliance which was obtained through constant stress measurements. The quantitative disagreement was attributed to the different flow behavior accessed in the two different measurements. The observed rheological behavior indicates that micellar packing and the intermicellar interaction potential plays a dominant role-this is most clear when discussed in the context of the viscosity behavior. The viscosity frequency dependence indicates that the interparticle interactions were becoming more hard sphere in nature with increasing concentration due to compression and interpenetration of the coronal layers under tight packing conditions.

*8.1.3.2 Tracer Microrheology:* In order to investigate the changes in the viscoelastic response of the system associated with changes in microstructure, tracer microrheology measurements were carried out over a wide range of Pluronic F108 concentrations varying from 3 to 35 wt %. As the technique allowed the observation of the viscoelastic behavior over a wide frequency range, a wide variety of interesting dynamical behavior was observed with changing microstructure, advocating the utility of the technique as a sensitive probe of microstructural and dynamical

changes. The mean squared displacement exhibited a dramatic change in the temporal variation at about 22.7 wt% indicating the probable onset of the FCC crystalline phase. The complex viscoelastic modulus also indicated that the system is essentially viscous when in the isotropic micellar solution phase and increasing elastic with increasing order in the FCC soft crystalline phase. Tracer microrheology underestimated the complex viscoelastic modulus plateau modulus (overestimated the creep compliance) compared with mechanical measurements for all the concentrations investigated. Sphere size sweep conducted on three different concentrations showed increasing disagreement between the creep compliance extracted with different sphere sizes as the Pluronic™ concentration was increased. This was indicative that either the longitudinal dynamic modes or structural heterogeneities are causing the tracer microrheology data to underestimate the complex viscoelastic modulus plateau modulus (overestimate the creep compliance)

The high frequency elastic modulus is one of the most direct probes of interparticle interaction potentials at short distances. The dependence of the high frequency elastic modulus on the intermicellar separation distance was studied as a means of investigating interparticle interactions in the soft crystals. It was observed that there is a strong dependence of the high frequency elastic modulus on the intermicellar separation distance. On attempting to model this dependence with a host of different interparticle interaction potentials, it was observed that the actual interaction potential exhibited a behavior that was intermediate to the hard and soft sphere type associated with similar systems. A definitive conclusion however cannot be drawn at this stage due to the accuracy of the estimated structural parameters and the use of a perfect crystal structure factor in model calculations. The high frequency elastic modulus, as determined through tracer microrheology studies, exhibited a slight frequency dependence that diminished

with increasing Pluronic™ F108 concentration. This is most likely due to the formation of stronger gels with increasing concentration. The frequency dependence observed here was weaker than that expected for a purely hard sphere dispersion. This may be a consequence of the softer intermicellar interactions in this system.

*8.1.3.3 Static Light Scattering:* This chapter has reported on a detailed static light scattering investigation into the Pluronic F108 system. Concentrations were chosen such that the entire phase range from isotropic micellar solution to an ordered FCC cubic phase could be investigated. The scattered intensity as investigated through the extracted zero angle Rayleigh Ratio showed an essentially monotonic increase with concentration until reaching the highest concentrations where it remains essentially unchanged. The zero angle Rayleigh ratio increase could primarily be attributed to increasing concentrations. A major concern was the strong angular dependence of the scattered intensity at low  $q$  wavevectors. An Ornstein-Zernicke fit of the high concentration regime indicated that the correlations lengths are extremely large. This indicates that  $R_{\square}(q) \sim q^{-2}$  which means  $q^2 \lambda^2 \gg 1$ . This makes the accuracy of the  $\square R_0$  values questionable. Although the magnitudes may vary, the qualitative trends in the data are however not expected to change dramatically. The osmotic compressibility and osmotic pressures were therefore extracted in order to gain a qualitative understanding of the behavior. It was observed that the osmotic compressibility increased up to 6wt% after which it remained essentially constant and then decreased at the higher concentrations. It is expected that  $\square \Pi / \square c$  should increase with increasing concentration, due to the increasing micellar interactions associated with increasing concentrations, thereby indicating that the extrapolated  $\square R_0$  values are not accurate, especially at high concentrations.

## ***8.2 Recommendations for Future Work:***

The three complex fluid systems investigated all exhibited interesting viscoelastic properties. The PEO system tracer microrheology and mechanical rheometry were in excellent agreement. Sphere size sweeps carried out on this system also led to a collapse of the creep compliance data, indicating that longitudinal dynamical modes are not affecting the extracted viscoelastic data. It would however be interesting to carry out temperature sweeps on this and other simple polymeric systems in order to investigate how the agreement between mechanical rheometry and tracer microrheology is affected as the solvent quality changes.

The two other investigated systems, the CTAB/NaSal wormlike micellar system and the Pluronic<sup>™</sup> F108 system both exhibit interesting viscoelastic behavior and also exhibited deviations from mechanical rheometry measurements. There is therefore requirements for further investigations on these systems. The recommended future experimental requirements for these two systems are as follows:

52. CTAB/NaSal worm like micellar system. Tracer microrheology exhibited deviations from mechanical rheometry measurements, Sphere size sweeps and tracking of the deviation with the bulk longitudinal elastic modulus indicate the possible role of the longitudinal dynamical modes on the extracted parameters. There are however certain other factors which need to be better understood in order to draw definitive conclusions with regard to the deviations. These are the effect of local heterogeneities in the system and the effect of the probe particles themselves. These will need to be investigated through cross correlation video particle trackking.

53. Pluronic<sup>TM</sup> F108 system: Tracer microrheology exhibited very interesting viscoelasticity and exhibited significant deviations from the mechanical rheometry measurements. The high frequency behavior indicates that the interaction potential in this system is in between a hard sphere and a soft sphere potential. However, this cannot be fully ascertained until an experimental determination of the actual structural parameters and radial distribution function are carried out. X-ray scattering studies are already planned by which the determination of these parameters can be achieved. In this respect it would also be interesting to look at other Pluronic<sup>TM</sup> systems which form crystals of different architecture and examine the utility of tracer microrheology for drawing conclusions with regard to the intermicellar interaction potentials through investigation of the high frequency behavior. In this regard, the effect of temperature on these systems should also be examined. The effects of local heterogeneity in these systems should be examined through cross correlation video particle tracking. However, the extremely slow motion of the probe particles in the system may preclude the use of the video particle tracking technique due to poor resolution of probe Brownian motion.

## **APPENDICES**

## APPENDIX A

FORTRAN Program to Evaluate Mean Squared Displacement from Correlation Function

!This Program evaluates the Mean Square Displacement from the  
!Correlation Function

```
Parameter(J=1000)
Character (len=20)::filename,MSDOutput
Real
qa,qb,qe,qp,q1,g1,g1acalc,g1adiff,g1bcalc,g1bdiff,g1pcalc,g1pdiff,gr(J),DELR(J),tol,L,LS,qc,T,I
,M
```

```
Integer status,nvals,p,k
```

```
nvals=1
```

```
write(*,*) 'Please Enter, Path Length of Cell, L*'
Read*, L,LS
```

!The following part of the program reads in the correlation function data from a file  
!specified by the user. It also gives error messages in the event that the file could  
!not be opened.

```
write(*,*)'Please enter the filename of the file containing the DWS Data'
```

```
Read(*,*) filename
```

```
Open(UNIT=3,File=filename,Status='old',Action='Read',IOSTAT=status)
```

```
openif:IF(status==0)Then
```

```
readloop:do
```

```
Read (3,*,IOSTAT=status)gr(nvals)
```

```
IF(status/=0)EXIT
```

```
nvals=nvals+1
```

```
enddo readloop
```

```
readif:If(status>0)then
```

```
write(*,88)nvals+1
```

```
88 Format('0','An error occured reading line', I6)
```

```
Else
```

```
Write(*,99)nvals
```

```
99 Format(' ','End of File Reached. There were',I6,'values in the file')
```

```
End if readif
```

```
Else openif
```

```
write(*,45)status
```

```
45 Format(' ','Error opening file:IOSTAT=',I6)
```

```
ENDif openif
```

```
Close(3)
```

!The main calculation part of the program begins from this point onwards.

!The value of the mean squared displacement is calculated using the Bisection

!method for determination of a root.

```
tol=0.00001
```

```
!
!Determination of the correlation function normalization coefficient
!
```

```
    q1=0.0
    Call Simp(q1,g1,L,LS)
    M=g1
    write(*,*)M
do 33 p=1,nvals
```

```
!
!This is where we set the endpoints for the bisection algorithm. The difference
!function must be negative at one point and positive at the other point. The pertinent
!quantities are all calculated via the Simpson's rule subroutine.
!
```

```
    if (gr(p).ge.1) then
        qp=0.00
        g1pcalc=1.0
        g1pdiff=0.0
        go to 77
    else
        do 47 k=1,p-1
            if (gr(p).eq.gr(k)) then
                DELR(p)=DELR(k)
                go to 78
            else
                goto 47
            endif
        47          continue
    endif
```

```
!
51    pi=4*atan(1.0)
    qa=0.1d-4
    qb=19.99
!
! write(*,62) qa,qb
! 62    format(e14.6,2x,e14.6)
!
    q1=qa
    Call Simp(q1,g1,L,LS)
    g1acalc=g1/M
    g1adiff=gr(p)-g1acalc
    q1=qb
    Call Simp(q1,g1,L,LS)
    g1bcalc=g1/M
    g1bdiff=gr(p)-g1bcalc
!
! write(*,66)g1acalc,g1bcalc,g1adiff,g1bdiff
! 66    format(e14.6,2x,e14.6,2x,e14.6,2x,e14.6)
!
```

!This is where the bisection point is calculated and the various decisions of the bisection algorithm are made. The iterations stop when the difference between the endpoints reaches a very small value (1e-5).

```

!
98      qp=qa+(qb-qa)/2
      If (abs(qa-qb).LT.tol) then
!
!      write(*,63)
! 63      format('We are in the then part')
      goto 77
      else
!
!      write(*,64)
! 64      format('We are in the else part')
      q1=qp
      Call Simp(q1,g1,L,LS)
      g1pcalc=g1/M
      g1pdiff=gr(p)-g1pcalc
!
!      write(*,92)qa,qb,qp,g1adiff,g1bdiff,g1pdiff
! 92      format(e14.6,2x,e14.6,2x,e14.6,2x,e14.6,2x,e14.6,2x,e14.6)
      if ((g1adiff*g1pdiff).gt.0.d0) then
          qa=qp
          g1adiff=g1pdiff
          goto 98
      else
          qb=qp
          g1bdiff=g1pdiff
          goto 98
      endif
!
!      write(*,61) q1,q2,g1,g2
! 61      format(e14.6,2x,e14.6,2x,e14.6,2x,e14.6)
!
!      goto 20
      endif
77      DELR(p)=((qp*532e-7*LS)/(L*2*pi))**2
78      Write(*,*)gr(p),g1pcalc,g1pdiff,DELR(p)
      open(unit=8,file='MSDOutput',status='old')
      write(8,41) DELR(p)
41      format(e14.6,5x)
33      continue
      STOP
      END

```

! The Subroutine Simp Calculates the values of the Correlation Functions  
! for the point to point geometry using the guessed values of Q.  
! The integration in the expression is evaluated using Simpson's 1/3 rule.

```

SUBROUTINE SIMP(q1,g1,L,LS,M)
Parameter (J=1000)
Real ODD, q1,g1,L,LS,M,T,I,EVEN

```

```

INTEGER p
DELTAX=0.0001
qe=20.0
N=REAL(N)
N=(qe-q1)/DELTAX
N=INT(N)
IF(MOD(N,2).EQ.1)N=N+1
N=REAL(N)
qe=(N*DELTAX)+q1
! Compute end terms
IF (q1.eq.0)Then
EN=0.0+F(qe,L,LS)
ELSE
EN=(F(q1,L,LS)+F(qe,L,LS))
ENDIF
! Compute odd terms
ODD=0
do 11 z=q1+DELTAX, qe-DELTAX, 2*DELTAX
    ODD=ODD+F(z,L,LS)
11 Continue
! Compute Even Terms
EVEN=0
do 22 z=q1+2*DELTAX, qe-2*DELTAX, 2*DELTAX
    EVEN=EVEN+F(z,L,LS)
22 Continue
! Calculate Area using Simpson's 1/3 Rule
g1=((DELTAX/3)*(EN+4*ODD+2*EVEN))
Return
End

```

```

Real Function F(x,L,LS)
Real Num,T,I,L,LS
E=(2*LS)/(3*L)
Y=(LS)/(L)
B=exp(-2*Y*x)
C=exp(-2*x)
G=(1+E*x)
H=(1-E*x)
I=exp(-(1-Y)*x)
Num=2*E*(G-H*B)
Den=(G**2)-((H**2)*C)
T=Num/Den
F=T*I*x
Return
End

```

## APPENDIX B

This Program Computes the viscoelastic parameters from the mean squared displacement. This program was done primarily by Chris Kloxin. It is included here for the sake of completeness.

```
%=====
% A script to read in words from a .txt file
%=====
clear
close all
format short g
warning off

move_all_files = 1;
delete_input_file = 1; %from current directory
user_define_file = 1;
units_cgs = 1;

% Define physical constants =====
kB = 1.38048e-23; %J/deg
% Experimental param & data conversion =====
T = 298; % temperature in Kelvin
MeanSqConvert = 1e-4; %Data comes in as cm^2
TimeConvert = 1; %Data comes in as seconds
UnitCreepConvert = 100*100/1e5; %Convert from SI to CGS (m2/N to cm2/dynes)
%
%=====
==

if user_define_file == 1;
    fprintf('Enter name of tab delimited file, including extention\n');
    %fprintf(' File must be in the format of: time [tab] mean sq disp\n');
    input_file = input('>> ','s');
    if exist(input_file)
        %void disp('file exist')
    else
        error(' File not found in current directory');
    end
    fprintf('Enter diameter of sphere (in mirons):\n')
    done = 0;
    while ~done
        input_diameter = input('>> ');
        if isnumeric(input_diameter);
            done = 1;
        end
    end
end
```

```

else
    fprintf(' -- Diameter must be numeric --\n');
    fprintf(' Re-enter diameter of sphere (in microns)\n');
end
end
else
    input_file = 'peo_test.txt';
    input_diameter = 1; %micron
end
a = input_diameter*1e-6/2; %Convert: sphere diameter (um) to sphere radius (m)
MeanSq2Creep = pi*a/kB/T; %Converts Mean square Displacement to Creep assuming SI units
if units_cgs == 1
    MeanSq2Creep = MeanSq2Creep*UnitCreepConvert;
end

% ===== MUST BE CHANGED WHEN INSTALLED
% =====
CURRENT_DIR = 'c:\samiul';
TEST_DIR = cd;
if ~isequal(lower(TEST_DIR),lower(CURRENT_DIR))
    error('File not installed in proper folder');
end
% =====

FNAME = 'ftikreg';
Fname.sol = [FNAME '.sol'];
if exist(Fname.sol);COMMAND = ['del ' Fname.sol];dos(COMMAND);end
Fname.adp = [FNAME '.adp'];%delete(Fname.adp);
if exist(Fname.adp);COMMAND = ['del ' Fname.adp];dos(COMMAND);end
Fname.dat = [FNAME '.dat'];%delete(Fname.dat);
%if exist(Fname.dat);COMMAND = ['del ' Fname.dat];dos(COMMAND);end
Fname.csv = [FNAME '.csv'];%delete(Fname.txt);
if exist(Fname.csv);COMMAND = ['del ' Fname.csv];dos(COMMAND);end
Fname.par = [FNAME '.par'];%delete(Fname.par);
if exist(Fname.par);COMMAND = ['del ' Fname.par];dos(COMMAND);end
Fname.exe = 'reg_prog.exe';

%INPUT DATA=====
RAW = load(input_file,'t');
RAW(:,1) = RAW(:,1)*TimeConvert;
MeanSqDisp = RAW(:,2);
RAW(:,2) = RAW(:,2)*MeanSqConvert*MeanSq2Creep;
L_raw = length(RAW);
fp00 = fopen(Fname.dat,'w');
for i = 1:L_raw

```

```

    fprintf(fp00,'%g\t%g\r\n',RAW(i,1),RAW(i,2));
end
fclose(fp00);
lower_value = ceil(log(RAW(1,1)));
upper_value = floor(log(RAW(L_raw,1)));
firstval = upper_value - lower_value + 1;

II = firstval;
Param(1).value = II;    %number of points
Param(1).note = 'ns';
Param(2).value = lower_value;    Param(2).note = 'smin';
Param(3).value = upper_value;    Param(3).note = 'smax';
Param(4).value = 1;    Param(4).note = 'dismod';
Param(5).value = 2;    Param(5).note = 'm';
Param(6).value = L_raw;    Param(6).note = 'n';
Param(7).value = 1;    Param(7).note = 'ne';
Param(8).value = 23;    Param(8).note = 'errmod';
Param(9).value = 1;    Param(9).note = 'error';
Param(10).value = 222;    Param(10).note = 'regmod';
Param(11).value = 0;    Param(11).note = 'lambda';
Param(12).value = 1;    Param(12).note = 'infmod';
Param(13).value = -10;    Param(13).note = 'lambst';
Param(14).value = 1;    Param(14).note = 'lambsp';
Param(15).value = 12;    Param(15).note = 'lambra';
Param(16).value = 1.00E-08;    Param(16).note = 'lampr';
Param(17).value = 200;    Param(17).note = 'lambit';
fp01 = fopen(Fname.par,'w');
for i = 1:17
    fprintf(fp01,'%g\t%s\r\n',Param(i).value,Param(i).note);
end
fclose(fp01);

% ===== DOS CALL TO FUNCTION =====
dos(Fname.exe);
% =====

LinParam = load(Fname.adp,'\t');
Je = LinParam(1,2);
eta = 1/LinParam(2,2);

% word ripper BEGIN
=====
fid = fopen(Fname.sol);    % assign handle to fid
[A,count] = fscanf(fid,'%c',inf); % get all characters in file as an array
fclose(fid);    % close file handle

```

```

k = 0;
%finds if the first character is a space or not
if ~isspace(A(1))
    k = k + 1;
    word = 1;
    STORE(k).fname = A(1);
else
    word = 0;
end

%Assigns words in file to structure STORE.fname
for i = 2:count
    if isspace(A(i))&(word == 1);    %finds if is a space immediately after word
        word = 0;
    elseif ~isspace(A(i))&(word == 0); %finds start of a word
        k = k + 1;
        word = 1;
        STORE(k).fname = A(i);    %assigns first letter of new word
    elseif ~isspace(A(i))&(word == 1); %finds if in a word
        STORE(k).fname = [STORE(k).fname A(i)]; %builds rest of the word
    end
end
end
% Word ripper END
=====

N = k;
j = 0;
COL_OF_DATA = 4;
for i = 1:COL_OF_DATA:N
    j = j + 1;
    TAU(j) = str2num(STORE(i).fname);
    L(j) = str2num(STORE(i+1).fname);
end
TAU = exp(TAU);

time = RAW(:,1);
num_pts = length(time);
num_taus = N/COL_OF_DATA;
for i = 1:num_pts
    J(i) = Je + time(i)/eta;
    for j = 1:num_taus
        J(i) = J(i) - L(j)*exp(-time(i)/TAU(j));
    end
end

%===== G prime/ G double prime =====
num_freqs = 100;

```

```

w = logspace(floor(log10(1/RAW(L_raw,1))),ceil(log10(1/RAW(1,1))),num_freqs);
clear i j k
for i = 1:num_freqs
    G_star_sum = 0;
    for k = 1:num_taus
        G_star_sum = G_star_sum + L(k)*TAU(k)*j*w(i)/(1+TAU(k)*w(i)*j);
    end
    G_star(i) = 1/(Je-G_star_sum+(1/eta/j/w(i)));
end
G_real = real(G_star);
G_imag = imag(G_star);
G_modulus = sqrt(G_real.^2 + G_imag.^2);
subplot(2,1,1);
loglog(w,G_real,'-r',w,G_imag,'-b');
legend('G''','G''''',4);
xlabel('\omega');ylabel('Elastic and viscous modulus');
subplot(2,1,2);
loglog(w,G_modulus);
xlabel('\omega');ylabel('Complex shear modulus');
figure

% =====Alpha Calc =====
for i = 1:num_pts
    top_sum = 0;
    bottom_sum = 0;
    for j = 1:num_taus
        top_sum = top_sum + L(j)/TAU(j)*exp(-time(i)/TAU(j));
        bottom_sum = bottom_sum + L(j)*exp(-time(i)/TAU(j));
    end
    ALPHA(i) = time(i)*(top_sum + 1/eta)/(Je - bottom_sum + time(i)/eta);
end
semilogx(time,ALPHA);
xlabel('time (s)');ylabel('\alpha');
figure

% ===== Velocity Auto Calc =====
c_cross = 1/MeanSqConvert/MeanSq2Creep;
for i = 1:num_pts
    first_sum = 0;
    last_sum = 0;
    for j = 1:num_taus
        first_sum = first_sum + L(j)*exp(-time(i)/TAU(j));
        last_sum = last_sum + L(j)/TAU(j)*exp(-time(i)/TAU(j));
    end
    VelAuto(i) = c_cross/6/time(i)*(Je/time(i) - 1/time(i)*first_sum - time(i)*last_sum);
end

```

```
loglog(time, VelAuto);title('Velocity Autocorrelation Function');xlabel('time
(s)');ylabel('VelAuto');figure;
```

```
% OUTPUT DATA TO FILE =====
```

```
fp = fopen(Fname.csv,'w');
fprintf(fp,'%s\r\n',date);
fprintf(fp,'Data in the form: F = Je + t/eta - sum(L*exp(-t/tau))\r\n\r\n');
fprintf(fp,'Je = ,%g,eta = ,%g\r\n\r\n',Je,eta);
fprintf(fp,',TAU,L\r\n');
for i = 1:N/COL_OF_DATA
    fprintf(fp,',%g,%g\r\n',TAU(i),L(i));
end
fprintf(fp,'\r\nLIST OF DATA\r\n\r\n');
fprintf(fp,'TIME,DATA,CREEP,ALPHA, VelocAuto\r\n');
for i = 1:num_pts
    fprintf(fp,'%g,%g,%g,%g,%g\r\n',time(i),RAW(i,2),J(i),ALPHA(i),VelAuto(i));
end
fprintf(fp,'\r\n\r\nomega,G",G""',MODULUS\r\n');
for i = 1:num_freqs
    fprintf(fp,'%g,%g,%g,%g\r\n',w(i),G_real(i),G_imag(i),G_modulus(i));
end
fclose(fp);
```

```
%===== Display fit and retardation spectrum =====
```

```
ScrSize = get(0,'ScreenSize');
subplot(2,1,1);
loglog(time,J,'b-',time,RAW(:,2),'r*','LineWidth',3,'MarkerSize',2);
title('Data and Fit');xlabel('Time (s)');
if units_cgs == 1
    ylabel('Creep (dynes/cm^2)^{-1}');
else
    ylabel('Creep (N/m^2)^{-1}');
end
```

```
subplot(2,1,2);
loglog(TAU,L,'o');
title('Retardation Spectrum');xlabel('\tau (s)');
if units_cgs == 1
    ylabel('L(\tau) (dynes/cm^2)^{-1}');
else
    ylabel('L(\tau) (M/m^2)^{-1}');
end
```

```
ylabel('L(\tau) (dynes/cm^2)^{-1}');
set(gcf,'Position',[ScrSize(3)/2 32 ScrSize(3)/2 (ScrSize(4)-100)])
drawnow
```

```

if move_all_files == 1 %=====
    CLOCK = clock;
    year = num2str(CLOCK(1));
    month = num2str(CLOCK(2));
    if length(month) == 1;month = ['0' month];end
    day = num2str(CLOCK(3));
    if length(day) == 1;day = ['0' day];end
    hour = num2str(CLOCK(4));
    if length(hour) == 1;hour = ['0' hour];end
    hour = ['_' hour];
    min = num2str(CLOCK(5));
    if length(min) == 1;min = ['0' min];end
    sec = num2str(floor(CLOCK(6)));
    if length(sec) == 1;sec = ['0' sec];end
    FOLDER = [year month day hour min sec];
    LABEL = [year month day];
    fprintf('Would you like to append title to output file (Y/N)? : \n');
    FoldAppend = input('>> ','s'); % File name
    if isempty(FoldAppend)|isequal(lower(FoldAppend),'n')|isequal(lower(FoldAppend),'no');
        FoldAppend = '';%void
    else
        if isequal(lower(FoldAppend),'y')|isequal(lower(FoldAppend),'yes')
            fprintf('Enter name to be appended\n')
            FoldAppend = input('>> ','s');
            FoldAppend = ['_' FoldAppend];
            FOLDER = [FOLDER FoldAppend];
        else
            FoldAppend = ['_' FoldAppend];
            FOLDER = [FOLDER FoldAppend];
        end
    end
    dir_made = mkdir(FOLDER);
    if dir_made == 2
        error(' Directory already exists');
    elseif dir_made == 0
        error(' Error in making directory');
    end
    NEW_DIR = [CURRENT_DIR '\ FOLDER];
    SOURCE = [CURRENT_DIR '\ Fname.csv];DEST = [NEW_DIR '\
Fname.csv];copyfile(SOURCE,DEST);
    if delete_input_file == 1;COMMAND = ['del ' Fname.csv];dos(COMMAND);end
    COMMAND = ['ren ' NEW_DIR '\ Fname.csv ' LABEL FoldAppend
'_out.csv'];dos(COMMAND);
    SOURCE = [CURRENT_DIR '\ Fname.sol];DEST = [NEW_DIR '\
Fname.sol];copyfile(SOURCE,DEST);

```

```

COMMAND = ['del ' Fname.sol];dos(COMMAND);
COMMAND = ['ren ' NEW_DIR '\ ' Fname.sol ' ' LABEL FoldAppend
'_regdata.txt'];dos(COMMAND);
SOURCE = [CURRENT_DIR '\ ' Fname.adp];DEST = [NEW_DIR '\
Fname.adp];copyfile(SOURCE,DEST);
COMMAND = ['del ' Fname.adp];dos(COMMAND);
COMMAND = ['ren ' NEW_DIR '\ ' Fname.adp ' ' LABEL FoldAppend
'_regconstants.txt'];dos(COMMAND);
SOURCE = [CURRENT_DIR '\ ' Fname.par];DEST = [NEW_DIR '\
Fname.par];copyfile(SOURCE,DEST);
COMMAND = ['del ' Fname.par];dos(COMMAND);
COMMAND = ['ren ' NEW_DIR '\ ' Fname.par ' ' LABEL FoldAppend
'_regparam.txt'];dos(COMMAND);
SOURCE = [CURRENT_DIR '\ ' Fname.dat];DEST = [NEW_DIR '\
Fname.dat];copyfile(SOURCE,DEST);
COMMAND = ['del ' Fname.dat];dos(COMMAND);
COMMAND = ['ren ' NEW_DIR '\ ' Fname.dat ' ' LABEL FoldAppend
'_reginput.txt'];dos(COMMAND);
SOURCE = [CURRENT_DIR '\ ' input_file];DEST = [NEW_DIR '\
input_file];copyfile(SOURCE,DEST);
end % if move_all_files is on
=====

```